Quantum Acoustics with high-overtone bulk resonators and superconducting qubits
High-Q planar devices, phononlasers, and quantum ghosts

Franse, W.J.M.

DOI
10.4233/uuid:55a416e1-4310-44e8-be98-3ccb7f82e5a0

Publication date
2024

Document Version
Final published version

Citation (APA)
Franse, W. J. M. (2024). *Quantum Acoustics with high-overtone bulk resonators and superconducting qubits: High-Q planar devices, phononlasers, and quantum ghosts*. [Dissertation (TU Delft), Delft University of Technology]. https://doi.org/10.4233/uuid:55a416e1-4310-44e8-be98-3ccb7f82e5a0

Quantum Acoustics with high-overtone bulk resonators and superconducting qubits

High-Q planar devices, phonon lasers, and quantum ghosts

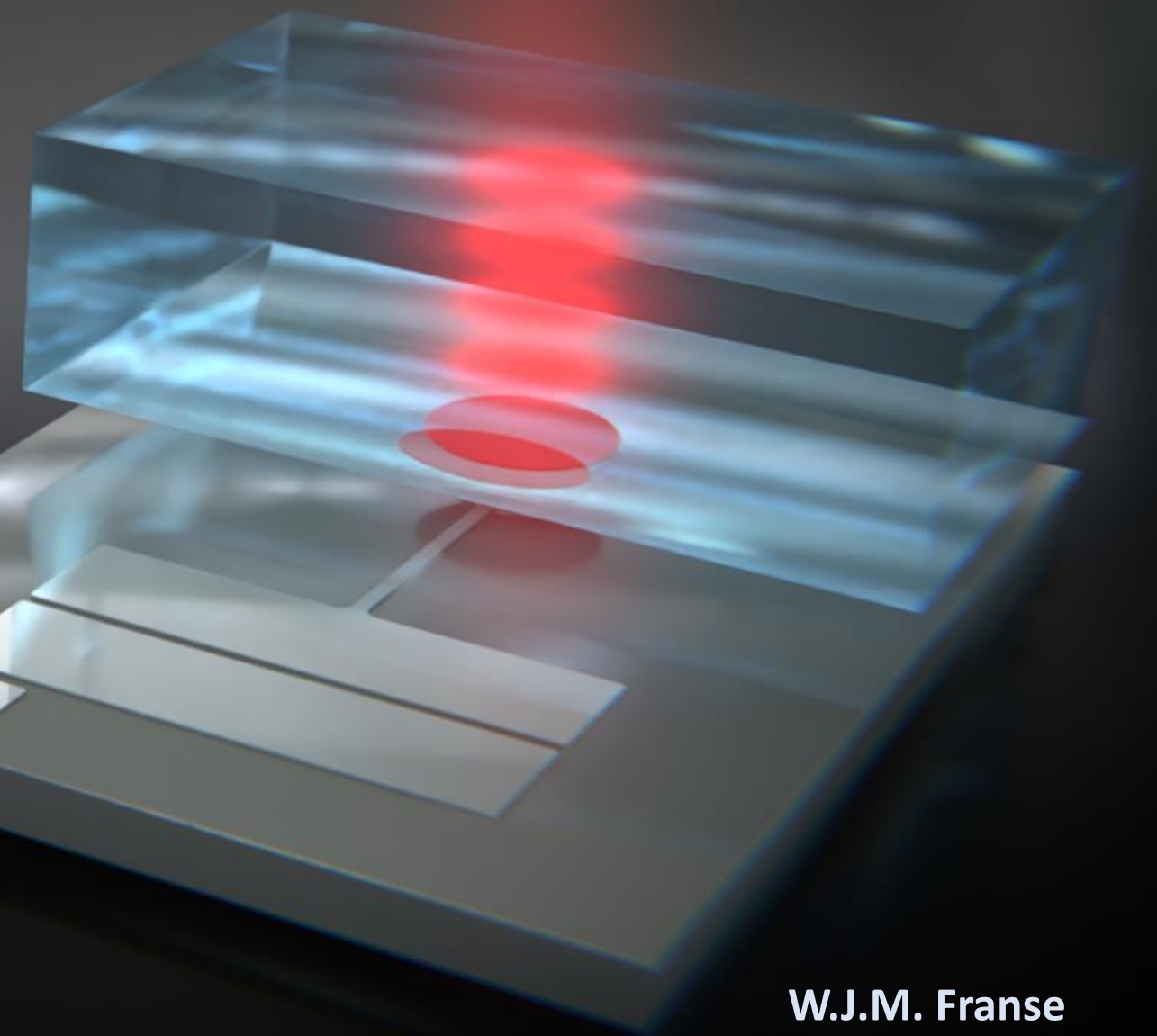

W.J.M. Franse

Quantum Acoustics with high-overtone bulk resonators and superconducting qubits

High-Q planar devices, phonon lasers, and quantum ghosts

Quantum Acoustics with high-overtone bulk resonators and superconducting qubits

High-Q planar devices, phonon lasers, and quantum ghosts

Dissertation

for the purpose of obtaining the degree of doctor
at Delft University of Technology
by the authority of the Rector Magnificus, prof.dr.ir. T.H.J.J. van der Hagen
chair of the Board for Doctorates
to be defended publicly on
Friday 16 February 2024 at 10:00 o'clock

by

Wilfred Jasper Maria Franse

Master of Science in Applied Physics,
Delft University of Technology,
born in Haarlem, The Netherlands

This dissertation has been approved by the promotors.

Composition of the doctoral committee:

Rector Magnificus,	chairperson
Prof. dr. G.A. Steele	Delft University of Technology, promotor
Prof. dr. S. Gröblacher	Delft University of Technology, copromotor

Independent members:

Prof. dr. Y. Chu	ETH Zürich, Switzerland
Prof. dr. M. Sillanpää	Aalto University, Finland
Dr. R.A. Norte	Delft University of Technology
Prof. dr. P.G. Steeneken	Delft University of Technology
Prof. dr. Ir. W.G. van der Wiel	University of Twente, The Netherlands
Prof. dr. Y.M. Blanter	Delft University of Technology, reserve member

Keywords: cQAD, cQED, HBAR, Highovertone bulk acoustic resonator (HBAR), Quantum acoustic, qubit, superconducting, Transmon

Printed by: Gildeprint, Enschede

Front & Back: Artistic depiction of a planar superconducting transmon qubit coupled to a sapphire HBAR, conceived by Enrique Sahagún.

Casimir PhD Series, Delft-Leiden 2023-43

ISBN 978-90-8593-588-9

An electronic version of this dissertation is available at
http://repository.tudelft.nl/.

For Samantha and our little girl

If you think you understand quantum mechanics,
you don't understand quantum mechanics.

Richard P. Feynman

Contents

Summary

The field of quantum acoustics studies high frequency sounds generated at low temperatures such that quantum mechanical effects become relevant. The studies mainly revolves around propagating quantized sound waves, or phonons, a collective excitation of atoms in solids or liquids. In quantum acoustics, the engineering and design tools described by circuit quantum acoustodynamics (cQAD) are used to develop quantum acoustic devices that are coupled to superconducting qubits. cQAD enabled the demonstrations of quantum ground state cooling mechanical objects, generating mechanical Fock-states, and Schrödinger cat states of motion. This makes quantum acoustic devices appealing candidates for applications such as quantum metrology, information processing, and quantum memory.

This thesis focuses on the coupling between a planar superconducting transmon qubit and a high-overtone bulk acoustic resonator (HBAR) and explore its possibilities. Here, experimental demonstrations are shown where the transmon is used to drive the HBAR into a phonon lasing state making it a *superconducting single-atom phonon laser*. Furthermore, the transmon-HBAR device is used to probe the nature of *ghost modes* observed in strongly driven nonlinear systems.

Chapter 1 will give a broad introduction to quantum acoustics along with a description of the advances in the field. Here, the goals and applications of planar superconducting transmon qubits coupled to HBARs will be outlined.

Chapter 2 will present the theoretical background and necessary tools for understanding the physical principles of the systems explored in this work. It starts by providing a detailed explanation and derivation for the transmon qubit Hamiltonian, describes the HBAR and its properties, and ends with an expression for the piezoelectric transmon-HBAR coupling.

Chapter 3 centers around the design and fabrication of the transmon-HBAR device utilized in this work. It starts with the description of using *qiskit-metal* to design the device followed by explanations of design considerations. Lastly, the chapter will focus on nanofabrication techniques and used setups needed to realize and measure the device.

Chapter 4 will be the first chapter to present experimental results, where the planar transmon - HBAR device was used to demonstrate the realization of a superconducting single-atom phonon laser using a flip-chip HBAR architecture. Gated two-tone spectroscopy shows that the qubit's ringdown gets extended due to re-excitement of the phonon mode in the lasing state, which exchanges excitations back into the qubit when qubit drive is switched off. Here, master equation simulations are used to fully describe the system and its lasing properties.

Chapter 5 provides a follow-up study of the phonon laser, where a mean-field solution is used to further explore the parameter space of the transmon-HBAR device in the acoustically induced transparency (AIT) regime. The mean-field solution is further used to give means to AIT systems being in the high-cooperativity and weak-coupling regime and their importance for creating a phonon laser.

Chapter 6 presents a phenomenological study on qubits that are strongly driven with a pump tone. Strong drive tones result in the emergence of subharmonic parametric excitations and *ghost modes* of the qubit ground-to-excited state manifold. Quantum acoustics is used to probe the nature of ghost modes, which shows that these do not interact with real systems.

Chapter 7 concludes the work done in this thesis with an overview of the performed investigations and outline future prospects in the field of quantum acoustics using transmon-HBAR devices.

Samenvatting

Het vakgebied van kwantumakoestiek bestudeert hoogfrequente geluiden die bij lage temperaturen worden gegenereerd waarbij kwantummechanische effecten relevant worden. Hierin draait het onderzoek met name om voortbewegende gekwantiseerde geluidsgolven ofwel fononen, een collectieve excitatie van atomen in vaste of vloeibare stoffen. In kwantumakoestiek worden ontwerptechnieken beschreven door circuit-kwantum-akoestodynamica die gebruikt wordt om kwantum-akoestische apparaten te ontwikkelen en te koppelen aan supergeleidende qubits. circuit-kwantum-akoestodynamica maakte demonstraties mogelijk waarbij mechanishe objecten zijn gekoeld naar kwantum-grondtoestanden, mechanische Fock-toestanden en Schrödinger cat-bewegingstaten werden gegenereerd. Dit maakt kwantum-akoestische apparaten aantrekkelijke kandidaten voor toepassingen zoals kwantum metrologie, kwantum informatie verwerking en kwantum geheugen.

Dit proefschrift richt zich op de koppeling tussen een planaire supergeleidende transmon qubits en een hoge-boventoon bulk akoestische resonator (HBAR) en onderzoekt diens toepassingsmogelijkheden. Hier worden experimentele demonstraties getoond waarbij de transmon wordt gebruikt om de HBAR in een fonon laserstaat te brengen, waardoor het een *fononlaser gekoppeld aan een supergeledenden enkele kunstmatige atom* wordt. Bovendien wordt het transmon-HBAR-apparaat gebruikt om de aard van *spookmodi* te onderzoeken die worden waargenomen in sterk aangedreven niet-lineaire systemen.

Hoofdstuk 1 zal een brede introductie geven over het onderzoeksveld van kwantumakoestiek, samen met een beschrijving van recente vooruitgangen behaald binnen het veld. Hier zullen ook de doelen en toepassingen van planaire supergeleidende transmon-qubits gekoppeld aan HBAR's worden geschetst.

Hoofdstuk 2 zal de theoretische achtergrond en noodzakelijke hulpmiddelen presenteren die nodig zijn voor het begrijpen van de fysica die in dit werk worden onderzocht. Het begint met het geven van een gedetailleerde uitleg en afleiding voor de Hamiltoniaan van een transmon qubit, beschrijft de HBAR en diens eigenschappen, en eindigt met een uitdrukking voor de piëzo-elektrische koppeling tussen de transmon en HBAR.

In **Hoofdstuk 3** staat het ontwerp en de fabricage van de transmon-HBAR dat in dit werk wordt gebruikt centraal. Het begint met een gebruiksomschrijving van *qiskit-metal* om de transmon-HBAR te ontwerpen, gevolgd door een uitleg over de ontwerpoverwegingen. Ten slotte zal het hoofdstuk zich richten op de nanofabricage en gebruikte meetopstellingen die nodig zijn om het apparaat te realiseren en te meten.

Hoofdstuk 4 zal het eerste hoofdstuk zijn waarin experimentele resultaten worden gepresenteerd, waarbij de planaire transmon-HBAR werd gebruikt voor een realisatie demonstratie van een supergeleidende enkele atoom fononlaser met één atoom met behulp van een flip-chip HBAR architectuur. Twee tonige poort spectroscopie laat zien dat de ringdown van de qubit wordt verlengd als gevolg van de fononmodus in zich in een laserstatus bevind. Deze wisselt excitaties terug de qubit in wanneer de qubit aandrijving wordt uitgeschakeld. In dit

hoofdstuk worden master equation simulaties gebruikt om het systeem en zijn lasereigenschappen volledig te beschrijven.

Hoofdstuk 5 vertoont een vervolgstudie van de fononlaser, waarbij een mean-field oplossing wordt gebruikt om de parameterruimte van het transmon-HBAR apparaat in het akoestisch inducerende transparantie (AIT) regime verder te onderzoeken. De mean-field oplossing wordt verder gebruikt om handvaten te geven aan AIT-systemen die zich in het hogecoöperatieve en zwakke-koppelingsregime bevinden en diens belang voor het creëren van een fononlaser.

Hoofdstuk 6 presenteert een fenomenologisch onderzoek naar qubits die sterk worden aangedreven met een pomptoon. Sterke aandrijvingstonen resulteren in de opkomst van subharmonische parametrische excitaties en *spookmodi* van de qubit's grond-naar-eerste-excitatie toestand. Kwantumakoestiek wordt gebruikt om de aard van spookmodi te onderzoeken, waaruit blijkt dat deze geen interactie hebben met echte wereldlijke systemen.

Hoofdstuk 7 sluit het werk in dit proefschrift af met een overzicht van de uitgevoerde onderzoeken en schetst toekomstperspectieven op het gebied van kwantumakoestiek met behulp van transmon-HBAR apparaten.

1

Introduction

Every mountain top is within reach
if you just keep climbing.

Barry Finlay, *Building across Hoofddorp train station*

The chapter starts with a historical overview on the relatively new field of quantum acoustics. Here, we describe achievements accomplished by the field and work our way to state-of-the-art devices. Following this, we focus on the main research themes presented in this work. We end the chapter with an outline of this thesis.

1

1.1. Quantum acoustics: a brief history

Piezoelectric materials, in particular piezoelectric ceramics, are one of the world's most utilized (machine) elements. Ever since the discovery of the *direct piezoelectric effect* in 1880 by the brothers Curie [1], who described this property as electric surface charge appearance due to deformation under external pressure, the piezoelectric element has been incorporated in numerous devices. Not only because of its use as sensor, e.g. pressure, from which electrical signals are measured, but also for its inverse use. The inverse effect is described, by the Curie brothers as well in 1881, as the *indirect piezoelectric effect* where an electrical charge on the surface deforms the piezoelectric. From its first practical use during World War I in sonar [2], to the mechanical shocks found in lighters, and sensors in weight scales, piezoelectrics are found all around us. Most people might only recognize piezoelectric materials as the "*buzzing elements*" in phones, alarm clocks, medical devices, and many more where it is also referred to piezoelectric transducer. Additionally, they are called electroacoustic transducers in the sense that it converts electrical energy into mechanical and vice versa, e.g. speaker and microphone, see Fig. 1.1.

Figure 1.1: Piezoelectric elements in everyday life. Piezoelectric element in middle is shown as a crystal structure with equal amount of positively and negatively charged atoms. When applying pressure (left atom schematic) a net charge appears on the surface and reversing this has the inverse effect (right atom schematic). Examples shown starting clockwise at top-left: submarine sonar, lighter, smartphone, weight scale, electroacoustic transducer, speaker, and microphone. Figures adapted from [3–9].

In recent decades, the piezoelectric transducers found their way into micro- and nanoscale devices on chips. To be more specific, they are nowadays found as electromechanical transducers in superconducting circuits in the mesoscopic scale for research in quantum physics. We fast forward to 2010, the year which we consider as the start of the field of quantum acoustics [10, 11]. This field studies the coupling of acoustic waves to superconducting quantum bits, i.e. qubits, which are artificial atoms made of superconducting materials [12]. O'Connell et al. [13] in 2010, were the first to measure the phonon number in a mesoscopic mechanical oscillator by utilizing the strong piezoelectric coupling between a superconducting qubit. Here, the piezoelectric element generated gigahertz frequency mechanical oscillations in a film bulk acoustic resonator (FBAR) and was used to swap single excitations from the qubit into the FBAR. In Fig. 1.2 we show a schematic visualization of this process.

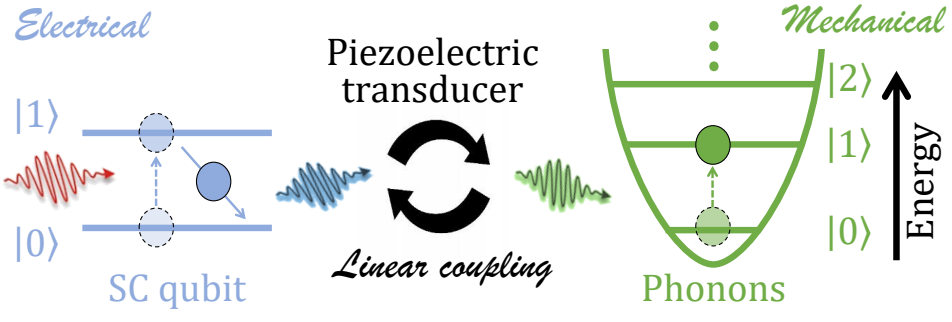

Figure 1.2: Visualization of excitation swap between SC qubit and acoustic resonator. Superconducting qubit (left) acts as a two-level system that, once excited from $|0\rangle \longrightarrow |1\rangle$ via a drive pulse (red arrow), swaps its excitation upon de-excitation (blue arrow) via the piezoelectric transducer into the acoustic resonator (right). The acoustic resonator gets excited from $|0\rangle \longrightarrow |1\rangle$ (green arrow) due to this swap.

The work done by [13] demonstrated the first quantum control at the single phonon level with a piezoelectric mechanical oscillator in the microwave regime cooled to a few millikelvin. In this design, two electrode sandwich a film of piezoelectric material as shown in Fig. 1.3.(a). In the years that followed, superconducting qubits have been coupled to multiple different forms of acoustic and mechanical resonators such as propagating surface acoustic waves (SAWs). Here, an interdigital transducer (IDT) is placed on top of a slab of piezoelectric material and converts electrical power into acoustic power in the form of a SAW. The SAWs, either propagating bidirectional [14] or confined between two Bragg mirrors [15–17], interact again with another IDT attached to a qubit on the same chip, see Fig. 1.3.(b,e). To reduce dielectric losses in the qubit, since it sits on a piezoelectric slab in previous devices, and achieve a higher signal to noise ratio along with controlling the coupling strength of the components the acoustic and qubit chip were separated in two chips [18, 19]. In this flip-chip geometry, the qubit (on bottom chip) inductively couples to an IDT generating SAWs on the other (top) chip, see Fig. 1.3.(d). The flip-chip geometry allows to experimentally verify, using quantum tomography, that phonons in SAW resonators are in quantum Fock states. Going from bulk to surface the field of quantum acoustics continued to explore smaller designs with new materials, such as the 500 nm wide nanomechanical resonators [20, 21], see Fig. 1.3.(c). Here, the piezoelectric material is suspended to confine the acoustic waves while still being coupled to *transmon qubits* [22] using electrodes on top of the piezoelectric.

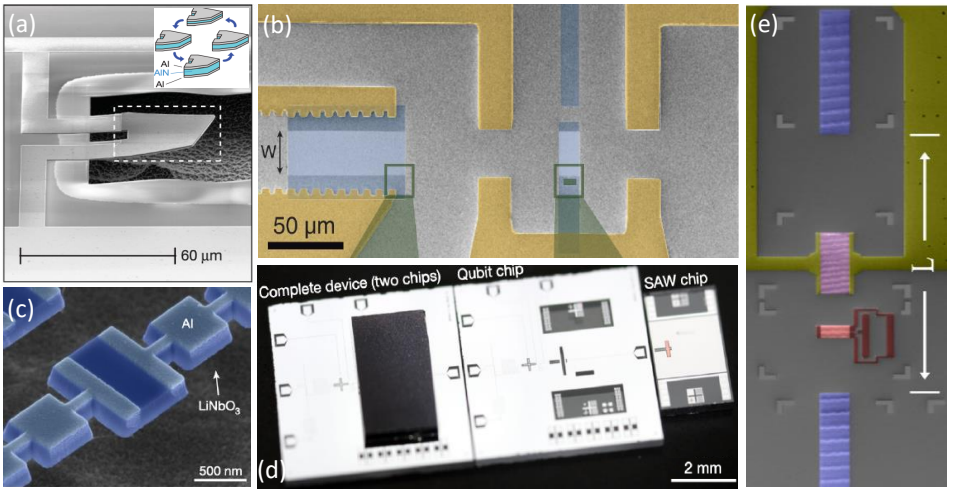

Figure 1.3: Photo gallery of quantum acoustic devices. (a) Shows a scattering electron microscope (SEM) image of the FBAR demonstrated in [13]. **(b)** Presents a SEM image of a transmon qubit (middle) being coupled to SAWs propagating from the IDT (left) [14]. **(c)** SEM image of a nanomechanical resonator presented in [20, 21]. **(d)** Lightmicrograph of disasembled flip-chip qubit to inductively coupled IDT generating a SAW on a separate chip from [18]. **(e)** Shows a SEM image of the device presented [16] where an IDT (yellow, purple) generates SAWs that are confined between two Bragg reflectors (blue) and are coupled to a qubit (red).

In recent years, bulk acoustic resonators have found their way back into the field with the introduction of coupling superconducting 3D qubits to high-overtone bulk acoustic resonators (HBARs) [23], see Fig. 1.4.(a). Recent achievements have shown strong coupling, where the coupling strength g is much larger than the loss rates of the qubit and mechanical resonator, between qubit and phonon modes of the HBAR, enabling tools for controlling quantum states in acoustic systems. Within the wide field of quantum acoustics, we refer to these engineering and design tools as circuit quantum acoustodynamics (cQAD), which is the acoustic equivalent of circuit quantum electrodynamics (cQED) [24–26]. Where cQED focuses on engineering and controlling quantum states in electromagnetic systems, e.g. dispersive readout of transmon qubits [22, 27, 28], cQAD is used in a variety of acoustic systems to, for example, prepare nonclassical phononic states [29], perform quantum tomography [29, 30], and demonstrate the preparation of Schrödinger cat states of motion [31]. A consequence of these developments, in bulk geometry, is that it opens the possibility to explore the properties of larger atoms than found by using SAW resonators. Recent studies have also shown planar (or 2D) superconducting qubits coupled to HBAR in strong coupling regime [32, 33], sideband control for selectively switching interaction [34], and the access to multiphonon transitions [35]. Fig. 1.4.(b) shows an schematic of a planar transmon qubit coupled to an HBAR in flip-chip geometry used in this work.

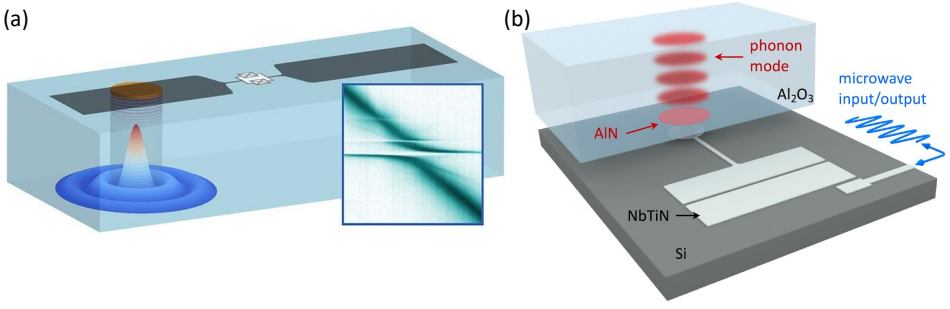

Figure 1.4: Schematic of transmon-HBAR devices. (a) Schematic of HBAR coupled to 3D transmon qubit. One side of the two aluminum islands covers a AlN piezoelectric which generates standing wave in sapphire substrate. Inset shows data of anti-crossing between qubit and phonon mode [23]. **(b)** Rendering of the transmon-HBAR device used in [36]. The device comprises two chips bounded in a flip-chip orientation. The top chip (HBAR chip) consists of 650 μm slab of sapphire, hosts the HBAR modes (red) and a film of aluminum nitride (red). The acoustic standing waves within the sapphire are generated by the film of aluminum nitride that piezoelectrically couples to the electric field of the transmons superconducting antenna (silver). The pocket-style transmon qubit on the bottom silicon chip couples with microwave signals (blue) to an on-chip readout resonator.

1.2. MOTIVATION COUPLING PLANAR SUPERCONDUCTING QUBITS TO HBARS

Building hybrid quantum systems [37] has always been of interest in order to take advantage of the unique properties in which individual quantum systems excel in. Examples are quantum dots which are small, scalable, and have relaxation times of a few milliseconds [38], trapped ions with reconfigurable connections [39], photons with extremely long coherence times [40], and off course superconducting qubits with fast gate times [41]. Coupling these systems together gives rise to hybrid quantum systems that can leverage the advantages of each subsystem simultaneously and perform different tasks that resemble classical computer components such as quantum processors, photonic interface, and quantum memory. Superconducting qubits have already been coupled to a variety of quantum systems such as mechanical resonators [42], spins [43], Rydberg atoms [44], and to SAWs and HBARs (see Sec. 1.1).

Exploring the coupling between HBARs and superconducting qubits is of particular interest since they are used as acousto-electric transducers and can couple to optics using Brillouin scattering [45–47]. This makes them an interesting quantum link for transmitting quantum information between superconducting qubits, optics, and acoustics using mechanical motion to bridge to other platforms as discussed earlier. Using HBARs specifically as acoustic cavities coupled to superconducting qubits instead of electromagnetic cavities, e.g. microwave resonators, is motivated by a few reasons. The HBAR is more compact compared to their electromagnetic counterparts since the speed of sound in crystalline structures is four to five orders of magnitude smaller than that of light in vacuum. Although both feature similar coherence times for similar frequencies, the loss mechanism in HBAR is fairly different, providing an interesting alternative depending on the restrictions in the system (design). In addition, the many gigahertz frequency modes available in HBARs typically present longer lifetimes, due to high quality factors, than qubits by several orders of magnitudes [48, 49]. This makes these phonon modes an excellent candidate to be used as a quantum memory, i.e. quantum ran-

dom access memory (qRAM) [50], in larger circuits consisting multiple superconducting qubits.

Furthermore, using coupled superconducting qubits and HBARs in planar geometry, in contrast to 3D transmons [51, 52], is of interest since it enables us to fit multiple transmon-HBAR devices on one chip. Doing so, we enable ourselves to design more complex and scalable quantum circuits consisting transmon-HBAR devices. On chip, not only can multiple transmon-HBAR devices be coupled to each other [35, 53], each transmon can be individually tuned in resonance frequency using dedicated flux line for flux tuning the qubits using a superconducting quantum interference device (SQUID).

1.3. Thesis outline

Where this chapter has presented an introduction and advances in the field, this thesis continues as follows. In **Chapter 2** we discuss the theoretical background and necessary tools for understanding the physical principles of the systems explored in this work. We provide a detailed explanation and derivation for the Hamiltonian of a transmon qubit, describe the operation principles of HBARs, and derive the expression for the piezoelectric coupling between the two. In **Chapter 3** we describe how we used *qiskit-metal* to design our device while discussing design considerations required for the engineering. Subsequently, we focus on nanofabrication techniques and used setups needed to both realize and measure the device. In **Chapter 4** we experimentally demonstrate the realization of a superconducting single-atom phonon laser using a flip-chip HBAR architecture. Our transmon-HBAR device resides in the high-cooperativity and weak-coupling regime for which we explore the parameter space using a mean-field solution as described in **Chapter 5**. Furthermore, in **Chapter 6** we present a phenomenological study on qubits that are strongly driven with a pump tone. Here, we show that strong drive tones result in the emergence of subharmonic parametric excitations of the qubit 01 manifold, and observe the appearance of ghost modes. We further probe the nature of ghost modes using quantum acoustics and show that these do not interact with real systems occupying the same frequency space. In **Chapter 7**, we conclude the work done in this thesis with a short overview of the performed investigations and outline future prospects in the field of quantum acoustics using transmon-HBAR devices.

2

Theory and Background

I am so clever that sometimes
I don't understand a single word of what I am saying.

Oscar Wilde

This chapter will provide the necessary theoretical tools for the understanding of the systems which are experimentally studied in the subsequent chapters. Along with mathematical descriptions, an intuitive idea of their physical interpretation will be provided as often as possible. The chapter starts with

2.1. Theory of Superconducting Qubits

In this section, we will discuss relevant subjects related to the transmon qubit. We start by describing the LC oscillator and quantizing its Hamiltonian. Afterwards, we introduce the nonlinear element called the Josephson junction and show how this changes the LC resonator's Hamiltonian to that of a qubit and describe it as a transmon. These descriptions will include some circuit quantum electrodynamic (cQED) principles as well. We end this section by describing a dispersive coupling between a readout resonator and transmon qubit.

2.1.1. The LC harmonic oscillator

In fields such as microwave optomechanics and cQED, the LC oscillator is the most fundamental electrical circuit. As Fig. 2.1 shows, it consists of a capacitor C in parallel to an inductor L. Over the years, LC oscillators have become a key element in the design of complex systems and are the basis to start from for designing superconducting qubits. Describing and understanding the LC harmonic oscillator is therefore a good starting point before moving on to transmon qubits.

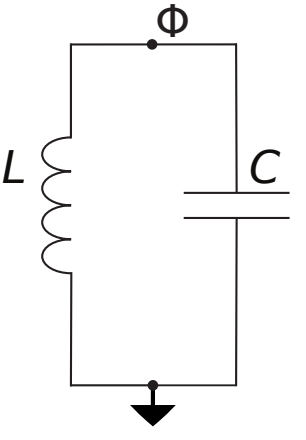

Figure 2.1: The LC oscillator circuit. Schematic of an LC oscillator with at the top the Flux node Φ and bottom ground node.

Classical LC oscillator description

Using the node variable representation, shown in Fig. 2.1, one can find two circuit nodes between the inductive, L, and capacitive, C, circuit elements. One is the ground node at the bottom and the node at the top is called the active node, which we call the Flux node Φ in the description below. Following the method of nodes, described in [54], we can write down the Lagrangian of this simple circuit (as a function of the Flux node) as

$$\mathcal{L} = \frac{C\dot{\Phi}^2}{2} - \frac{\Phi^2}{2L}. \tag{2.1}$$

Here, the generalized flux Φ is defined from the node potential V as $V(t) = \dot{\Phi}$. The conjugate momentum, corresponding to the node charge, is then defined as $q = \frac{\partial \mathcal{L}}{\partial \dot{\Phi}} = C\dot{\Phi}$. Following a

Legendre transformation, for a system with a single degree of freedom, we obtain the following Hamiltonian (total energy of the circuit)

$$H = \dot{\Phi} q - \mathcal{L} = \frac{q^2}{2C} + \frac{\Phi^2}{2L}, \tag{2.2}$$

with the equations of motion

$$\dot{\phi} = \frac{\partial H}{\partial q}, \dot{q} = -\frac{\partial H}{\partial \phi}. \tag{2.3}$$

An intuitive interpretation for Eq. 2.2 is by thinking of the total circuit energy as being stored in both the electrical energy in the capacitor and magnetic energy in the inductor.

Quantum LC oscillator description

By promoting the canonical variables q and Φ to quantum operators $\hat{q}$ and $\hat{\Phi}$, with the canonical commutation relation $[\hat{q}, \hat{\Phi}] = i\hbar$, Eq. 2.2 takes the form

$$\hat{H} = \frac{\hat{q}^2}{2C} + \frac{\hat{\Phi}^2}{2L}. \tag{2.4}$$

By introducing the LC oscillator's natural resonance frequency $\omega_0 = 1/\sqrt{LC}$, we can rewrite the above equation as

$$\hat{H} = \frac{\omega_0^2 C}{2}\left(\frac{\hat{q}^2}{C^2\omega_0^2} + \hat{\Phi}^2\right). \tag{2.5}$$

Now, by following the ladder operator method [55], we introduce the annihilation and creation operators $\hat{a}$ and, respectively, $\hat{a}^\dagger$. These ladder operators represent the removal or, respectively, addition of photons in the system and satisfy the bosonic commutation relations $[\hat{a}, \hat{a}^\dagger] = 1$ and are written as

$$\hat{a} = \sqrt{\frac{\omega_0 C}{2\hbar}}\left(\hat{\Phi} + i\frac{\hat{q}}{\omega_0 C}\right) \quad \text{and} \quad \hat{a}^\dagger = \sqrt{\frac{\omega_0 C}{2\hbar}}\left(\hat{\Phi} - i\frac{\hat{q}}{\omega_0 C}\right). \tag{2.6}$$

Using this, we arrive at the Hamiltonian of the quantum harmonic oscillator (QHO)

$$\hat{H}_{\text{QHO}} = \hbar\omega_0\left(\hat{a}^\dagger\hat{a} + \frac{1}{2}\right). \tag{2.7}$$

Note that we could also rewrite the operators $\hat{\Phi}$ and $\hat{q}$ as

$$\hat{\Phi} = \Phi_{\text{zpf}}\left(\hat{a} + \hat{a}^\dagger\right) \quad \text{and} \quad \hat{q} = \frac{q_{\text{zpf}}}{i}\left(\hat{a} - \hat{a}^\dagger\right), \tag{2.8}$$

where Φ_{zpf} and q_{zpf} are the zero-point fluctuations, a measure of the variance ("quantum jitter") of the observable flux or charge when the system is in its ground state (lowest energy possible). They are determined by the impedance $Z = \sqrt{L/C}$ of the corresponding mode

$$\Phi_{\text{ZPF}} = \sqrt{\langle 0|\hat{\phi}^2|0\rangle} = \sqrt{\frac{\hbar Z}{2}} = \sqrt{\frac{\hbar}{2\omega_0 C}}, \tag{2.9}$$

$$q_{\text{ZPF}} = \sqrt{\langle 0|\hat{q}^2|0\rangle} = \sqrt{\frac{\hbar}{2Z}} = \sqrt{\frac{\hbar\omega_0 C}{2}}, \tag{2.10}$$

Now, we see that our harmonic LC oscillator has discrete quantum eigenstates $|0\rangle$, $|1\rangle$, $|2\rangle$, ... with energies $\hbar\omega/2$, $3\hbar\omega/2$, $5\hbar\omega/2$ as shown in Fig. 2.2.

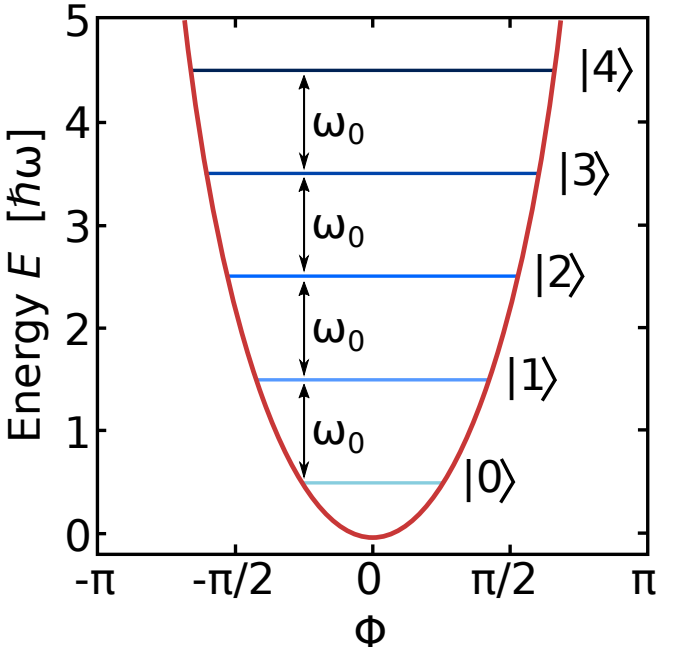

Figure 2.2: The Harmonic LC oscillator. Energy level spacing of a harmonic LC oscillator with equidistant energy level spacing.

As Fig. 2.2 shows, the harmonic oscillator has the unique property that its energy levels are equally spaced. For the use as a qubit, this is not desirable since we want to distinguish energy transitions from one another, e.g. $|0\rangle \leftrightarrow |1\rangle$ and $|1\rangle \leftrightarrow |2\rangle$. Therefore, as we show and explain in the next sections, we will introduce the nonlinear element: the Josephson junction.

2.1.2. Josephson Junctions and SQUIDs

The Josephson Junction

As a non-linear, non-dissipative circuit element, the Josephson junction [56] plays an important role in the field of superconducting qubits [57]. The variation that is mostly used is the so-called Supercondcutor-Insulator-Superconducton (SIS) Josephson junctions and, as the name implies, consists of two superconducting electrodes with an insulating layer in between them [58], as shown in Fig. 2.3.

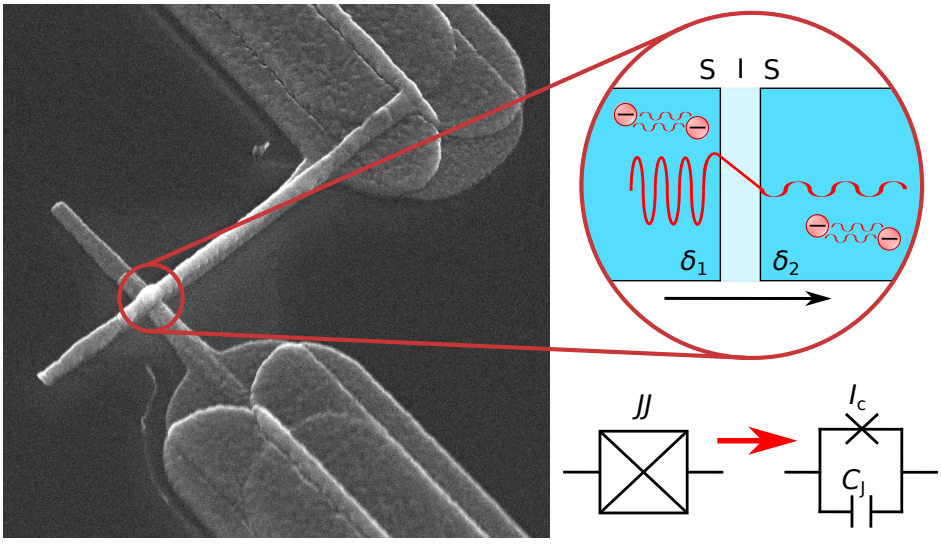

Figure 2.3: The Josephson Junction. Left: Scanning Electron Micrograph (SEM) of an SIS junction consisting of two superconducting electrodes (Al) with an insulating layer (AlO_X) in the middle. **Top-right:** Schematic zoom-in of the SIS junction. Cooper pairs tunnel through the insulating barrier as a supercurrent which is proportional to the phase difference between the two electrodes, $\delta_1 - \delta_2$. **Bottom-right:** shows a circuit representation of a Josephson junction. A Josephson junction can be considered as a lumped element I_c resonant circuit with a non-linear inductance and parasitic capacitance C_J due to the two superconducting electrodes. SEM made by J.Koenig.

As the figure shows in the zoom-in panel (top-right, red), the wave function of each superconducting electrode decays but still overlaps inside the insulating barrier. This allows for the quantum tunnelling of Cooper pairs [59] through the barrier from one electrode to the other as a supercurrent [60]. This effect is expressed in the Josephson equations below [56].

$$I = I_{JJ,0} \sin \phi \tag{2.11}$$

$$\frac{d\phi}{dt} = \frac{2eV}{\hbar} \tag{2.12}$$

Here, $I_{JJ,0}$ is the critical current of a single junction, i.e. maximum current to maintain superconductivity, of the junction and $\phi = \delta_1 - \delta_2$ is the phase difference between the two superconducting electrodes. The value of I_0 depends on the thickness of the insulating layer, the area, and the resistance of the junction at room temperature. When the junction is biased

with a voltage larger than the critical voltage, V_c, the resistance has a non-zero value, but the current has an oscillation frequency of $\omega = 2eV/\hbar$ [61]. This is referred to as the Josephson effect.

When we take the derivative of Eq. 2.11 and substitude this into $\frac{\partial \phi}{\partial t}$ of Eq. 2.12 and using the relation $V = L\frac{dI}{dt}$, we end up with the Josephson inductunce L_J:

$$L_J = \frac{\Phi_0}{2\pi I_{JJ,0}}, \tag{2.13}$$

where ϕ has become $\Phi_0 = h/2e = 2.07e^{-15}\mathrm{Tm}^2$ which is called the flux quantum. For the majority of superconducting circuits, the Josephson junction is solely used as a nonlinear inductor. Note that the Josephson junction can still act as a small resonant circuit with a small parasitic capacitance [62]; see circuit schematics in Fig. 2.3. The capacitance resides between the two superconducting electrodes, whose resonance frequency, called the plasma frequency, typically lies around tens to hundreds of gigahertz.

The SQUID

Now that we have discussed the single Josephson junction, we will place two of them in parallel inside a superconducting loop as shown schematically in Fig. 2.4. This is a well-known circuit element called the (dc) SQUID, which stands for a Superconducting QUantum Interference Device.

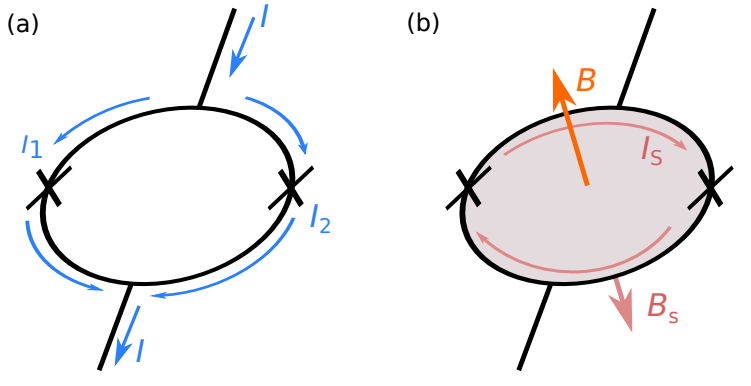

Figure 2.4: Schematic of a SQUID. In **(a)** is a schematic representation of the SQUID when no magnetic field is applied. The current distribution, I, through the two junctions here is equal and represented with I_1, I_2. When applying a magnetic field, B, the schematic in **(b)** shows that a screening current I_S is generated to compensate for the threading flux.

In the absence of a magnetic field, we describe the current distribution in a SQUID as follows

$$I = I_1 + I_2 = I_{JJ,0}(\sin\varphi_1 + \sin\varphi_2), \tag{2.14}$$

where we assume the SQUID is formed by two Josephson junctions with a sinusoidal current phase relation (Eq. 2.11) and equal critical currents of I_{c0}. In Eq. 2.14 I_1 and I_2 are the supercurrents flowing through each junction (or SQUID arm). As a consequence of placing the

junctions in a superconducting loop, the total phase change around the SQUID loop must always equal multiples of 2π. This boundary condition generates a correlation between the phase differences of the two Josephson junctions as

$$\varphi_2 - \varphi_1 = 2\pi \frac{\Phi}{\Phi_0} \tag{2.15}$$

where Φ is the magnetic flux thread by the SQUID loop and Φ_0 is the flux quantum. This is also known as fluxoid quantization. When applying a magnetic field B perpendicular to the SQUID loop creates a magnetic flux Φ_{out}. In turn, the SQUID generates a screening current $I_s = \frac{I_{JJ,0}}{2}(\sin\varphi_1 - \sin\varphi_2)$ which tries to compensate for the threading flux by adjusting the phase difference $\varphi_2 - \varphi_1$ as shown in Eq. (2.15). Writing down the SQUID's critical current I_c as

$$I_c(\Phi) = 2I_{JJ,0}\left|\cos\left(\frac{\pi\Phi}{\Phi_0}\right)\right|, \tag{2.16}$$

where the total flux is given by $\Phi = \Phi_{\text{out}}$ (assuming loop inductance negligible). Intuitively one can say that the fulfillment of the fluxoid quantization can be translated into an effective reduction of the SQUID critical current as the former will oscillate between a maximum value of $2I_{JJ,0}$ when $\Phi/\Phi_0 = n\pi$ and 0 when $\Phi/\Phi_0 = \frac{n\pi}{2}$, $n \in \mathbb{Z}$. Furthermore, the SQUID inductance can be written as

$$L_{SQ}(\Phi) = \frac{L_J}{2\left|\cos\left(\frac{\pi\Phi}{\Phi_0}\right)\right|}, \tag{2.17}$$

where L_J is the Josephson inductance of a single junction from Eq. 2.13. Since in Eq. 2.17 we can see that the SQUID's inductance is dependent on the applied flux, the SQUID has become a flux-tunable element. When replacing the inductor of our previous harmonic LC oscillator with a SQUID loop, the natural frequency of this new circuit becomes flux-tunable since the inductance has become flux-tunable according to $\omega_0 = \frac{1}{\sqrt{L_{SQ}(\Phi)C}}$.

2.1.3. Superconducting Transmon Qubits

As previously stated, when replacing the inductor of the LC oscillator with our nonlinear inductor, the Josephson junction L_J, we can create our superconducting qubit. The inductance of the junction, previously "ignored", varies with the current, i, going through it, $L_J(i)$. For our newly formed LC oscillator, from now on called transmon, this inductance increases with the fluctuations of the current going through it. The natural frequency of our transmon $\omega_n = 1/\sqrt{L_J(i)C}$ will thus acquire a dependence on n, the state of the circuit, as we will show in the following section. Due to this property, the frequency of the transitions between levels becomes non-equidistant, turning the Harmonic LC oscillator into an anharmonic one. By tuning an AC source coupled to the transmon to a specific frequency $\omega_n - \omega_{n-1}$, one can transfer the population of state $|n-1\rangle$ to the state $|n\rangle$ and back. These states are analogous to the eigenstates of a natural atom and due to similarities, the transmon qubit has acquired the nickname of an artificial atom. Fig. 2.5 shows circuit diagrams of the LC oscillator and transmon with corresponding energy potentials.

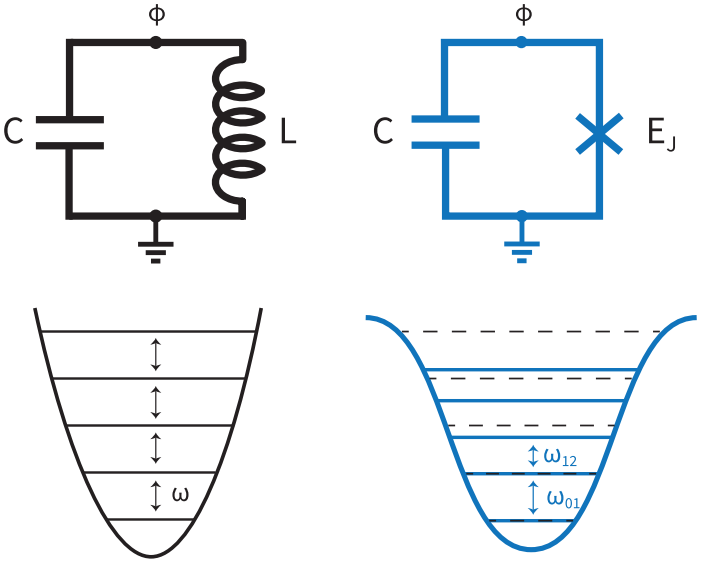

Figure 2.5: LC oscillator (black) and transmon (blue) circuit and their potentials. The cosine potential of the transmon (right) leads to a 2π-periodic wavefunction in the flux coordinate Φ (not shown). For large E_J/E_C ratios it is well-approximated by a Duffing oscillator potential with a negative anharmonicity $\omega_{12} - \omega_{01} \simeq -E_C/\hbar$ [63].

Transmon as anharmonic oscillator

In this section, we will derive the Hamiltonian for the transmon. We start by considering the simple transmon circuit from Fig. 2.5, where the X is a single Josephson junction. Here, we take the Josephson energy $E_J = \Phi_0 I_{JJ,0} = \Phi_0^2/L_J$ to describe the potential, or inductive, energy that is stored in the system as $E_J\cos(\phi)$. Even though, as stated in Sec. 2.1.2, the Josephson junction naturally forms a parallel LC circuit, we add a shunted capacitor to form a transmon qubit [22]. The shunted capacitance C_S together with the capacitance in the junction, C_J have

a total capacitance of $C = C_S + C_J$. The large shunted capacitance [1] minimizes the qubit's charging energy $E_C = \frac{e^2}{2C}$. We define the discrete number of Cooper pairs, $\hat{N} = \frac{\hat{q}}{2e}$, as being the conjugate operator of $\hat{\phi}$. By Taylor expanding to fourth order in the non-linear inductive energy (the cosine), we obtain the Hamiltonian

$$\hat{H} = 4E_C\hat{N}^2 + \frac{1}{2}E_J\hat{\phi}^2 - \frac{E_J}{4!}\hat{\phi}^4 \tag{2.18}$$

As previously shown for the LC circuits, we introduce quantum operators in the harmonic oscillator basis and write:

$$\hat{\phi} = \left(\frac{2E_C}{E_J}\right)^{1/4}(\hat{a}^\dagger + \hat{a}) \qquad \hat{N} = i\left(\frac{E_J}{32E_C}\right)^{1/4}(\hat{a}^\dagger - \hat{a}) \tag{2.19}$$

Neglecting the constant contributions and the fast oscillating terms ($\hat{a}^{(\dagger)n}$ with $n \geq 2$), we obtain the Kerr oscillator Hamiltonian:

$$\hat{H} = \hbar\omega\hat{a}^\dagger\hat{a} + \frac{\alpha}{2}\hat{a}^\dagger\hat{a}^\dagger\hat{a}\hat{a} \tag{2.20}$$

with $\omega \approx (\sqrt{8E_CE_J} - E_C)/\hbar$.

This Hamiltonian can be shown to possess non-degenerate eigenenergies, which can be quantified by looking at the anharmonicity α of the system, with $\alpha = \omega_{12} - \omega_{01} \approx -E_C/\hbar$. The transition frequencies between successive states are given by

$$E_n - E_{n-1} = \hbar\omega - n\alpha. \tag{2.21}$$

One can see that for zero anharmonicity ($\alpha = 0$), all energy levels become equidistant once more and we end up with the harmonic LC oscillator Hamiltonian (Eq. 2.7). If, on the other hand, α is sufficiently large, we can define a computational subspace, $|0\rangle$ and $|1\rangle$, on the two lowest-energy states: the ground and first excited state. [2] Keep in mind that by defining this subspace, we have obtained a qubit, not a transmon qubit. To get the qubit into the transmon limit, we aim to design the circuit such that $E_J/E_C \geq 50$.

Practical Operation Limitations: temperature and frequency

Now, we have described analytically what our transmon qubit is. However, we are still bound by practical limitations. Most superconductors need to be cooled down to a few Kelvin and the most commonly used material in nanofabrication of superconducting qubit is aluminum. Aluminum is mostly used for the fabrication of the Josephson junction to form a SIS junction. As also explained later in Sec. 3.2.1, aluminum has a native oxide layer of 2-3 nm thickness which serves as a tunnel barrier [67, 68]. Aluminum becomes superconducting at $T_c = 1.2$, for which the superconducting gap, i.e. the energy necessary for an incoming photon to break Cooper-pairs, is given by $1.76\,k_BT_c$ [69], which translates to ~ 44 GHz. These form hard upper limits to the operation temperatures and frequencies. Due to microwave equipment used in our dilution refrigerators, we usually design the transmons to operate in the $4 - 8$ GHz range.

[1] Charge fluctuations are harder to mitigate than flux fluctuations [64] and the superconducting community has hence shifted towards the $E_J \gg E_C$ regime by choosing large values of C_S [22].
[2] Higher energy levels still exist [65], though they can be exploited to implement gate operations [66].

Conveniently, as shown in [70], for decreasing frequency, the quality factor increases. For the lower limit, we consider the energy in our system by the following equation

$$E = k_B T = \hbar\omega, \tag{2.22}$$

with Boltzmann's constant k_B, temperature T and frequency ω. This is an important consideration, not only for operating the transmon in its ground and first excited state but also for situations where the temperature is sufficiently large enough for the environment to have enough thermal energy to significantly raise the average number of quanta and excite the qubit into higher energy states. When considering the average number of quanta in an oscillator $\bar{n}$, we can calculate this with the following

$$\bar{n} = \frac{1}{\exp\left[hf/k_B T\right] - 1}\,. \tag{2.23}$$

The temperature to which the transmon is coupled to a thermal bath should be (at least) $T \ll \hbar\omega_{01}/k_B$, where ω_{01} is taken as the transition frequency between its two lowest states (ground and first excited state). This is a critical lower limit on the temperature. When not kept in check, the environment is able to influence our experiment in unpredictable ways and could become a source of decoherence. For this reason, we need to cool our circuit and everything it is connected to, e.g. substrate, cables, and mounting stages. This is achieved by using a dilution refrigerator which could reach temperatures of a few miliKelvin. Unfortunately, the actual on-chip temperature differs from the temperature measured by the fridge [71]. This temperature difference goes up to the $\sim$ 100 mK.

2.1.4. Coupling and readout of a transmon qubit

Now that we have described our qubit, we need to talk about how we readout out its quantum state. More importantly, we need a way of measuring the qubit's quantum state without destroying it [72, 73]. One method that we show here is to weakly couple the qubit to a microwave resonator. This so-called readout resonator could readout by sending in a microwave tone and analyzing the signal it reflects back. The reflection can be measured directly or via, as done throughout this work, a microwave transmission line (feedline). In planar chips, the resonator and feedline are realized by coplanar waveguides (CPWs). Fig 2.6 shows an overview of a complete feedline-resonator-qubit circuit. The advantage of such a circuit is that one could frequency multiplex readout resonators (and therefore also qubits) to one input/output line and measure a multitude of qubits. In this section, we will briefly discuss transmission lines, CPWs and how these two are used for measuring the qubit in the dispersive regime.

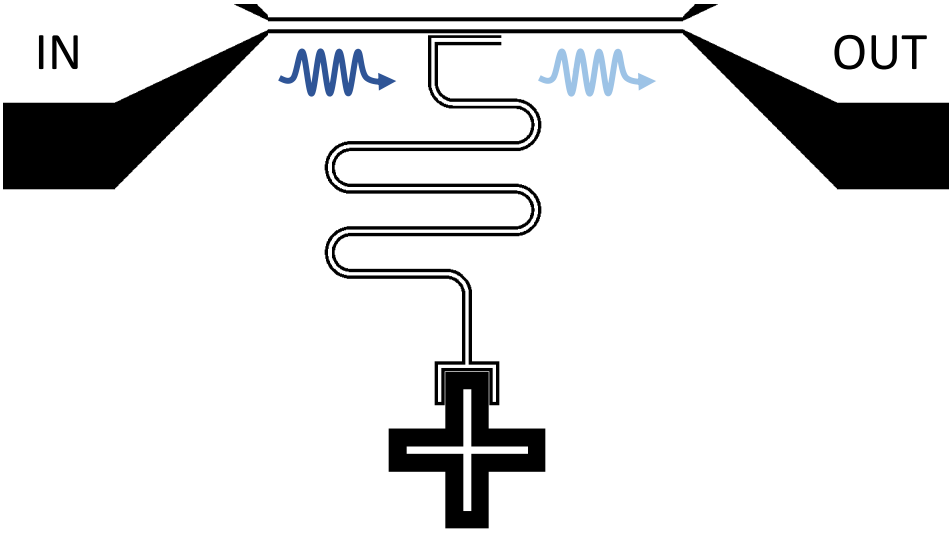

Figure 2.6: Readout resonator qubit layout. Circuit schematic of a qubit (cross at the bottom) capacitively coupled to a CPW readout resonator (meandering line in middles) which is inductively coupled to a microwave transmission line (top CPW going from input to output launchpad).

Coplanar waveguides as transmission lines

In this work, two types of microwave transmission lines were used, coax cables and on-chip transmission lines. The coax cables are used to connect the microwave sources and measurement equipment to our device. Typically, and conventionally, these have an impedance of 50 Ω [3]. For high frequency (typically > 10 kHz [75]) and a good conductor, the characteristic impedance of a transmission line Z_0 approximated by

$$Z_0 = \sqrt{\frac{L}{C}}, \tag{2.24}$$

[3] For air dielectric coax, the average between 30 Ω (best power handling) and 77 Ω (lowest loss) is 53.5 Ω, the geometric mean is about 48 Ω. For this reason, the choice of 50 ohms can be considered a compromise between power handling capability and signal loss per unit length. [74]

with L the inductance and C the capacitance. The on-chip transmission line, the coplanar waveguides (CPW), is a two-dimensional realization of the coaxial line made of superconducting material. The CPW consists, as shown in Fig. 2.7, of a long centre pin that is shielded with a coaxial capacitance to the ground. The feedline CPW (top line in Fig. 2.6), used to connect the on-chip devices to the coax cables, needs to be designed such that its characteristic impedance matches that of the coax transmission lines (50 Ω). This is needed to minimize or even prevent reflections at the interfaces, e.g. launch pads. The impedance of the CPW is calculated in the following manner [76]:

$$Z_0 = \frac{30\pi}{\sqrt{\epsilon_{\mathrm{eff,t}}}} \frac{K(k'_{\mathrm{t}})}{K(k_{\mathrm{t}})}, \tag{2.25}$$

where K is the elliptic integral of the first kind and $\epsilon_{\mathrm{eff,t}}$ the effective permittivity calculated by

$$\epsilon_{\mathrm{eff,t}} = \epsilon_{\mathrm{eff}} - \frac{\epsilon_{\mathrm{eff}} - 1}{\frac{(b-a)/2}{0.7t} \frac{K(k)}{K'(k)} + 1}, \tag{2.26}$$

with

$$\epsilon_{\mathrm{eff}} = 1 + \frac{\epsilon_{\mathrm{r}} - 1}{2} \frac{K(k')K(k_1)}{K(k)K(k'_1)}. \tag{2.27}$$

Here, k, k_{t}, k'_{t} and k' are calculated by

$$k_{\mathrm{t}} = \frac{a_{\mathrm{t}}}{b_{\mathrm{t}}} \qquad k = \frac{a}{b}$$
$$k'_{\mathrm{t}} = \sqrt{1 - k_{\mathrm{t}}^2} \qquad k' = \sqrt{1 - k^2}.$$

k_1 and k'_1 are calculated as

$$k_1 = \frac{\sinh(\frac{\pi a_{\mathrm{t}}}{4h})}{\sinh(\frac{\pi b_{\mathrm{t}}}{4h})} \qquad k'_1 = \sqrt{1 - k_1^2}, \tag{2.28}$$

with

$$a_{\mathrm{t}} = a + \frac{1.25t}{\pi}\left[1 + \ln\left(\frac{4\pi a}{t}\right)\right] \qquad b_{\mathrm{t}} = b - \frac{1.25t}{\pi}\left[1 + \ln\left(\frac{4\pi a}{t}\right)\right]. \tag{2.29}$$

The parameters a, b, t and h used above are, respectively, the strip width, the distance between grounds, metal thickness and the height of the substrate. Parameters are shown in Fig. 2.7. From the above equations, we see that only widths, thicknesses and substrate material are important for designing a transmission line with a characteristic impedance of 50 Ω. In this work, CPWs are not only used as transmission lines but also as superconducting resonators (for qubit readout) [77, 78].

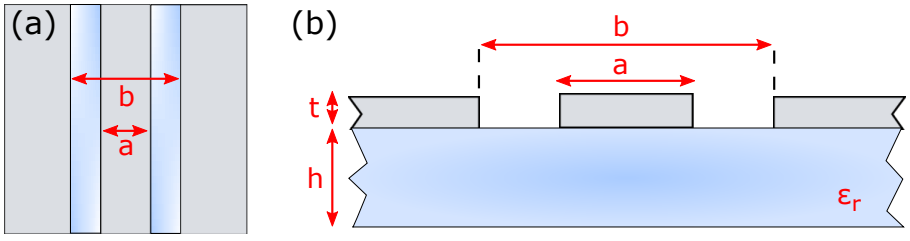

Figure 2.7: Schematic of coplanar waveguide (CPW). Panel **(a)** shows the partial top view and **(b)** the side view. Both panels have the dimensions a as the width of the middle strip, b the distance between the grounds, t the thickness of the metal, and h the height of the substrate ϵ_r. Illustration adapted from [76]. e.g. the calculated impedance is $\sim$ 50 Ω for $a = 50\ \mu$m, $b = 100\ \mu$m, and $t = 20$ nm metal on $h = 500\ \mu$m silicon ($\epsilon_r = 11.8$).

Coplanar waveguides as resonators

When taking the length and end connections of the CPW into account, we can start designing our resonators. When the centre pin is capacitively connected to the ground (open ends), a standing wave is formed with maximum voltage (zero current) at the two ends. By doing so, we have realized a half-wave ($\lambda/2$) resonator. If one end is open and the other shorted to ground, we have a quarter-wave ($\lambda/4$) resonator [77, 79]. Following [78] we can calculate the resonator frequencies for quarter-wave, $f_{\lambda/4}$, and half-wave, $f_{\lambda/2}$, with

$$f_{\lambda/4} = \frac{c}{\sqrt{\epsilon_{\text{eff}}}}\frac{1}{4l} \qquad f_{\lambda/2} = \frac{c}{\sqrt{\epsilon_{\text{eff}}}}\frac{1}{2l}, \tag{2.30}$$

which depend, for set ϵ_{eff} and Z_0, on the CPW resonators length l. The resonance frequency could also be describe as $\omega_0 = 1/\sqrt{(L_k + L_g)C_g}$ for which we can calculate the geometric inductance L_g and capacitance per unit length C_g following [76]. Where L_g and C_g are purely based on material choice, geometric design, and temperature independent, the kinetic inductance L_k, on the other hand, plays an interesting role in superconducting resonators [80]. For $L_k = \left(\frac{m}{2n_s e^2}\right)\left(\frac{l}{A}\right)$ with n_s the Cooper pair density, m the electron mass, and A the cross-sectional area of the CPW center pin. While the CPW transitions to the superconducting phase, the average Cooper pair density increases and consequently L_k.

Due to a decade of advances in nano-fabrication, CPW resonators with very high-quality factors, simplistic and compact designs can be produced [70, 81], which enables the storage of quantum states for over millions of oscillation cycles before decaying to the ground state. When coupling these resonators to transmon qubits, a circuit equivalent of atom-light interaction at the quantum level is realized. This field, called circuit quantum electrodynamics (cQED) [82], is the solid-state analog of cavity QED where microwave photons and CPW resonators are used instead of lasers and optical cavities. In cavity QED, atoms are placed inside optical cavities; however, in cQED, transmon qubits, playing the role of artificial atoms, are usually capacitively coupled to CPW resonators, as will be discussed in the next section.

2.1.5. Dispersive coupling and readout of superconducting qubits

Measuring the frequency of qubit's energy transitions can be done by dispersive readout through a CPW readout resonator. This is a commonly used method for qubit readout in superconducting circuits, which is indirect and suitable for quantum-nondemolition (QND) measurements [72]. An advantage of this readout scheme is that it could also be used in time-domain experiments [83]. Dispersive readout relies on measuring the microwave response of a (CPW) resonator that is coupled to the qubit off-resonantly [82, 84].

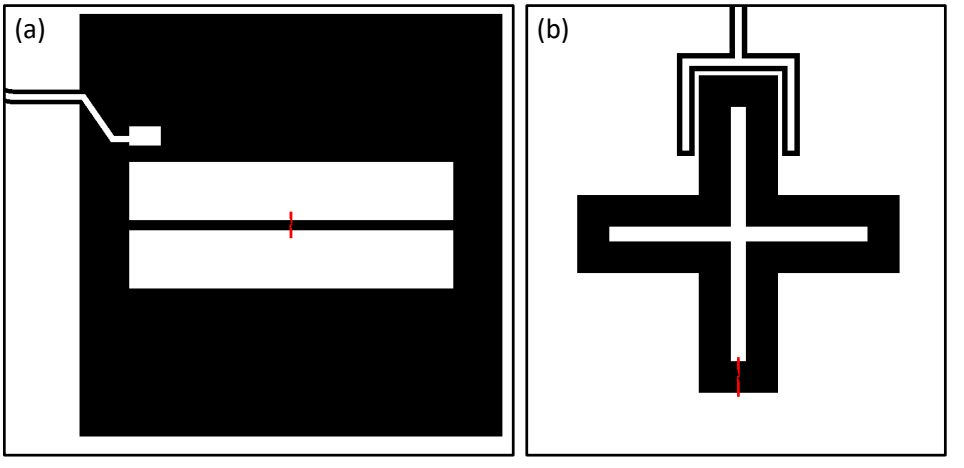

Figure 2.8: Qubit configurations: Pocket transmon and Xmon. Here, we show two configurations of capacitive coupling between a CPW readout resonator and a double capacitor island **(a)** or single island **(b)** transmon qubit. In both panels, the Josephson junction is represented in red and it either shorts the two capacitor islands (a) or shorts the island to the ground (b). In (a), the end of the CPW resonator is brought close to one of the transmon islands and the capacitance between the two is determined by the length of the CPW's end and it's distance to the transmon island. In (b), the end of the CPW resonator is formed as a "fork" to wrap around one arm of the transmon. Here, the capacitance is mainly influenced by the distance between the fork and arm and the length of the fork wrapped around the transmon arm.

Typically, as shown in Fig. 2.8.**a**, this readout is achieved by placing the open end of the CPW resonator in close proximity to one of the capacitor pads (superconducting islands) of the double island transmon. Or, as shown in Fig. 2.8.**b**, the open end of the CPW resonator is formed as a capacitor ("fork") which capacitively connects to one arm of a single island transmon qubit. In both situations, we allow oscillations of charge (voltage anti-node at CPW's end) on the CPW resonator side of the capacitor to induce small current oscillations on the transmon side. This is referred to as "coupling" and can be quantified through the "linear coupling" g. If we populate the CPW resonator with a single photon, such that the CPW-qubit state is $|1g\rangle$, and let the system evolve, this quanta will oscillate back and forth between the resonator and transmon at a rate g, realizing Rabi oscillations [4] [85]. This results in a dipole-dipole interaction, described by the Jaynes-Cummings model $\hbar g(\hat{a}^\dagger \hat{c} + \hat{c}^\dagger \hat{a})$ [86], where $\hat{c}^{(\dagger)}$, $\hat{a}^{(\dagger)}$ describe the annihilation (creation) of photons in readout resonator and qubit excitations, respectively.

[4] The CPW-qubit system is in strong coupling regime when $g \gg \gamma$, meaning that at least one Rabi oscillation occurs before the quantum state of the qubit decays, γ, due to interactions with the environment.

When the transmon qubit and CPW resonator frequencies are far apart relative to the coupling rate g ($\Delta = \omega_r - \omega_{01} \gg g$), the interaction is effectively described by the following dispersive Hamiltonian

$$H/\hbar = \omega_{01}\hat{a}^\dagger\hat{a} + \frac{\alpha}{2}\hat{a}^\dagger\hat{a}^\dagger\hat{a}\hat{a} + \omega_r\hat{c}^\dagger\hat{c} + \chi\ \hat{a}^\dagger\hat{a}\ \hat{c}^\dagger\hat{c}. \tag{2.31}$$

The dispersive coupling strength χ is approximately given by [22]

$$\chi = \frac{g^2\alpha}{\Delta(\Delta+\alpha)}, \tag{2.32}$$

where $\alpha \sim -E_C/\hbar$ is the transmon anharmonicity.

This coupling, also referred to as longitudinal or cross-Kerr coupling (χ is the cross-Kerr interaction strength), is particularly interesting as it can result in entanglement between the qubit and the resonator without excitation exchange. In this case, one could influence the other. When the transmon changes state, thus changing the inductance L_J, the frequency of the CPW resonator changes as well since L_J will have a small contribution to the total inductance of the resonator. On the other hand, exciting the resonator leads to a change in the current fluctuations in the junction and, therefore, its inductance L_J, which in turn changes the transition frequencies of the transmon.

This dispersive interaction is used in such a way that when the qubit is excited, the resonator frequency shifts ($\omega_r + \chi$) [84]. If $\chi/\hbar \gg \kappa$, one can thus infer the state of the qubit. A system where χ is sufficiently large for qubit state measurements and control is said to be in the *strong dispersive coupling regime*. In practice, and in this work, the CPW resonator, in turn, is measured by coupling it to a feed-line (as shown in Fig. 2.6) and measuring the transmission (or reflection) of a continuous wave (CW) microwave signal. The qubit's transition frequency can be measured by probing at the resonator frequency while scanning with a second tone around the expected qubit frequency until a resonator shift in phase or amplitude is observed. This is called two-tone spectroscopy and will be explained in more detail in Sec. 3.3.3.

2.2. High overtone Bulk Acoustic Resonators

In this section, we will discuss all relevant theory on High overtone Bulk Acoustic Resonators, how material choice and geometry design influences accessible resonator frequencies, and how piezoelectric coupling is used to coupling it to a transmon qubit.

2.2.1. Basic overview of an HBAR

A High overtone bulk acoustic resonator (HBAR) is a type of bulk acoustic wave (BAW) resonator and, in bare basics, consists of two layers: (1) a "thin" piezo-electric film, which is grown on (2) a thick low loss substrate. When the piezo-electric film is activated with an external alternating electric field $\vec{E}$, an acoustic wave propagates through the body (bulk) of the substrate as a longitudinal wave in the thickness direction, z. Here, in the substrate, the solid-air interfaces at the substrate surfaces form a structure that is a phononic equivalent to an optical Fabry-Perot cavity. The structure forms a standing wave resonance that confines the energy of the vibrations into the substrate, thus making the substrate act as a bulk acoustic cavity. A basic HBAR configuration is illustrated in Fig. 2.9 (a).

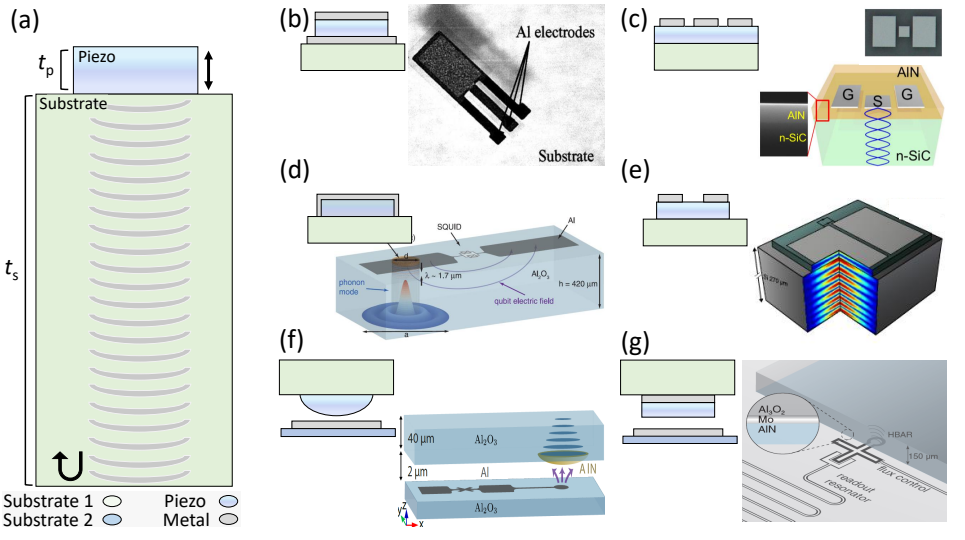

Figure 2.9: Schematic of HBAR principle and overview of different types of HBARs. (a) Schematic overview of basic HBAR. When a piezo-electric film of thickness t_p is actuated due to an electric field, $\vec{E}$, it generates propagating acoustic waves into a substrate, with thickness t_s. The interfaces between substrate-air (bottom) and substrate-piezo (top) act as mirrors and the substrate resembles a phononic Fabry-Pero cavity. **(b)** HBAR where electrodes on top and bottom of piezo generated the changing $\vec{E}$ to actuate the piezo [87]. **(c)** Parallel plate electrodes acting as ground-source-ground (G-S-G) on n-SiC substrate [88]. **(d)** Capacitor pad of a 3d-transmon qubit covering the entire piezo. $\vec{E}$ between transmon's capacitor pads actuates the piezo [23]. **(e)** 2d-transmon qubit where parallel plate capacitor pads ontop of the piezo provide the electric field [32]. **(f)** HBAR with convex lens-shaped piezo is flipped on top of a 3d-transmon qubit which emits $\vec{E}$ from an antenna to actuate the piezo [89]. **(g)** HBAR, with electrode between piezo and substrate, flipped on top of a 2d-transmon qubit. $\vec{E}$ is generated between transmon's capacitor pad and electrode underneath piezo [34].

Fig. 2.9 also shows multiple implementations of the HBAR and configurations for generating an electric field across the piezo-electric film and creating propagating acoustic waves inside the substrate. Fig. 2.9 (b,c) show HBARs at room temperature, which have a piezo sandwiched between two electrodes or, respectively, planar electrodes (ground-source-ground, GSG) on top of the piezo. In Fig. 2.9 (d-g) the HBAR was integrated in 3d- (d,f) and 2d-transmon qubits (e,g), which are inside a dilution refrigerator set at a few tens of mK. In Fig. 2.9(d) the electric field generated by the qubit capacitor pads actuates the piezo-electric film creating a piezoelectric coupling between qubit and HBAR. In (e) the same is done for a planar (2d) transmon qubit. In Fig. 2.9 (f) the HBAR and transmon chips were separated by flip-chip geometry. Here, the electric field of the qubit, emitted from an antenna, extends across a vacuum gap between the two chips and through the piezo-electric film and allows for piezoelectric transduction. The piezo here is also shaped as a plano-convex lens to focus the acoustic waves. Fig. 2.9 (g) is the 2d-transmon equivalent of (f) except for the use of a lens-shaped piezo and the addition of an electrode between piezo and HBAR-substrated which enhances the coupling between HBAR and qubit.

2.2.2. Q-factor, fundamental mode and free spectral range

As stated in the previous section, the HBAR forms a phononic Fabry-Pérot resonator. The substrate, when at low temperatures and correct geometry, will form standing acoustic waves, or standing modes, from the generated acoustic waves. Almost all of the acoustic energy generated in the HBAR is confined in the substrate since this is much thicker than the piezoelectric film. The ability to store energy is characterized by the quality factor, Q-factor, defined as the rate of energy loss per cycle in oscillating systems [77]:

$$Q = 2\pi \frac{\text{energy stored}}{\text{energy lost per cycle}}. \tag{2.33}$$

The quality factor of HBARs is heavily influenced by the losses of the substrate, such as defects and roughness at piezo-substrate or air-substrate interfaces. The Q-factor can also be rewritten in terms of resonance frequency, ω, and decay rate, κ, or rate of energy loss:

$$Q = \frac{\omega}{\kappa}. \tag{2.34}$$

Here, κ can also be viewed as the inverse of the acoustic lifetime of the phonons. A low decay rate, or high Q-factor, ensures that the acoustic energy stays long in the substrate resulting in long phonon lifetimes. When the system is cooled down to cryogenic temperatures, e.g. inside a dilution refrigeration, the acoustic lifetime increases.

The HBAR, as the name implies, supports high overtone modes, which explicitly states that the resonator operates at gigahertz (GHz) frequencies. This can already be seen when one calculates the frequency of the fundamental mode, which is given by

$$f_0 = \frac{v_p}{2t_p}, \tag{2.35}$$

where t_p and v_p are the film thickness and, respectively, the acoustic velocity of the piezo-electric material. For $t_p \sim 900$ nm and $v_p \approx 1.11^4$ m/s, as used throughout this thesis, the corresponding frequency of the piezo-electric layer is around 6 GHz. As Eq. 2.39 shows, the most strongly excited resonances occur when the half wavelength of the acoustic wave is equal to the thickness of the piezoelectric film. This is what we call the fundamental mode and it is the center frequency of modes that the piezo-electric film modulate through a frequency spectrum. Fig. 2.10 shows two examples of fundamental modes for an HBAR.

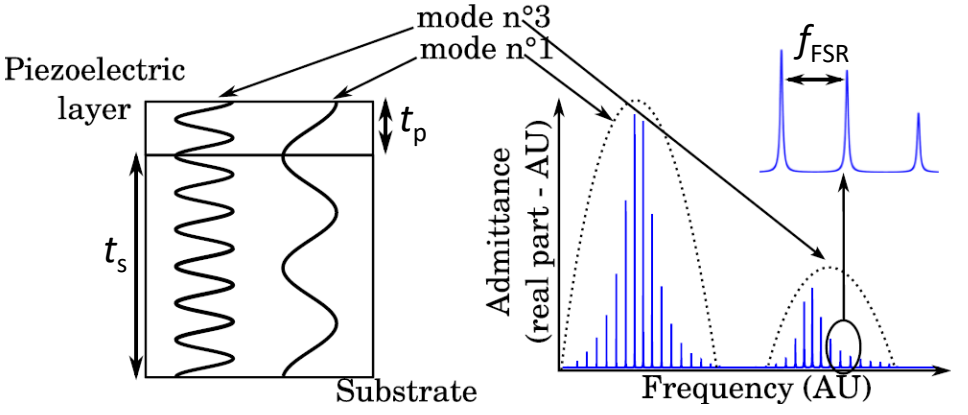

Figure 2.10: HBARs fundamental modes and free spectral range. Left: The principle of the HBAR shows the first and third fundamental mode generation. Right: a global view of the real part of the admittance showing the mode spacing called free spectral range (FSR) of the resonator. Figure adapted from [90].

Since we can modulate through a number of modes around a fundamental mode, with the use of the piezo, the HBAR exhibits a dense spectrum of equally spaced acoustic modes. This gives us access to a number of harmonic oscillators, as shown in the figure above. The mode spacing between two consecutive resonances is called the free spectral range (FSR) of the HBAR and is inversely proportional to the thickness of the substrate. The lowest frequency of the HBAR is also defined by the FSR and is given by

$$f_{FSR} = \frac{v_s}{2t_s}, \tag{2.36}$$

where v_s is the acoustic velocity in the substrate and t_s is the substrate thickness. Typically, the substrate thickness is between 200 - 700 μm, giving an FSR of a few tens of megahertz. Since the thickness of the piezo-electric layer can be synthesized to be a few micrometers, we can design HBARs to operate at frequencies of 1-12 GHz. This allows us to realize a resonant interaction with superconducting transmon qubits which, as stated in Sec. 2.1.3, typically operate at a few gigahertz frequencies.

2.2.3. PIEZOELECTRICITY, STRESS AND STRAIN

So far, we have discussed piezo-electric elements and how they generated acoustic standing waves in the HBAR, but never explained the working principle behind it. In this section, we will discuss piezoelectricity and how an electric field changes the shape of a piezo. The stress and strain the piezo exerts on the substrate will, in turn, create standing waves. We end the section by working out the coupling term between HBAR and qubit.

Piezoelectricity is the linear interaction between electrical and mechanical quantities. A material is considered to be piezo-electric when the following two effects occur: the piezoelectric effect and the inverse piezoelectric effect. As shown in Fig. 2.11 on the left, an electric surface charge is induced on the material by applying stress, $\vec{T}$, and mechanically deforming it. Because of this stress, the material becomes electrically polarized, which generates an electric field across the material and creates a surface charge. In the inverse effect, see the right panel of Fig. 2.11, a mechanical deformation of the material is caused by applying a surface charge. This generates an electric field and causes the material to strain, $\vec{S}$ [91].

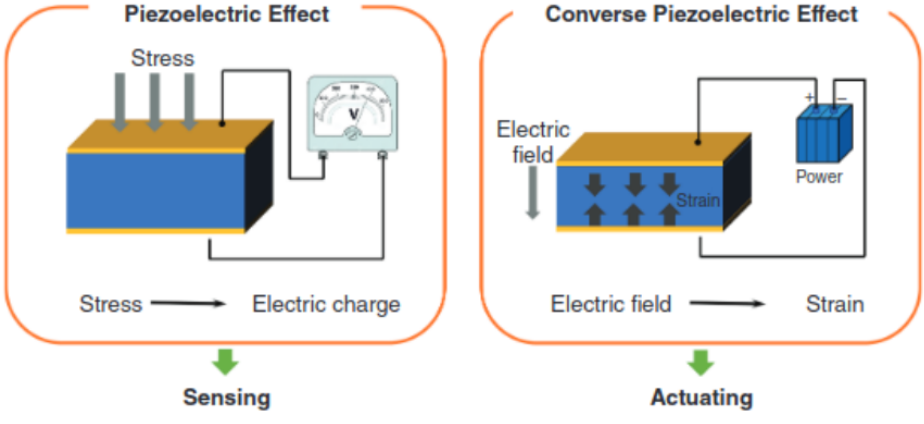

Figure 2.11: Piezoelectric and inverse piezoelectric effect. Left: Example of piezoelectric effect. When applying stress on a piezoelectric material, it induces a voltage on the sides. Right: Example of the inverse piezoelectric effect. Here it shows that by applying an electric field on a piezoelectric material leads to a deformation. Figure adapted from [92]

The mathematical description of piezoelectricity can be written as Eq. 2.37, where we introduce the influence of an electric field and the total internal stress $\vec{T}$ that the piezo-electric material experiences is [93]:

$$\vec{T} = c^E \vec{S} - e \vec{E}, \tag{2.37}$$

here c^E is the elastic coefficient of the material evaluated under a constant electric field, $\vec{S}$ is the strain in the material, and e is the piezoelectric stress matrix. The total electric displacement field $\vec{D}$ is produced by the external electric field, $\vec{E}$, and the piezoelectric effect caused by the strain, $\vec{S}$:

$$\vec{D} = \epsilon^s \vec{E} + e \vec{S}, \tag{2.38}$$

ϵ is the permittivity of the piezoelectric material under constant strain. The matrix equations Eq. 2.37 and Eq. 2.38 are the constitutive equations for the piezoelectric effect, which relates

electric and mechanical variables in a form of electromechanical coupling [94]. It provides a mechanism to transduce an electrical signal into mechanical motion and vice versa.

Piezoelectric coupling: qubit and HBAR

In order to describe the piezoelectric coupling between a superconducting transmon qubit and an HBAR, we assume that the piezo-electric material can interact with the electric field of the qubit in any of the shown configurations of Fig. 2.9 (d-g). Here, the electric field can be described with three spatial components. Each of these can induce different kinds of strain in the piezo-electric material, which in turn results in longitudinal or transverse acoustic waves in the HBAR's substrate. The strain vector in the substrate assumes the form: $\vec{S} = (S_x, S_y, S_z, S_{yz}, S_{xz}, S_{xy})$. Here, S_i describes normal strains where the deformation is an expansion/compression along the xyz-axis (longitudinal waves). S_{ij} are the shear strains in the planes yz, xz or xy (shear waves).

Since piezoelectricity is a linear body interaction between strain tensor $\vec{S}$ and the electric field $\vec{E}$, we use the induced strain in the piezoelectric-material due to the electric field $\vec{S} = d\,\vec{E}$, with d the piezoelectric (coupling) tensor. This we combine with a simplified version of Eq. 2.37 to obtain the stresses induced by the qubit's electric field. This gives us $\vec{T} = c\,\vec{S} = cd\,\vec{E}$, which we use to describe the energy E_{el} stored in the HBAR by a volume integral:

$$E_{el} = -\int \vec{T}(x)\,\vec{S}(x)dV \tag{2.39}$$

To simplify, we assume the electric field to be dominant along the z-axis and we focus on the only longitudinal wave generated. For this reason, there is only one component of interest: $S_z(x) = dE_z(x)$. In this specific case, relation Eq. 2.39 above takes the following form, which we simultaneously equate to the interaction energy of the Jaynes-Cummings Hamiltonian:

$$H_{int} = -c_{33}d_{33}\int E_z(x)S(x)dV \tag{2.40}$$

Where c_{33} and d_{33} are the stiffness and piezoelectric tensor components in the z-direction.

Let us now quantize the electric field and strain tensor of Eq. 2.40 to $\hat{E}$ and, respectively, $\hat{S}$ in terms of ladder operators $\hat{a}^\dagger$, $\hat{a}$, $\hat{b}^\dagger$ and $\hat{b}$. For the electric field, we use for the quantization the following ladder operators ($\hat{a}^\dagger$, $\hat{a}$), frequencies ω_n, permittivity (relative ϵ_r and vacuum ϵ_0) and normalized field mode distribution $f_n(x)$ respecting $\int_V \epsilon_r(x)f_n^*(x)f_m(x)\mathrm{d}V = \delta_{nm}$ following [95] (Ch.8):

$$\hat{E}(x,t) = \sum_{n=1}^{N}\left(-\sqrt{\frac{\hbar\omega_n}{2\epsilon_0}}f_n(x)\hat{a}_n(t) + H.c.\right) = \sum_{n=1}^{N}(E_n(x)\hat{a}_n(t) + H.c.) \tag{2.41}$$

Following the steps from [95], we us the single mode quantum strain tensor:

$$\hat{S}(x,t) = \sqrt{\frac{\hbar}{2\rho\omega}}\nabla h(x)\hat{b}(t) + H.c. \tag{2.42}$$

The multimode extension of Eq. 2.42 can be written as:

$$\hat{S}(x,t) = \sum_{m=1}^{M} \sqrt{\frac{\hbar}{2\rho\omega_m}} \nabla h_m(x) \hat{b}(t) + H.c. = \sum_{m=1}^{M} \left(\hat{S}_m \hat{b}_m(t) + H.c. \right) \tag{2.43}$$

where mode m has frequency ω_m, density ρ, normalized shape $h_m(x)$ and is created (annihilated) by operator $\hat{b}_m(t)$ ($\hat{b}_m^\dagger(t)$). We can rewrite Eq. 2.40 as:

$$H_{int}(t) = \frac{\hbar}{2} \sum_{n,m=1}^{N,M} \sqrt{\frac{\omega_n}{\rho\epsilon_0\omega_m}} \int dV (f_n^i(x)\hat{a}_n(t) + H.c.) c_{33} d_{33} ((\nabla h_m)^{jk}(x)\hat{b}_m(t) + H.c.) \tag{2.44}$$

we have written the spatial indices on top of the mode shapes in this equation to avoid confusion with mode number n, m. Defining a coupling matrix and assuming a real strain mode shape$(\nabla h_m)^*(x) = \nabla h_m(x) \forall m$, we can rewrite the interaction Hamiltonian in a clearer way:

$$H_{int}(t) = \hbar \sum_{n,m} \left(g_{n,m} \hat{a}_n^\dagger + g_{n,m}^* \hat{a}_n \right) \left(\hat{b}_m + \hat{b}_m^\dagger \right) \tag{2.45}$$

with coupling strength $g_{n,m}$ as:

$$g_{n,m} = \frac{1}{2} \sqrt{\frac{\omega_n}{\rho\epsilon_0\omega_m}} \int dV (f_n^i)^* c_{33} d_{33} (\nabla h_m)^{jk} \tag{2.46}$$

It can be further simplified by moving to the rotating frame using

$$U_1 = e^{i\left(\sum_n \omega_{e,n} \hat{a}_n^\dagger \hat{a}_n + \sum_m \omega_{h,m} \hat{b}_m^\dagger \hat{b}_m \right) t}. \tag{2.47}$$

By doing RWA, assuming g is real and using $\Delta_{nm} = \omega_{h,m} - \omega_{e,n}$:

$$H_{int} = \hbar \sum_{nm} g_{nm} \left(\hat{a}_n^\dagger \hat{b}_m e^{-i\Delta_{nm} t} + \hat{a}_n \hat{b}_m^\dagger e^{i\Delta_{nm} t} \right), \tag{2.48}$$

where the index $h(e)$ refers to the HBAR electric and magnetic modes. We further simplify this equation by focusing on one mode, where $n = m$, and therefore rewrite Eq. 2.48, as shown in SI of [23], into:

$$H_{int} = \hbar g (\hat{a}\hat{b}^\dagger + \hat{a}^\dagger \hat{b}). \tag{2.49}$$

Now that we have derived an equation for the coupling strength g (Eq. 2.46) and simplified the quantized interaction Hamiltonian H_{int} (Eq. 2.49), it becomes clear that in order to maximize g, we have two choices. For one, we can pick a piezo-electric material with a desirable set of ρ, c_{33} and d_{33}, see Sec. 3.1.3 for discussion on material choice. For the second option to maximize g, we should try to match the profile of the electric field along the z-axis to the strain profile of the acoustic mode we are targeting as much as possible. This results in maximizing the normalized field mode distribution, f_n, in the z-axis. The stronger the electric field in this direction, the stronger the piezo-electric coupling is to the HBAR! In practice, this means getting the emitted electric field of the qubit as close as possible to the HBAR's piezo.

2.3. Driven transmon-HBAR device

Now that we have derived the coupling strength, g, for the piezo-electric element of the HBAR with an electric field of the transmon qubit it interacts with, we can now write down the Hamiltonian of our driven transmon-HBAR system. We start by considering our full system, as schematically shown in Fig. 2.12. Here, we show the full coupling scheme of our system which includes a CPW transmission line, readout resonator (RO), transmon qubit and an HBAR. We sent both a RO probe and qubit drive, ω_r and, respectively, ω_d, through the transmission line. When the qubit is excited, it dispersively shifts the RO frequency by χ, which could be readout. The qubit is also linearly coupled to HBAR with coupling strength, g.

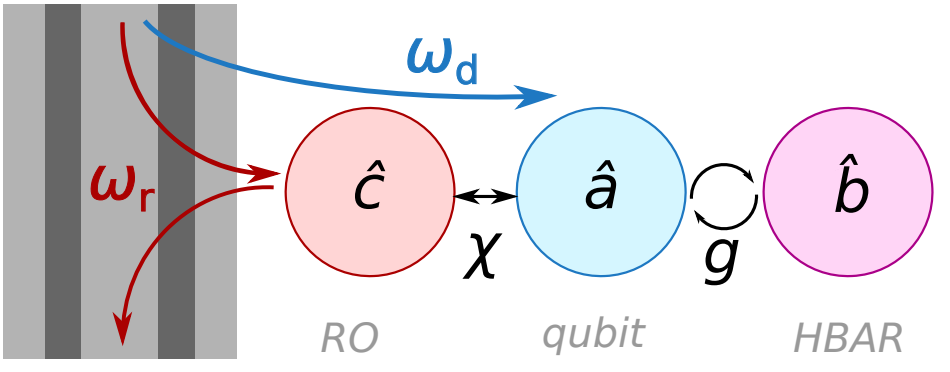

Figure 2.12: Coupling scheme of full readout resonator, transmon and HBAR system. Here, we show the full coupling scheme of our system for which we sent a probe signal through a CPW transmission line at the readout resonator's (RO, represented by $\hat{c}$) natural frequency, ω_r. When sending in a drive tone, ω_d, through the transmission line and RO, the qubit ($\hat{a}$) is excited and dispersively shifts the RO frequency by χ. Here, qubit and HBAR ($\hat{b}$) couple with a coupling strength, g.

In this section, we only consider the transmon-HBAR system since the readout resonator in this scheme only reflects the reactions the qubit has with the HBAR and drive tone. For our Hamiltonian describing the transmon-HBAR system, we write the following:

$$\hat{H}_0 = \hbar\omega_a \hat{a}^\dagger \hat{a} + \hbar\omega_b \hat{b}^\dagger \hat{b} + \hbar g(\hat{a}^\dagger \hat{b} + \hat{a}\hat{b}^\dagger). \tag{2.50}$$

Here, qubit's 01-transition frequency and HBAR resonance frequency of interest are denoted by ω_a and, respectively, ω_b with the corresponding annihilation (creation) operators $\hat{a}(\hat{a}^\dagger)$ and $\hat{b}(\hat{b}^\dagger)$. When driving this system, we can write down the total Hamiltonian as:

$$\hat{H} = \hat{H}_0 + \hat{H}_d \tag{2.51}$$

where $\hat{H}_d = i\hbar\epsilon_d(\hat{a}e^{i\omega_d t} + \hat{a}^\dagger e^{-i\omega_d t}) \sim i\hbar\epsilon_d(\hat{a} - \hat{a}^\dagger)\cos(\omega_d t)$ is the driving term with ω_d and ϵ_d the driving frequency and, respectively, driving strength. The fully written Hamiltonian becomes

$$\hat{H}_0 = \hbar\omega_a \hat{a}^\dagger \hat{a} + \hbar\omega_b \hat{b}^\dagger \hat{b} + \hbar g(\hat{a}^\dagger \hat{b} + \hat{a}\hat{b}^\dagger) + i\hbar\epsilon_d(\hat{a}e^{i\omega_d t} + \hat{a}^\dagger e^{-i\omega_d t}). \tag{2.52}$$

To this we apply the unitary transformation $\hat{U} = e^{i\omega_a \hat{a}^\dagger \hat{a} t + i\omega_b \hat{b}^\dagger \hat{b} t}$ to remove the time dependence from the driving term. Following [96] we use $\hat{H}' = \hat{U}\hat{H}\hat{U}^\dagger - i\hbar\hat{U}\partial\hat{U}^\dagger/\partial t$ on Eq. 2.52

and we see that the first three terms are unchanged for this transformation:

$$H'_{\mathrm{a}} = \hat{U}(\hbar\omega_{\mathrm{a}}\hat{a}^{\dagger}\hat{a})\hat{U}^{\dagger} \quad = \hbar\omega_{\mathrm{a}}\hat{a}^{\dagger}\hat{a}, \tag{2.53}$$

$$H'_{\mathrm{b}} = \hat{U}(\hbar\omega_{\mathrm{b}}\hat{b}^{\dagger}\hat{b})\hat{U}^{\dagger} \quad = \hbar\omega_{\mathrm{b}}\hat{b}^{\dagger}\hat{b}, \tag{2.54}$$

$$H'_{\mathrm{int}} = \hat{U}(\hbar g(\hat{a}^{\dagger}\hat{b} + \hat{a}\hat{b}^{\dagger}))\hat{U}^{\dagger} \quad = \hbar g(\hat{a}^{\dagger}\hat{b} + \hat{a}\hat{b}^{\dagger}). \tag{2.55}$$

The second term (time derivative) of the Hamiltonian transformation to the rotating frame becomes:

$$-i\hbar\hat{U}\frac{\partial\hat{U}^{\dagger}}{\partial t} = -\hbar\omega_{\mathrm{d}}(\hat{a}^{\dagger}\hat{a} + \hat{b}^{\dagger}\hat{b}). \tag{2.56}$$

Transforming the driving term $\hat{H}_{\mathrm{drive}} = i\hbar\epsilon_{\mathrm{d}}(\hat{a}e^{i\omega_{\mathrm{d}}t} + \hat{a}^{\dagger}e^{-i\omega_{\mathrm{d}}t})$ is a bit trickier as can already be seen when written out in full:

$$\hat{U}\hat{H}_{\mathrm{drive}}\hat{U}^{\dagger} = i\hbar\epsilon_{\mathrm{d}}e^{i\omega_{\mathrm{a}}\hat{a}^{\dagger}\hat{a}t + i\omega_{\mathrm{b}}\hat{b}^{\dagger}\hat{b}t}(\hat{a}e^{i\omega_{\mathrm{d}}t} + \hat{a}^{\dagger}e^{-i\omega_{\mathrm{d}}t})e^{-i\omega_{\mathrm{a}}\hat{a}^{\dagger}\hat{a}t - i\omega_{\mathrm{b}}\hat{b}^{\dagger}\hat{b}t} \tag{2.57}$$

By using the Baker-Campbell-Hausdorff formula [97] $e^{L}Ae^{-L} = A + [L, A] + \frac{1}{2}[L, [L, A]] + \ldots$, the commutation relation $[\hat{a}, \hat{a}^{\dagger}] = 1$, and exponential series we eventually can derive Eq. 2.57 to the form:

$$\hat{U}\hat{H}_{\mathrm{drive}}\hat{U}^{\dagger} = -i\hbar\epsilon_{\mathrm{d}}(\hat{a} - \hat{a}^{\dagger}). \tag{2.58}$$

Combining all of the above, we write our full time-independent transmon-HBAR Hamiltonian:

$$\hat{H}' = \hbar\omega_{\mathrm{a}}\hat{a}^{\dagger}\hat{a} + \hbar\omega_{\mathrm{b}}\hat{b}^{\dagger}\hat{b} + \hbar g(\hat{a}^{\dagger}\hat{b} + \hat{a}\hat{b}^{\dagger}) - \hbar\omega_{\mathrm{d}}(\hat{a}^{\dagger}\hat{a} + \hat{b}^{\dagger}\hat{b}) - i\hbar\epsilon_{\mathrm{d}}(\hat{a} - \hat{a}^{\dagger}). \tag{2.59}$$

Rearranging this equation and using $\Delta_{\mathrm{a}} = \omega_{\mathrm{d}} - \omega_{\mathrm{a}}$ and $\Delta_{\mathrm{b}} = \omega_{\mathrm{d}} - \omega_{\mathrm{b}}$ we end up with:

$$\hat{H}'/\hbar = -\Delta_{\mathrm{a}}\hat{a}^{\dagger}\hat{a} - \Delta_{\mathrm{b}}\hat{b}^{\dagger}\hat{b} + g(\hat{a}^{\dagger}\hat{b} + \hat{a}\hat{b}^{\dagger}) + i\epsilon_{\mathrm{d}}(\hat{a} - \hat{a}^{\dagger}). \tag{2.60}$$

3

Device Design, Fabrication and Measurement Setup

"Jarvis! Sometimes you got to run before you can walk."

Tony Stark, Iron Man (2008)

In this chapter, we discuss how the devices for this work were designed using the Python package Qiskit-metal and what work was done prior to getting to a final design. Afterwards, the final fabrication and assembly recipe will be described. This recipe is the final result of countless hours being spent in both the Kavli Nanolab Delft cleanroom, one of the biggest academic cleanrooms in Europe, and performing measurements in state-of-the-art dry dilution refrigerators. We end the chapter by explaining both measurement setup and methods.

3.1. Device design, material choice and testing

In this section, we start out by describing how we use a Python package called *Qiskit-metal*, an open-source CAD software [98], to design our device. As Fig. 3.1 shows in a workflow overview, we need to first take concepts together with wanted dimensions for our qubit and readout resonators to enter into qiskit-metal. Unfortunately, two major parameters, the kinetic inductance L_K and Josephson energy E_J, we need for our final design but do not know their values upfront. For this reason, as explained further in Sec. 3.1.1, we use qiskit-metal to design test chips which we measure and extract the sought values for our main simulation. As the workflow in Fig. 3.1 also shows, we enter values into qiskit-metal, and render designs which are simulated in Ansys [99] (Q3D, HFSS). After these simulations, analysis is performed in qiskit-metal using LOM (Lumped Oscillator Model analysis on extracted capacitance matrix) and PyEPR (eigenmode simulations for energy participation ratio analysis). From the analysis results, we then either update our design and re-simulate or export the final design as a GDS file.

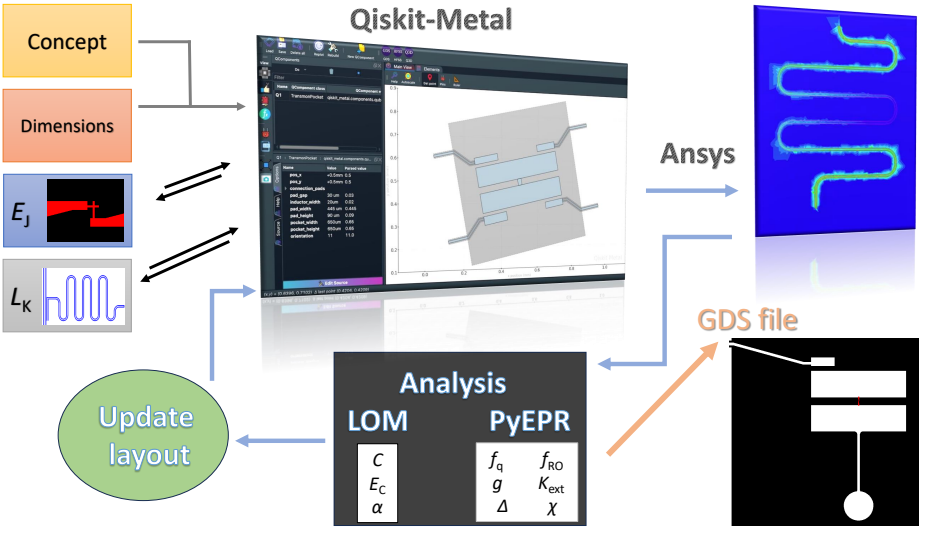

Figure 3.1: Schematic of workflow using *Qiskit-metal*. In this work Qiskit-Metal is used to take in dimensions and concepts to create and render 2D designs for our superconducting qubits and needed circuitry. Qiskit-metal exports renders to Ansys (Q3D or HFSS) to perform finite element simulations and later extracts the results to perform LOM and PyEPR analysis. In turn, we can extract wanted parameters such as C, E_c, α, f_q, f_{RO}, g, κ_{ext}, Δ and χ needed for our designing a transmon qubit with readout resonator (as explained in Ch.2). Then we either update our layout and rerun simulation and analysis or export a GDS file ready for fabrication. Figures adapted from the tutorial page of [98].

3.1.1. Design conditions and choices

For our design we have control over the coupling between the qubit and the readout resonator, g, their detuning from one another Δ (thus also $\chi = (g^2\alpha)/(\Delta(\Delta+\alpha))$), and the external decay rate, κ_{ext}, of the resonator due to its coupling to a feed-line. We also have control over the charging energy ($E_C = e^2/2C$), which enables us, when knowing the Josephson energy E_J, to design the qubit into the transmon limit ($E_J/E_C \geq 50$).

Another important number to consider is the $T_{\text{Purcell}} = 1/2\pi\kappa_{\text{Purcell}} = \kappa_{\text{ext}}/(2\pi(g/\Delta)^2)$, which is the relaxation time enhanced due to the presence of the readout resonator. This is also known as the Purcell effect [100]. As state-of-the-art transmons approach relaxation times of hundreds of microseconds, T_{Purcell} needs to be taken into account during design. Doing so ensures that it does not limit the qubit lifetime. To ensure the validity of the dispersive Hamiltonian at high photon numbers in the readout resonator, one also needs to take the critical photon number $n_{\text{crit}} = \Delta^2/(2g)^2$ into account [101]. If n_{crit} is exceeded, the dispersive approximation (Eq. 2.31 from Sec. 2.1.3) to the Jaynes-Cummings Hamiltonian breaks down and higher-order nonlinear terms need to be considered [1]. We optimize the readout conditions by appropriately choosing these parameters and summarize the chosen upper and lower bounds for each parameter in Table 3.1.

Table 3.1: Table of lower and upper bound design conditions The table shows the conditions we set out for designs for the charging energy E_C, Josephson energy E_J, readout resonator frequency f_{RO}, qubit 01-transition frequency f_q, their coupling strength g, the dispersive shift of the qubit on the readout χ, the readout resonator's external decay rate κ_{ext}, and the Purcell time T_{Purcell}. If the parameter has no upper bound (-), then we only have a minimum requirement.

	E_C (MHz)	E_J (GHz)	f_{RO} (GHz)	f_q (GHz)	g (MHz)	κ_{ext} (MHz)	χ (MHz)	T_{Purcell} (μs)
Lower bound	-	20/40	5	5.50	100	1	5	10
Upper bound	400/800	-	7	6.50	200	2	10	-

A few notes on the table above:

- We have chosen E_J to be 20 GHz for fixed frequency (single junctions) and 40 GHz for flux tunable (SQUIDs) qubits. $\sim$ 190 nm wide junctions coincide for both single as SQUID junctions, see Sec. 3.1.1: *Josephson inductance and junction width*.
- These numbers give hard upper bound for E_C, to design the qubit into the transmon limit. However, lower is better for our transmon regime.
- We specifically design our qubits to be around 6 GHz to maximize the overlap with the chosen HBAR fundamental mode (see Sec. 3.1.3).
- We design our readout resonators to be about $\Delta = 1$ GHz away from the qubit, either below or above the set 6 GHz.
- For T_{Purcell} we have set a minimum value so that the qubit's T_1 is not limited by readout resonator design but rather by either fabrication or measurement setup.

For the full HBAR-transmon design, we want a piezoelectric coupling between the transmon qubit and the HBAR. For this, we chose to use a flip-chip geometry (see Fig. 3.2(a)) where two separate chips (qubit and HBAR) are flipped on top of each other and glued into place. This geometry comes with advantages such as simplifying the overall fabrication, separately optimizing designs, and interchanging top & bottom chips (different designs or materials).

[1] When $g \gg \kappa$, the critical photon number, $n_\kappa = \kappa\Delta/\chi^2$ needs to be considered since for large n_κ the resonator becomes nonlinear due to higher-order dispersive shift contributions.

Most of all, this separation helps reduce qubit decoherence, unlike qubits placed directly on top of the piezo (see devices from [23, 32]). Another advantage is that it helps extend phonon coherence in the HBAR [29].

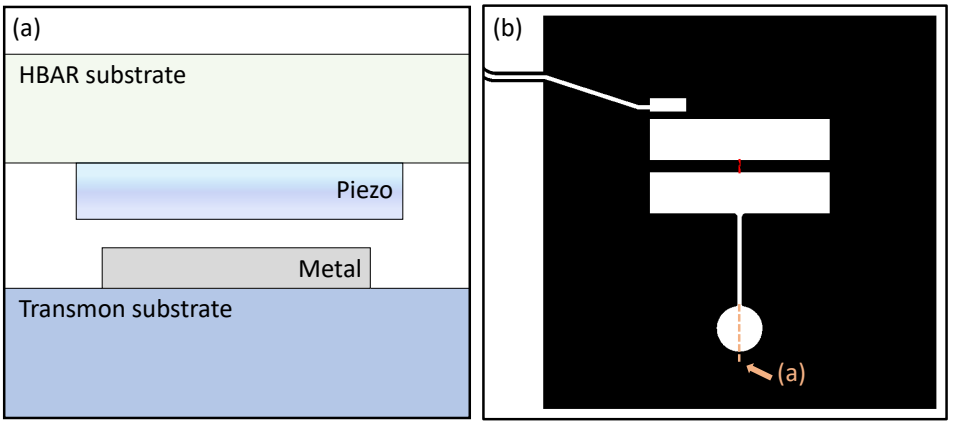

Figure 3.2: Schematic of the flip-chip HBAR-transmon device. **(a)** Schematic side view of the flip-geometry where the top chip (HBAR chip) consists of a substrate used for the HBAR and a cylinder piezo. The piezo is aligned with the antenna disk from the transmon chip (bottom chip). The side view position is shown in (b). **(b)** also shows the design for the pocket transmon, for which metal ground is relatively far from the island. To the bottom island, an antenna is attached and the transmon is read out via a CPW (top left line structure). White is metal; black is the exposed substrate.

From a qubit design perspective, we chose to use a pocket transmon [102], which consists of two superconducting islands inside a grounding box. To one of the islands, we attach an antenna (rod + disk) as shown in Fig. 3.2(b). The piezoelectric disk from the HBAR chip will be flipped on top of the antenna disk. The advantage of this design is that a reduction of metal ground surrounding the antenna (as done in [34]) allows for focusing of the electric field at the antenna's end, which helps maximize the electric field emitted from the transmon through the piezo. More details on the design will be discussed in Sec. 3.1.2.

From a material choice perspective, we use two materials for our qubits. For the bulk circuitry we chose niobium titanium nitride (NbTiN) as a superconductor. NbTiN is chosen because of its high critical temperature $T_c \approx 14.4$ K [103], low quasiparticle densities at millikelvin temperatures [104] and NbTiN CPWs have shown $Q_i > 10^6$ at cryogenic temperature [105]. Also, from a practical perspective, we, as a group, have gained a lot of experience with NbTiN in the past few years [63, 106–108]. However, designing with qiskit-metal is relatively new and, as will be explained in the next section, we need to incorporate the kinetic inductance L_K into the simulations. For our Josephson junction, we chose to use Manhattan style (SIS) junction with aluminum (Al) and aluminum-oxide (AlO_x) [109]. This style of the junction is less sensitive to resist height variations compared to Dolan junctions [110, 111], which allows it to be used on a non-planar base and has a higher yield of successful devices. For our simulations, as explained in the next sections, we need to know our Josephson inductance L_J for a chosen junction width. For this reason, before continuing with the full simulation, as shown in Fig. 3.1, we first collect the values L_K and L_J via measurements as explained in the next two sections.

KINETIC INDUCTANCE

Out of the box, qiskit-metal [98] only gives you the option to change the substrate material. However, for the metal layer, it is not possible to change material properties (easily). When one wants to simulate the eigenmode frequencies of their system (PyEPR & Ansys HFSS) this is not a problem. However, in our case, when a superconductor becomes superconducting and is subjected to an alternating electric field, the mobile charge carriers in the superconductor (Cooper pairs) experience a force due to their inertia [112]. The conductor behaves like an inductor due to the motion of the mobile charge carriers, and its inductance, the kinetic inductance $L_K = \frac{m_e}{ne^2}\frac{l}{A}$, depends on the Cooper pair density n (increases with decreasing temperature). Hence, our resonator's resonance frequency $\omega_0 = 1/\sqrt{LC}$ changes due to this additional inductance to $\omega_0 = 1/\sqrt{(L_g + L_K)C}$.

With qiskit-metal we can extract the resonance frequency solely based on the geometric inductance, L_g, but can not compensate for the kinetic inductance up front. The kinetic inductance depends on material type, thickness, purity, and fabrication. For this reason, we came up with a different solution with the help from *S. Hawaldar from IISC* and an active qiskit-metal community member. S. Hawaldar implemented kinetic inductance in HFSS, which seems to be able to simulate measured frequencies of fabricated CPW resonators (using specific branches for PyEPR [113] and qiskit-metal [114]). For our method, we design multiple frequencies multiplexed $\lambda/4$ resonators coupled to a single feedline in qiskit-metal. This design is inspired by the cavity reference chip used by our collaborators at *SRON* [103]. As shown in Fig. 3.3, all CPW resonators have spacing 6/10/6 μm (gap/centerpin/gap) and are distanced 22 μm from the 8/20/8 μm feedline. Each differs in the total CPW length, l_{tot}, and coupling length, l_{coup}, which influence their resonance frequency and, respectively, external decay rate, κ_{ext}.

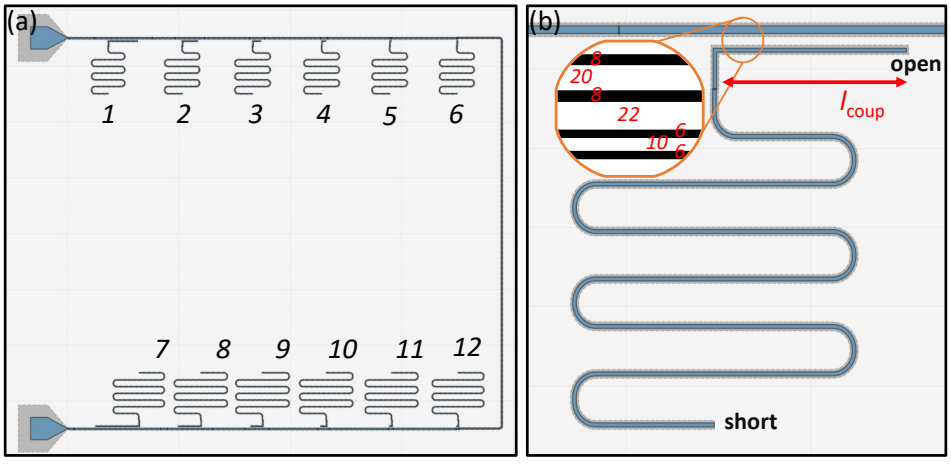

Figure 3.3: Qiskit-metal design for reference CPW resonators. (a) Overview of twelve CPW resonators coupled to one feeline. Resonators 1-6 are simulated to be 6.3-6.8 GHz and resonators 7-12 from 4.3 - 4.8 GHz. All are spaced 100 MHz apart. **(b)** Zoom in on one CPW resonator, which is open at one end (top) and shorted at the other (bottom) to form a $\lambda/4$ resonator. Inset in (b) shows CPW spacing of 6/10/6 μm (gap/center pin/gap) and couple distant of 22 μm from the 8/20/8 μm feedline. Each resonator (1-12) differs in total length (short-open), l_{tot}, and coupling length, l_{coup}.

After performing the standard eigenmode simulation [98] in qiskit-metal, we fabricate the design following steps 0-3 as discussed in Sec. 3.2.1. Then we wire bond the chip to a printed circuit board (PCB) and perform single-tone VNA spectroscopy on the chip while cooled to a few mK in a dilution refrigerator (see Sec. 3.3.1 & 3.3.3). Both simulation and measurement results are presented in Table 3.2 for the corresponding resonator numbers. We can already see that the resonance frequencies are always, arbitrarily, lower than the simulated frequencies. This makes sense since the kinetic inductance adds up to the total inductance of the resonators and thus lowers the resonance frequency, $\omega_0 = 1/\sqrt{(L_g + L_K)C}$.

Table 3.2: CPW resonator simulation and measurement results Table shows the qiskit-metal eigenmode simulation results and single-tone VNA spectroscopy results in a dilution refrigerator. Resonator numbers correspond with numbers shown in Fig. 3.3(a).

Resonator nr.	1	2	3	4	5	6
Simulated freq. [GHz]	6.313	6.402	6.513	6.604	6.697	6.804
Measured freq. [GHz]	5.211	5.280	5.369	5.456	5.527	5.614

Resonator nr.	7	8	9	10	11	12
Simulated freq. [GHz]	4.309	4.411	4.510	4.605	4.687	4.790
Measured freq. [GHz]	-	3.649	3.730	3.806	3.879	3.975

Now we re-simulated the design again, but in the environment for PyEPR and qiskit-metal developed by S. Hawaldar. We render and export feedline with a CPW resonator, as shown in Fig. 3.3(b), to Ansys HFSS. S. Hawaldar's code adds 50 Ω loads to the ends of the feedline and add kinetic inductance properties to the metal layer in Ansys HFSS. We run the simulation code, as shown below, in a loop where we sweep the kinetic inductance properties (kinetic_inductance_params) till the new simulation results for all CPW resonators match the measured frequencies for one kinetic inductance value.

```
resoantor_nr = 1 # enter number 1-12 to select what resonator to simulatate
eig_res.sim._render(name="Readout",
    selection = ['short_to_ground_resonator_'+ str(resoantor_nr),
    'Resonator_'+ str(resoantor_nr),
    'Coupler_resonator_'+ str(resoantor_nr)],
    solution_type='eigenmode', vars_to_initialize=eig_res.sim.setup.vars,
    open_pins=[],  box_plus_buffer = False,)
    kinetic_inductance_params=1.4052e-3)
eig_res.sim._analyze()
eig_res.get_frequencies()
```

As it turns out, for our 100 nm thick NbTiN on 525 μm silicon substrate and following fabrication steps 0-3 in Sec. 3.2.1, we need to insert a surface inductance of 1.4052 pH/□ [2]. This gives us the needed correction to simulate our superconducting (NbTiN) structures (bulk qubit circuitry, feedlines and readout resonators).

[2] This method also shows to have ~ 0.53 pH/ □ for 200 nm NbTiN, which corresponds with the results from [103].

JOSEPHSON INDUCTANCE AND JUNCTION WIDTH

Simulating qubits with Josephson junctions in Ansys HFSS for eigenmode analysis is not straightforward since the Josephson junction is a non-linear element. Qiskit-metal circumvents this by exporting your qubit design to Ansys and placing a lumped element inductor (rectangular element) with a given inductance L_J. Once the design is ready for fabrication, qiskit-metal imports an assigned junction geometry in the final GDS file. For this, we need to know what inductance to assign to a single junction (or zero flux-tuned SQUID inductance) for a given width. Therefore, we need to know the relation between junction width (for single and SQUID junctions) and their Josephson inductance L_J for our specific junction type and fabrication. Once we know this, we can assign a junction width and inductance for our simulations to correspond with the set out Josephson energies ($E_J = 20/40$ GHz) from Sec. 3.1.1.

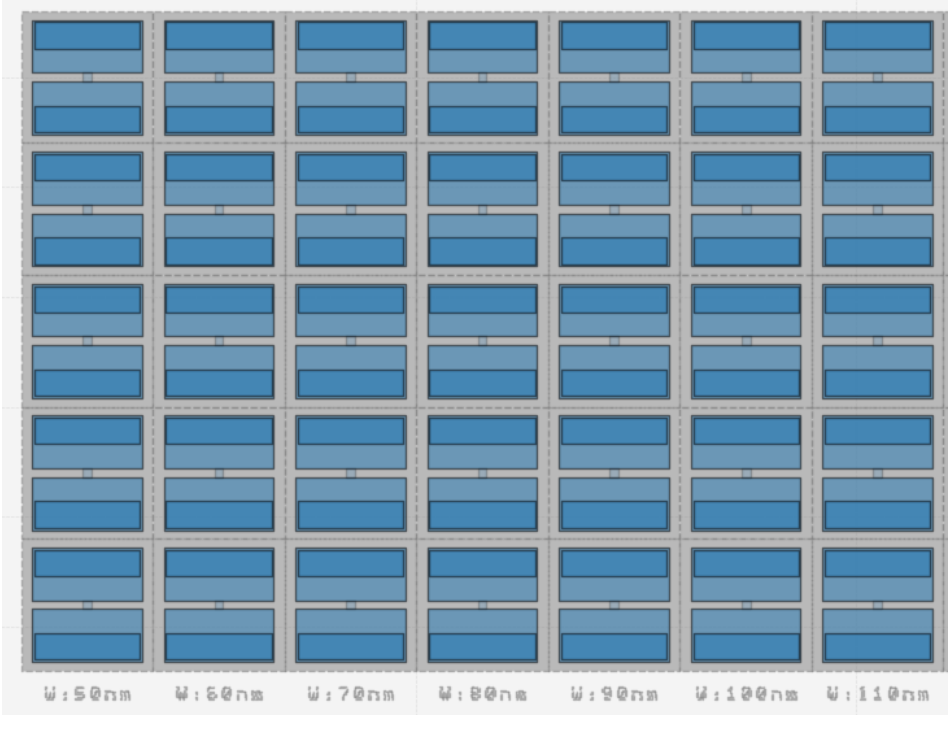

Figure 3.4: Qiskit-metal design of single junction test chip. A small section of the total chip shows five identical junctions of width 50-110 nm in steps of 10 nm. Each test junction will be fabricated with two NbTiN islands, a Manhattan-style Al junction shorting them, and Al pads on top for better probe contact.

We designed a junction test chip consisting of, as partially shown in Fig. 3.4, repeating elements containing two superconducting islands (NbTiN) shorted by a Manhattan style ($Al/AlO_x/Al$) Josephson junction with varying junction width. Each superconducting island also has an Al layer evaporated on top for better contact with probe needles for testing. The junction width is varied from 50 to 300 nm in steps of 10 nm and copied five times for statistics. We created (not shown in the figure) four areas with the described variation, which either have a single junction or a SQUID loop of 5×5, 10×10 or $10 \times 40\ \mu m^2$.

After fabricating this junction test chip, following steps 0-6 in Sec. 3.2.1, we are ready to perform a two-probe conductance measurement. For this measurement, we place the chip on a stage which has a weak vacuum to fix its position. Two tungsten needles, attached to micromanipulators, are placed on top of each Al/NbTiN pad as shown in Fig. 3.5. The measurement is performed at room temperature while a direct current is applied to the junctions via the probe needles. The voltage drop across the junction is measured with a custom-built junction measurement box [115], see schematic on the right of Fig. 3.5, which is connected to a multi-meter in order to determine the junction resistance. Normal multi-meters can not be used directly on the junctions since these apply a too-large current and create a short circuit in the junctions. For this reason, the measurement box is used to get a lower current that is suitable for the junctions and amplifies the output voltage, V_{out}, for a connected multi-meter to readout. The electrical circuit of the junction measurement box is shown in Fig. 3.5. In the schematic, the resistance R can be varied between 1 kΩ, 100 kΩ and 10MΩ and changes the current sent through the junction.

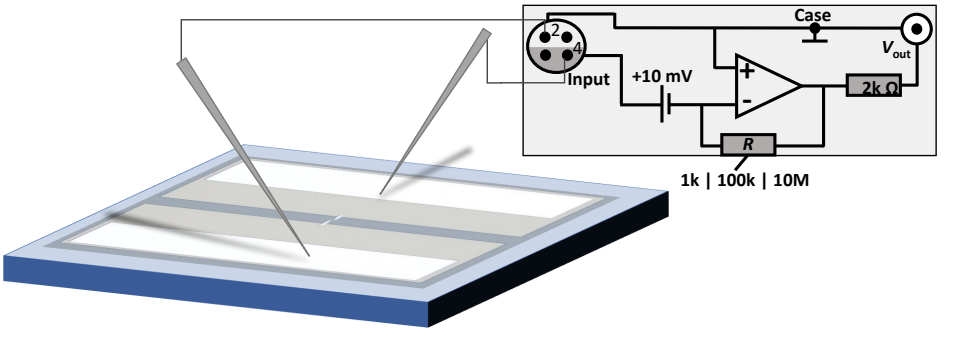

Figure 3.5: Two probe measurements of test junctions. Schematic of probe setup with electrical circuit of the junction measurement box.

Test results for the single junction measurements are shown in Fig. 3.6, where we plot the resistance R_N, junction inductance L_J and Josephson energy E_J against junction widths. For these results, we measured the voltage (mV) over the junction using the procedure described above, where we put the box resistance to 100 kΩ. To calculate R_J, L_J and E_J, we used the following equations [116]:

$$R_N = \frac{1.05}{V_{out}} \quad [\text{k}\Omega] \tag{3.1}$$

$$L_J = \frac{1.24}{1.03 \cdot (V_{out} \cdot 1e^{-3})} \quad [\text{nH}] \tag{3.2}$$

$$E_J = (1.03 \cdot 132) \cdot (V_{out} \cdot 1e^{-3}) \quad [\text{GHz}] \tag{3.3}$$

Using the equations above and measurements taken with the junction measurement box (in mV) we calculate and plot the R_N, L_J, and E_J for different junction widths in Fig. 3.6.

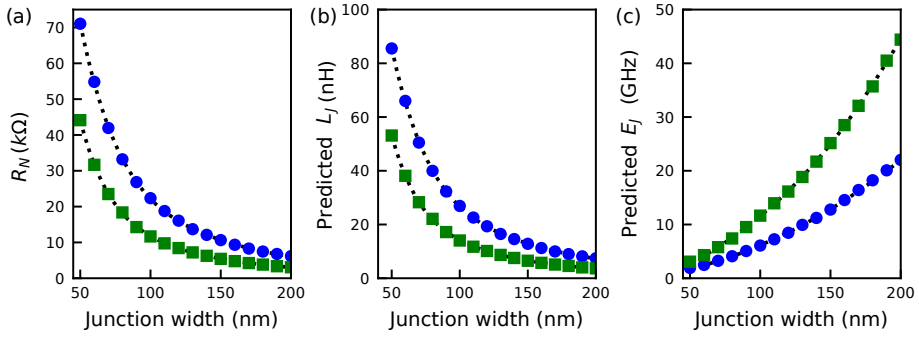

Figure 3.6: Results from two probe measurements. Plots showing the calculated single junction (round blue markers) and SQUID loop (green diamond markers) parameter values for given junction widths (nm) with **(a)** Junction resistance R_N, **(b)** predicted Josephson inductance L_J, and **(c)** predicted Josephson energy E_J. Values were calculated using Eq. 3.1 following the example from [116]. All junctions are measured at room temperature according to Fig. 3.5

From these measurements and calculations (using Eq. 3.1), we predicted that for Josephson energies E_J of 20 or 40 GHz for single junctions or, respectively, SQUIDs we need a junction width of 190 nm. This junction width corresponds with a Josephson inductance L_J of 8 or, respectively, 4 nH. Now that we have chosen our parameters, we can continue with qiskit-metal for our full design.

3.1.2. Qiskit-metal for design and simulation

As explained in Sec. 3.1.1 we decided on creating a pocket transmon with an antenna attached to one of the superconducting islands. The other island will be capacitively coupled to a readout resonator which in turn is coupled to a feedline. To be consistent with earlier tests, we use for the CPW readout resonator the *gap/center pin/gap* distances of 6/10/6 μm and for the feedline 8/20/8 μm. In Fig. 3.7, we show a detailed design of a readout resonator with our pocket transmon qubit with dimension variables. For our simulations, we enter a surface inductance of 1.4052 pH/□ and use a Josephson inductance of 8 nH for fixed frequency (single junction) qubits and 4 nH for flux tunable (SQUID) qubits. We run the simulations and optimize the given variables from Fig. 3.7 (b,c) to meet the design requirements from Table 3.1.

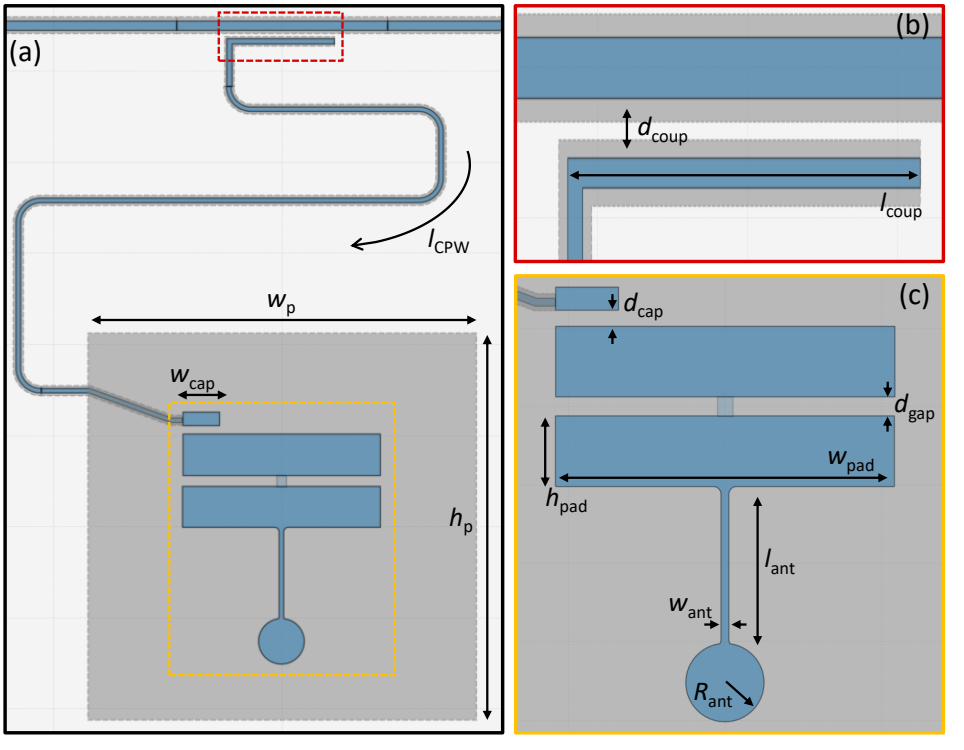

Figure 3.7: Qiskit-metal design of a single readout resonator coupled to a pocket transmon with antenna. Panel **(a)** Shows the overview of the one single pocket transmon with readout resonator. Here, we focus on total CPW length (l_{CPW}) of the readout resonator (which includes l_{coup}), pocket width (w_p), pocket height (h_p), and coupling capacitor width (w_{cap}). **(b)** Zoom in on the readout resonator to feedline coupler, with a focus on dimensions such as coupler length (l_{coup}) and gap separation (d_{coup}). **(c)** shows the pocket transmon with dimensions such as the gap between the coupling capacitor and top island (d_{cap}), island gap (d_{gap}) and island width (w_{pad}) and height (h_{pad}). Here, an antenna is attached to the bottom island with antenna width (w_{ant}), length (l_{ant}), and disk radius (R_{ant}) at the end of the antenna.

As one can see from the figure above, there are many dimensions to adjust and keep track of when designing the readout resonator and transmon qubit. We list what important dimensions [3] are concerning the variables from Table 3.1:

- The readout resonator frequency f_{RO} depends on, for fixed CPW *gap/center pin/gap*, on the total CPW length, l_{CPW} (including coupler length l_{coup}). The longer the CPW, the lower its frequency.
- For its external decay rate κ_{ext} we mainly adjust the feedline coupler's length, l_{coup}, and gap separation d_{coup}. Increasing l_{coup} and decreasing d_{coup} will increase κ_{ext}.
- For the qubit frequency f_q we fixed the Josephson inductance L_J and only adjusted the readout resonator coupling capacitor (depending on w_{cap} and d_{cap}), the capacitance between the islands (h_{pad}, w_{pad}, and d_{pad}), and capacitance of islands with the antenna to ground (h_{pad}, w_{pad}, d_{pad}, l_{ant}, w_{ant}, and R_{ant}). Capacitance to ground mainly depends on pocket width and height, w_p,h_p. The further away, the lower the capacitance.
- The anharmoncity, $\alpha \sim E_C$, is inversely proportional to the transmon's capacitance. The larger the transmon islands are, and the closer together they get, the smaller α becomes.
- The capacitive coupling between readout resonator and the transmon, thus their coupling strength g mainly depends on the capacitor dimension, w_{cap}, and distance to transmon, d_{cap}. The wider w_{cap} and smaller d_{cap} gets the larger the coupling.
- Inherently, the dispersive shift, χ, and the Purcell time, $T_{Purcell}$, depend on detuning, Δ, and on the variables (f_{RO}, f_q, and g) listed above. (Sec. 3.1.1).

When doing the Ansys simulations, we check if the qubit mode has a sufficiently large electric field at the antenna's disk (see Fig. 3.8(a)). To ensure that when the HBAR's piezoelectric is placed close to the antenna, we maximize the piezoelectric coupling (see Sec. 2.2.3). We want to design the antenna sufficiently away from the two superconducting islands to ensure it does not interfere with the capacitance between the two islands. This is the case for an antenna with length $l_{ant} = 250\,\mu$m, width $w_{ant} = 10\,\mu$m, and disk radius $R_{ant} = 50\,\mu$m.

For simulating our design, we start by using Ansys Q3D with the qiskit-metal LOM analysis to extract the capacitance matrix from which we calculate $E_C \sim \alpha$ and check if $E_J/E_C \geq 50$. If so, we continue the simulation by exporting the design to Ansys HFSS and use eigenmode analysis with (qiskit-metal's) PyEPR to extract χ, f_{RO}, f_q, and readout resonators Q-factor. From these we calculate κ_{ext}, g, and $T_{Purcell}$. All numbers will be compared and tested to the set design condition from Sec. 3.1.1. Once the design passes the condition test after looping through (sometimes seemingly never-ending) simulations, we continue with the device.

[3] Keep in mind: all dimensions influence the variables in a way, but here we identify the ones that influence specific variables the most.

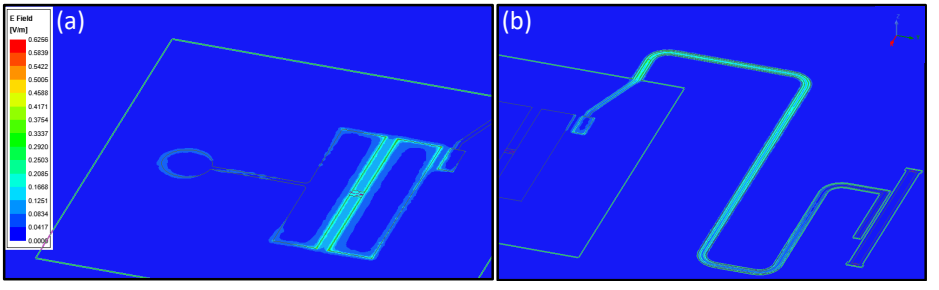

Figure 3.8: EM field simulations in Ansys HFSS. All simulation results plot the electric field in V/m. Panel **(a)** Shows the transmon qubit 01-transition mode. In the data, we can see that the strongest electric field is between the two islands, followed by the coupling capacitor of the readout resonator, and the final strongest electric field resides in the antenna disk. **(b)** Simulation result of readout resonator mode.

In our final full chip design, where in Fig. 3.9 we only show one feedline; we couple multiple devices to one feedline. These devices are three fixed frequency transmons, two flux tunable transmons, and one single CPW resonator. The last one is a known device which should always be visible during measurements. Since multiple readout resonators are coupled to one feedline, we need to make sure these are frequency multiplexed. This means they should not have similar resonance frequencies, and therefore we space them at least a $\sim$ 200 MHz apart. In principle, we could design the qubits to be at the same resonance frequency, but we like to keep a detuning of $\Delta \approx 1$ GHz. In the final design, we have two feedlines which are an exact copy of the one shown in Fig. 3.9. The only difference is that one will have an HBAR chip flipped on top and the other remains as a control line to check differences from the HBAR devices. Differences we expect are HBAR modes visible in measurements, different qubit decay times (like T_1 and T_2), and shifts in frequencies due to the HBAR chip.

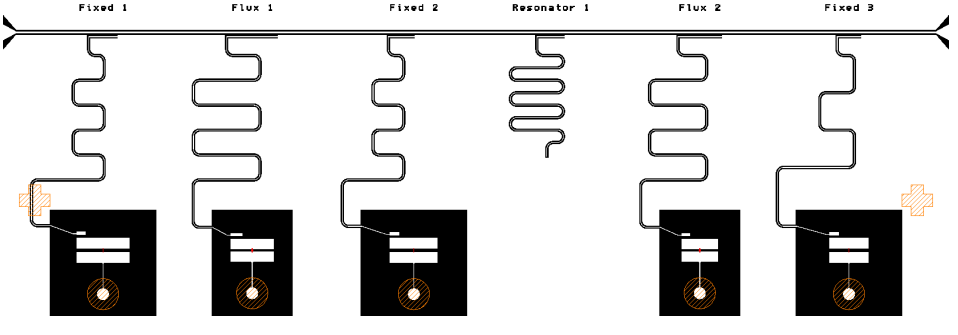

Figure 3.9: Top feedline of full chip design. The devices shown in the figure consist of three fixed frequency transmons, two flux tunable transmons, and one single CPW resonator. Here, the colors white indicate metal (NbTiN), black is exposed substrate (Si), red are the Josephson junctions, and orange the AlN cylinders in on the flipped HBAR chip.

One significant advantage of the 2D qubit architecture (compared to 3D) is already visible in the design: we have the possibility to design multiplex devices on one chip. This enables us, in future research, to design chips with multiple transmon-HBAR devices which are each flux tunable and interact with one another.

3.1.3. DESIGN HBAR AND MATERIAL CHOICES

Making high-quality reproducible piezoelectric layers is challenging. For this reason, we chose to commercially acquire wafers from *Kyma Technologies* (part number AT.U.100.1000.B)). These wafers are made from 650 μm thick sapphire with $\sim$ 1 μm piezoelectric layer of aluminum nitride (AlN). From these wafers, as explained in Sec. 3.2.2, we etch $\sim$ 900 nm thick AlN cylinders with a diameter of 250 μm. This diameter was chosen to ensure that the HBAR completely covers the end of the qubit's antenna without covering the transmon islands. Etching away the piezoelectric layer everywhere else also reduces unwanted modes on the chip. This diameter also gives a buffer in case of misalignment during flipping (see Sec. 3.2.3).

Following the equations of Sec. 2.2.2, and using the longitudinal sound velocity $v \approx 1.11^4$ m/s, which corresponds with the sound velocity of sapphire and AlN [23, 117], we calculate a fundamental mode of about 6 GHz and FSR of 8.538 MHz. These are the numbers we will be looking for during measurements.

3.2. Fabrication

This section is divided into two sections: the fabrication of the qubit sided chip and fabrication of the HBAR sided chip. We start by describing the qubit chip.

3.2.1. Fabrication of planar Superconducting transmon qubit

In this section, we describe the full qubit sided chip. In short, as shown in Fig. 3.10, the chip is fabricated in two electron beam lithography (EBL) steps. In the first EBL step (steps 0 - 3) the bulk circuitry, e.g. transmon islands and CPWs, is etched into the NbTiN layer. In the second EBL step (steps 4 - 6) the Al-AlO_x-Al junctions are fabricated using a double-angle shadow evaporation technique with intermediate in-situ oxidation. The wafer preparation and NbTiN deposition (step 0) are outsourced to Dutch institute for Space Research (SRON) [103], but the fabrication is still described here for the sake of completeness. After receiving the NbTiN deposited wafers, we continue our fabrication process independently at the *Delft Kavli NanoLab* [118] starting from step 1.

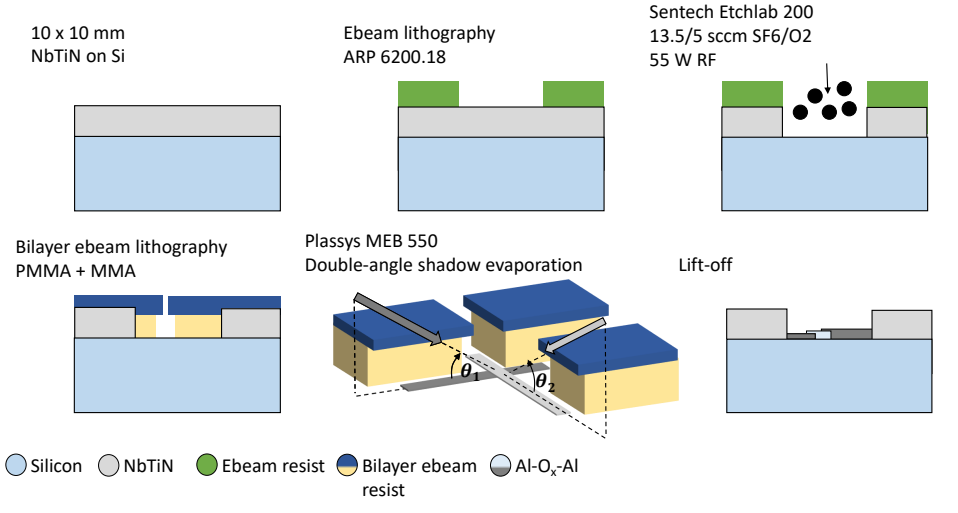

Figure 3.10: Fabrication transmon chip. Drawings show a step-by-step process for fabricating our 2D transmon qubits. Top row (left to right) steps 0-3 are shown. Step 0: Preperation of Si wafer + NbTiN deposition. Steps 1-3: EBL spin, expose, development, and etching of NbTiN. Steps 4-6 (bottom row, left to right): spin, expose and development of bilayer ebeam resist. double angle shadow evaporation of Al-AlO_x-Al junctions and it's lift-off are shown in the last two panels. Note: Drawings not to scale.

Step 0: Preperation of Si wafer surface and NbTiN deposition

First, a 4" silicon double side polished (DSP) wafer of 525 μm thickness is chemically treated to remove unwanted contaminants. We immerse the wafer face-up in a beaker with 110°C phosphoric acid (H_3PO_4) for 30 minutes. Afterwards the wafer is immediately rinsed for 30 seconds in a D.I. H_2O bath at 80°C to dissolve the acid for 30 seconds and transferred to another D.I. H_2O bath at room temperature for an arbitrary timed second rinse (usually 30-60 seconds). Next, the wafer is installed in a wafer holder and immersed in the quick dump rinser for a

6-minute program. Then, the wafer is continuously blow-dried with a nitrogen (N_2) gun while spinning with 2000 rotation per minute (rpm) for 2 minutes. [4] After the surface treatment, the wafer is quickly transferred into the *LLS801 sputtering machine* (at the SRON facility) (preferably within 2 minutes). The LLS801 is a refurbished and customized industry-based sputtering machine, which deposits NbTiN by means of DC magnetron sputtering. A stoichiometric NbTiN film is obtained by using a 99.8% pure $Nb_{0.7}Ti_{0.3}$ target and a continuous N_2 flow to nitrodize the target during the deposition. We end up with a final metal film thickness of $\sim$ 100 nm. After deposition, the 4" wafer is transferred from our collaborators at SRON back to our clean room.

STEP 1: PREPARATION

After the full wafer depostion of 100 nm thick NbTiN layer, we further our fabrication by dicing the 4" wafer into 10×10 mm chips. At this point, after receiving the wafer, we do not need to clean the surface. So, we immediately start by spin coating the wafer with S1805 [119] photoresist at 1000 rpm and perform a 5 minute bake on a 90°C hotplate. This photoresist layer is needed protect the wafer during dicing.

Next, we mount the wafer in the dicing machine (*DAD 3220* from Disco Hi-Tec Europe GMbH), see right panel Fig. 3.11. Dicing is used for cutting partially (scribing) or completely (singulation) of our wafer. For this technique a dicing blade, which has diamond particles embedded in resin, will rotate at high speed in a spindle (top-left panel Fig. 3.11) and move through the substrate at a certain depth and feedspeed (movement speed across sample). During dicing the blade slowly breaks/shatters as it grinds away material from the substrate, and new diamond particles (deeper in the resin) continuously offer new sharp points. The high rotation speed and strong friction of the diamonds particles on the diced substrate generate an important amount of heat which need to be extracted. For this reason, cooling water is supplied near the dicing blade/substrate contact point in order to thermally stabilize the process. When using the right blade and dicing parameters, perfect edges can be created (even for very brittle materials like sapphire).

Dicing, throughout this work, is used to cut chips into workable sizes or trim into a final format (see later on for the Top chip in Sec. 3.2.2). One could also choose to dice at the end of a full-wafer process to end up with a bunch of chip, e.g. in bottom-left panel Fig. 3.11.

[4] Inspection with a high intensity electric torch (10000 lumens) is recommended. This is done to ensure that the front side of the wafer is free of micron sized particles. If not, repeat the last steps by placing the wafer back into the quick dump rinser until the wafer has zero visible particles.

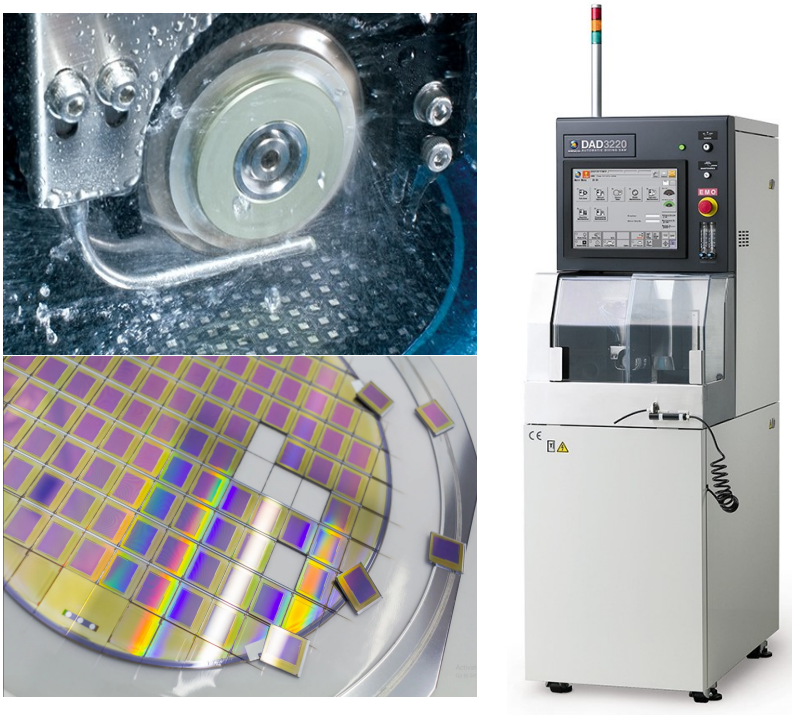

Figure 3.11: Informative photos on dicing. Top-left: Spindle with dicing blade during process. Bottom-left: example final result of dicing a fully processed wafer [120]. Right-panel: photo of used DAD3220 dicing machine [121].

Step 2: Patterning

Before we can pattern our bulk circuitry, we first need to strip the photoresist from the diced sample. We place the sample in beaker of acetone and perform an ultrasonic clean for 5 minutes at the highest power. This is an easy option to dissolve the photoresist as much as possible. Afterwards, we transfer the sample into an isopropyl alcohol (IPA) solution and perform 5 minute ultrasonic clean. To dry the chip we use a high pressure N_2 gun. To remove any residual particles, the last nanometers layer, an oxygen plasma is used. This 2 minute O_2 descum is performed in the *PVA Tepla 300* [122], which was set to have O_2 flow rate of 600 sccm and radio frequency (RF) power of 600 W. The PVA Tepla 300, is a microwave plasma system that can operate at higher pressures ($\approx$ 1 mbar). Here, the higher pressure is used to create an isotropic plasma which removes organic residues everywhere uniformly.

Next, the sample is quickly transported to a spin coater. Here, we spin a 800 nm layer of AR-P 6200.18 [123] on the clean NbTiN layer using a 4000 rpm spin setting followed by a 2 minute bake at 160°C on a hotplate. We place the sample into the *Raith EBPG-5200* for electron beam (E-beam) exposure after determining the centre of the chip (measured chip corners with respect to the E-beam holder Faraday cup) using the Raith-supplied alignment microscope, the *Leica Z16 microscope*. The resist is exposed using 146 nm beam (256 nA beam current, 400

μm final aperture size) and dose of 315 $\mu\mathrm{C}/\mathrm{cm}^2$. Afterwards, the resist is developed for 1 minute in a pentyl acetate solution, followed by a 5 second rinse in Ortho-xylene (O-xylene [124]) which slows the development down to a stop. To rinse the sample, we used a 1 minute dip in IPA (this option reduces the amount of residues) followed by blow-drying the sample with an N_2 gun. To harden the resist, for the following dry-chemical etching process in step 3, we perform a post-bake of 2 minutes on a 130°C hotplate (hardbake). The described process above is depicted in Fig. 3.10 steps 1 and 2.

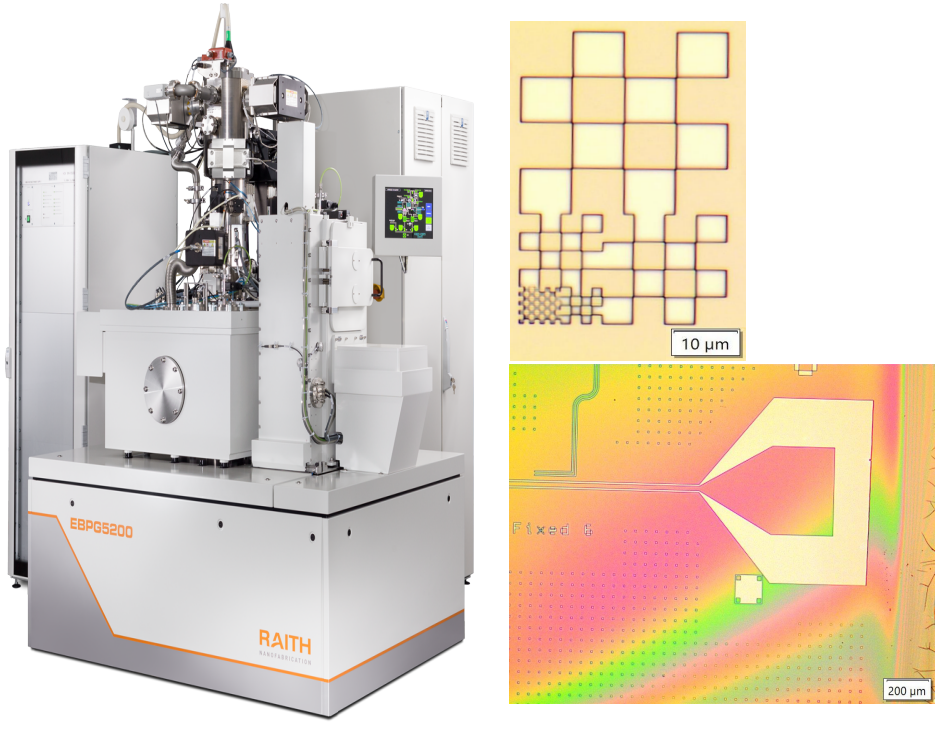

Figure 3.12: Picture of E-beam system (left) [125] and micrographs of checkerboard (top-right) and launch-pad (bottom-right) concerning the author's notes.

Some notes from the author concerning the figure above. In the design a checkerboard (top-right micrograph Fig. 3.12) was included to check, after development, if the exposure settings were correct and did not cause unwanted overexposure. In the bottom-right micrograph in Fig. 3.12, we can see a rainbow colored fringing effect cause by *edge bead*. This is a phenomena that occurs during spin coating where resist accumulates at the edge of the wafer (corners of square sample) several times the nominal thickness of the resist. In some cases, the resist could even wrap around the sample contaminating the backside as well. Fig. 3.12 bottom-right micrograph also shows cracks in the resist film on the sample edge. To harden the resist, spinned photoresist can start to embrittle at temperatures above 130°C by reacting with atmospheric oxygen. The cracks are a consequence of different thermal expansion coefficient of resist and substrate. These cracks could make the resist locally useless as a mask. However, in our case this effect is mostly seen at the edges of the sample and are of no concern since

the cracks are far away from the devices under test. If one does see this effect in unwanted or critical areas one could try to prevent this by lowering the hardbake temperature, slow cooling (turn off hotplate and leave chip on) or slowly ramping up the temperature for the hardbake [126]

Step 3: Etching

After patterning, we remove the exposed NbTiN by performing a reactive ion etch (RIE) in the *Sentech Etchlab 200 F1*. In here, the sample is placed on a quartz plate of a cylindrical vacuum chamber ($P_{\text{chamber}} = 10\ \mu$bar). The bottom plate, on which the quartz plate sits on, effectively acts as a capacitor plate. The gas that is mainly used to generate the plasma during the etching is sulfur hexafluoride (SF_6), of which the reaction, during the generation of the plasma (electron-impact ionization of SF_6), becomes [127, 128]:

$$\mathrm{e}^- + \mathrm{SF}_6 \rightarrow 2\mathrm{e}^- + {\mathrm{SF}_5}^+ + \mathrm{F}^* \tag{3.4}$$

Other ionization reactions, which induce electron loss in the plasma, are:

$$\mathrm{e}^- + \mathrm{SF}_6 \rightarrow \mathrm{SF}_5 + \mathrm{F}^- \tag{3.5}$$

$$\mathrm{e}^- + \mathrm{SF}_6 \rightarrow {\mathrm{SF}_6}^- \tag{3.6}$$

The rate constant of Eq. 3.5 exceeds that of Eq. 3.6, thus the generation of F^- exceeds that of ${\mathrm{SF}_6}^-$. Therefore, we mainly end up with a plasma mixture of SF_5^+ and F^- ions, fluorine radicals [129] (F^*) radicals and electrons. Another gas that is used is oxygen (O_2), which serves as a stabilizer and prevents the fluorine to recombine, which keeps the reactive F^* concentration high. The SF_6 and O_2 gasses enter the vacuum chamber through small inlets, in the top plate of the vacuum chamber, and exits through the vacuum pump system at a flow rate of 13.5 and, respectively, 5 sccm. To ionize this gas mixture, an RF-field with a power of 55 W is applied between the top and bottom plates. Charge on the bottom plate builds up and create a negative potential. While heavier (positive) ions are hardly accelerated, the electrons are accelerated towards the bottom plate (cathode). This creates a DC bias which attracts the positively charged free radicals from the gas mixture towards the sample.

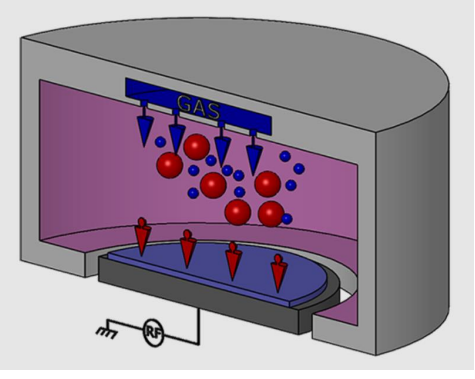

Figure 3.13: Schematic of RIE etching machine. Drawing shows the gas inlet via the top of the vacuum chamber which lets in the SF_6 and O_2 gasses. The generated plasma mainly contains SF_5^+ (red spheres) and free radicals like F^* and O^* (blue spheres).

At the sample, the (reactive) ions can both physically and chemically etch materials on your sample. This allows for selective etching of device layers (anisotropic etch). In our specific case, the SF_5^+ ions accelerate down to the sample with enough kinetic energy to both remove the NbTiN atoms from the film by physical collision and the F^* radicals are absorbed on the NbTiN surface and undergo a chemical reaction. The product of the chemical reactions are released from the surface through desorption and diffuse back into the main gas flow. This etching process takes place at room temperature and an etch rate of approximately 65 nm/min is achieved (90 second etch for 100 nm of NbTiN).

The F^* radicals also react with the resist creating fluorocarbons, which could cause side wall passivation and results in a more anisotropic etch. For this reason, oxygen is used as a stabilizer to suppress the fluorocarbon passivation by the formation of CO_2. The downside of O_2 is that it increases the etch speed through the resist, causing the need for a very thick or hard resist layer (see previous paragraph). Another downside of SF_6 in combination with O_2 is that it also reacts with silicon, our sample substrate. When not taking this into account, the etch will continue once the exposed NbTiN is etched away. To prevent overetching in the the silicon, laser end point detection is used to determine when the material is fully etched through. In this method the reflectivity of the surface is measured with a laser. Because the reflectivity of NbTiN is higher than silicon, the reflected power will drop when the silicon is exposed. As a rule of thumb, we etch for 5 to 10 seconds more, once the power drops, to ensure that we are fully through the NbTiN layer throughout the entire sample.

Since the reaction between F^* radicals and the resist creates a passivation layer, we follow the RIE process up with an in-situ oxygen descum (50 sccm O_2,100 W, 10 μbar) of 20 seconds without breaking vacuum. After the sample is taken out of the etcher, the remaining E-beam resist is stripped off the sample using dimethylformamide (DMF) in an au bain-marie set to $\approx 88^\circ$C for 1 hour. Now, the etched areas should be exposed silicon. In order to double check that our etch is complete, we quickly test the conductivity of this area with the use of a probe station. The presummed exposed silicon areas measured to be very high resistant (several GΩ) and the stripped NbTiN film is about 100 kΩ (same as after step 0).

Step 4: Patterning double resist layer

After stripping the E-beam resist, the sample is put back into the *PVA Tepla 300* for a 1 minute O_2 descum set at a flow rate of 200 sccm and 100 W RF power. This will ensure that any residual particles of the resist is removed. After the descum, we start applying a bilayer resist stack to create our Manhattan [109] Josephson junction. We start by placing the chip on a 180°C hotplate for 2 minutes to evaporate water vapour from the surface. Afterwards, we quickly apply a $\sim$ 100 – 200 nm layer of MAA 8.5% EL6 [130] on the chip by spin coating it at 2000 rpm. Before applying the second layer, we bake the resist for 3 minutes at 180°C. This thin layer is used to promote lift off. On top of this layer a thick resist ($\sim$ 600 nm) of 950 PMMA A6 is spun at 1500 rpm and baked once more at 180°C for 5 minutes.

The junctions were patterned by E-beam lithography using a dose of 1700 $\mu C \cdot cm^{-2}$. The bilayer was developed using a cold H_2O:IPA in a 1:3 mixture for 2 minutes in an ultrasonic bath set to the lowest power. Afterwards, the chip is cleaned with IPA (15 second swirl in beaker) and dried using a high pressure N_2 gun. Fig. 3.14 shows a schematic of the double resist layer with evaporation angles $\theta_{1,2}$. The figure shows that a combination of double resist, with an undercut, and choosing evaporation angles, $\theta_{1,2}$, for rotation angles 0° and 90°, we can create Manhattan Josephson junction. For this we use double angle shadow evaporation technique, which we will discuss briefly in the next section.

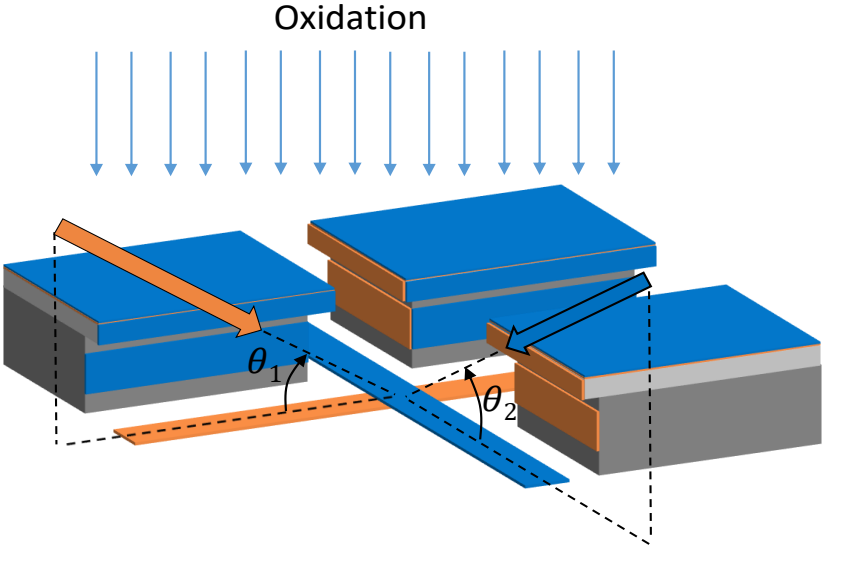

Figure 3.14: Double angle evaporation for Manhattan Josephson junctions. Schematic is a cartoon depicting the double angle evaporation and use of a bilayer E-beam resist. Here, the developed features are designed to be deeper than their width. This allows metal to be deposited to the substrate when parallel to a channel, but block metal in the orthogonal channel.

STEP 5: DOUBLE ANGLE EVAPORATION

After resist development, we first clean the now exposed silicon surface with an oxygen plasma in the *Sentech Etchlab 200*. The chamber pressure is brought to 10 μbar with an oxygen flow rate of 20 sccm. The system is set to an RF power of 20 W and RF bias of 100 W for a 45 s descum to remove any residual resist. This procedure is called plasma ashing and a downside to this oxygen plasma treatment is that it introduces oxides on the silicon surface (were later on Al/AlO_x/Al Josephson junction are deposited). The oxide layer thickness increases with plasma duration [131] and consists many silicon oxides, SiO_x, $0<x<2$ [132], mainly SiO_2. Various adsorbates can attach to SiO_2, like hydroxyl groups (-OH) to build a layer of silanol which is hydrophilic and thus making the silicon surface hydrophilic as well [70, 133]. Even without the plasma, exposure of the silicon surface to air forms a oxide layer, native oxide, and will grow on the surface nonetheless [67]. Fortunately, silicon is one of few materials with a slow growth rate and will self-limit to a thickness of ~2 nm in a matter of hours [68]. Meaning that one has time between clean and metal deposition before the native oxide layer is grown. Nevertheless, this thin layer of amorphous native silicon oxide is known to contain a considerable amount of two level systems (TLSs) to which qubit are known to couple to [70, 134], which is an unwanted consequence. The SiO_2 is removed by using a Buffered Oxide Etch (BOE). BOE is a mixture of 7 parts 40% ammonium fluoride (NH_4F) and 1 part 49% HF hydrofluoric acid (HF). HF removes SiO_2 according to the reaction $\mathrm{SiO_2 + 6HF \rightarrow H_2SiF_6 + 2H_2O}$, where it forms fluorosilicic acid, H_2SiF_6, and H_2O. The H_2SiF_6 is soluble in the sample (meaning it diffuses deeper into the silicon) and is thus removed from the substrate. The result of this reaction is that the HF is removes from the surface where we need it for the removal of SiO_2. For this reason, NH_4F is used to replenishes the HF concentration ($\mathrm{NH_4F \longleftrightarrow NH_3 + HF}$). This results in an even concentration and constant etch rate throughout the process [135, 136].

As procedure, we first dip the sample in DI water for ~5 seconds to see that the bottom of the chip is hydrophilic (DI water wetting or sheeting across the whole surface of the wafer) [137]. The bottom is checked since the exposed area on the top is too small for the naked eye to check this effect (100s of nm^2). Afterwards, the chip is immersed in a 1:1 mixture BOE:H_2O for 45s followed by two 30s DI water dips to stop the etch and dilute the acid. If the etch of SiO_2 is successful, the DI water will not adhere to the back, except for a few isolated drops, and the silicon surface has become hydrophobic. Note: *if this is not the case repeat the BOE:H_2O dip for an additional 30s till it has become hydrophobic.* After the acid clean the chip is dried with a high pressure N_2 gun and quickly placed onto a cassette of the *Plassys MEB550 S2* Aluminum evaporator, see left photo of Fig. 3.15. The chip is aligned and as shown in Fig. 3.14 alignment is important for our Aluminum evaporation. Even when the alignment is slightly off, the junction arms might not intersect (no junction creation) or the cross sectional area is unpredictable making the Josephson inductance, L_J, unpredictable.

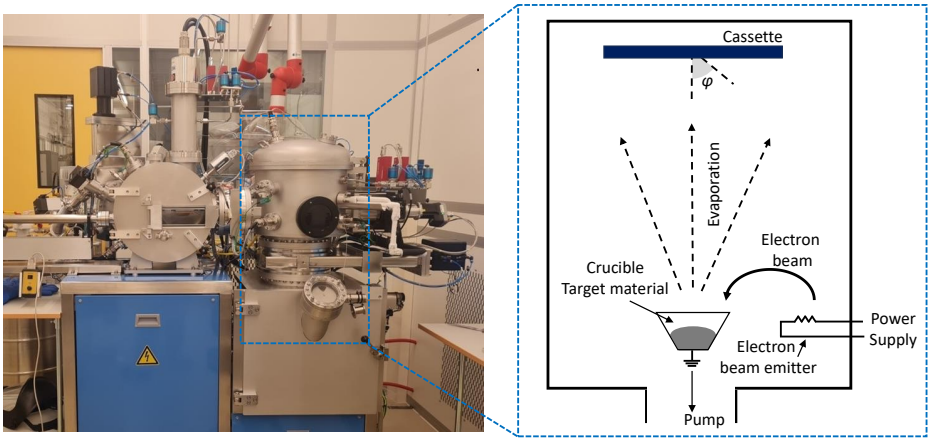

Figure 3.15: Plassys MEB550 S2 electron beam heating evaporator. Left: a photo of the Clean room Plassys. Right: Schematic showing an electron beam (bottom right) focused on a target material crucible (bottom) underneath the substrate (top).

For the following evaporation step, we use a similar technique as described in [135, 138] and is performed in the *Plassys MEB550 S2*. The Plassys is a system capable of depositing material from different tilt and rotation angles without breaking vacuum, which is important for junction fabrication. As shown in the schematic of Fig. 3.15, the Plassys uses an electron beam source consisting of cathode filaments that releases electrons. Using this electron beam, which is focused onto a crucible using a magnetic field, a small spot on the material within the crucible is warmed up. Once warmed up, the material will start to evaporate from the crucible and eventually deposits on the substrate. The advantage of electron beam evaporation is that it could evaporate more material than a thermal source (warming up entire crucible with a resistive wire) and has less impurities (crucible itself could start to evaporate in thermal sources and introduce contamination). The deposition rate of the electron beam is typically between 10-100 Å/s, which is higher than the thermal source (1-20 Å/s). Another advantage of our Plassys, is that it uses dynamic oxidation [5]. With dynamic oxidation, after a certain pressure is reached, oxygen is pumped out at the same rate as fresh oxygen is added to the system. This results in a continuous flow of oxygen and keeps adding fresh oxygen to the forming AlO_x layer.

We place the cassette (face down) in the Plassys, which is pumped to a pressure of 3e-7 mbar before the sample is transferred from the load lock to the main chamber. Before we evaporate the Al layers we try to reduce the contamination in the vacuum of the main chamber. First, a crucible filled with titanium (Ti) is heated to evaporate a thin (20 nm) layer in the chamber. During this step, since Ti is unwanted for our device, the sample is shielded. Here, the Ti is used as a "getter material" a reactive material which removes unwanted contamination from the vacuum. Ti either reacts with or adsorbs the contamination which removes it from the chamber. Inside the chamber a piezoelectric material (e.g. quartz) is placed to monitor the rate and amount of material deposited. This piezoelectric is electrically driven and starts

[5] $Al/AlO_x/Al$ formed during dynamic oxidation in the presence of UV light show a smoother interface with less grain boundaries [135]

oscillating. When a material is deposited on the piezoelectric it will induce a frequency shift, which is used to determine the deposition rate [139].

After the preparation of the main chamber, we start performing a double-angle shadow evaporation technique with an intermediate in-situ oxidation to create Manhattan-style junctions [109] . One main advantage of the Manhattan junction, over Dolan junctions [110, 111], is that it is less sensitive to resist height variations. The first layer of Al is deposited under an 35° angle (ϕ in Fig. 3.15) to form a 35 nm layer for the bottom electrode at angle $\theta_1 = 0°$ in Fig. 3.14. To form an aluminum oxide (AlO_x) layer on top of the bottom electrode, the chamber is filled with O_2 until it reaches a pressure of 1.3 mbar, which is maintained for 11 minutes. To evaporate the second 75 nm thick Aluminum layer, the substrate is rotated into position $\theta_2 = 90°$ of Fig. 3.14 while still tilting the cassette to $\phi = 35°$ (see Fig. 3.15). To terminally cap the junctions the 11 minute oxidation step is repeated once more.

With this technique one should always take deposition directions, deposition thickness t, rotation axis $\theta_{1,2}$, angle ϕ, feature width w and resist stack height h into account. Both on their own and in combination to each other. Some examples to show unwanted effects:

- Placement on Plassys cassette is important. The more the device is in the center the better. Evaporation angles differ once you go further to the cassette's edges!
- Incorrect thickness of second layer results in improper contact between top and bottom electrode. In our case, the bottom electrode creates a shadow during the second deposition causing the aluminum to not connect. This happens when the second layer is thinner than the first layer.
- During the deposition of the Al the tilt and rotation, depending on w and h, for each deposition step is important. Tilt too shallow or too large will result in open or, respectively, shorted circuits Setting an incorrect rotation could result in unwanted overlap between electrode layers or small of a junction areas, see Fig. 3.16.a. Note that these defects could also arise due to misalignment of the cassette with respect to the sample.
- Evaporation direction influences the junction electrodes to bulk circuitry connection. When evaporating towards the edges of the bulk circuitry, in our case capacitor pads, Aluminium step coverage is most optimal. This ensures that there is enough surface for the electrodes to connect to the rest of the circuit. However, evaporating away from or parallel to the edge of the bulk circuitry results in no connection (due to shadowing) or, respectively, inadequate step coverage. Some solution to these problems are:
  - Have pads sticking out of the bulk circuitry and connect the junction electrodes perpendicular to these pads. See panel b of Fig. 3.16. [6]
  - Create keyholes like cutouts in the bulk, see panel c of Fig. 3.16. This ensures that one always evaporates towards the bulk circuit for both electrodes.

[6] In hindsight, this might be the best solution for having Al/AlO_x since this allows one to have little chance to create spurious capacitance or inductance at the junctions (see Sec. 2.1.2) and reduces the amount of AlO_x and thus the amount of TLSs the qubit could couple to. Although not used in the devices throughout this thesis, it is recommended for next generations of (HBAR)-qubit devices.

– When bulk circuitry pads are parallel (capacitor) and have no pads sticking out, the second layer needs to be evaporated parallel to the edges. When the first evaporation layer (green false color in Fig. 3.16.d) is evaporated away from the edge it creates a gap between bottom electrode and capacitor pad due to the shadow of this edge (blue inset, Fig. 3.16.d). When evaporating the second layer (yellow false color in Fig. 3.16.d) parallel to the same edge and it is large enough the top electrode has a better connection to the bulk circuitry. To improve the connection, the second layer should be close to the thickness of your bulk circuit (our device 75 of 100 nm).

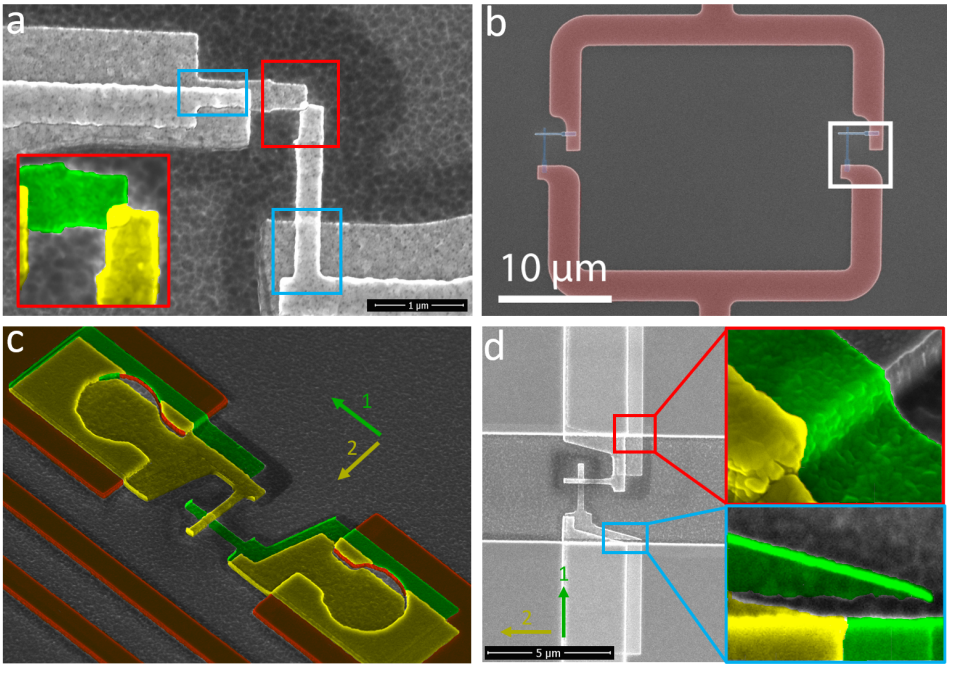

Figure 3.16: Scanning electron micrographs of Manhattan Josephson Junctions. a) Example of junction misaligned at evaporator. Misalignment causes smaller junction area (red outline). Bottom left inset shows false color image of junction (green bottom and yellow top layer). Image also shows unintended overlap of larger electrode pad and junction arms (blue outline). b) Junction perpendicularly connected to cutouts of bulk circuitry (red: NbTiN, blue: Al), image adapted from [138]. c) Junction with keyhole like cutout in the bulk circuitry (NbTiN, colored red) to which the Aluminum electrodes (green bottom layer, yellow top layer) always have a proper step coverage independent of evaporation direction. Arrows indicate evaporation direction to corresponding colored layer. d) Parallel capacitor pads shorted by a single junction with false colored zoom ins. Red zoom in shows good step coverage of bottom electrode (green) to top capacitor pad. Blue zoom in shows shadow effect by bottom capacitor for the bottom layer, while having a "decent" connection of the top layer (yellow). Arrows indicate evaporation direction for corresponding colors. Photos from a, c and d taken by R.C. Dekker

Step 6: Lift-off and probe test

After the Aluminum deposition, the qubit chip is immersed in n-methyl-2-pyrrolidinone (NMP) solution set to 88° C for an overnight lift-off. Next, a pipette is used to circulate NMP in the beaker to remove most of the crumbling Aluminum followed by a 2 minute ultrasonic bath. The chip is then cleaned by immersing it in an IPA solution for a 2 minute ultrasonic clean followed by a careful N_2 gun blow dry. After performing lift-off the qubit chip is done, see bottom-left panel of Fig. 3.17 for a light microscope image of one of the finished qubits. The chip is now ready for testing. As described in Sec. 3.1.1, we the junctions width is 190 nm, see top-left panel of Fig. 3.17 for SEM image of a finished junction. To check the junction resistance during this round of fabrication, we perform a two-probe conductance measurement (as described in Sec. 3.1.1) onto on-chip test junctions (right panel of Fig. 3.17). Performing such a probe test on actual qubit junctions might result in accidentally destroying the junctions with the probe needles or shorting of the junctions due to incorrect settings.

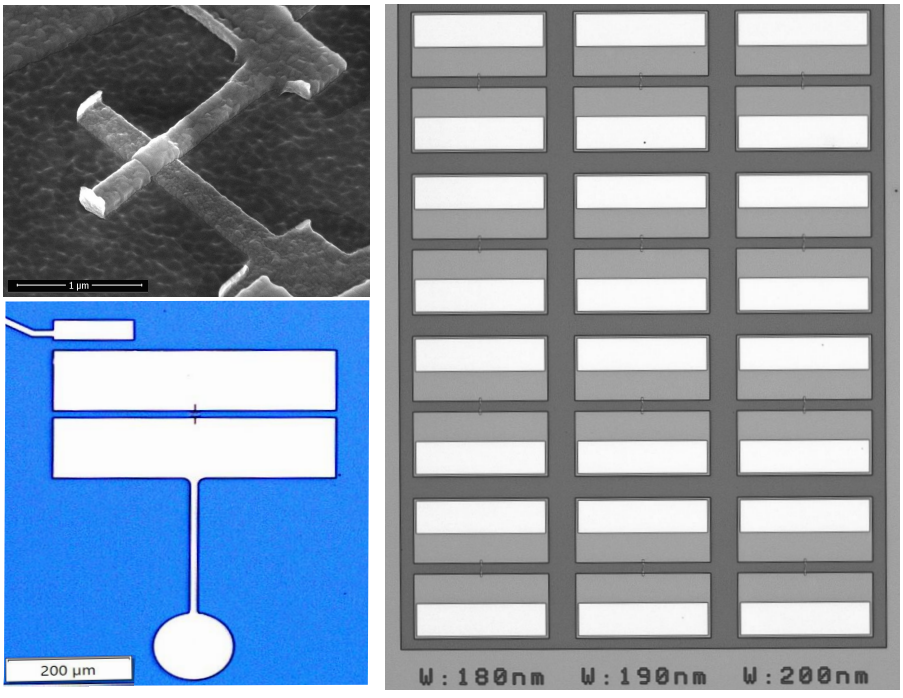

Figure 3.17: Photos of finished Junction and test area. Top-left: SEM of a finished junction. Bottom-left: False colored zoom in photo, using a light microscope, of finished Transmon qubit (Blue: exposed Si, white: NbTiN). Right: False colored light microscope image of junction test area used for room temperature two-probe conductance measurements. The test area consist of four identical junctions shorting two 150x400 μm NbTiN (light grey) with Al (white) probe pads for 180, 190 and 200 nm wide junctions.

Once the test junctions were within spec, which is $\sim$ 6.5-7.0 kΩ for our 190 nm Josephson junctions, the fabrication on the qubit sided chip is concluded and we can continue with the fabrication of the HBAR sided chip.

3.2.2. Fabrication HBAR chip

In this section, we describe the full HBAR sided chip. In short, as shown in Fig. 3.18, the chip is fabricated in one laser writer step, for which the design only consists of 250 μm diameter circles and alignment markers (crosses). Commercially bought $\sim$ 1 μm Aluminum Nitride (AlN) on $\sim$ 650 μm Sapphire wafer (4" from *Kyma technologies*) is covered with $\sim$ 4.5 μm thick negative photo resist. After laser writing and development, the photo resist layer is used as a mask for a Chlorine etch of the exposed AlN. After the etch we are left with $\sim$ 900 nm AlN cylinders used as a basis for our HBAR. The fabrication described in this section is performed at the *Delft Kavli NanoLab* [118] starting from step 1.

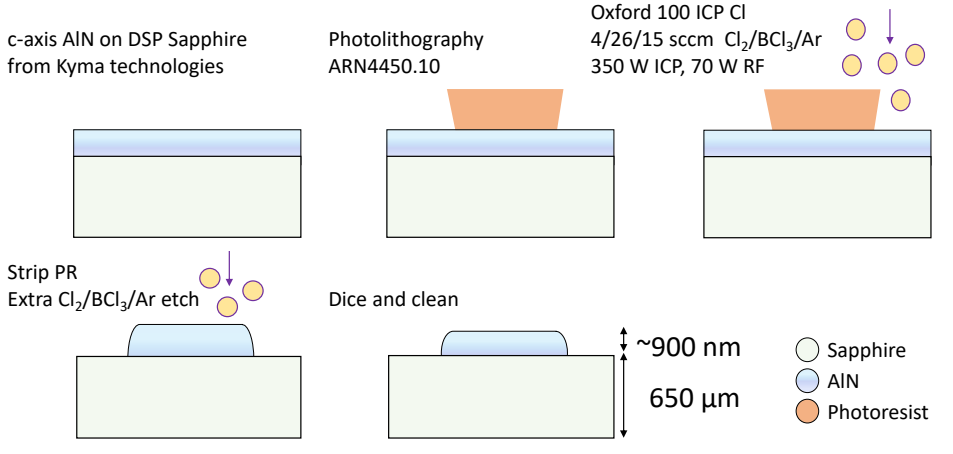

Figure 3.18: Fabrication HBAR chip. Drawings show a step-by-step process for fabricating our HBAR chip. Not to scale.

Step 0: Growth of AlN on Sapphire by Kyma technologies

For the HBAR chip, we begin with double-side polished (DSP) 4" sapphire wafers with a thickness of 650 μm. On one side of the sapphire wafer, a 1 μm thick film of c-axis oriented AlN (Kyma technologies, Part number: AT.U.100.1000.B), which we commercially bought from *Kyma technologies*. Kyma is a leading supplier of crystalline AlN and gallium nitride (GaN) buffer templates. Typically these templates and materials are used for a broad range of high performance nitride semiconductor device applications. For example these buffer templates are used in blue LEDs in electronic devices, bulk GaN growth, and for (in our case) research purposes. The advantage of buying these wafers instead of developing a recipe on our own, is that we now can start etching from a wafer with a reliable AlN crystalline structure (overall growth) with an assured defect percentage.

Kyma technologies epitaxially grows the c-plane AlN templates on top of the sapphire substrates by pulsed DC magnetron sputtering, using their patented and proprietary III-N Physical Vapour Deposition of NanoColumns (PVDNC) technology [140–142]. With "normal" Physical Vapour Deposition (PVD), see PVD sputtering in Fig. 3.19 (a), being a process in which solid matter is vaporized and transported through vacuum/low-pressure chamber as vapour. In

Sec. 3.2.1 we explained one form of PVD already, namely evaporation. Another form is sputtering [143] wherein typically a plasma is struck using the heavy inert gas Argon (e.g. Ar $\longrightarrow$ Ar^+). The plasma is between two parallel plates which are connected to a DC power source. The Ar^+ ions are accelerated towards a metal target (at the cathode) and physically knock off neutral components of the target material. These sputtered atoms travel through the vacuum chamber and are condensed on a substrate (at the anode).

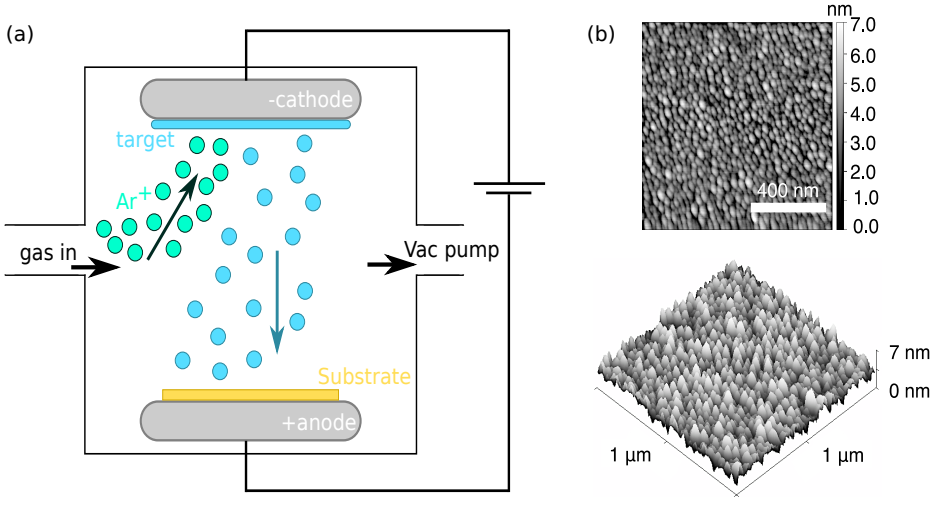

Figure 3.19: Sputtering PVD and PVDNC of AlN on sapphire. (a) Schematic of sputtering PVD system, wherein Ar^+ is accelerated two a (metal) target positioned at the cathode. The ions physically knock off atoms from the target which will travel through the vacuum chamber and condense on the substrate at the anode. **(b)** Atomic Force Microscopy (AFM) images of the commercially available c-plane AlN film (200 ± 10nm) on sapphire (430 μm) wafers from Kyma Technologies. AFM shows the surface of the film layer made of nanocolumns of AlN. These nanocolumns allow the epi-grower to employ a wider range of growth temperature and precursor supersaturation for subsequent epilayers. The RMS of these surfaces is around 1 nm. [141]

However, with Kyma's PVDNC technology they can grow AlN templates consisting of a thin layer of nanocolumnar crystalline AlN (AFM in Fig. 3.19 (b)) on a sapphire or silicon substrate. PVDNC produces an AlN thin film that is crystalline with the [0001] direction parallel to the growth direction (with options for different directionality). These nanocolumns allow the epi-grower to employ a wider range of growth temperature and precursor supersaturation for subsequent epilayers. This PVDNC technology has excellent scalability and nucleation repeatability. Once the epilayer resembles more or less the metalorganic chemical vapour deposition (MOCVD) [144] where two gasses, a metal organic precursor(e.g. TMGa) and and oxidizer (e.g. H_2O), enter a growth chamber much like the one from Fig. 3.19 (a). The growth chamber is typically set at moderate pressures (10–100 Torr) resulting in epitaxial growth over a high temperature substrate. Compared to MOCVD PVDNC has several advantages like: eliminating the sapphire pre-treatment and nucleation layer growth steps, better repeatability compared to 2-step GaN on sapphire, and PVDNC growth temperature closer to MOCVD growth temperatures than other PVD processes.

Step 1: Dice and preparation

Once the DSP AlN on sapphire wafers are ordered and received in a wafer box, Fig. 3.20 (a), we already see a minor inconvenience working with these materials: they are both transparent. As Fig. 3.20 (b,c) show it hard to tell which side is the top side with AlN. Luckily the wafer box has writing on it where the deposition face is facing towards. However, to prevent future headaches, we need to keep track of the top side during fabrication.

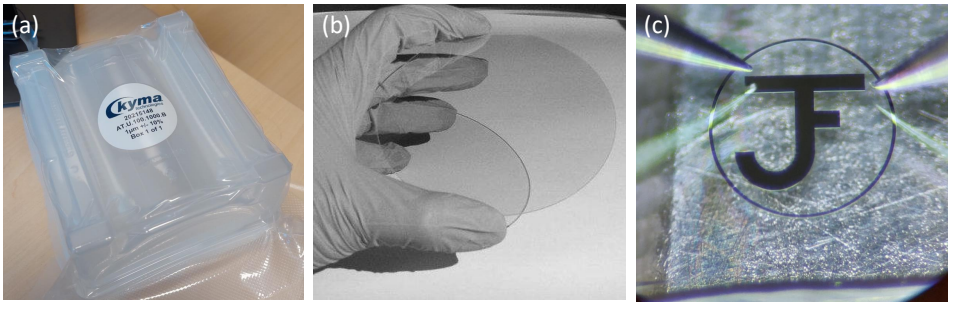

Figure 3.20: AlN on Sapphire Kyma technology wafers. (a) Photo of received AlN 1 μm on 650 μm sapphire. Box (not shown) indicates at the front the deposition face of the wafer. **(b)** Photo showing the transparency of a single AlN on sapphire wafer [145]. **(c)** Zoom in picture of an Al structure on a 10×10 mm^2 AlN on sapphire chip.

We take out the wafer and immediately spin dicer resist (S1805 [119]) on top of the AlN side of the wafer. This is to both protect it during dicing and to visually keep track of the wafer's top side. Following the same steps as described in Sec. 3.2.1 we once again dice the wafer into 10×10 mm^2 chip for further processing. Only now we use a different dicer blade: the VT07 [146]. For hard and brittle materials (e.g. sapphire), soft bond dicing blades, such as resin bond, are usually recommended, whereas a harder bond material, such as electroplated nickel bond, will be preferred for softer materials. Since sapphire is a brittle material, we reduce the feed speed of our spindle and, instead of going all the way through the wafer, we make cuts in steps of 150 μm in depth. This all is done to ensure a smooth cut at the edges with the least amount of cracks and splinters.

Step 2: Patterning and laser writing

After dicing we strip the dicing resist of the chip before spinning new photoresist. One needs to be careful at this point to keep track of the wafer's top side (AlN side). Therefore, before we strip the resist, we take pictures of all corners of the chip. Luckily the tiny cracks and breaks at each corner are not the same and makes it easy to track the top side. For stripping, similar to Sec. 3.2.1, we place the sample in a beaker with PhotoResist Stripper PRS3000 and perform an ultrasonic clean for 5 minutes at the highest power. Afterwards, we transfer the sample into an IPA solution, perform 5 minute ultrasonic clean, and dry the chip with a high pressure N_2 gun. We remove residual particles by placing the chip for 5 minutes in the PVA Tepla 300 for O_2 descum (200 sccm, 600 W). Before spinning the new resist we put the chip on a 150°C hotplate to evaporate water vapour from the surface and *in situ* deposit the adhesion promotor hexamethyldisilazane (HMDS) by using a vapor treatment in a nitrogen atmosphere.

Afterwards, the sample is immediately transferred to a spin coater. We apply the negative photoresist AR-N4450.10 [147] using a 6000 rpm spin setting and bake the chip pre-exposure for 8 minutes on a 90°C hotplate.

We then place the chip in the maskless μMLA laserwriter from *Heidelberg Instruments*, see Fig. 3.21 (a) . The laserwriter is equipped with a 1 μm laser beam which exposes the resist by scanning across it with a 365 nm LED source and is able to expose minimum feature sizes of 0.6, 1, and 3 μm [148, 149]. The advantage of this system, as the name already implies, is that it does not need a mask for the UV lithography exposure due to the use of a Spatial Light Modulator (SLM), mirror and focusing lens. As Fig. 3.21 (b) shows the laser light is can be focused in Z-direction while a chip moves on an XY-stage. For large structures, such as our 250 μm diameter disks, the total writing time is done under 5 minutes.

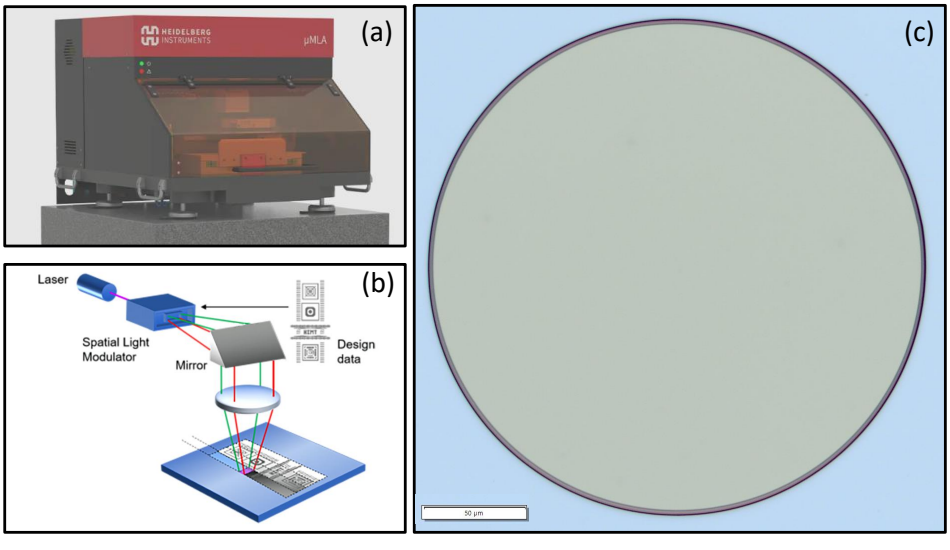

Figure 3.21: Heidelberg's μMLA Laserwriter and HBAR structure. (a) Photo of the maskless μMLA laserwriter from *Heidelberg Instruments*. **(b)** Schematic where a 365 nm LED laser source goes through a Spatial Light Modulator (SLM), is reflected of a mirror and focus on a chip placed on a XY-stage [149]. **(c)** False colored light microscope picture of developed AR-N4450.10 photoresist on AlN/sapphire substrate.

For our exposure we use a dose of 220 mJ/cm^2 and defocusing of -4. After exposure another 10 minute bake (post-exposure bake) on a 100°C hotplate is required to complete the cross-linking process for negative photoresist. We develop the photoresist by placing it for 140 seconds in a beaker of MF321, rinse it for 15 seconds with a watergun, followed by a 30 second swirl in a D.I. H_2O beaker before blow drying it with a high pressure N_2 gun. We end up with circular regions of $\sim 4.2 - 4.5$ μm thick AR-N4450.10 as shown in Fig. 3.21 (c). This relatively thick photoresist layer serves as a mask in the following etching step described in the next section.

Step 3: Etching

For etching we use the *Oxford Plasmalab system 100*, which is an Inductively Coupled Plasma (ICP) RIE etcher mainly used for chlorine based etches (i.e. ICP-Cl etcher). The system consists of a top and a bottom chamber, which are connected openly as shown in Fig. 3.22 (a). In the top part a coil is wrapped around a quartz wall chamber to which an RF current, I, is sent through. This alternating current induces a oscillating magnetic field, which in turn generates an oscillating electric field in the top chamber. For sufficient RF power (ICP power), the electric field ignites a plasma which stays in the top chamber since the circular electric field (Fig. 3.22 (b)) has no component in the direction of the sample table. Doing so, ensures that electrons remain within the plasma and more readily ionize gas particles, resulting in high plasma densities. A second RF source is connected to the sample table, which acts as a cathode. Heavy (positive) ions are hardly accelerated but the lighter electrons are accelerated towards the cathode. This effectively creates a DC bias which attracts the positively charged free radicals towards the sample. At the sample, the reactive ions chemically etch the materials of interest. This enables selective etching when carefully selecting precursor gasses.

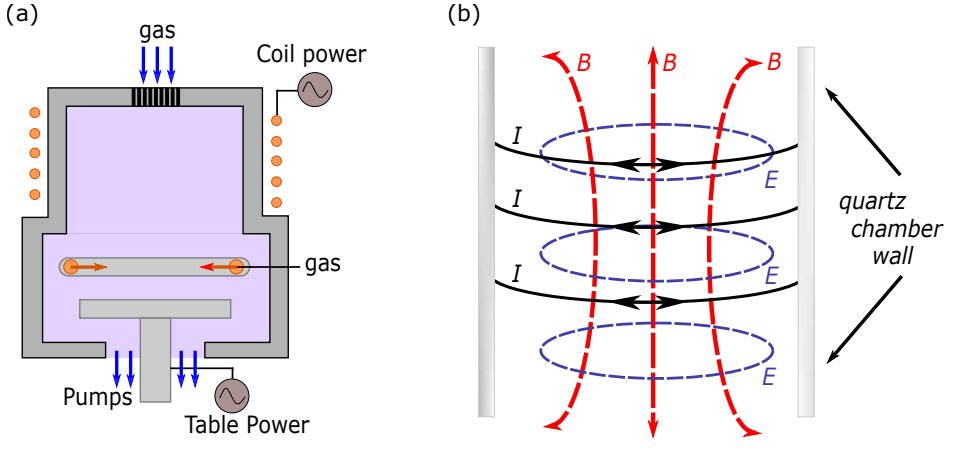

Figure 3.22: Schematic and principle of a ICP RIE system. (a) Illustration of the ICP system, where at the top a coil is wounded around a quartz chamber. The sample table (bottom) is connected to a second RF source. **(b)** Visualization of the electric, E, and magnetic, B, field responsible for creating the plasma, created by an alternating current, I, through the coil.

For etching our AlN into cylinders of 250 μm diameter and a thickness of $\sim$ 900 nm, we introduce the gasses Boron-trichloride (BCl_3), Chlorine (Cl_2) and Argon (Ar) into the chamber [150]. Both Cl_2 plasma and the gas itself readily etch aluminium based materials such as AlN and sapphire (Al_2O_3). BCl_3 is known to remove residual oxygen from a chamber, remove native oxides through sputtering and scavenging oxygen, and etches both Al_2O_3 [150] and AlN [151]. By-products of the reactions with BCl_3 create the deposition of polymers on side walls [152, 153], which helps to increase an anisotropic etch in lateral direction. Adding Ar to the plasma helps to suppress etch rates and, if needed, perform actinometry (technique to determine unknown gas concentrations while having a known noble gas concentration). The gas flows of

$Cl_2/BCl_3/Ar$ are set to 4.0/26.0/10.0 sccm, with a chamber of 8 mTorr. RF and ICP power are set to 70 W and, respectively, 350 W. The sample stage is kept at a temperature of 50°C. From these settings we found etch rates of ~200 nm/min for the AR-N photoresist mask and ~52 nm/min for the AlN / Sapphire layers.

During the development of the etch recipe we found out that the resist mask exponentially etches due to heating of the plasma etch. For this reason, to suppress this and maintain a constant photoresist etch rate of ~200 nm/min we used the following steps:

1. Condition chamber and heat sample table to 50°C
2. Load sample into chamber and pump to vacuum
3. 2 minute O_2 descum + Pump out gasses (1 min.)
4. *Loop 7 x*:
   (a) 3 min. AlN etch ($Cl_2/BCl_3/Ar$)
   (b) Pump out (1 min.)
   (c) Ar through chamber (2 min, 100 sccm)
   (d) Pump out (1 min.)
5. 30s O_2 descum + 1 minute pump out

Both O_2 descums were both set to (50/800 W RF/ICP, 50 sccm, chamber pressure of 50 μbar) and this oxygen plasma to remove any residual particles from the surface. At the start of etching this means the removal of a few nanometers of residual photoresist from spin coating. During etching, teflonization (or hardening after exposure to atmosphere) may occur preventing the use of chemicals like PRS for removing the resist after etching. For this reason, we perform a quick oxygen plasma etch and chamber pump out (remove gasses and aerosol particles) to remove the teflonization layer before exposing the chip to atmosphere. The total etch time of the AlN is about 21 minutes, with which we etch ~100 nm into the sapphire layer. At this point we end with $\sim$ 1 μm of AlN and, at most, 300 μm of AR-N photoresist. Doing so, we ensure ourselves that there is no unwanted AlN anywhere else on the chip.

Step 4: Extra etch and check

At this point, the AlN layer is shaped as desired, but does not have the correct thickness. We still need to remove roughly 100 nm of AlN to get our ~ 900 nm layer. First, we strip the chip from any residual AR-N photoresist by submerging it in a beaker of PRS3000, which is placed in an ultrasonic bath set to the highest level for 2 minutes. Following this strip we clean the chip by a similar ultrasonic bath of 2 minutes in both a beaker of acetone and a beaker of IPA. The chip is then blow dried with a high pressure N_2 gun.

The chip is placed back into the ICP-Cl etch for another 30s O_2 descum, 2 minute $Cl_2/BCl_3/Ar$ etch followed by a final 2 minute oxygen plasma clean as described in the previous section. We end up with finished AlN disks as shown in Fig. 3.23.

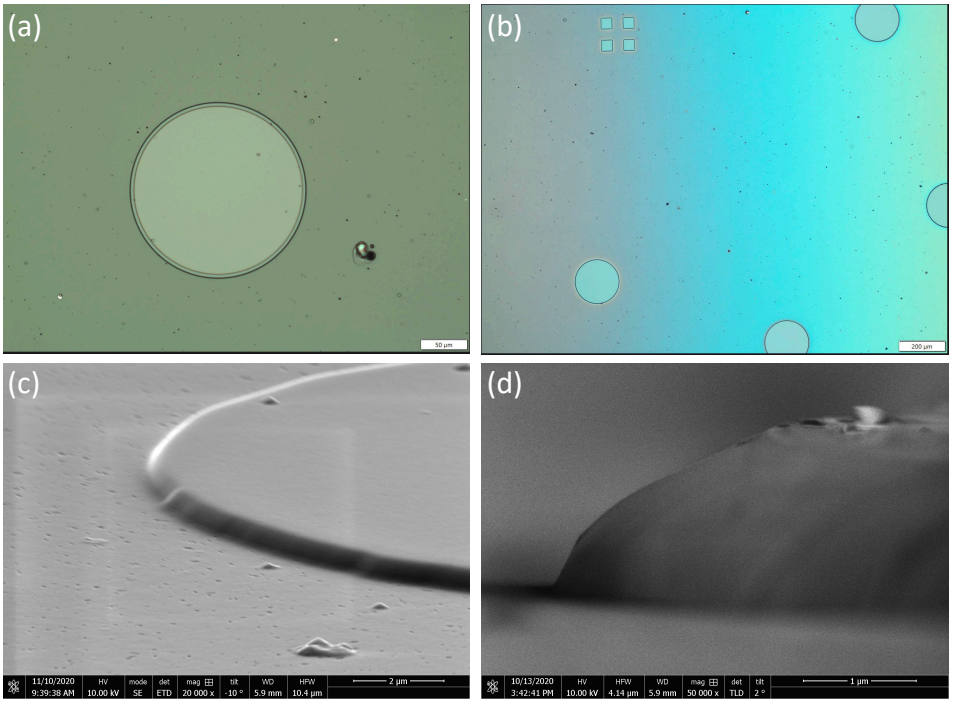

Figure 3.23: Light microscope and SEM images of finished AlN cylinders. (a) Finished ~900 nm thick AlN disk after the second 2 minute $Cl_2/BCl_3/Ar$ etch. Light micrograph shows gradient step in height at the edge of the disk due to the use of AR-N photoresist with undercut. **(b)** Lightmicrograph of several AlN disks and markers in between the 21 and 2 min etch step. Photo, as does (a), show several black spots spread over the surface. These spots attribute to re-deposition of sapphire on to the surface. **(c)** Top view SEM image of the finished AlN disk. **(d)** Side view SEM image of the finished AlN disk.

In Fig. 3.23 (a,b) we can see several black spots which we attribute to redeposition of sapphire since we slightly etch into this. Considering the size of the spots (see Fig. 3.23 (a,c)) this should not interfere with our device and measurements. Although not pursued during this work there are a few options to try and reduce this redeposition. One could time the etch to stop at the exact time it hits the sapphire surface. This is a tedious works since, as all clean room users

know, fabrication conditions slightly change over time due to maintenance of equipment and use of machinary for other processes. Another possibility is that the spots are boron related. Therefore, one could tweak the flow rates of both Cl_2 and BCl_3 to optimize the etch rate(s) and deposition of these spots.

Step 5: Clean and extra dice

For our final step in the HBAR chip fabrication we dice our 10×10 mm^2 sapphire chip into 1.5×8 mm^2 pieces. Each piece contains five AlN disks which we will align over the qubit's antenna (design shown in Sec. 3.1.3 and 3.1.2). As described in Step 1 of the HBAR chip fabrication in this section, we use same dicer settings and dicer photoresist S1805. After dicing we perform a final clean on the smaller HBAR chips. The chips were removed one-by-one from the dicer foil in submerged in acetone for a 3 minute ultrasonic bath set to the highest setting. Afterwards we do a similar 2 minute ultrasonic clean in IPA, swirl the chips in a fresh IPA beaker and end the clean with a N_2 gun blow dry. Doing so we end up with five usable HBAR chips from fabricating one 10×10 mm^2 AlN on sapphire chip, which is beneficial for both testing, swapping devices, and using for multiple full HBAR-transmon devices. Photos of the finished HBAR chips can be found in Fig. 3.24.

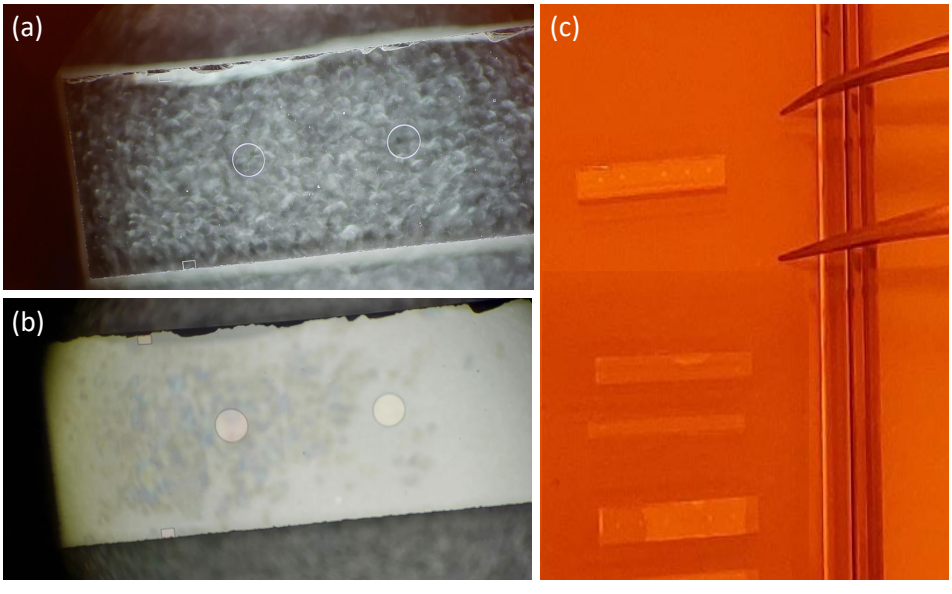

Figure 3.24: Finished HBAR chip diced in 1.5×8 **mm^2 pieces. (a)** Dark field light microscope photo of diced HBAR chip. **(b)** Bright field light microscope photo of same diced HBAR chip. **(c)** Photo of different diced HBAR chips with tips of tweezers on the right as reference.

3.2.3. Flip-chip assembly

Now that the fabrication of both the qubit and HBAR chip is done we start assembling them in flip-chip geometry. For this, as shown in Fig. 3.25, we begin by placing the qubit chip on a XY-stage which holds it in place using a light vacuum. We pick up the HBAR chip and flip it, with the AlN disks pointing downwards, onto the qubit chip. The chip is roughly placed and aligned by using sharp tipped tweezers. Using probe needles attached to micromanipulators (*Karl Suss MicroTec PH150 Precision Micromanipulator*[7]) we align the HBAR disks with the transmon antennas in XY-direction using chip markers. Once aligned, the probe needles are moved on top of the HBAR chip. The probe needles are now used to both push the chip down and hold it into place while a tapered fiber is used to apply two-component epoxy (Loctite EA 3430) on the sides of the top chip. We let the epoxy cure for several hours.

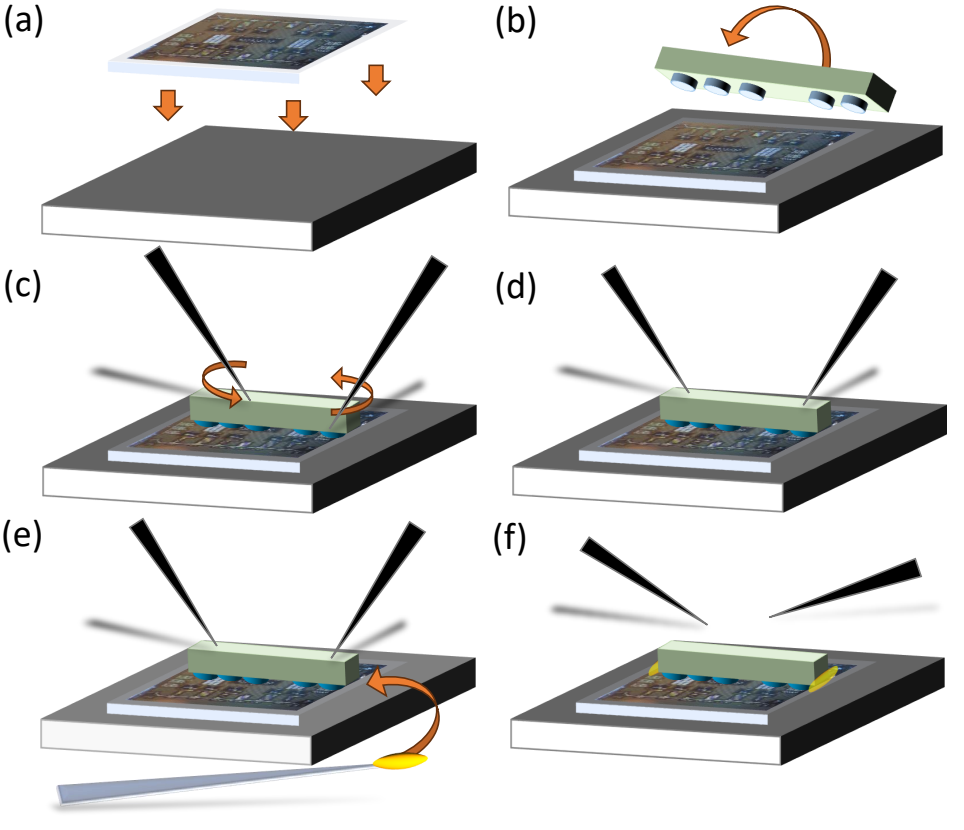

Figure 3.25: Flip-chip assembly of full HBAR-transmon device. **(a)** Placing bottom (qubit) chip onto a vacuum chuck. **(b)** Flipping HBAR chip onto qubit chip with sharp tipped tweezers. **(c)** Probe needles on micromanipulators help to align the HBAR chip. **(d)** Push chip down with needles to keep in place. **(e)** Apply epoxy with tapered optical fiber. **(f)** After curing finished needles removed from chip.

[7] Manipulator has an screw accuracy of 250/500 μm / rev and feature resolution of 3 μm

To suppress the amount of glue creeping under the chip we try to use a minimum amount on the fiber tip. The tapered tip actually helps to not form a too large ball of glue. Putting pressure on the chip before applying the glue helps. If we would first apply glue, flip the chip, and apply pressure then the glue tends to creep further underneath the chip. On the other hand, applying pressure reduces the vacuum gap, for which we see the make a rough estimation by observing interference fringes and the colour patterns. From White-Light Michelson Interferometer setups [154], for example, and other work [155] we know that for a smaller vacuum gap between our chips the contrast of interference pattern decreases, see Fig. 3.26.

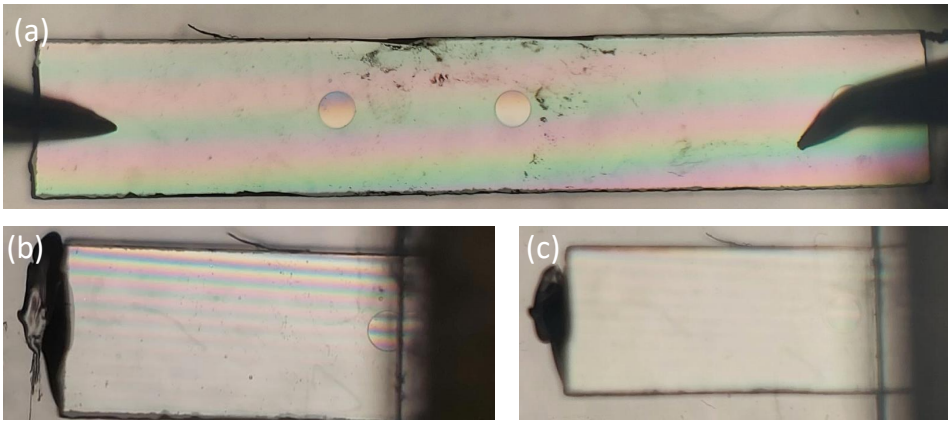

Figure 3.26: Light microscope pictures of white light interference pattern. Applying arbitrarily more pressure (going from (a) to (c)) contrast of interference pattern decreases.

After the epoxy has dried we move the assembled flip-chip to a Printed Circuit Board (PCB). We glue the chip in the PCB's recess with the use of GE varnish (GE-7031). This varnish, a commonly used low-temperature adhesive and electrical insulator owing to its high thermal conductivity and mechanical strength at low temperatures, is traditionally used to thermally anchor wires at cryogenic temperatures. When cured the chip is wirebonded to the PCB using a *Westbond 4000 "E" system* from West•Bond Inc. with AlSi alloy (99 %-1 %) bond wires. For good electrical contact and thermalization, we use three bonds per launch pad, and as many bonds as possible on the ground planes. To connect our PCB to the outside world for electrical measurements we solder straight plug semi-detent SMP connectors [8] onto our PCB. The finished device (see Fig. 3.27) is mounted in a copper box and loaded into our setup (see Sec. 3.3).

[8] 19S102-40ML5 straight plug PCB, from Rosenberger Hochfrequenztechnik GmbH & Co. KG

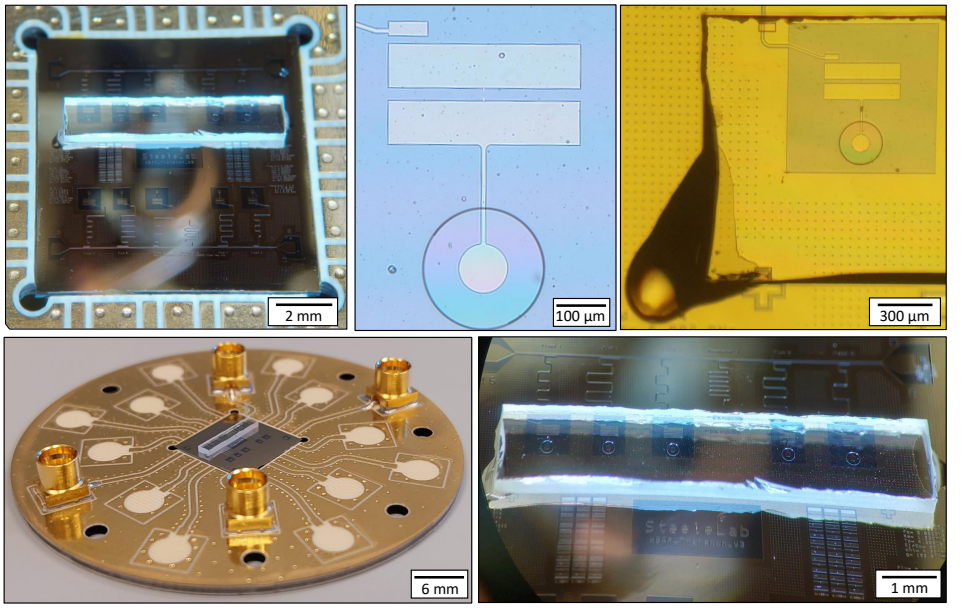

Figure 3.27: Photo collection of finished HBAR-transmon device. Several photos taken under a light microscope showing full chip (top-left), zoom in of HBAR + transmon (top-middle), epoxy glue creep between chips (top-right), and HBAR chip glued in place closeup (bottom-right). Bottom-left also shows a wide angle picture of HBAR-transmon chip in PCB.

3.3. SETUP AND MEASUREMENT METHODS

In these final sections, we describe our used setups. We will discuss the dilution refrigerator, several Vector Network Analyser (VNA) based measurements, and end with our gated spectroscopy setup serving as time domain measurement.

3.3.1. CRYOFREE DILUTION REFRIGERATOR

The majority of measurements in this work were performed in the cryofree dilution refrigerator *Oxford Instruments Triton 200*. All measurements on the completed HBAR-transmon device were performed inside this fridge, whose base temperature is $\sim 10 - 20$ mK. In Fig. 3.28, we show the total system schematic needed to cool down to base temperature.

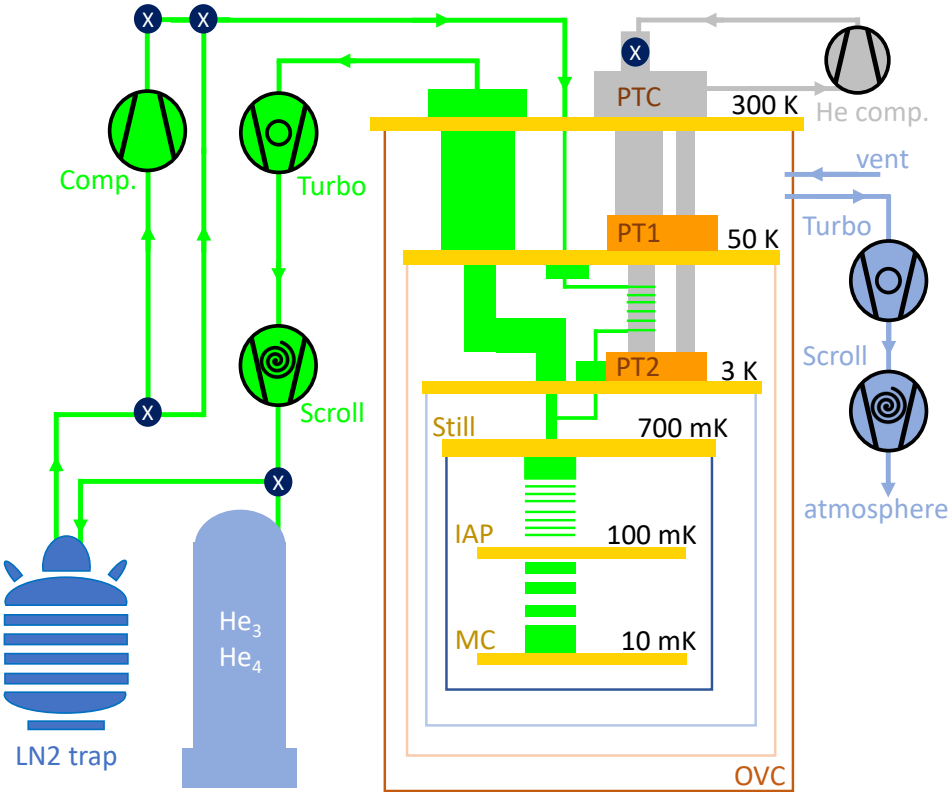

Figure 3.28: Overview of entire cryofree dilution refrigerator setup. The main unit consists of six stages with temperatures (top to bottom) of 300K, 50K, 3K, 700mK, 100mK and $\sim$ 10mK with shielding (red to blue squares). On the mixing chamber (MC) plate, we mount our devices. For system control, we have three process lines. To pump the OVC to vacuum, the light blue line is used and consists of a scroll and turbo pump and a vent line. To cool the 50 and 3 K stages a pulse tube cooler is used, which consists of a pulse tube unit (in fridge PT1 & PT2) and He compressor. To cool the system to the base temperature, we use the green process. This consists of a turbo and scroll to pump around the He_3/He_4 mix through the dilution unit inside the fridge. This line also has a He_3/He_4 tank for storage, LN2 dewar with a trap for filtering, and a compressor to condense the mix during cooldown.

As Fig. 3.28, there are three main processes needed to cooldown the dilution refrigerator. The light blue lines for pumping the system to vacuum, the grey lines to cool the two stages to 50 and 3 K with the use of a pulse tube, and the green lines to cool the last stages to 700, 100 and 10 mK with the use of a dilution unit which is pre-cooled with the PT1 and PT2 head of the puls tube.

The vacuum inside the fridge is created by using a turbo and a scroll attached to the back (a backing pump). The scroll pump, a spiral compressor, first creates a vacuum of about 10^{-3} mbar and serves as a backing pump for the turbo molecular pump. Due to fast rotating fine fin propellers, the turbo pump "literally" pushes air molecules out of the system by using drag force to change the momentum of the molecules. The vacuum is needed to remove heat transfer between the Outer Vacuum Chamber (OVC), which is at room temperature, and the cold stages.

The pulse tube cools, as shown in Fig. 3.29, by achieving a pressure difference between two ends inside a tube or, as $PV = nRT$, a temperature difference inside the tube. The cold side of the tube is connected to a regenerator, which typically contains a net-shaped porous substance with a large heat capacity. The regenerator acts as a reservoir of heat. The cold side of the pulse tube enters a heat exchanger, which cools the system of interest before re-entering the pulse tube as a hot gas. The hot gas is compressed by the cold gas from the regenerator and is pushed out through a water cooler before going back to the He compressor and starting the cycle over. The process described here is for a single-stage pulse tube. When attaching a second regenerator (and heat exchanger) in series to the first regenerator described, we end up with our two-stage pulse tube.

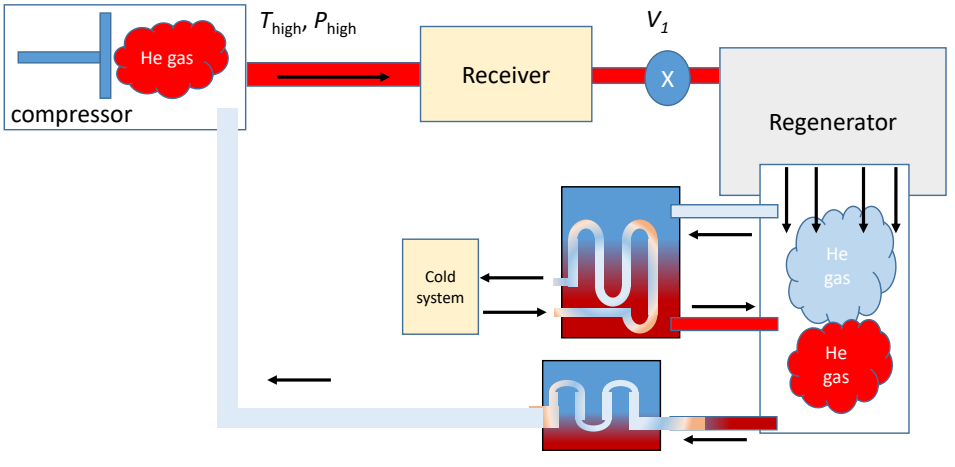

Figure 3.29: Overview of single-stage pulse tube cooling process. Compressor pressurizes He gas, heat-carrying medium in the procedure, which increases its temperature. High temperature and high pressure He enters a receiver which collects the gas to an optimal volume till valve (V_1) opens to supply gas to the pulse tube itself. Gas enters the regenerator, from where the gas expands and cools down inside the tube. The cool gas goes through a heat exchanger, which effectively cools down the system of interest. Warm gas exits the exchanger and enters the pulse tube. Cool gas compresses the hot gas inside the tube and the hot goes through a second heat exchanger to cool it down before re-entering the compressor.

The dilution unit uses a mixture of He isotopes, He_3 and He_4 at a concentration of 6.6 percent of He_3, which is a standard technique to cool to $\sim 10 - 20$ mK, see Fig. 3.30 (b) for a phase diagram of the mixture. The mixture starts as a gas in a "dump" tank and will be condensed into liquid. Condensing requires sufficiently high pressures and sufficiently low temperatures. For this reason, the mixture is compressed using a compressor (top-left green line Fig. 3.28) before passing through heat exchangers located on the pulse tube (between PT1 & PT2) in order to cool the gas to ~ 4 K. By using a Joule-Thompson stage [9], consisting of an efficient heat exchanger located inside the still pumping line (between 3 K & 700 mK stage) and an impedance [10], the mixture is condensed. A heat exchanger inside the still (700 mK stage) cools the returning He_3 liquid before it reaches the continuous heat exchanger, which is located between the still (700 mK) and Intermediate anchoring plate (IAP, 100 mK), and cools the He_3 below 100 mK. Once the mixture is cooled below 870 mK, the liquid separates into two different liquid phases: He_4 rich and He_3 rich. In the mixing chamber (MC), the dilution cooling occurs due to the enthalpy difference between the concentrated (incoming) and the diluted (outgoing) liquid. The lower density He_3 liquid stacks on top of the diluted liquid, which is predominantly He_4 with a 6.6 % fraction of He_3. At a certain temperature, the He_3 of the diluted liquid selectively evaporates (as gas) and dissolves in the He_3 rich top liquid floating on top. Here, cooling is achieved by the entropy difference between the two phases. Fig. 3.30 (a) shows a schematic overview of the dilution unit with and example photo from Blue Fors [156].

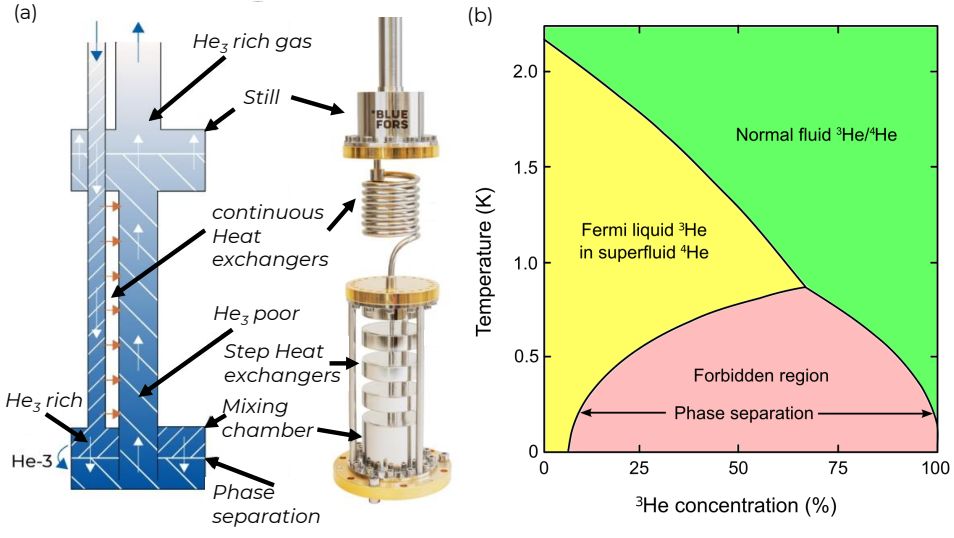

Figure 3.30: Overview of dilution unit and He_3/He_4 phase diagram (a) Schematic overview of dilution unit containing a still, mixing chamber, continuous, and step heat exchangers. The schematic shows an overview of He_3 flow through the system while the photo from Blue Fors [156] shows real-world components to link the schematic to. **(b)** Phase diagram of He_3/He_4 mixture showing that above 870 mK the two phases in the same phase, below 870 mK, there are two distinct phases with lighter He_3 and denser He_4. At 600 mK vapour pressure of He_3 is larger than He_4; thus, He_3 will evaporate preferentially [157].

[9] In traditional dilution refrigerators, helium gas is condensed by a separate pumped liquid He_4 stage, the 1 K pot
[10] gas undergoes isenthalpic expansion.

The diluted He_3 flows from the MC to the still, where it is evaporated and circulated through the system by a turbo and scroll pump back to the condensing line at the top. While going through the system, the mixture passes through an external cold trap (LN2 trap in Fig. 3.28). The trap contains activated charcoal and is immersed in liquid nitrogen (LN2) filled vacuum dewar. In the cold trap, contaminants in the mixture (water vapour, nitrogen, hydrocarbons, metal outgassing, pump oil and 'O'-ring lubricants) will either freeze on the cold surfaces or are adsorbed by the charcoal. Even in completely leak-tight systems, the mixture will always contain small amounts of contaminants which need to be filtered out to avoid blockages.

3.3.2. Wiring and measurement setups

Having described how the dilution refrigerator cools our sample, we now explain how they are electrically measured. Starting with the internal wiring setup as shown in Fig. 3.31. Since we measure in transmission, we have an RF in- and output line. The material for the RF cables should have high electric conductivity, low thermal conductivity, and reasonably small microwave signal loss. For the lower stages, from 10 mK to 3 K, we use a superconducting wire niobium-titanium (NbTi) for both in- and output lines. Superconductors must have $\Delta E \sim 1.76\, k_B T_c$ to break Cooper pairs and for the electrons to carry thermal energy. Below T_c, electrical current can be carried by paired electrons (resistanceless) while only the unpaired electrons carry heat. NbTi wires with a $T_c \sim 10$ K are used, allowing simultaneous low insertion loss, high electron conductivity, and low thermal conductance. Note that Nb could be used, but the thermal conductivity of NbTi is much lower than that of Nb. The cables between the 300 K and 3 K stage are made of stainless steel (SS). The SS wires loss is neglected for the input line and will not contribute much to the Signal-to-noise ratio (SNR) at the output line due to the large gain of the high electron mobility transistor (HEMT) amplifier, which is 40 dB.

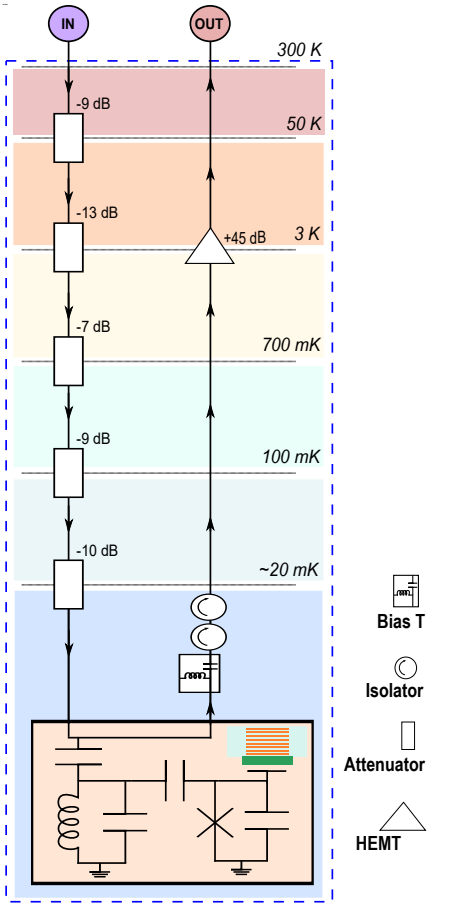

Figure 3.31: Schematic wiring diagram in Triton dilution refrigerator. Input line (left) has 48 dB attenuation, the bottom shows the circuit diagram HBAR-transmon device and an output line (right) with a HEMT amplifier (+45 dB).

A downside of having low/inefficient cooling power at low temperatures [158] (at our sample and a few stages above) is that the input power of our incoming electrical signals needs to be reduced greatly. Otherwise, one might run the risk of heating the system. Even with the device mounted to the 10-20 mK base plate, it still experiences some active heat load due to the wires connected to the room temperature measurement equipment, which could also couple thermal noise to our samples. Therefore, to reduce the input power and suppress this noise, we attach several signal attenuators (-9, -13, -7, -9, and -10 dB), each thermally anchored at each stage (from 50 K to the $\sim$ 20 mK). Assuming constant RF attenuators over the entire frequency range, the total distributed attenuation of 48 dB (excluding intrinsic cable losses) would still not be enough to cool the electronic noise to base temperature. Instead, this thermal noise levels out between 70 and 100 mK at low frequencies. We could keep adding attenuators to the input line to lower the thermal noise as much as possible, but the temperature of our base plate ($\sim$ 20 mK) already places a lower bound to our sample temperature and, therefore, the required lowest noise temperature. Besides, due to low electron-phonon coupling at these temperatures, the electrons most likely have slightly higher temperatures than the base plate. For this reason, 48 dB attenuation should be sufficient for our measurements.

While attenuation is important for the import line, the readout of our electrical signal is also of importance. At This line, we need to amplify the electrical signals coming from our sample. For this, we use a HEMT amplifier, LNF_LNC4_8A, which is operational at and mounted on the 3 K stage and amplifies our signals with a gain of 40 dB. A dc voltage, supplied by twisted pair looms and a 24-pin cinch connector is applied to the HEMT in order to operate the amplifier. At the output line, between the HEMT amplifier and sample, we generally attach additional microwave components such as a bias tee and isolators. The bias tee, viewed as an ideal capacitor and ideal inductor, allows AC signals to go through to the HEMT amplifier but does not allow DC noise to come back from the amplifier into the sample. In addition, RF signals are directed one way (towards the HEMT) due to the use of an isolator, a two-port device which transmits RF signals in one direction only.

3.3.3. MICROWAVE MEASUREMENT EQUIPMENT SETUPS

Now that we have discussed the dilution refrigerator and its inside wiring, we will now explain the external microwave measurement setups. For our measurements, we use multiple spectroscopy setups with a Vector Network Analyser (VNA) playing a central role. A VNA is an instrument that measures the network parameters of electrical networks, such as the most commonly measured scattering parameters or S-parameters, for which we measure reflection and transmission signals. The VNA is built in such a way that it can send out test frequencies and measure the reflection S_{11}, or transmission S_{21} signal coming from a device under test (DUT). For example, with a two-port VNA, port 1 (P1) sends the test frequency and measures S_{11}, while port 2 (P2) is mostly used in our setup to measure S_{21} [11]. Inside the VNA the test frequency is generated by a variable continuous wave (CW) source or signal generator. This generated test frequency can subsequently be adjusted in power by using a variable attenuator. When, for example, sending the test frequency to P1, the signal is split, using a microwave splitter, in two directions. One arm of the splitter (reference channel) feeds the signal to a reference receiver and the other arm (test channel) connects to P1 via a directional coupler

[11] P1 and P2 could also be set to measure transmission S_{12} and, respectively, reflection S_{22} with P2 sending the test frequency.

(through signal). The side coupled port of the directional coupler feeds the reflected signal from P1 to a test receiver. In a similar way, transmitted signals entering via P2 feed the signal to a different (coherent) test receiver. Here, coherent receivers share the same reference oscillator, or Local Oscillator LO, and can measure the test signal's amplitude and phase at the test frequency. All complex receiver output signals are fed into a processor, which mathematically processes the data and displays the chosen parameters in a chosen format on a display.

Single & two tone VNA spectroscopy

For readout resonator and qubit spectroscopy, using a VNA, two setups are important for collecting device parameters, namely single-tone and two-tone spectroscopy. For single tone spectroscopy, as shown in Fig. 3.32 (A), we connect the port 1 and 2 of the VNA to the input and, respectively, output ports of the dilution refrigerator and we sweep both probe frequency, ω_p, and power, P_{probe}. With single-tone spectroscopy, the frequency and line width of the readout resonator are measured for a single probe power. For increasing probe power, see Fig. 3.32 (B), the resonance frequency changes for readout resonators that are dispersively coupled to qubits. For low powers, the readout resonator will start off in the so-called dressed regime in which the dispersive coupling between qubit and resonator is valid. When increasing the power, the resonators enter the critical regime (frequency increases), wherein the dispersive approximation breaks down due to exceeding the resonator's critical photon number. In the final regime, the bare regime, the probe power increased so much that the resonator shifts to its bare frequency, and it becomes uncoupled from the qubit. Here, the strong drive saturates the qubit and decouples it from the resonator, which has to do with exceeding the critical photon number and with increasingly high currents in the qubit. For high currents, the Josephson junction exceeds its critical current, I_c, and becomes Ohmic, so non-superconducting, once more. From this measurement, we can extract the readout resonator's dressed frequency and what probe power, for a given set of attenuation at port 1, we need to dispersively readout our qubit.

Dispersive qubit readout is done by two-tone spectroscopy, as schematically shown in Fig. 3.32 (C). For two-tone spectroscopy, we combine the probe tone from the previous setup with a second tone, with drive frequency ω_d, and send both signals into the dilution refrigerator input port. The combining of the signals is done by using a directional coupler. In this measurement, we continuously sent a probe signal (fixed frequency and power) while sweeping the drive frequency and power, P_{drive}. When the drive frequency corresponds to a qubit transition frequency (for a given power), we excite the qubit and dispersively shift the readout resonators. As the data shows in Fig. 3.32 (D), multiple frequencies are measured in this setup which correspond to a multi-photon transition from the qubit's ground state to higher energy levels. Examples are the qubit transition frequency $\omega_{02}/2$ and $\omega_{03}/3$ where two or, respectively, three photons are used to go from the ground to the second or third excited state. In the shown example data, these transitions are continuously driven, and as the system is subject to dissipative processes, the qubit will reach a steady state. From these measurements, we can extract qubit parameters such as it ω_{01} transition frequency, anharmonicity α, and qubit line width (preliminary).

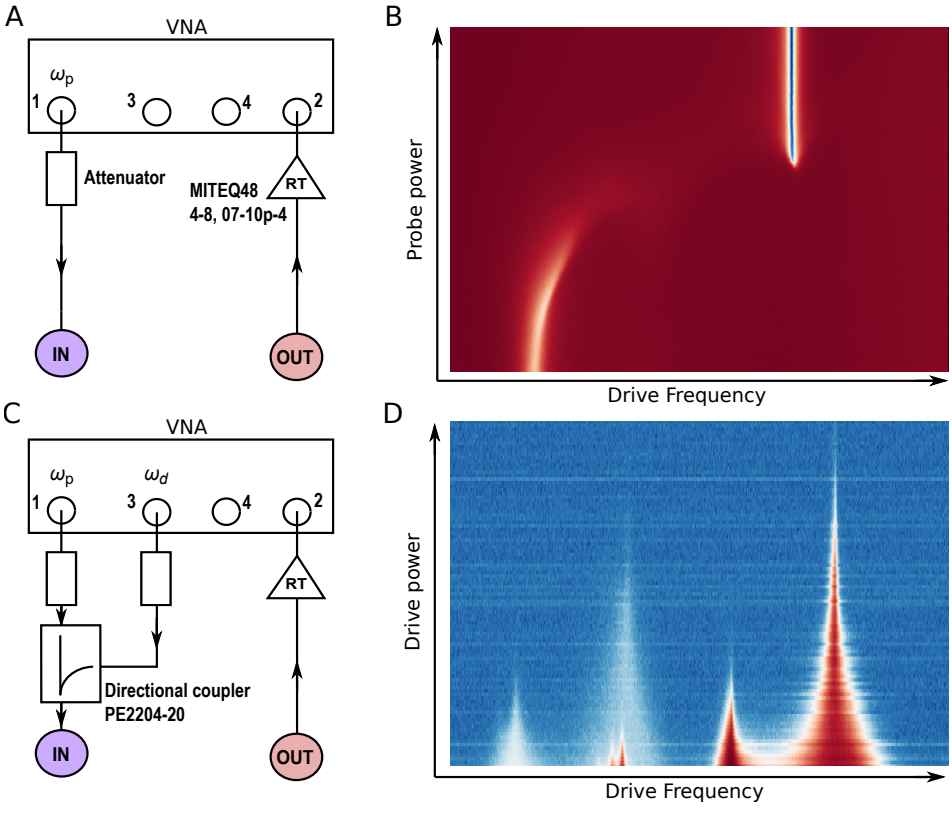

Figure 3.32: Single and Two-tone measurement setup and example data. (A) Single tone setup where probe frequency ω_p is sent from VNA port 1 through attenuators before entering the input port of the dilution refrigerator (as seen in Fig. 3.31). The signal from the device, coming out of the dilution refrigerator, is amplified by a MITEQ room temperature amplifier and measured at port 2 of the VNA. **(B)** Measurement result of a readout resonator where ω_p is sweep for increasing probe power P_{probe}. **(C)** Two-tone spectroscopy setup wherein, in addition to panel (A) a second port (port 3) with attenuators is combined with the signal of port 1 by using a directional coupler. In this measurement the probe signal ω_p is set to a specific readout frequency while a drive signal ω_d is swept in both frequency and power, P_{drive} for which qubit spectroscopy data is shown in **(D)**. In both color plots, red is a high value S_{21}, in dBm, response and blue is low.

Stark shifting with two-tone spectroscopy

For our HBAR-transmon device, the acoustic resonance frequencies are fixed in frequency space, but we are able to shift the qubit's 01-transition frequency by making use of the AC Stark shift [159, 160]. Using this technique we can shift the qubit frequency ω_q according to $\Delta\omega_q = 2\epsilon^2(\frac{1}{\omega_q - \omega_s})$, with ϵ the drive amplitude and ω_s the (Stark) drive frequency. By connecting another Signal Generator (SG) to our current two-tone spectroscopy setup from Fig. 3.32, as shown in Fig. 3.33 (A), we sent a third tone into our system. For this Stark tone we set to an arbitrary drive frequency and increase its power, or drive amplitude, to shift our qubit frequency, see Fig. 3.33 (B).

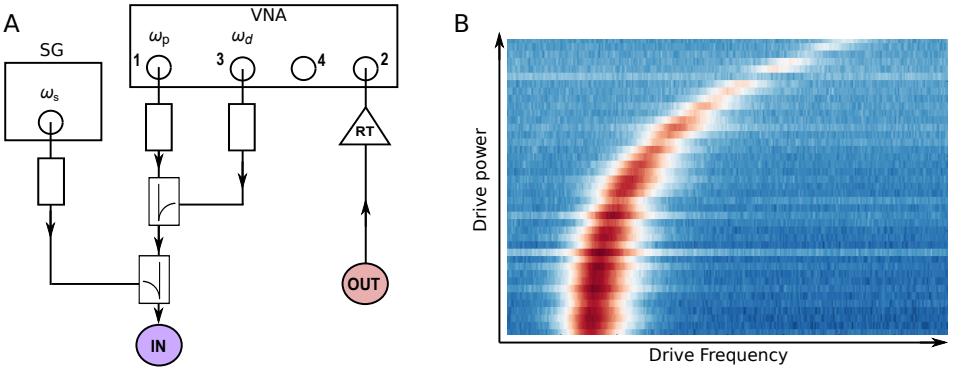

Figure 3.33: AC Stark shift two-tone spectroscopy. (A) Schematic overview of measurement setup for which, compared to two-tone from Fig. 3.32, an extra Signal Generator (SG) is added. Probe signal for fixed power and frequency ω_p is sent through port 1 and measured at port 2 of the VNA. The drive frequency, ω_d, is swept for fixed power. A third tone, the Stark tone at ω_s, is generated by SG and combined with a directional coupler with the other two tones before going into the dilution refrigerator. **(B)** Shows example data of Stark shifting the qubit's 01-transition.

GATED TWO-TONE SPECTROSCOPY MEASUREMENT SETUP

For the gated two-tone measurement, VNA ports 1 and 2 are set up as previously shown in Fig. 3.32 (C). We fix the probe tone at port 1 in frequency and power for which we measure the S_{21} at port 2. An external SG serves as a (qubit) drive tone, which is passed through a microwave RF switch before being combined with the readout tone using a directional coupler. The switch is triggered by a Pulse Generator (PG), as shown in Fig. 3.34 (A), which effectively gates the incoming drive tone to excite the qubit. The VNA is synchronously triggered by SG to take averaged traces. Fig. 3.34 (B) shows example data of an averaged time trace of the dispersively shifted readout resonator for an exited (high level) and unexcited (low level) qubit.

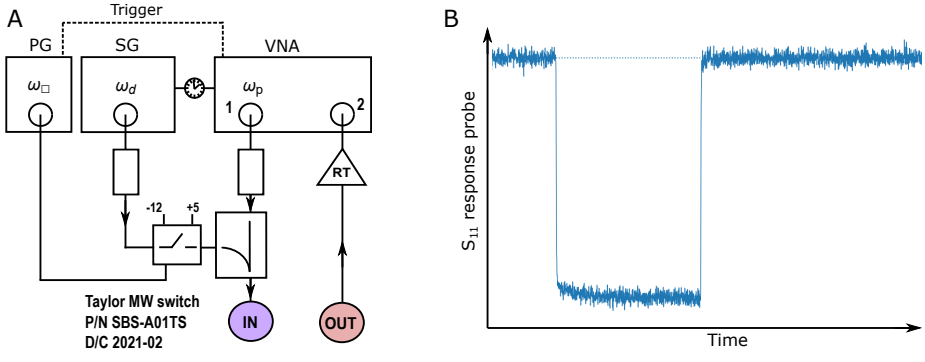

Figure 3.34: Gated two tone spectroscopy. (A) Schematic overview of the external setup for which, compared to two-tone from Fig. 3.32, an extra Signal Generator (SG) provides the qubit drive tone and synchronously triggers the VNA. The probe signal, fixed in frequency and power, is sent from port 1 and measured at port 2 of the VNA. Here, we fix the drive frequency ω_d and use a Pulse Generator (PG) operating a microwave switch to gate our drive tone. Upon qubit excitation, see **(B)**, the readout resonator is in a high S_{21} response signal, but when the switch is shut, the qubit is not excited the qubit and the readout resonator is in a low S_{21} response signal.

All research data and code supporting the findings described in this thesis are available in 4TU.Centre for Research Data at **doi: 10.4121**

4

A Superconducting Single-Atom Phonon Laser

Anything will lase if you hit it hard enough.

Arthur L. Schawlow

The development of quantum acoustics has enabled the demonstration of cooling mechanical objects to their quantum ground state, generation of mechanical Fock-states, and Schrödinger cat states. Such demonstrations have made mechanical resonators attractive candidates for quantum information processing, metrology, and exotic tests of quantum gravity theories. Here, we experimentally demonstrate a direct quantum-acoustic equivalent of a single-atom laser. A single superconducting qubit coupled to a high-overtone bulk acoustic resonator is used to drive the onset of phonon lasing. We observe both the absence of a sharp lower lasing threshold and characteristic upper lasing threshold, unique predictions of single-atom lasing. Lasing of a bulk object with an unprecedented 25 μg mass represents a new regime of laser physics and provides a foundation for the integration of phonon lasers with on-chip devices.

This chapter is available as an arXiv preprint (2312.13948) *A Superconducting Single-Atom Phonon Laser*. C.A. Potts, **W.J.M. Franse**, V.A.S.V. Bittencourt, A. Metelmann and G.A. Steele.

4.1. Introduction

The development of the laser in the early 1960s has proven to be one of the most important breakthroughs in modern physics. The laser found its niche in the advancement of atomic physics, resulting in numerous groundbreaking discoveries such as spectroscopic measurements of atomic species [161, 162], laser cooling of atoms [163, 164], and the realization of Bose-Einstein condensation [165, 166]. Beyond this, lasers are indispensable tools in areas like gravitational wave detection [167], biology [168], chemistry [169], and even in medicine [170].

The advancements enabled by optical lasers have motivated the development of lasing states of mechanical vibrations — phonon lasers. Coherent sources of phonons are interesting for coupling mechanical strain to electron spins and color centers [171], coherent driving of magnetic spin-waves [172, 173], improving the resolution of force sensors [174], fundamental tests of quantum mechanics [175], and nonlinear phononics [176]. However, to date, phonon lasing has been realized only with the center of mass motion of levitated microspheres or ions [175–178], limiting the integrability of these coherent phonon sources. In other examples of phonon lasers in literature, the *lasing* state is the result of dispersive or dissipative optomechanical coupling [171, 174, 179–182] — without population inversion — which are well described as mechanical parametric instabilities [183] or as optically driven pulsed semiconductor heterostructures [184–186].

This article demonstrates, for the first time, the direct phononic analog of a *single-atom* optical laser [187–189]. A single two-level artificial atom driven coherently into population inversion couples to a bulk on-chip phonon mode generating a lasing state. The lasing is observed through a dramatically extended ringdown of the artificial atom excited by the phonon laser and demonstrates the nearly threshold-free nature of single-atom lasers. We also observe a unique predicted feature of single-atom lasers, an upper lasing threshold [188, 190, 191]. Our experimental observations agree with the theoretical and numerical models we use to characterize the system. Moreover, the bulk nature of the phonon mode may allow the future integration of color centers or quantum dots, enabling strain engineering or coherent mechanical driving. The coherent state generated via phonon lasing may also be used as an efficient displacement pulse for the generation of high-amplitude Schrodinger cat states [192]. Future implementations of this architecture may even enable *phonon* spectroscopy of vibrational or electronic transitions of complex molecules and crystal structures [193] or even biological samples [194].

4.2. Experimental Setup

Our device comprises a flip-chip $\hbar$BAR architecture with two bonded device chips [192, 195–198]. We have implemented a fully on-chip integration, which can multiplex different devices on a single silicon chip [53, 199]. A single feedline is coupled to the individual superconducting fixed-frequency transmon qubits. The transmon qubits were fabricated from niobium-titanium nitride for the bulk structures with aluminum Josephson junctions. A sapphire substrate, 650 μm thick, was positioned above each transmon qubit and bonded to the silicon substrate, see Fig. 4.1. The sapphire chip supports a set of longitudinal high-overtone bulk acoustic wave resonances (HBARs) separated by a free spectral range of 8.54 MHz. The elec-

tric field of a transmon qubit coherently couples to the strain of an HBAR acoustic mode via a disk of piezoelectric aluminum nitride patterned on the sapphire. Each qubit on the chip is nearly resonant with an HBAR mode of interest; in such a way, a pair of qubit-HBAR modes behaves like a single atom coupled to a phononic mode. The qubits were read out via on-chip microwave resonators using standard circuit quantum electrodynamics techniques [200, 201]. Our device is similar to those used in previous work generating mechanical Schrödinger cat states [192] and for circuit quantum acoustodynamics [198].

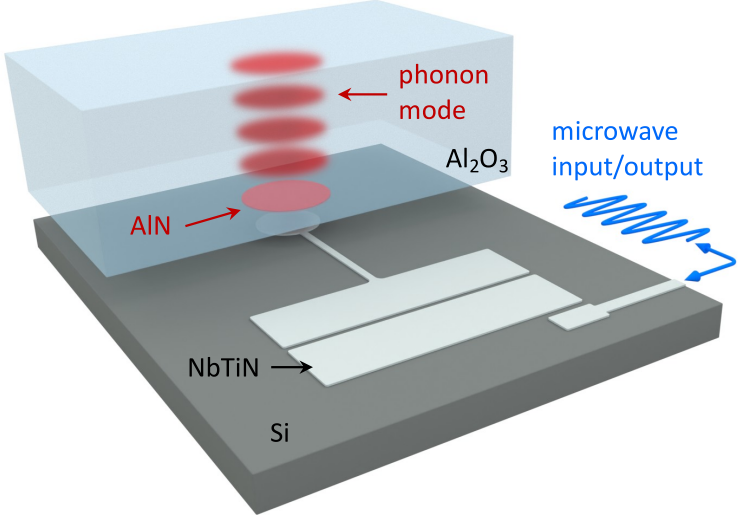

Figure 4.1: Schematic of the on-chip ħBAR device. Rendering of the ħBAR device. The ħBAR device comprises two chips bounded in a flip-chip orientation. The top chip is 650 μm of sapphire, hosts the HBAR modes (red) and is coupled to the superconducting antenna using an aluminum nitride pad (red). The pocket-style transmon qubit (silver) is fabricated from NbTiN on the bottom silicon chip and coupled to the feedline via an on-chip readout resonator (blue).

Using the dispersive shift of a coupled linear readout resonator, we can measure the steady-state qubit population [200]. In the limit where the qubit and the readout resonator are far detuned in frequency, the qubit-cavity Hamiltonian can be written as:

$$\hat{\mathcal{H}}/\hbar = \omega_r \hat{a}^\dagger \hat{a} + \frac{1}{2}\omega_q \hat{\sigma}_z + \chi \hat{\sigma}_z \hat{a}^\dagger \hat{a}, \tag{4.1}$$

where $\omega_{r,q}$ are the readout and qubit frequency, $\hat{a}^{(\dagger)}$ is the photon annihilation (creation) operator, $\hat{\sigma}_z$ is the qubit population operator, and χ is the qubit-state dependent frequency shift of the readout resonator. The coupling between the phonon and the qubit is described by a resonant Jaynes-Cummings interaction [198], given by the Hamiltonian:

$$\hat{\mathcal{H}}_{\text{int}}/\hbar = g_{\text{qb}}(\hat{\sigma}_+ \hat{b} + \hat{\sigma}_- \hat{b}^\dagger), \tag{4.2}$$

where g_{qb} is the coupling rate between the qubit and the phonon mode, $\hat{\sigma}_\pm$ are the qubit

raising and lowering operators, and $\hat{b}^{(\dagger)}$ is the phonon annihilation (creation) operator; see Fig. 4.2(a).

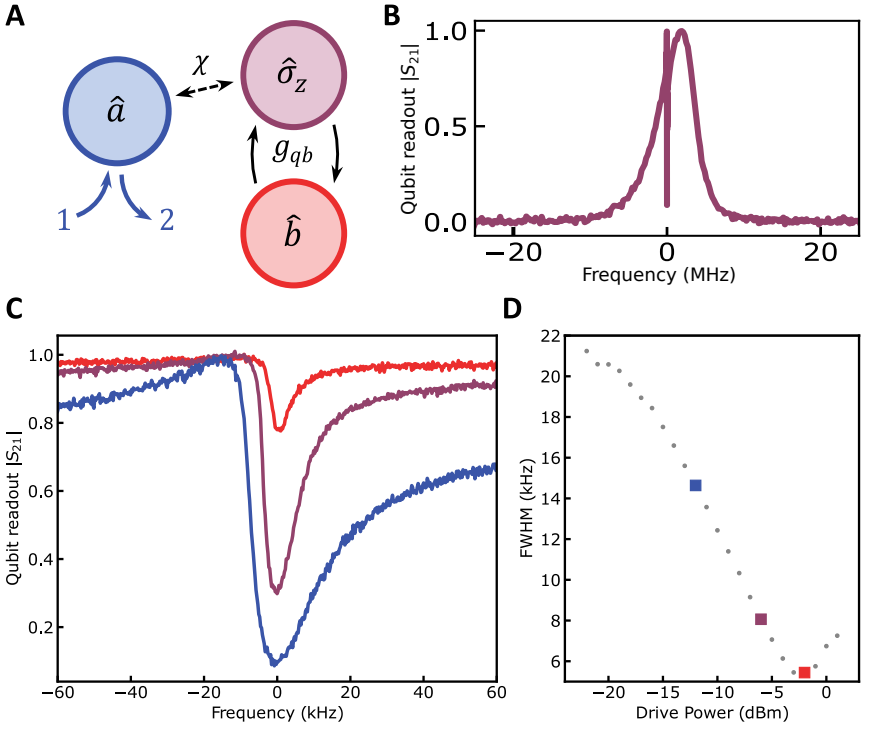

Figure 4.2: Qubit-induced acoustic linewidth narrowing. (A) Definition of modes and the coupling rates between the modes. The readout resonator $\hat{a}$ has input-output modes labelled 1 and 2. **(B)** Measured two-tone spectroscopy for drive power of -12.0 dBm set at room temperature. **(C)** Measured phonon-induced transparency window as a function of qubit drive power. Starting from the lowest curve, drive powers are -12.0, -6.0, and -2.0 dBm set at room temperature, respectively. With increasing power, two features can be noticed. The transparency window reduces in depth, and the full-width half-maximum linewidth narrows. **(D)** Extracted experimental full-width half-maximum of the transparency window as a function of qubit drive power. Colored points match the corresponding curves in (C).

The qubit's state was measured by applying a weak probe tone on resonance with the readout resonator and monitoring the transmitted signal as a second tone was swept near the qubit frequency. The transmission spectrum at the readout frequency directly maps to the qubit occupation $\langle\hat{\sigma}_z\rangle$; see Fig. 4.2(b). The asymmetry of the qubit spectrum is due to the finite photon population within the readout resonator [202, 203] and is well described by our theoretical model. Moreover, the narrow transparency window within the qubit spectrum results from the coherent swaps between the qubit and the phonon mode. In this work, the qubit and the phonon frequency were detuned by approximately 3.3 MHz. See the discussion in the supplementary text for full details. However, as will be discussed below, coherent Rabi oscillations between the qubit and phonon modes do not provide a clear picture of the dynamics at high drive powers.

4.3. PHONON LASING

Three distinct features can be observed within the two-tone spectrum when increasing the qubit drive power. First, the qubit linewidth is power-broadened [202, 204]. Large qubit drive powers increase the qubit decay rate due to increased stimulated emission. Less intuitive is the gradual disappearance and narrowing of the phonon-induced transparency window; see Fig. 4.2(c). The total linewidth of the transparency window is proportional to the phonon linewidth and demonstrates an inverse dependence on the drive power; see Fig. 4.2(d). This dependence is reminiscent of linewidth narrowing described by the Schawlow-Townes equation and is a known property of lasing states [205]. These features can be understood by considering the schematic shown in Fig. 4.3(a).

As described before, the qubit and phonon modes coherently exchange excitations at the lowest qubit drive powers, which can be understood as a bosonic beam-splitter-type interaction. However, as the qubit drive power increases, the qubit is excited by the drive and coherently exchanges an excitation with the phonon mode. But before the phonon mode can exchange the excitation back to the qubit, the external drive re-excites the qubit. The qubit excitation can again be coherently swapped into the phonon mode, causing the phonon mode to climb the Fock state ladder. In the steady state, this process results in a phonon mode described by a large coherent state; i.e. the phonon mode starts lasing. A strong qubit drive allows the phonon mode to accept energy from the qubit but prevents the qubit from accepting energy from the phonon mode; see Fig. 4.3(a). This process also provides an intuitive understanding of the reduced visibility of the transparency window. As the drive power increases, the phonon mode no longer exchanges energy with the qubit; therefore, probing the qubit provides no information about the phonon mode.

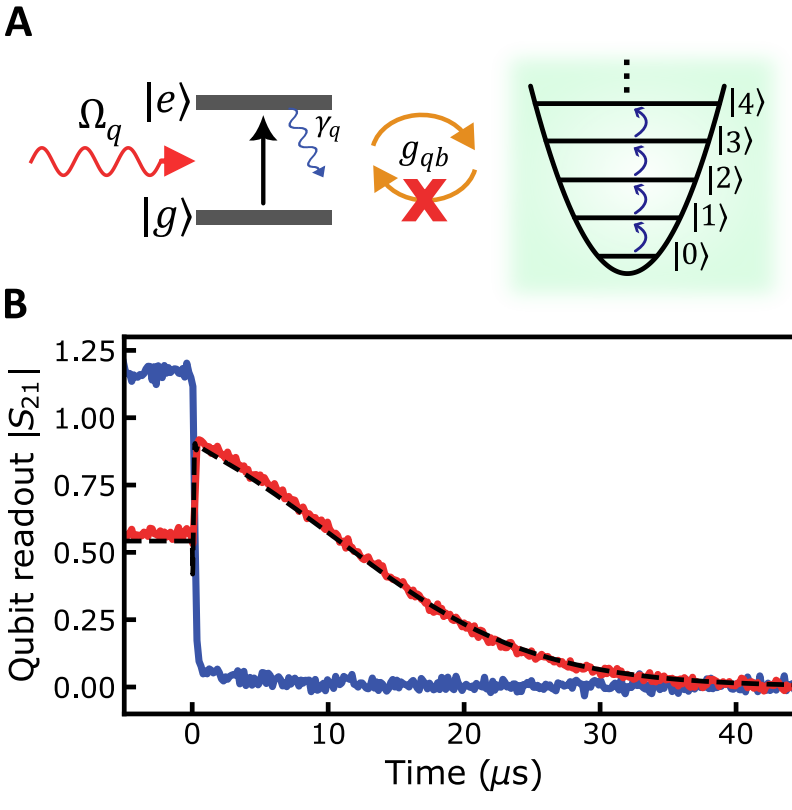

Figure 4.3: Phonon lasing observed through qubit ringdown dynamics. (A) Schematic of the coupled qubit-phonon system. The qubit acts as an artificial two-level atom, with ground state $|g\rangle$ and excited state $|e\rangle$. A coherent drive of strength Ω_q drives the qubit between its ground and excited state. The qubit coherently interacts with the phonon mode at a rate g_{qb}. The qubit is rapidly re-excited for strong pump powers, resulting in a one-directional energy flow into the phonon mode. This process results in phonon lasing. (B) Measured qubit ringdown for a qubit drive of -3.0 dBm. Blue line: the qubit drive is detuned from the HBAR by 250 kHz with the phonon mode in the non-lasing state, decaying on a time scale of the $\sim$ 200 ns decay of the qubit. Red line: The qubit drive is tuned directly on resonance with the HBAR mode, exciting it into the lasing state, exhibiting a dramatically longer, non-exponential decay due to re-excitation from the coherently excited phonon mode. The master equation simulation (dashed black line) is plotted over the data.

Finally, at the highest qubit drive powers, the qubit linewidth has been increased such that the rapid decay of the qubit population results in a *self-quenching* of phonon lasing [190]. Counterintuitively this results in an *upper* lasing threshold above which the phonon mode is no longer lasing. Instead, the qubit incoherently exchanges excitations with the phonon mode, reducing the phonon amplitude. It should also be noted that the phonon mode statistics are no longer described as a coherent state above the upper threshold. This process has been described previously in the context of single-atom photon lasers [187] and is captured by our theoretical description; see the supplementary text.

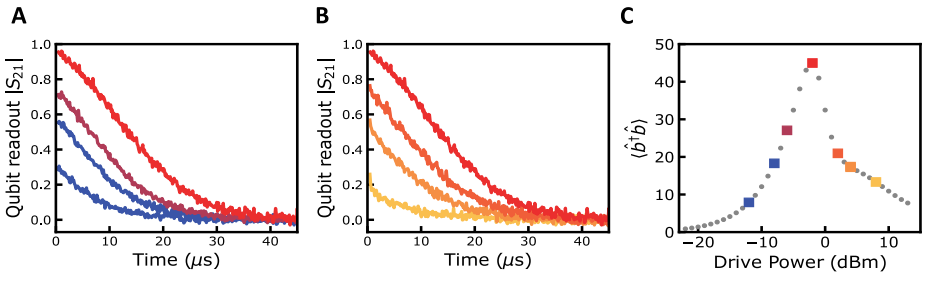

Figure 4.4: Unique signatures of single-atom lasing. (A) Measured gated qubit ringdown for a qubit drive of -12.0, -8.0, -6.0 and -2.0 dBm. With increasing drive power, the gated qubit ringdowns increase in amplitude and duration as the phonon mode population increases. (B) Measured gated qubit ringdown for a qubit drive of -2.0, 2.0, 4.0, and 8.0 dBm. For all measurements, the qubit drive is tuned directly on resonance with the HBAR mode. With increasing drive power, the gated qubit ringdowns decrease in amplitude and duration as the phonon mode population decreases above the self-quenching threshold. For all measurements in (A) and (B), the qubit drive is tuned directly on resonance with the HBAR mode. (C) Simulated phonon state population $\langle \hat{b}^\dagger \hat{b} \rangle$ as a function of qubit drive power. The phonon population is maximum at a drive power of approximately -2.0 dBm and decreases for drive powers above the upper lasing threshold. The individual trace colors in (A) and (B) correspond to the matching colors within the phonon population plot.

4.4. GATED TWO-TONE SPECTROSCOPY

Directly probing the phonon mode is not possible in the current experimental configuration since the readout is performed via the two-level system and not through a propagating photon mode [175, 176]. Direct measurements of the Rabi oscillations between the qubit and phonon state could be possible and have been previously used to measure Fock-states in ħBAR devices [197]. However, this data would provide little clarity due to the short lifetime of our qubit and the multiplicity of simultaneous Rabi oscillation frequencies given by $2g_N = 2\sqrt{N}g_{qb}$, which scale with the phonon mode amplitude N.[197] Instead, we rely on the mismatch between the decay rate of the phonon mode $\tau \sim 25\ \mu$s and that of the qubit. Using gated two-tone ringdown measurements, we can distinguish pure qubit decay from qubit decay driven by a highly excited phonon state. If the phonon mode is highly excited—in the absence of an external drive—the coherent Jaynes-Cummings interaction will continually drive the qubit, resulting in an extended relaxation of the qubit population compared to its intrinsic relaxation rate.

Gated two-tone measurements were performed, driving the qubit until the system reached its steady state; at this point, the drive was switched off using an RF switch. During the entire sequence, the frequency of the readout resonator is monitored using a vector network analyzer, averaging multiple traces triggered synchronously with the RF switch; see the supplementary text for more information. This measures the expectation value of the qubit population $\langle \hat{\sigma}_z \rangle$ as a function of time, with a temporal resolution of 50 ns.

First, the drive power was set near the peak of the lasing amplitude and was detuned 250 kHz above the HBAR resonance. The gated two-tone measurement was performed, and the blue data points in Fig. 4.3(b) show the resulting time domain measurement and a ringdown on the order of $\sim$ 200 ns. This corresponds to the intrinsic T_1 decay of the transmon qubit. A second

measurement was performed at the same drive power, but the drive was tuned resonant with the HBAR. A ringdown on the order of 25 μs is observed for this configuration, represented by the red data points in Fig. 4.3(b). The extended ringdown confirms the highly excited phonon amplitude of the mechanical state. When the qubit drive is switched off, the phonon mode can exchange excitations with the qubit, continually re-exciting the qubit until the phonon mode has decayed back to its ground state. Moreover, near the peak phonon amplitude, in contrast to a thermal state, the coherent state generated by the lasing results in a qubit ringdown that is *not* exponential; instead, the qubit ringdown is approximately linear. This feature is captured by our numerical model, the dashed curve in Fig. 4.3(b). Moreover, our model also captures the ring-up of the qubit and is described within the supplementary information.

We can estimate the phonon population from our numerical model by fitting the spectroscopic and ringdown data. The estimated phonon population is shown in Fig. 4.4(c) as a function of qubit drive power. At a power of -2.0 dBm, the phonon population is nearly maximized, corresponding to the ringdown in Fig. 4.4(a,b), and the upper lasing threshold is clearly visible as the phonon population rapidly reduces with increasing drive power. The upper threshold is experimentally confirmed by performing a set of gated ringdown measurements at a series of qubit drive powers. With increasing qubit drive power, the individual ringdown traces grow in amplitude and increase in duration, corresponding to the increasing phonon population, as shown in Fig. 4.4(a). At a drive power of -2.0 dBm, the phonon ringdown obtains its peak amplitude and duration, indicating a peak in the phonon population, shown in Fig. 4.4, which agrees with the minimum in the transparency window linewidth, shown in Fig. 4.2(b). Further increasing the qubit drive power beyond -2.0 dBm the qubit ringdown decreases in amplitude and duration, a direct indication of the self-quenching nature of the single-atom phonon laser, see Fig. 4.4(b). The upper threshold is a defining signature of a single-atom laser [190], and the agreement between the gated qubit ringdown and our numerical simulations indicates that we have indeed demonstrated a single-atom phonon laser.

4.5. Conclusion

This article demonstrates the experimental realization of a phononic analog to the optical single-atom laser. Our experiment consists of a superconducting single-atom, realized using a transmon style qubit coupled resonantly to an HBAR mode. When driving on resonance with the HBAR mode, the intrinsic non-linearity of the qubit-phonon coupling generates a highly excited phonon state — the phonon laser. A key feature of this experiment is the population inversion of a two-level atom rather than the parametric instability driving phonon excitations. Moreover, the phonon mode is confined in a bulk longitudinal mode within a sapphire substrate. The bulk nature may allow the phonon laser's integration with additional on-chip architectures, such as color centers or quantum dots.

Our results have demonstrated the successful generation of a coherent phonon laser, and we have further demonstrated a counterintuitive feature of phonon lasers, an upper instead of a lower lasing threshold [191]. The size of the coherent lasing state achieved in this work was limited by both the qubit and phonon linewidth. However, the primary limiting factor was the phonon linewidth. Decreasing the decay rates will reduce the upper lasing threshold power and increase the peak lasing amplitude. Future studies could include a linear probe of the

phonon mode to probe the phonon statistics. Such an on-chip phonon laser promises to provide a highly coherent source of phonons, which have applications from sensing to quantum information processing.

4.6. Supplementary Information

4.6.1. Device Fabrication

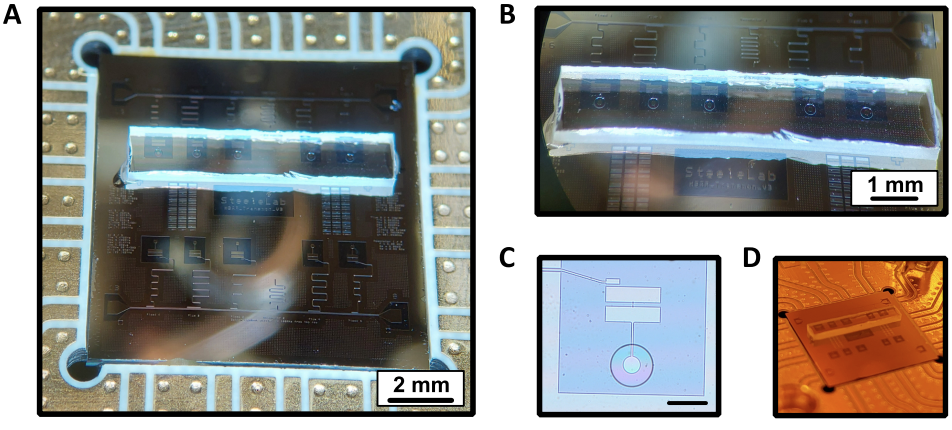

Figure 4.5: Fabricated flip-chip HBAR Device. (A) Optical micrograph of the assembled flip-chip device. The top feedline of qubits is fabricated with a flip-chip of sapphire, and the bottom feedline has no sapphire flip-chip as references. (B) Zoomed optical micrograph of the flip-chip assembly. (C) Optical micrograph of the qubit with the sapphire chip assembled on top. The overlap between the antenna and the 250μm aluminum nitride piezoelectric transducer is visible. The scale bar is 250μm. (D) Optical micrograph of the entire chip loaded in the printed circuit board.

Qubit Chip

The device fabrication starts with a 10x10mm chip 525 μm thick high resistivity $\langle 100 \rangle$ silicon deposited with 100 nm of niobium-titanium nitride (NbTiN). The NbTiN film was deposited by the Dutch Institute for Space Research (SRON) following the process described in [206]. A layer of photoresist (AR-P 6200.18, 4000 rpm) was patterned, exposed (EBPG 5200, 315 μm/cm^2) and developed (Pentylacetate, O-xylene, IPA) to form the bulk circuitry (transmon islands and coplanar waveguides). The exposed NbTiN was removed using a reactive ion etch (Sentech Etchlab 200, 13.5 sccm SF_6 + 5 sccm O_2, 55 W, 10 μbar) followed by an in-situ oxygen descum (50 sccm O_2,100 W, 10 μbar). After stripping the photoresist, a bilayer resist stack (MAA 8.5% EL6, 2000 rpm and PMMA A6 950k, 1500 rpm; baked for three and five minutes at 180 C°, respectively) was used for patterning the Josephson junctions (190 nm width). The junctions were patterned using e-beam lithography. The bilayer was developed using Cold H_2O: IPA (1:3) and cleaned afterwards with IPA. After cleaning the exposed silicon surface with an oxygen descum (200 sccm, 100 W) and acid clean (BoE(7:1):H_2O, 1:1), the chip was placed in an aluminum evaporator (Plassys MEB550). Double-angle shadow evaporation with intermediate in-situ oxidation was used to create Manhattan-style junctions. The aluminum was evaporated at a 35° angle relative to the substrate at a rotational angle of 0° and 90°. The top and

bottom electrodes were 35 and 75 nm thick, respectively. After the first evaporation step, the aluminum was oxidized to create the AlO_x tunnel barriers. Following the second evaporation step, a second oxidation step was performed to cap the junctions with a passivation layer. After performing liftoff in NMP, the qubit chip was finished.

HBAR Chip

The HBAR chip started with double-side polished four-inch sapphire wafers with a 1 μm thick film of c-axis oriented AlN (Kyma technologies, AT.U.100.1000.B). The wafer was diced into 10x10mm chips for easier processing. A photoresist layer (AR-N 4450.10, 6000 rpm) was used to pattern circular regions, 250μm in diameter, to mask the AlN. A reactive ion etch in an Oxford 100 was performed to create AlN disks (Cl_2/BCl_3/Ar at 4.0/26.0/10.0 sccm, 350 W ICP power, 70 W RF power). Following the reactive ion etch, the AlN layer has the proper shape but not the correct thickness. After stripping the photoresist, the chip was placed again inside the etcher to etch the AlN to $\sim$ 900 nm thickness.

4

Flip Chip

Once fabrication on both chips was done, the HBAR chip was diced into 8x2 mm chips. The HBAR chip was then flipped on top of the qubit chip with the AlN layer facing down. Using probe needles, the AlN disks were aligned with the transmon antennas. Once aligned, the probe needles held down the chips in position while a tapered fiber was used to apply two-component epoxy (Loctite EA 3430) on the sides of the top chip; see Fig. 4.5. After the epoxy was cured, the chip was wire-bonded and installed onto the baseplate of the dilution refrigerator.

4.6.2. Measurement Setup

Two-Tone Spectroscopy

All measurements were performed within a dilution refrigerator operating at a base temperature $T \sim 20$ mK. A schematic of the dilution refrigerator setup and the room-temperature electronics are shown in Fig. 4.6. The device was mounted on the mixing chamber plate of the dilution refrigerator and connected to a set of coaxial cables. The device was measured in transmission, with the resonators coupled in a 'notch'-style geometry. The output signals went into a cryogenic HEMT (High Electron Mobility Transistor) amplifier (LNF-LNC4-8A), followed by additional room-temperature amplification (Miteq AFS3-04000800-07-10P-4). The input line was attenuated at each stage to reduce the electron temperature and the thermal radiation at the input port of our device. A total of 48 dB of attenuation was used, plus any additional attenuation from the coaxial cables.

The two-tone spectroscopy was measured using a vector network analyzer (VNA). Port one and port three were combined using a directional coupler, with port three attached to the -20 dB coupling port. Port one was set into zero span mode and output a constant signal tuned on resonance with the Stark shifted readout resonator, ω_r, with an output power of -25 dBm. An additional 60 dB of attenuation was added to this signal before the directional coupler. Port 3 was used as a spectroscopic tone and was swept near the qubit frequency, and its power was varied throughout the experiment and had an additional 40 dB of attenuation. The combined signals from port one and there were then connected to the input line of the dilution refrigerator.

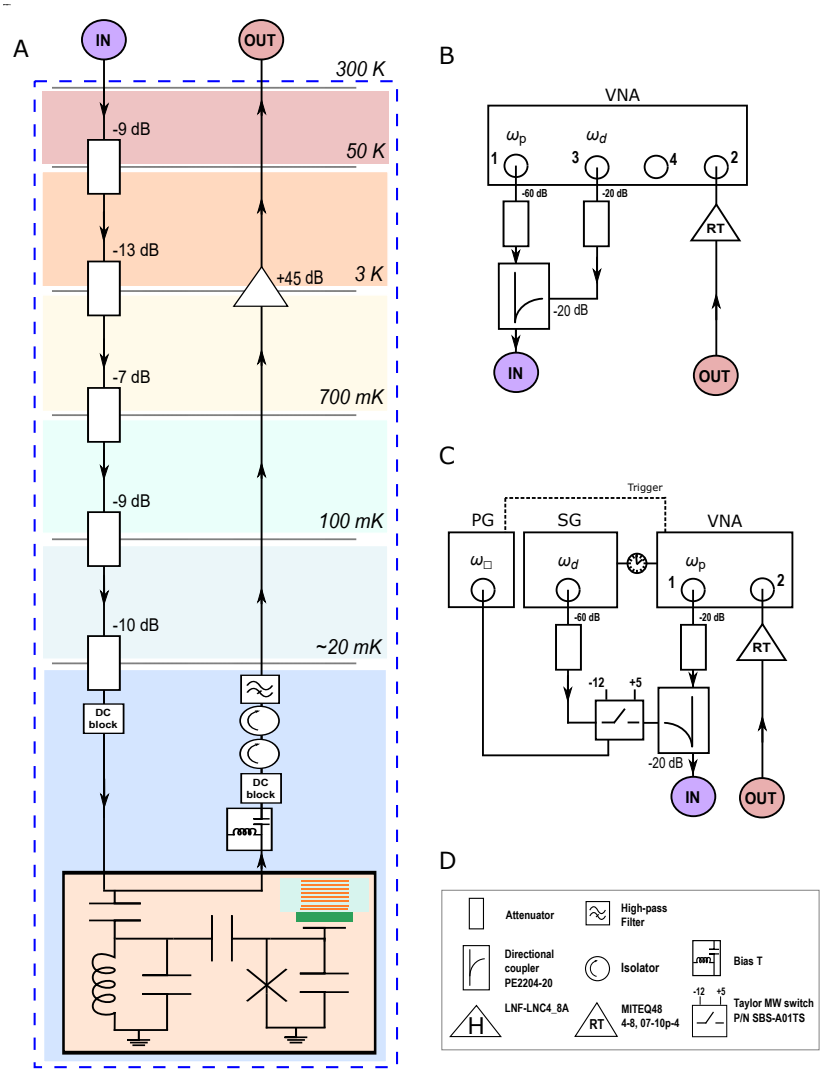

Figure 4.6: Schematic of the measurement setup. To the left is the general Dilution refrigerator wiring setup. Outside the refrigerator, we used two different setups. In (b), we show our Two-tone spectroscopy configuration used for qubit spectroscopy. Here, we sent a weak continuous wave tone (readout resonator probe) from the vector network analyzer (VNA) port one and a second continuous wave tone (qubit drive) from the VNA port 3. These two signals are combined by using a directional coupler before entering the dilution refrigerator. The signal from the dilution refrigerator goes through a room-temperature amplifier before it goes to port 2 of the VNA. In (c), we show are "time domain" setup. Here, we replaced output port 3 of the VNA with a signal generator (SG) to provide the drive tone. A switch (*Taylor MW switch*) together with a pulse generator (PG, *Rigol DG1022*) is placed between the directional coupler and the signal generator.

The output from the dilution refrigerator was directly connected to port 4 of the VNA set in zero span mode at the readout resonator frequency ω_r. Two-tone spectroscopy was performed by slowly sweeping the qubit drive tone, ensuring the system has reached its steady state and monitoring the readout resonators transmission spectrum S_{21}.

Gated Two-Tone Spectroscopy

For the gated two-tone measurement, port one of the VNA was set up just as in the two-tone measurement. An external signal generator generated the qubit drive tone. The qubit drive tone was passed through an RF switch before being combined with the readout tone using a directional coupler. The RF switch was triggered using a pulse generator at a 3 kHz repetition rate. The signal generator was set to a 22.5% duty cycle, so the qubit drive was off for 75 μs per trace. The VNA was synchronously triggered by the signal generator allowing for 65536 trace averages to be performed (maximum setting). Each trace averaged measurement was repeated 75 additional times to improve the signal-to-noise ratio further.

4

4.6.3. Theory

System Hamiltonian and Master Equation

The system consists of a microwave cavity coupled to a transmon qubit which in turn is coupled to an HBAR phonon mode. The transmon qubit can be considered, up to a good approximation, to be a two-level system. The readout cavity is driven two with coherent tones: one at a frequency ω_p, which we call the probe tone, and one at a frequency ω_d, which we call the drive tone. The experiment measures the coupling between the qubit and the phonon mode via two-tone spectroscopy performed via the cavity. The procedure consists of considering the cavity detuned from the qubit, setting the probe tone at the (shifted) cavity frequency and varying the drive tone close to the qubit Lamb-shifted frequency. The transmission of the cavity carries information about the qubit correlations $\langle\hat{\sigma}_z\rangle$. The phonon mode has a frequency close to the qubit frequency.

We model the system with the Hamiltonian

$$\begin{aligned}\frac{\hat{\mathcal{H}}}{\hbar} &= \omega_r \hat{a}^\dagger \hat{a} + \omega_b \hat{b}^\dagger \hat{b} + \frac{\omega_q}{2}\hat{\sigma}_z + g_{qc}(\hat{a}\hat{\sigma}_+ + \hat{a}^\dagger\hat{\sigma}_-) + g_{qb}(\hat{b}^\dagger\hat{\sigma}_- + \hat{b}\hat{\sigma}_+) \\ &\quad + \epsilon_d(\hat{a}e^{i\omega_d t} + \hat{a}^\dagger e^{-i\omega_d t}) + \epsilon_p(\hat{a}e^{i\omega_p t} + \hat{a}^\dagger e^{-i\omega_p t}),\end{aligned} \tag{4.3}$$

where $\hat{a}^{(\dagger)}$ are the annihilation (creation) operators for the readout cavity with frequency ω_r, $\hat{b}^{(\dagger)}$ are the annihilation (creation) operators for the HBAR mode with frequency ω_b, $\hat{\sigma}_z$ is the qubit population operator with qubit frequency ω_q. The couplings are defined by the rates g_{qc} between the qubit and the readout cavity and g_{qb} between the qubit and the HBAR mode, where we assume that $g_{qc} \gg g_{qb}$. Finally, the two drives are described by the amplitude $\epsilon_{p,d}$ with frequencies $\omega_{p,d}$. The system is operated in the cavity-qubit dispersive regime $g_{qc} \ll |\omega_r - \omega_q|$. We then consider the standard Schrieffer-Wolff transformation up to the first order

in $g_{qc}/|\omega_r - \omega_q|$. Defining $\chi = g_{qc}^2/(\omega_q - \omega_r)$, the transformed Hamiltonian reads

$$\frac{\hat{\mathcal{H}}'}{\hbar} = \frac{\tilde{\Omega}_q}{2}\hat{\sigma}_z + \omega_r \hat{a}^\dagger \hat{a} + \omega_b \hat{b}^\dagger \hat{b} + \chi \hat{a}^\dagger \hat{a}\hat{\sigma}_z + g_{qb}(\hat{b}^\dagger \hat{\sigma}_- + \hat{b}\hat{\sigma}_+) - \frac{g_{qb}}{g_{qc}}\chi(\hat{a}^\dagger \hat{b} + \hat{a}\hat{b}^\dagger)\hat{\sigma}_z + \sum_{j=p,d} \epsilon_j(\hat{a}e^{i\omega_j t} + \hat{a}^\dagger e^{-i\omega_j t}) + \frac{g_{qc}}{\omega_r - \omega_q}\sum_{j=p,d}\epsilon_j(\hat{\sigma}_+ e^{i\omega_j t} + \hat{\sigma}_- e^{-i\omega_j t}). \tag{4.4}$$

The Lamb-shifted qubit frequency is $\tilde{\Omega}_q = \omega_q + \chi$. Given the system's parameters, we will discard the qubit-mediated beam-splitter term $\frac{g_{qb}}{g_{qc}}\chi(\hat{a}^\dagger \hat{b} + \hat{a}\hat{b}^\dagger)\hat{\sigma}_z$. Furthermore, in the two-tone spectroscopic setup, we can retain only the probe term for the cavity and only the drive term for the qubit. With such approximations, we have

$$\frac{\hat{\mathcal{H}}'}{\hbar} = \frac{\tilde{\Omega}_q}{2}\hat{\sigma}_z + \omega_r \hat{a}^\dagger \hat{a} + \omega_b \hat{b}^\dagger \hat{b} + \chi \hat{a}^\dagger \hat{a}\hat{\sigma}_z + g_{qb}(\hat{b}^\dagger \hat{\sigma}_- + \hat{b}\hat{\sigma}_+) + \epsilon_p(\hat{a}e^{i\omega_p t} + \hat{a}^\dagger e^{-i\omega_p t}) + \epsilon_d(\hat{\sigma}_+ e^{i\omega_d t} + \hat{\sigma}_- e^{-i\omega_d t}), \tag{4.5}$$

where we have defined $\epsilon_d = \frac{g_{qc}\epsilon_d}{\omega_q - \omega_r}$. It is convenient to move to a frame co-rotating with the pump and the probe frequencies, for which the Hamiltonian in Eq. (4.5) reads

$$\frac{\hat{\mathcal{H}}'_{rot}}{\hbar} = -\frac{\Delta_q}{2}\hat{\sigma}_z + (-\Delta_r + \chi)\hat{a}^\dagger \hat{a} - \Delta_b \hat{b}^\dagger \hat{b} + \chi \hat{a}^\dagger \hat{a}\hat{\sigma}_z + g_{qb}(\hat{b}^\dagger \hat{\sigma}_- + \hat{b}\hat{\sigma}_+) + \epsilon_p(\hat{a} + \hat{a}^\dagger) + \epsilon_d(\hat{\sigma}_+ + \hat{\sigma}_-), \tag{4.6}$$

where $\Delta_b = \omega_d - \omega_b$, $\Delta_q = \omega_d - \tilde{\Omega}_q$, and $\Delta_r = \omega_p - \omega_r + \chi$. We have defined the readout cavity detuning Δ_r to included the Lamb shift, however, this decision is arbitrary. The density matrix of the system ρ has dynamics described by the master equation

$$\partial_t \rho = -\frac{i}{\hbar}[\hat{\mathcal{H}}'_{rot}, \rho] + \kappa \mathcal{L}[\hat{a}]\rho + \gamma_b \mathcal{L}[\hat{b}]\rho + \Gamma_1 \mathcal{L}[\hat{\sigma}_-]\rho + \frac{\Gamma_\phi}{2}\mathcal{L}[\hat{\sigma}_z]\rho. \tag{4.7}$$

Here κ is the cavity decay, γ_b is the phonon decay, Γ_1 is the qubit population decay, and Γ_ϕ is the qubit dephasing. We have assumed zero temperature and ignored small corrections to the dissipator due to the Schrieffer-Wolff transformation.

4.6.4. QUBIT TWO-TONE SPECTROSCOPY

Following the arguments presented in [202], ignoring the qubit-phonon coupling, in the dispersive regime, $\arg[\langle \hat{a}(t)\rangle]$ is directly related to the qubit population $\langle \hat{\sigma}_z(t)\rangle$. By recording the phase of the readout resonator, one can then obtain the qubit absorption spectrum

$$S(\omega) = \frac{1}{2\pi}\int_{-\infty}^{\infty} dt e^{i\omega t}\langle \hat{\sigma}_-(t)\hat{\sigma}_+(0)\rangle_s, \tag{4.8}$$

where $\langle\cdot\rangle_s$ indicates that the expectation value is taken in the steady state.

It was shown that for a qubit-cavity system, the qubit absorption spectrum is given by [202]

$$S(\omega) = \frac{1}{\pi}\sum_{j=0}^{\infty}\frac{1}{j!}\mathrm{Re}\left(\frac{(-A)^j e^A}{\Gamma_q^{(j)}/2 - i(\omega - \Omega_q^{(j)})}\right) \equiv \sum_{j=0}^{\infty} S_j(\omega), \tag{4.9}$$

with

$$
\begin{aligned}
A &= D_{ss}\left(\frac{\kappa/2 - 2i\chi}{\kappa/2 + 2i\chi}\right), \\
B &= \chi(\bar{n}_e + \bar{n}_g - D_{ss}), \\
D_{ss} &= \frac{2\chi^2(\bar{n}_e + \bar{n}_g)}{(\kappa/2)^2 + 2\chi^2}, \\
\bar{n}_e &= \frac{\bar{n}_g(\kappa/2)^2}{(\kappa/2)^2 + (2\chi)^2}, \\
\Gamma_q^{(j)} &= 2\gamma_q + \kappa(j + D_{ss}), \\
\omega_q^{(j)} &= \tilde{\omega}_q + B + 2j\chi .
\end{aligned}
\tag{4.10}
$$

4

In the above equations, $\omega_q^{(j)}$ and $\Gamma_q^{(j)}$ are the frequency and linewidth of the qubit with the readout resonator in the state $|j\rangle$, respectively. The intrinsic qubit linewidth, with the readout resonator in its ground state, is given by $\gamma_q = \Gamma_1/2 + \Gamma_\phi$, where Γ_1 is the longitudinal relaxation rate, and Γ_ϕ is the pure dephasing rate. The qubit frequency $\omega_q^{(0)}$ is ac Stark shifted by B from its intrinsic value ω_q. We have also assumed that the readout drive is on resonance with the readout resonator, i.e. $\Delta_r = 0$, and the readout resonator has a full-width half-maximum linewidth κ. In the limit $\chi \sim \kappa$ and with $\Delta_r = 0$, the components $S_j(\omega)$ have non-Lorentzian lineshapes and can even be negative. The sum of these individual components can result in an asymmetry of the qubit spectrum, as seen in Fig. 4.7(a).

We perform spectroscopy of the qubit by monitoring the transmission coefficient S_{21} of the readout resonator as a function of the qubit drive frequency ω_d. The probe tone was fixed at the Stark-shifted readout resonator frequency with the qubit in its ground state $\omega_c^g/2\pi = 4.91$ GHz, such that $\Delta_r = 0$ and held at a constant power $\mathcal{P}_d = -25$ dBm, set at room temperature. The probe line has a total of 108 dB of attenuation, ensuring the average number of photons in the probe mode on average is much less than one.

To fit the measured spectrum, we use the expression,

$$
|S_{21}| = \mathcal{A}\sum_{j=0}^{10} S_j(\omega) + C, \tag{4.11}
$$

where $\mathcal{A}$ is a conversation factor between $S_j(\omega)$ and $|S_{21}|$ and C is a constant offset of the spectrum. The value of the Fock basis was truncated to $j = 10$, and the linewidth of the readout resonator was independently determined and fixed; see Table. 4.1. The fitting parameters include the intrinsic qubit frequency ω_q, the power broadened qubit linewidth $\Gamma_q(\mathcal{P}_d)$, where $\mathcal{P}_d$ is the qubit drive power, the qubit dispersive shift χ, the probe mode occupancy with the qubit in its ground state $\bar{n}_g$, and conversion factor $\mathcal{A}$, and the constant offset C.

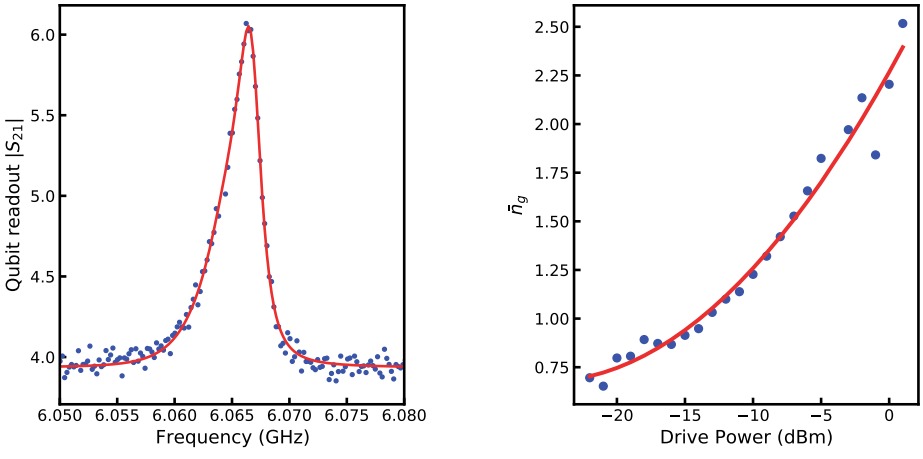

Figure 4.7: Two-tone qubit spectroscopy measurements. (A) Experimental two-tone qubit spectrum (blue) and the qubit spectrum determined from a fit to Eq. 4.11 (red). The qubit drive power at room temperature was set to -20.0 dBm. (B) Extracted value of the readout resonator photon population as a function of qubit drive power.

An example spectrum and its fit are shown in Fig. 4.7(a). First, the value of the dispersive shift was determined to be $\chi = -1.2 \pm 0.2$ MHz, which agreed with our designed value. This value was then fixed, and the data was fit for all qubit drive powers to determine the remaining values. We found that the ground state readout photon population depended on the qubit drive power. This is likely due to the heating of the silicon substrate because the qubit drive tone was applied via the readout resonator. The value of $\bar{n}_g(\mathcal{P}_d)$ is shown in Fig. 4.7(b). The zero power qubit linewidth was also extracted by extrapolating the measured power-broadened qubit linewidth to zero power and was determined to be $\gamma_q(0) = 0.420 \pm 0.04$ MHz, which agrees with our $\gamma_q = \Gamma_1/2 + \Gamma_\phi \geq 1/2T_1$ limit determined using a time-domain measurement with $T_1 = 180 \pm 30$ ns. The comparison between our spectroscopy and time domain measurements indicates that our qubit decay is dominated by decoherence, and therefore we have ignored intrinsic dephasing in our model since qubit dephasing will be dominated by power-induced dephasing induced by the qubit drive tone.

4.6.5. Master Equation Simulations

Qubit Spectroscopy

We simulate the dynamics of the master equation Eq. 4.7 using the Python package Qutip [207]. We first compare the measured qubit spectrum without the phonon mode to the Qutip steady-state simulations. To begin, we must consider the non-zero photon population of the readout resonator. The finite population results in an asymmetry in the qubit spectrum, as well as additional measurement-induced dephasing. To include the finite readout population in our simulation, the readout drive ϵ_p was set such that the average population $\langle \hat{a}^\dagger \hat{a} \rangle = \bar{n}_g(\mathcal{P}_d)$. This ensured that for each qubit drive power, the readout resonator had the appropriate number of steady-state photons.

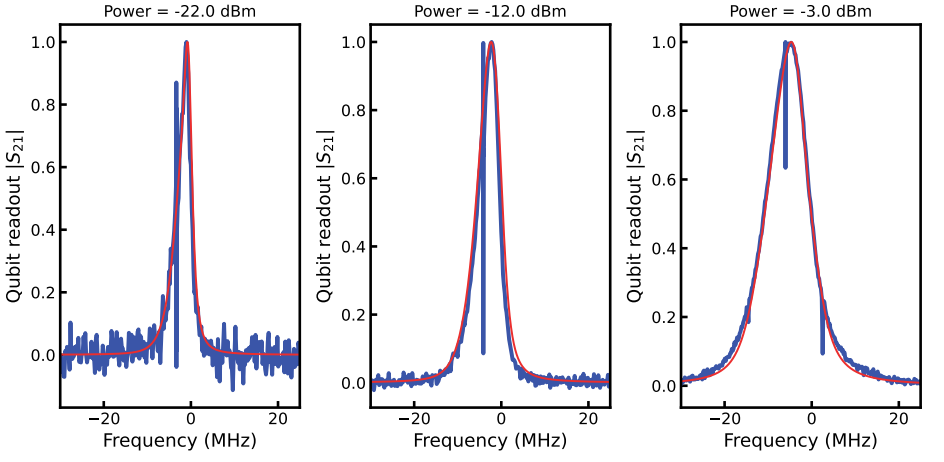

Figure 4.8: Two-tone qubit spectroscopy measurements. (A) Experimental two-tone qubit spectrum (blue) overlapped with the qubit spectrum determined from the master equation simulation (red). The frequency is defined as the detuning from the bare qubit frequency. The qubit drive power at room temperature was set to -12.0 dBm. (B) Qubit spectrum and master equation simulation for a qubit drive power of -6.0 dBm. (C) Qubit spectrum and master equation simulation for a qubit drive power of -3.0 dBm. The feature at $\sim$ 0 MHz is an additional HBAR mode, one free-spectral range from the HBAR mode of interest for this work. The only parameter that was varied within the simulation was the room-temperature value of the qubit drive.

To account for qubit power-broadening, the qubit drive power in the simulation had to be calibrated. As stated above, $\varepsilon_d = \frac{g_{qc}\epsilon_d}{\omega_r - \Omega_q}$, where $\epsilon_d = \sqrt{\kappa_{ext}}\sqrt{\mathcal{P}_d/\hbar\omega_d}$, κ_{ext} is the external coupling rate to the readout resonator, and $\mathcal{P}_d$ is the drive power in Watts at the coupling port of the readout resonator. Therefore, the drive coefficient ε_d can be written in the form

$$\varepsilon_d = \sqrt{10^{(\mathcal{P}_{RT}+\delta)/10}} \tag{4.12}$$

where δ calibrates the room-temperature power to the corresponding value of $\mathcal{P}_d$ accounting for all losses and multiplicative factors. The value of δ was determined by matching the simulation to the power-broadened qubit spectrum at multiple qubit drive powers. A set of qubit spectra is shown in Fig. 4.8 where it can be seen that the master equation simulation is in excellent agreement capturing the qubit asymmetry at low power, and the power-broadened qubit spectrum at higher drive powers. It should be noted the measured transmission signal S_{21} is proportional to the qubit population $\langle\hat{\sigma}_z\rangle$ only if the appropriate signal quadrature is measured. Here this was determined by calculating the rotation angle that minimized the signal in the out-of-phase quadrature. To confirm, we compared our single-trace two-tone data with a direct measurement of the readout resonator frequency at several qubit drive powers. At the highest drive powers, we observed a slight deviation resulting from signal mixing into the out-of-phase quadrature. However, this was at the drive powers above the self-quenching threshold and resulted in a slight mismatch between our experimental and simulated two-tone traces.

Gated Ringdown

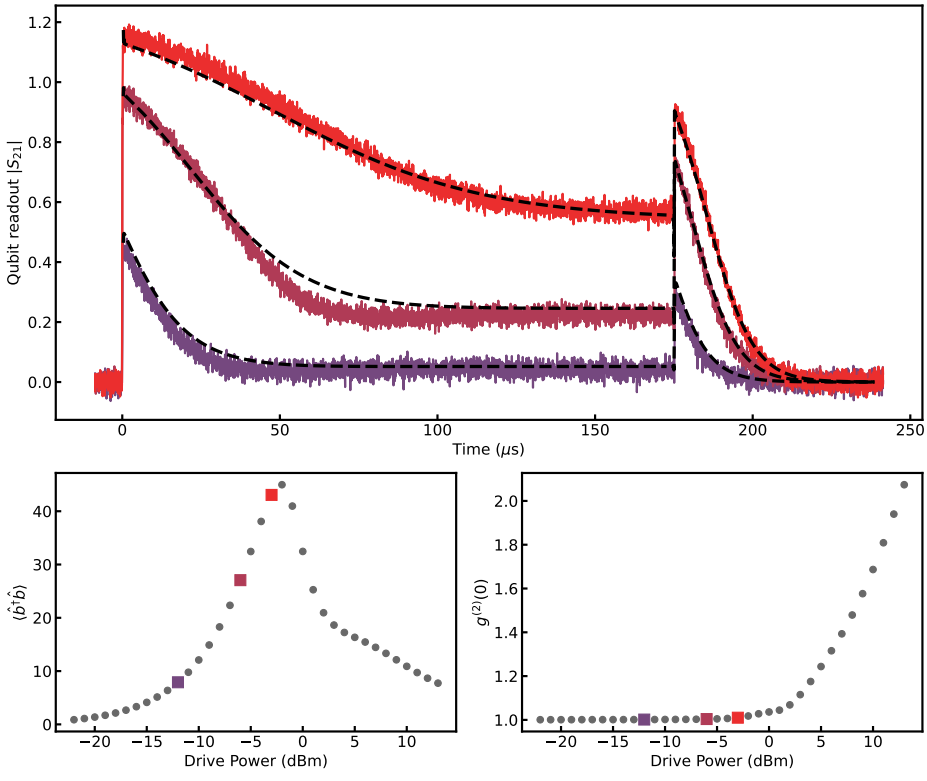

Figure 4.9: Gated two-tone qubit spectroscopy. (A) Experimental gated two-tone measurements for qubit drive powers -12.0, -6.0, -3.0 dBm. The master equation simulations at the same drive power are plotted as dashed black lines. The simulation has an excellent agreement for the ringdown data for all powers and a slight deviation from the ring-up data. This could be attributed to higher-order non-linearities we are not considering within our simple master equation model. However, the agreement between the experiment and simulation is good for all powers. (B) Simulated phonon state population $\langle \hat{b}^\dagger \hat{b} \rangle$ as a function of qubit drive power. (C) Simulated second-order phonon correlations $g^{(2)}(0)$ as a function of qubit drive power.

Following the calibration of the qubit spectrum, the phonon mode was included in the master equation simulation. The value of the coupling rate g_{qb} and the phonon linewidth γ_b were determined by performing a fit to the time domain gated two-tone measurements. The fit was determined by fitting both the ringdown (as shown in the main text) and also the ring-up of the qubit. The best-fit values were then compared at multiple drive powers; see Fig. 4.9(a). We extracted a value of the qubit phonon coupling of $g_{qb}/2\pi = 162$ kHz and a phonon linewidth of $\gamma_b/2\pi = 6.81$ kHz. From this set of simulations, the steady-state phonon population and phonon statistics can be estimated for multiple drive powers. We observe a good agreement between the numerical simulation and the ring-up data and an excellent agreement between the ringdown data for all powers. Deviations in the ring-up simulations likely result from

higher-order nonlinearities we are not considering in our model.

The master equation simulations directly calculate the time dynamics of $\langle \hat{\sigma}_+ \hat{\sigma}_- \rangle$, this value has been scaled by the same constant factor for all powers to give a direct comparison to our two-tone measurement. Since we expect the variation in the transmission coefficient measured in the two-tone measurement to be proportional to $\langle \hat{\sigma}_+ \hat{\sigma}_- \rangle$, see Eq. 4.5 and Ref. [202]. From our simulation, we calculate the phonon population and second-order correlation function for multiple drive powers, shown in Fig. 4.9(b,c). For low drive powers, the phonon statistics are described by a coherent state, $g^{(2)}(0) \approx 1.0$, as expected for a laser. However, as discussed in the main text, single-atom lasers exhibit self-quenching above a given upper-threshold power. This can be seen in both the phonon population, as a rapid decrease in the populations, and in the phonon statistics as $g^{(2)}(0) > 1.0$ for drive powers above the self-quenching threshold.

Table 4.1: Symbols and parameters

Parameter	Symbol
Microwave mode frequency	$\omega_c = 2\pi \times 4.910$ GHz
Microwave mode decay	$\kappa = 2\pi \times 2.897$ MHz
Phonon mode frequency	$\omega_b = 2\pi \times 6.064$ GHz
Phonon mode decay	$\gamma_b = 2\pi \times 6.81$ kHz
Qubit frequency	$\Omega_q = 2\pi \times 6.067$ GHz
Qubit energy relaxation rate	$\Gamma_1 = 2\pi \times 0.840$ MHz
Qubit phase relaxation rate	$\Gamma_\phi < 2\pi \times 0.08$ MHz
Qubit-phonon coupling	$g_{qb} = 2\pi \times 162$ kHz
Dispersive cavity-qubit coupling	$\chi = -2\pi \times 1.2$ MHz
Lamb-shifted qubit frequency	$\tilde{\Omega}_q = \Omega_q - \chi$
Qubit drive frequency	ω_d, varied around Ω_q
Cavity probe frequency	ω_p, set at the Stark-shifted cavity frequency

All research data and code supporting the findings described in this thesis are available in 4TU.Centre for Research Data at **doi: 10.4121**

5

Quantum Acoustics in the High-Cooperativity and Weak-Coupling Regime

"Everything should be made as simple as possible, but not simpler."

Albert Einstein

In the field of quantum acoustics, recent experimental demonstrations have shown that driven planar superconducting qubits coupled to a high-overtone bulk acoustic resonator can generate a phonon-lasing state. Making such systems a direct quantum-acoustic equivalent of a single-atom laser. In this work, we demonstrate that a mean-field solution agrees with full master equation simulations and experimental data. Further investigation shows how the mean-field solutions reveal phonon laser features such as higher phonon occupancy, lower peak drive power, and upper lasing threshold power, which indicate that the mean-field solutions can be used as a fast estimator for designing devices used for phonon lasing.

This chapter is being prepared for publication as *Quantum Acoustics in the High-Cooperativity and Weak-Coupling Regime*. **W.J.M. Franse**, V.A.S.V. Bittencourt, C.A. Potts, A. Metelmann, & G.A. Steele

5.1. Introduction

In the newly emerging field of quantum acoustodynamics (cQAD), superconducting transmon qubits [22, 28, 83] have been coupled to multiple different forms of mechanical modes such as propagating surface acoustic (SAW) [14, 18, 19], film bulk acoustic resonators (FBARs) [13], ultra-high-frequency (UHF) nanoresonator [208], nanomechanical resonators [20, 21] and high - overtone bulk acoustic resonator (HBAR) coupled to either 3D [23, 29, 209] or 2D transmons[32–35]. An exciting experimental regime is that of strong coupling, with the qubit-phonon coupling strength g_{qb} much larger than the loss rates of the qubit and mechanical oscillator, $g_{qb} \gg \{\gamma_q, \gamma_b\}$. In this regime, the preparation of non-classical phononic states [29, 30], and the performance tomography and entanglement [210] has been achieved. However, strong coupling has limitations in the sense that it becomes difficult to directly drive the phonon mode and generate highly excited coherent states, which is required in the preparation of Schrödinger cat states of motion [31]. Lately, because of the focus on strong coupling in cQAD, the weak coupling has largely ignored and left unexplored. Having a weaker coupling in these hybrid systems, one could increase the phonon number in the phonon mode.

Other coupling regimes, depending on the relative value of the coupling strength and the dissipation rates, are also of interest. For instance, when weakly coupled $\gamma_b < g_{qb} < \gamma_q$, the dissipation of the qubit becomes dominant in the coupled system, and the hybridization between the mechanics and qubit disappears. Instead, a transparency window in the qubit spectrum emerges due to the weak coupling to the mechanics. This regime we refer to as acoustically-induced-transparency (AIT), an acoustic analog of the more known electromagnetically induced transparency (EIT) [211], optomechanically induced transparency [212, 213] and magnomechanically induced transparency [214–216]. Aside from coupling strength, we can quantify the efficiency in exchanging photons and phonons in hybrid systems using a dimensionless constant, the cooperativity $C = 4g_{qb}^2/\gamma_b\gamma_q$ [96]. Optomechanical systems often work in a regime of weak coupling ($g < \{\gamma, \kappa\}$) but strong quantum cooperativity ($C > n_{th}$), with n_{th} the thermal photon number [217] In the cQAD case, strong quantum cooperativity corresponds to $C > 1$ since $n_{th} \approx 0$. Therefore, it is interesting to explore possibilities in this unaddressed regime of cQAD.

Here, we have used AIT in the high-cooperativity and weak-coupling regime in the same planar 2D transmons coupled to HBARs used to experimentally demonstrate the quantum-acoustic equivalent of a single-atom laser [36], which is not possible for strongly coupled systems. In this work, we extend our analysis of an HBAR coupled to a planar 2D transmon qubit operating in the weak-coupling (AIT) regime with high cooperativity. Our device is a flip-chip design where both transmon qubit and HBAR are fabricated on separate chips with cooperativity of 36.72. Using a mean-field solution, we examine the spectrum of an AIT system and demonstrate that the solution agrees well with the master equation simulations [36] for low qubit drive powers. We further show how the mean-field analysis describes a great deal of the results captured in the master equation solution of the AIT systems. Under an appropriate drive, the AIT system becomes a phonon laser for which mean-field could be used to explore its parameter space. Using our mean-field solution, we demonstrate features of the phonon laser, such as higher phonon occupancy, lower peak drive power, and upper lasing threshold power. Our results provide not only new insights into understanding the phonon laser but also give a means to efficiently optimize and understand the AIT regime. Allowing one to explore the

parameter space of transmon-HBAR devices outside the strong coupling regime and operate them as phonon lasers.

5.2. Device Description and AC-Stark shift

Our device consists of two feedlines, with each five multiplexed readout resonators coupled to five niobium-titanium nitride transmon qubits. The top line has the HBAR chip flipped on top, and the bottom line is an exact copy for control measurements. In this flip-chip architecture, the top chip consists of five cylindrical-shaped aluminum nitride piezoelectric transducers on a sapphire substrate. The bottom chip includes superconducting transmons and a coplanar waveguide readout resonators on a silicon substrate; see Fig. 5.1(a). The piezoelectric layer is designed to have a thickness, t_p, of ∼900 nm, so the most strongly excited resonances f_o occur at ∼ 6 GHz according to $f_o = v_p/2t_p$, where v_p is the acoustic velocity in the piezoelectric material ($v_{AlN} \approx 1.14 \times 10^4$ m/s). The mode spacing between two consecutive resonances, the free spectral range (FSR), of the phononic resonator, is given by $f_{FSR} = v_s/2t_s$, where v_s is the acoustic velocity in sapphire (∼ 1.11×10^4 m/s,) and t_s the HBAR thickness. Therefore, a 650 μm sapphire substrate has a FSR of 8.538 MHz. An optical micrograph of a single transmon qubit with an HBAR, see Fig. 5.1(b), shows the piezoelectric cylinder is visible as the big circle with white light interference. The interference pattern suggests a gap between the piezoelectric disk and the silicon substrate of ∼ 1 μm. For fabrication and assembly details, see Appendix 5.5.1.

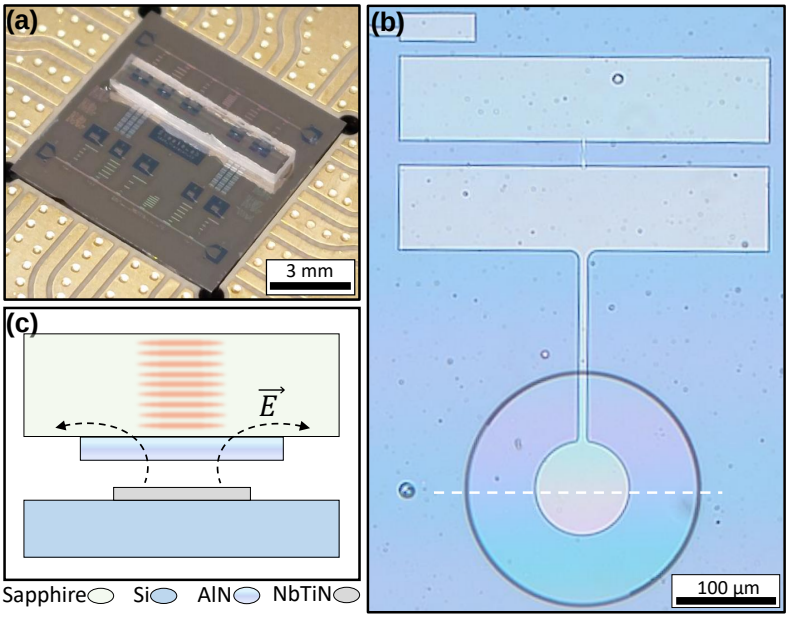

Figure 5.1: 2D Transmon flip-chip HBAR device. (a) Photo of the entire chip **(b)** Optical image of transmon with HBAR on top. Fringes in HBAR suggest a gap distance of a few micrometers between top and bottom chip. **(c)** Schematic side view of assembly drawn at the dashed white line in (b). The antenna of the transmon qubit emits an alternating electric field, $\vec{E}$, to actuate the piezoelectric, which in turn generates a standing wave in the sapphire substrate.

The flip-chip device is cooled to a temperature of ~20 mK in a commercial dilution refrigerator (Triton200-10, Oxford instruments). Using single and two-tone spectroscopy, see Appendix 5.5.2, we measured our readout resonator (4.910 GHz) to be ~1.07 GHz detuned from our qubit's ground-to-excited state transition frequency (ω_{eg} = 6.067 GHz). Using master equation simulations from previous work [36] we determined the qubit and phonon mode linewidths to be 420 MHz and, respectively, 6.81 kHz.

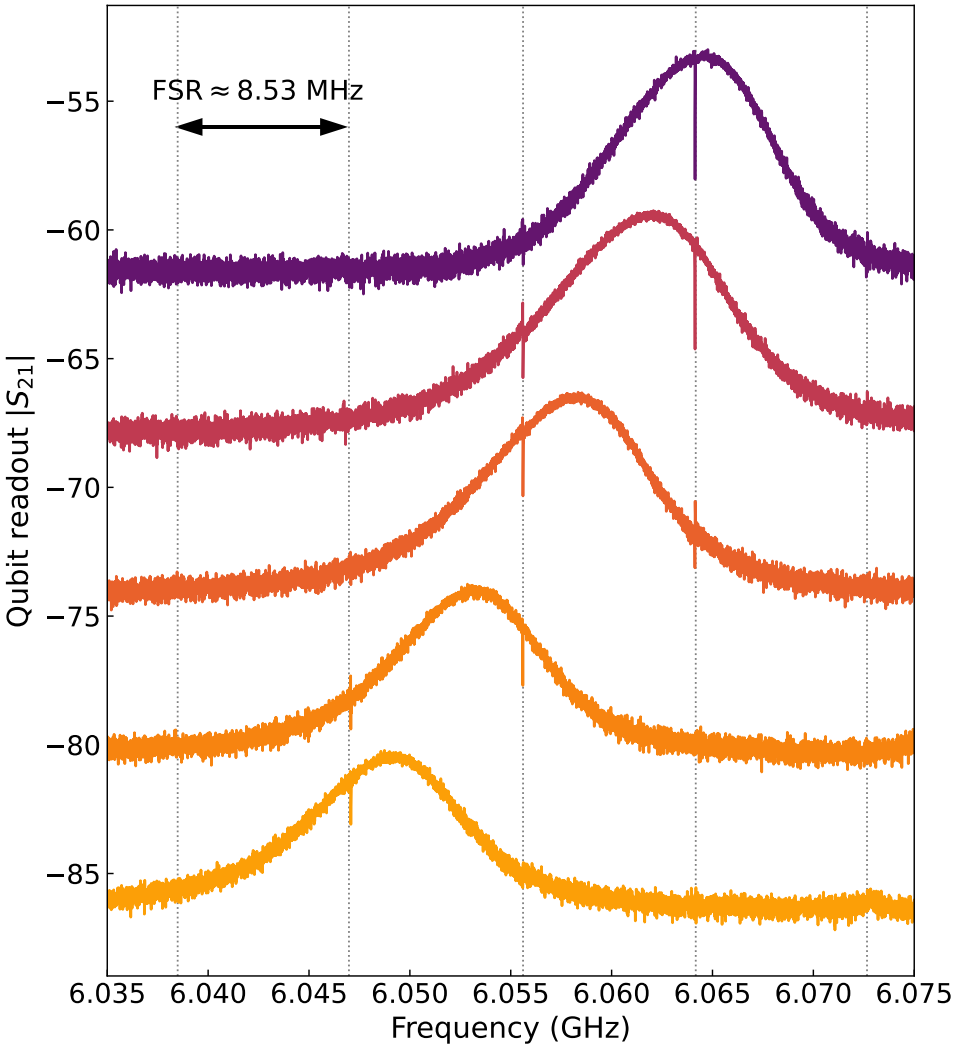

Figure 5.2: AC-Stark shift showing multiple qubit-phonon couplings. Shift of qubit $\omega_{eg}/2\pi$ transition using a Stark drive (f_{stark} = 6.09605 GHz). Two-tone spectroscopy linecuts for different Stark powers (top to bottom: -22.0, -15.5, -12.0, -9.0, -7.5 dBm). Color plot of two-tone spectroscopy data qubit frequency that shifts to a lower frequency by applying a Stark drive that increases with power. The plot shows HBAR resonances separated by a measured FSR of 8.538 MHz corresponding to a 650 μm Sapphire substrate.

To confirm that we have coupled to HBAR resonances, we use the AC-Stark effect [159, 218, 219] to shift the qubit's resonance frequency. We added a third tone (called Stark tone) which is +30 MHz detuned from the qubit frequency, f_{stark} = 6.09605 GHz. By slowly ramping up the power of the Stark tone while performing two-tone spectroscopy, we can shift our qubit in frequency as is shown in Fig. 5.2. In this measurement, the qubit drive is set such that power broadening allows the simultaneous measurement of multiple HBAR resonances within the qubit linewidth while performing the AC-Stark shift. These resonances occur every 8.538 MHz, which equals the before-mentioned FSR we designed our HBAR to have and confirms we indeed have direct coupling between the HBAR and transmon qubit.

5.3. MEAN-FIELD SOLUTION

After confirming the transmon-HBAR coupling, we performed once more two-tone spectroscopy with sufficiently low probe ($P_{\text{p}} = -25$ dBm) and qubit drive power ($P_{\text{d}} = -22$ dBm) so only one acoustic mode became visible within the qubit peak as an AIT window. For this measurement we left out the Stark tone and averaged 20 times. To suppress measurement time, we performed segmented qubit drive frequency sweeps. In a span of 200 kHz around the acoustic mode, frequency points were spaced 250 Hz apart, but in a larger span of 20 MHz around the qubit ω_{eg} transition they were spaced 250 kHz apart. The data (grey dots) is shown in Fig. 5.3, where panel (a) shows full AIT of qubit with one coupled acoustic mode and (b) shows a zoom in of the HBAR mode.

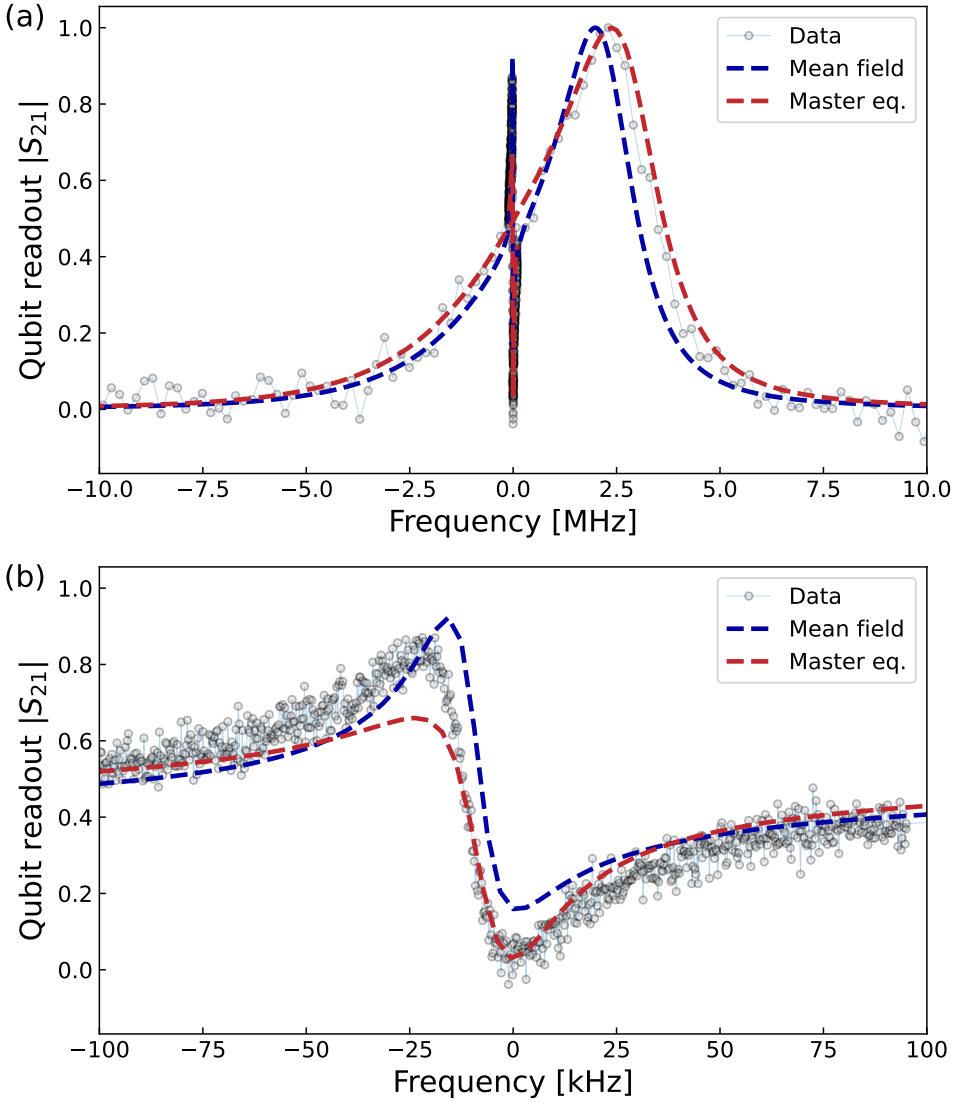

Figure 5.3: Two-tone qubit spectroscopy of AIT in qubit transition peak. Experimental two-tone data of qubit 01-transition coupled to a single HBAR mode at 6.064 GHz (grey dots). Both panels also show the qubit spectrum determined from mean-field (blue dashed line) and master equation simulations (red dashed line). **(a)** Full AIT of qubit with one coupled HBAR mode. **(b)** Zoom in of the HBAR mode.

In Fig. 5.3 we furthermore compare the experimental data to a full master equation simulation (red dashed line) and semi-classical mean-field approximation (blue dashed line). For a description of the full master equation simulation we refer to our previous work in [36]. For our mean-field approximation we start with an Hamiltonian in a frame co-rotating with the drive and the probe frequencies $\omega_{d,p}$, which is written as:

$$\begin{aligned}\frac{\hat{\mathcal{H}}'_{\text{rot}}}{\hbar} = &-\frac{\Delta_q}{2}\hat{\sigma}_z + (-\Delta_r + \chi)\hat{a}^\dagger\hat{a} - \Delta_b\hat{b}^\dagger\hat{b} + \chi\hat{a}^\dagger\hat{a}\hat{\sigma}_z \\ &+ g_{qb}(\hat{b}^\dagger\hat{\sigma}_- + \hat{b}\hat{\sigma}_+) + \epsilon_p(\hat{a} + \hat{a}^\dagger) + \epsilon_d(\hat{\sigma}_+ + \hat{\sigma}_-),\end{aligned} \tag{5.1}$$

where $\Delta_q = \omega_d - \tilde{\Omega}_q$, $\Delta_r = \omega_p - \omega_r$ and $\Delta_b = \omega_d - \omega_b$. $\hat{a}^{(\dagger)}$ are the annihilation (creation) operators for the readout cavity with frequency ω_r, $\hat{b}^{(\dagger)}$ are the annihilation (creation) operators for the HBAR mode with frequency ω_b, and $\hat{\sigma}_z$ is the qubit population operator with qubit frequency ω_q. The Lamb-shifted qubit frequency is $\tilde{\Omega}_q = \omega_q + \chi$ with χ as the qubit dispersive shift. We describe the two drive amplitudes with $\varepsilon_{d,p}$. Following the steps described in Appendix 5.5.4, where we used the mean-field approximation $\langle\hat{o}_1\hat{o}_2\rangle \approx \langle\hat{o}_1\rangle\langle\hat{o}_2\rangle$, we solve the ODE and Fourier transform the mean-field dynamics giving the qubit spectrum shown as blue curves in Fig. 5.3. The plot demonstrate that mean-field, when using parameter values found in Appendix 5.5.3, captures most of the physics of the transmon-HBAR transparency window experimental data. We do recognize that both master equation and mean-field do not capture the phonon peak completely, which probably has to do with nearby transversal modes in the HBAR [23, 29] that are not accounted for in the master equation and mean-field.

When further following the steps described in Appendix 5.5.4 we get the non-linear equation for the phonon steady-state

$$\bar{b} = -\frac{g_{qb}}{\lambda_b\bar{\lambda}_q}\frac{\Gamma_1(g_{qb}\bar{b} + \varepsilon_d)}{\Gamma_1 + 4\text{Re}[\bar{\lambda}_q^{-1}]|g_{qb}\bar{b} + \varepsilon_d|^2}, \tag{5.2}$$

where g_{qb} is the coupling between qubit and HBAR mode, and Γ_1 is the qubit population decay. We numerically compute the mean-field phonon number $n_b = |\bar{b}|^2$. We can solve Eq. 5.2 numerically and obtain the steady-state phonon number as a function of power. We like to note that Eq. 5.2 can exhibit a bistable behavior depending on the parameter regime, as it is known from theoretical [220–222] and experimental [223] studies of the driven-dissipative Jaynes-Cummings model. The results using experimental parameters [36] are shown in Fig. 5.4.

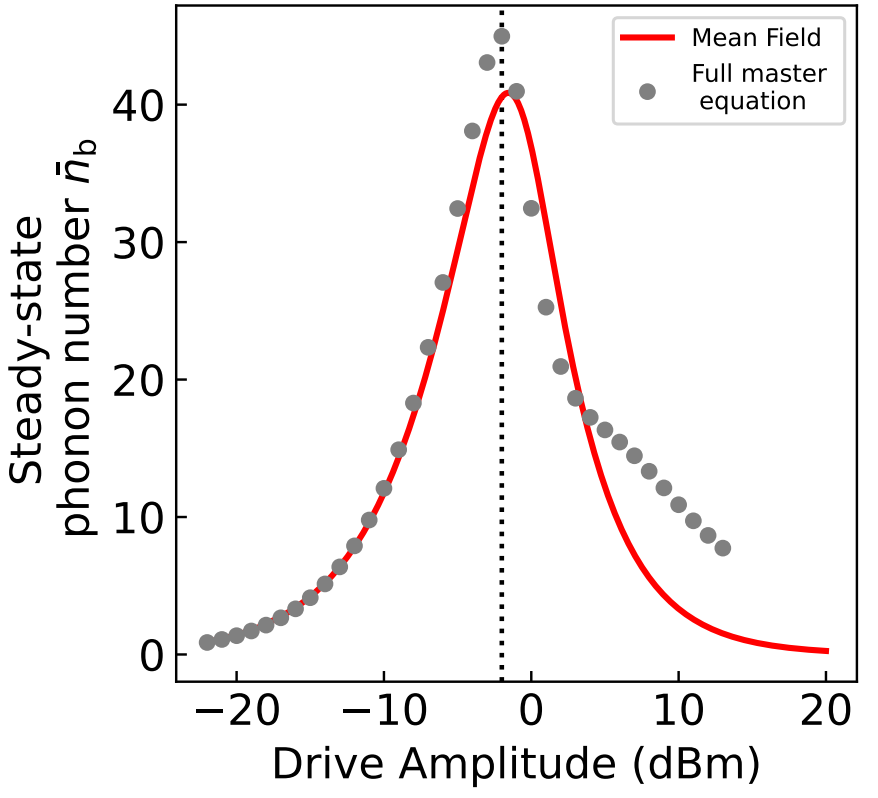

Figure 5.4: Mean-field description of the system. Steady-state phonon number as a function of the qubit drive power. The red line depicts the result obtained with the mean-field solution of Eq. (5.2), the gray points depict the results from simulations of the full master equation simulation. The dashed vertical line indicates the drive power that saturates the steady-state phonon number. Both mean-field and master equation simulation show a maximized phonon populaion at a drive power of -2.0 dBm. The parameters used are given in Table 5.1.

Fig. 5.4 shows steady-state phonon number as a function of qubit drive power for both the mean-field solution (red line) and the full master equation (grey dots). Here, the mean-field agrees well with the full master equation simulations which in turn matched experimental data as presented in [36]. Mean-field especially agrees for low qubit drive powers even though there is a significant discrepancy between the models for qubit drive powers higher than the upper threshold and in the peak phonon number. This discrepancy between mean-field and master equation simulations is related to both the mean-field approximation itself and the procedure used to obtain the effective qubit-phonon dynamics, see Appendix 5.5.4. Nonetheless, mean-field solution still demonstrates key features of a phonon laser, such as higher phonon occupancy, lower peak drive power, and upper lasing threshold power. Therefore, the mean-field solution can be used as a fast estimator for key numbers such as the power required for maximum phonon number, which indicates the upper threshold for the lasing (the self-quenching of the phonon laser). This fast estimator can be of service for designing and improving phonon lasers in future research.

5.4. Conclusion

In this work, we presented a follow-up study on the phonon laser and used a mean-field solution to demonstrate it agrees well with previous work where a full master equation was used to numerically simulate feature of the single-atom phonon laser. Using AC-Stark shift with two-tone spectroscopy we demonstrated that the qubit spectrum showed AIT windows due to its coupling to an HBAR. We showed that the mean-field solution agrees with full master equation simulations and, subsequently, with experimental data. We used the mean-field solution to reveal phonon laser features such as higher phonon occupancy, lower peak drive power, and upper lasing threshold power. The mean-field Allows one to explore the parameter space of transmon-HBAR devices outside the strong coupling regime and operate them as phonon lasers. This fast estimator can be of use in future research to improve design parameters for a phonon laser, such as the maximum phonon and its required power, which could lead to on-chip source of highly coherent phonons.

5.5. Supplementary Information

5.5.1. Fabrication

Fabrication is done on two separate chips and we start off by explaining the qubit chip.

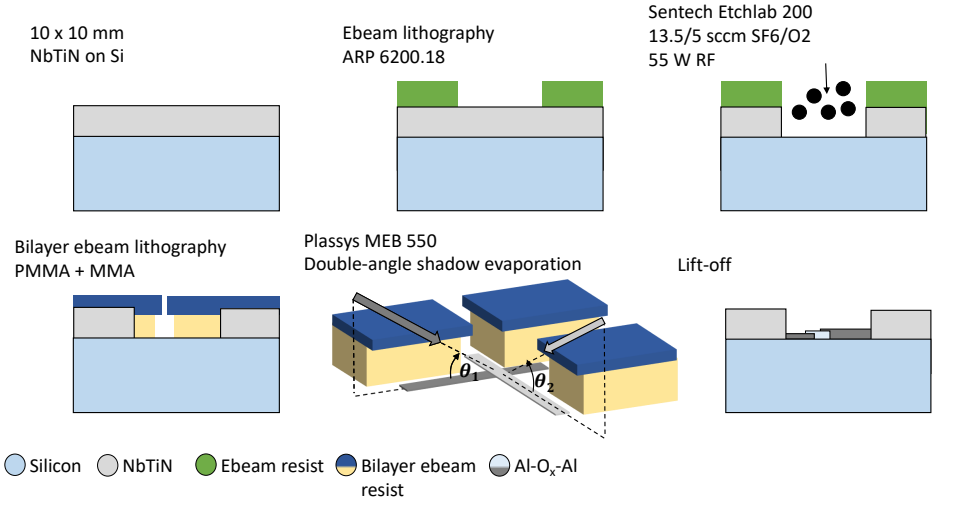

Figure 5.5: Fabrication transmon chip. Drawings show a step-by-step process for fabricating our 2D transmon qubits. Not to scale.

We started out with a 10x10mm chip 525 μm thick high resistivity $\langle 100 \rangle$ silicon chip with a 100 nm NbTiN deposition layer. The NbTiN deposition step has been outsourced to the Dutch Institute for Space Research (SRON) following the process described in [103]. A layer of photoresist (AR-P 6200.18, 4000 rpm) was exposed (EBPG 5200, 315 μm/cm^2) and developed (Pentylacetate, O-xylene, IPA) to form the bulk circuitry (transmon islands and coplanar waveguides). After patterning, we performed a reactive ion etch (RIE) in the Sentech Etchlab 200 (13.5 sccm SF_6 + 5 sccm O_2, 55 W, 10 μbar) followed by an in-situ oxygen descum (50 sccm O_2,100 W, 10 μbar). After stripping the photoresist, a bilayer resist stack (MAA 8.5% EL6, 2000 rpm and PMMA A6 950k, 1500 rpm. Baked 3 and, respectively, 5 minutes at 180 C°) was used for patterning the Josephson junctions (190 nm width). The junctions were patterned by e-beam lithography using a dose of 1700 μ Ccm^{-2}. The bilayer was developed using Cold H_2O: IPA (1:3) and cleaned afterwards with IPA. After cleaning the exposed silicon surface with an oxygen descum (200 sccm, 100 W) and acid clean (BoE(7:1):H_2O, 1:1) the chip was placed in an Aluminum (Al) evaporator (Plassys MEB550). We used double-angle shadow evaporation with an intermediate in-situ oxidation technique to create Manhattan-style junctions. We evaporated Al at 35° evaporation angle for 0° and 90° rotation. This created 35 and 75 nm thicknesses for the top- and bottom-electrode. After each evaporation step, we oxidized the electrodes to create AlO_x tunnel barrier or to terminal cap the junctions using a passivation layer around them. After performing liftoff in NMP the qubit chip was done. Fig. 5.5 above shows the step-by-step process just described.

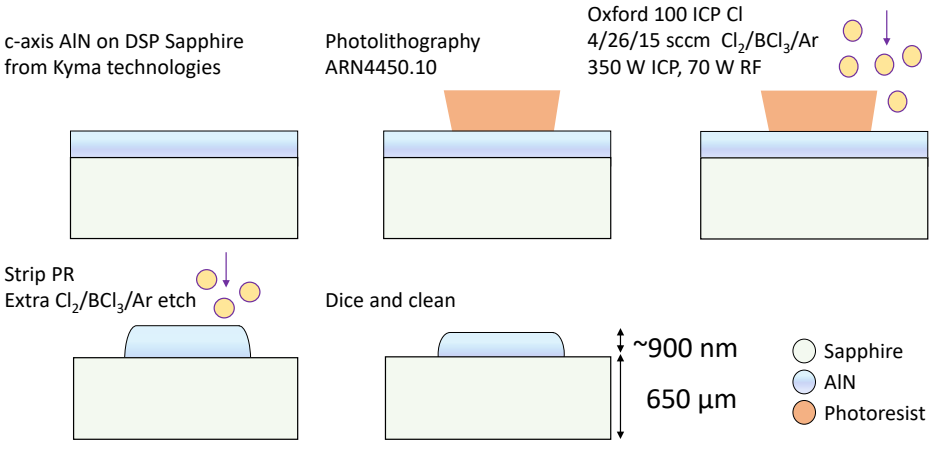

Figure 5.6: Fabrication HBAR chip. Drawings show a step-by-step process for fabricating our HBAR chip. Not to scale.

For the HBAR chip, we begin with double-side polished (DSP) 4" sapphire wafers with on one side a 1 μm thick film of c-axis oriented AlN (Kyma technologies, AT.U.100.1000.B). The wafer was diced into 10x10mm chips for easier processing. We used a photoresist layer (AR-N 4450.10, 6000 rpm) to pattern circular regions to mask off the AlN. We then perform RIE in an Oxford 100 etcher to create AlN disk shapes ($Cl_2/BCl_3/Ar$ at 4.0/26.0/10.0 sccm, 350 W ICP power, 70 W RF power). At this point, the AlN layer is shaped as we desire, but does not have the correct thickness. After stripping the photoresist, the chip was placed again inside the etcher to etch the AlN to $\sim$ 900 nm thickness. Fig. 5.6 above shows the step-by-step process just described.

Once fabrication on both chips was done, we diced the HBAR chip into 8x2 mm chips. This chip was flipped on top of the qubit chip (so the AlN layer facing down at this point). Using probe needles, we aligned the AlN disks with the transmon antennas. Once aligned, the probe needles held down the chips in position while a tapered fiber was used to apply two-component epoxy (Loctite EA 3430) on the sides of the top chip. After the epoxy dried, the chip was wire bonded and placed into our dilution refrigerator.

5.5.2. Measurement Setup

All the experiments reported in this paper were performed in a dilution refrigerator (Triton200-10 Cryofree dilution refrigerator system, Oxford instruments) operating at a base temperature of $\sim$20 mK. A schematic of the experimental setup and the external configurations used in the different experiments can be seen in Fig. 5.7.

The PCB (Printed Circuit Board) onto which the fabricated sample was wire bonded was placed on the mixing plate of the dilution refrigerator and connected to two frequency coaxial lines. These coaxial lines were used as input/output microwave lines to measure the readout resonators in a capacitively side-coupled transmission configuration.

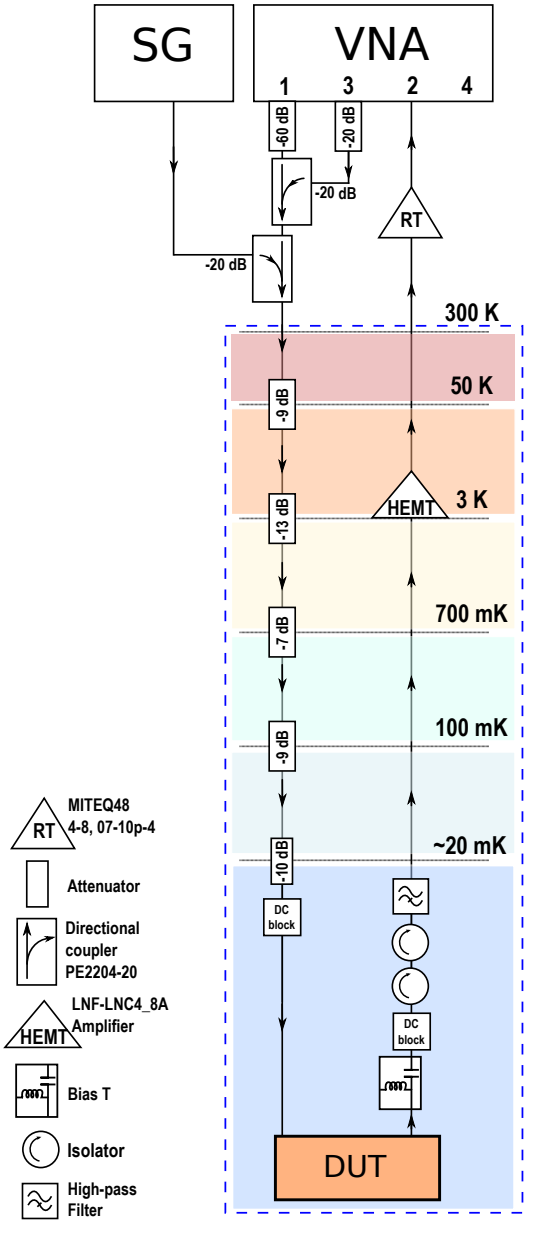

Figure 5.7: Schematic of the measurement setup. To the right is the general Dilution refrigerator wiring setup. Outside the refrigerator, depicted on the top, we used one setup operated in for two measurements. In the configuration on the top we show our Two-tone spectroscopy configuration including an additional signal generator (SG) to perform AC Stark shifts on our qubit while performing qubit spectroscopy. We sent a weak continuous wave tone (readout resonator probe) from the vector network analyzer (VNA) port 1 and a second continuous wave tone (qubit drive) from the VNA port 3. These two signals are combined by using a directional coupler before entering the dilution refrigerator. The signal from the dilution refrigerator goes through a room-temperature amplifier before it goes to port 2 of the VNA. The drive tone coming from the SG is combined with the two VNA signals using a second directional coupler.

Outside the dilution refrigerator, we connected the coaxial lines to a vector network analyzers (VNA, Keysight PNA N5222A, 10MHz-26.5 GHz). For this we used port 1 as a probe signal, port 3 as the qubit drive source and port 2 for readout. For our AC Stark shift experiments we used a signal generator (SG, Rohde & Schwarz (SMB 100A, 100 kHz - 12.75 GHz))

For our probe signal, we had a total estimated attenuation of -108 dB (excluding cable attenuation). For our Qubit drive, we had a total estimated attenuation of -148 dB (excluding cable attenuation). For our Stark signal, we had a total estimated attenuation of -68 dB (excluding cable attenuation). Our high electron mobility transistor (HEMT, LNF-LNC4_8A) has a gain of +44 dB. Our room temperature amplifier (RT, MITEQ48, 4-8,07-10p-04) has a gain of +35 dB.

5.5.3. Device details

Table 5.1 gives the device parameter for the readout resonator (RO), transmon qubit and HBAR resonator. The anharmonicity, $E_c \sim \alpha/2\pi = 2\left(\frac{\omega_{fg}}{2} - \omega_{eg}\right) \approx -260$ MHz, is measured using the two-tone spectroscopy measurement and looking at the higher transitions via multi-photon processes. E_J was measured by probing similar on-chip test junctions. The dispersive shift, χ, is amount the readout resonator shifts when qubit is in either the ground or excited state. The detuning, Δ, between qubit and readout resontor. g_{rq} and γ_{HBAR} are the coupling rates between qubit and readout resonator and, respectively, qubit and HBAR. $\kappa, \gamma, \gamma_{HBAR}$ are the decay rates of the readout resonator, qubit and, respectively, HBAR resonator. All parameter values where extracted from fits and measurements that can be found in [36].

Table 5.1: Device parameters RO, transmon and HBAR.

Parameter	Value
$\omega_{RO}/2\pi$	4.910 GHz
$\kappa/2\pi$	2.897 MHz
$\chi/2\pi$	-1.2 MHz
Δ	$\sim$ 1.07 GHz
g_{rq}	81.04 MHz
$\omega_{eg}/2\pi$	6.067 GHz
E_c/h	$\sim$ 260 MHz
E_J/h	40.2 GHz
$\gamma/2\pi$	425 kHz
$\omega_{phonon}/2\pi$	6.064 GHz
$\gamma_{HBAR}/2\pi$	6.81 kHz
g_{qh}	162 kHz

5.5.4. Semi-Classical Theory and mean field approximation

We can obtain a semi-classical description for the phonon laser. To do so, we need to eliminate the read-out cavity from the full master equation that models the system dynamics, and obtain an effective description for the qubit-phonon dynamics. This is done by a qubit-dependent cavity displacement followed by a partial trace over the read-out cavity [224].

We start by following the steps from the supplementary information of [36] to write down a frame co-rotating with the pump and the probe frequencies with the Hamiltonian written as follows:

$$\begin{aligned}\frac{\hat{\mathcal{H}}'_{\text{rot}}}{\hbar} &= -\frac{\Delta_q}{2}\hat{\sigma}_z + (-\Delta_r + \chi)\hat{a}^\dagger\hat{a} - \Delta_b\hat{b}^\dagger\hat{b} + \chi\hat{a}^\dagger\hat{a}\hat{\sigma}_z \\ &\quad + g_{qb}(\hat{b}^\dagger\hat{\sigma}_- + \hat{b}\hat{\sigma}_+) + \epsilon_p(\hat{a} + \hat{a}^\dagger) + \epsilon_d(\hat{\sigma}_+ + \hat{\sigma}_-),\end{aligned} \tag{5.3}$$

where $\Delta_q = \omega_d - \tilde{\Omega}_q$, $\Delta_b = \omega_d - \omega_b$ and $\Delta_r = \omega_p - \omega_r$. Here, the Lamb shift is included with the readout cavity such that for $\Delta_r = 0$, the readout resonator is resonant with the probe drive. The density matrix of the system ρ has dynamics described by the following master equation

$$\begin{aligned}\partial_t\rho &= -\frac{i}{\hbar}[\hat{\mathcal{H}}'_{\text{rot}}, \rho] + \kappa\mathcal{L}[\hat{a}]\rho + \gamma_b\mathcal{L}[\hat{b}]\rho \\ &\quad + \Gamma_1\mathcal{L}[\hat{\sigma}_-]\rho + \frac{\Gamma_\phi}{2}\mathcal{L}[\hat{\sigma}_z]\rho,\end{aligned} \tag{5.4}$$

where γ_b is the phonon decay, κ is the cavity decay, Γ_1 is the qubit population decay, and Γ_ϕ is the qubit dephasing. Here we assumed zero temperature and ignored small corrections to the dissipator due to the Schrieffer-Wolff transformation [225].

Now that we have obtained the full master equation in Eq. (5.4), we apply the unitary transformation $\mathbb{P}$ given by

$$\hat{\mathbb{P}} = \hat{\Pi}_e\hat{\mathcal{D}}(\alpha_e(t)) + \hat{\Pi}_g\hat{\mathcal{D}}(\alpha_g(t)), \tag{5.5}$$

where $\hat{\Pi}_{e(g)} = |e(g)\rangle\langle e(g)|$ are the projectors into the qubit excited (ground) state and we take $\alpha_{e,g}(t)$ as the coherent amplitudes of the cavity field provided that the qubit is in the excited or ground state, respectively. Those satisfy the equations

$$\begin{aligned}\dot{\alpha}_e &= \left[i\left(\Delta_r - \chi\right) - \frac{\kappa}{2}\right]\alpha_e - i\epsilon_p, \\ \dot{\alpha}_g &= \left[i\left(\Delta_r + \chi\right) - \frac{\kappa}{2}\right]\alpha_g - i\epsilon_p.\end{aligned} \tag{5.6}$$

From these dynamical equations, we have the following expressions for the excited and ground state readout cavity occupancy in the steady-state :

$$\begin{aligned}\bar{n}_e &= |\bar{\alpha}_e|^2 = \frac{\epsilon_p^2}{(\Delta_r - \chi)^2 + \frac{\kappa^2}{4}}, \\ \bar{n}_g &= |\bar{\alpha}_g|^2 = \frac{\epsilon_p^2}{(\Delta_r + \chi)^2 + \frac{\kappa^2}{4}}.\end{aligned} \tag{5.7}$$

The density matrix in the displaced frame is $\tilde{\rho} = \hat{\mathbb{P}}^\dagger\rho\hat{\mathbb{P}}$, and the master equation transforms to

$$\partial_t\tilde{\rho} = \hat{\mathbb{P}}^\dagger\partial_t\rho\hat{\mathbb{P}} - \hat{\mathbb{P}}^\dagger(\partial_t\hat{\mathbb{P}})\tilde{\rho} - \tilde{\rho}(\partial_t\hat{\mathbb{P}}^\dagger)\hat{\mathbb{P}}, \tag{5.8}$$

where $\hat{\mathbb{P}}^\dagger\partial_t\rho\hat{\mathbb{P}}$ is obtained by transforming Eq. (5.4).

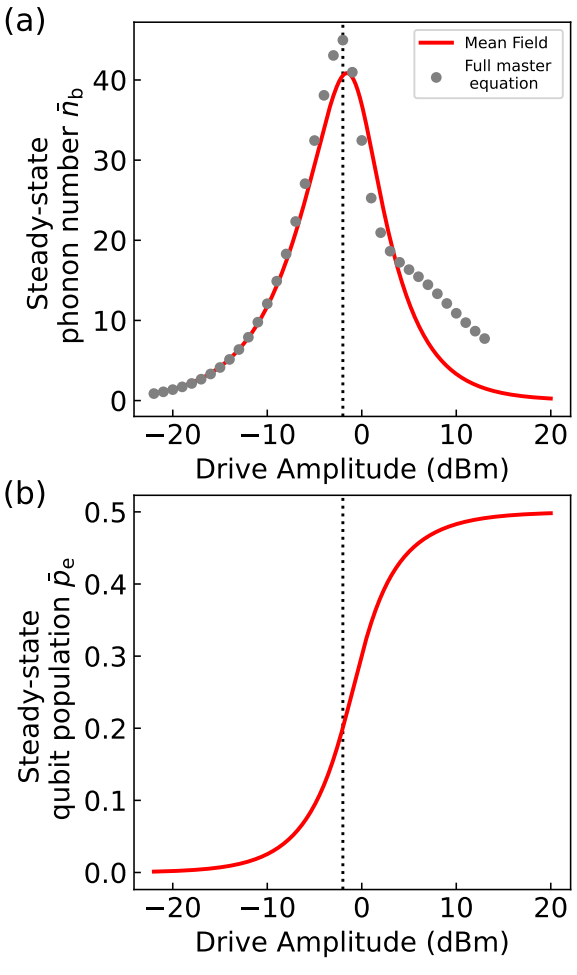

Figure 5.8: Mean-field description of the system. (A) Steady-state phonon number as a function of the qubit drive power. The red line depicts the result obtained with the mean-field solution of Eq. (5.17), the gray points depict the results from simulations of the full master equation (5.4). The dashed vertical line indicates the drive power that saturates the steady-state phonon number. We notice a good qualitative agreement between the mean-field solution and the master equation simulation, a part from a discrepancy in the peak phonon number. (B) Steady-state qubit population $\bar{p}_e$ as a function of the qubit drive power. The parameters used are given in Table 5.1.

We can then obtain an effective master equation by tracing out the cavity and assuming that, in the displaced frame, the cavity is empty. We get the following effective master equation for the qubit-phonon density matrix ϱ in a frame co-rotating with the qubit drive frequency

$$\begin{aligned}\partial_t \varrho = &-\frac{i}{\hbar}[\hat{\mathcal{H}}_{\text{eff}}(t), \varrho] + \gamma_b \mathcal{L}[\hat{b}]\varrho + \Gamma_1 \mathcal{L}[\hat{\sigma}_-]\varrho \\ &+ \frac{\gamma_\phi(t) + \Gamma_\phi}{2}\mathcal{L}[\sigma_z]\varrho,\end{aligned} \tag{5.9}$$

where the effective Hamiltonian is

$$\begin{aligned}\frac{\hat{\mathcal{H}}'_{\text{rot}}}{\hbar} &= -\frac{\Delta_q - \mathcal{B}(t)}{2}\hat{\sigma}_z - \Delta_b \hat{b}^\dagger \hat{b} \\ &\quad + g_{qb}(\hat{b}^\dagger \hat{\sigma}_- + \hat{b}\hat{\sigma}_+) + \varepsilon_d(\hat{\sigma}_+ + \hat{\sigma}_-).\end{aligned} \tag{5.10}$$

The cavity induced qubit frequency shift $\mathcal{B}(t)$ and dephasing rate $\gamma_\phi(t)$ are given by

$$\begin{aligned}\mathcal{B}(t) &= 2\chi \text{Re}[\alpha_g(t)\alpha_e^*(t)], \\ \gamma_\phi(t) &= 2\chi \text{Im}[\alpha_g(t)\alpha_e^*(t)].\end{aligned} \tag{5.11}$$

The effective dynamics given by the master equation (5.9) corresponds to that of a driven two-level system, with a time-dependent frequency and dephasing rate, coupled to a harmonic oscillator via a Jaynes-Cummings interaction.

From the effective master equation Eq. (5.9), we obtain the following set of equations

$$\begin{aligned}\partial_t\langle\hat{b}\rangle &= \left(i\Delta_b - \frac{\gamma_b}{2}\right)\langle\hat{b}\rangle - ig_{qb}\langle\hat{\sigma}_-\rangle, \\ \partial_t\langle\hat{\sigma}_-\rangle &= \left(i(\Delta_q - \mathcal{B}(t)) - (\gamma_q + \gamma_\phi(t))\right)\langle\hat{\sigma}_-\rangle \\ &\quad + 2ig_{qb}\langle\hat{b}\hat{\Pi}_e\rangle - ig_{qb}\langle\hat{b}\rangle + 2i\varepsilon_d\langle\hat{\Pi}_e\rangle - i\varepsilon_d, \\ \partial_t\langle\hat{\Pi}_e\rangle &= ig_{qb}\left(\langle\hat{b}^\dagger\hat{\sigma}_-\rangle - \langle\hat{b}\hat{\sigma}_+\rangle\right) + i\varepsilon_d(\langle\hat{\sigma}_-\rangle - \langle\hat{\sigma}_+\rangle) \\ &\quad - \Gamma_1\langle\hat{\Pi}_e\rangle,\end{aligned} \tag{5.12}$$

where $\hat{\Pi}_e = |e\rangle\langle e|$.

The above equations include terms like $\langle\hat{b}^\dagger\hat{\sigma}_-\rangle$, which require further equations to be solved. We adopt a *mean field* approximation $\langle\hat{o}_1\hat{o}_2\rangle \approx \langle\hat{o}_1\rangle\langle\hat{o}_2\rangle$, and from now on we use the following notation

$$\begin{aligned}\langle\hat{b}\rangle &\equiv b \\ \langle\hat{\sigma}_-\rangle &\equiv s_- \\ \langle\hat{\Pi}_e\rangle &\equiv p_e.\end{aligned} \tag{5.13}$$

Using the mean-field approximation, Eqs. (5.12) yield

$$\begin{aligned}\partial_t b &= -\lambda_b b(t) - ig_{qb}s_-(t), \\ \partial_t s_- &= -\lambda_q(t)s_-(t) + i(2p_e(t) - 1)(g_{qb}b(t) + \varepsilon_d), \\ \partial_t p_e(t) &= 2\text{Im}\left[s_-^*(t)\left(g_{qb}b(t) + \varepsilon_d\right)\right] - \Gamma_1 p_e(t).\end{aligned} \tag{5.14}$$

where we have defined

$$\begin{aligned}\lambda_b &= -i\Delta_b + \frac{\gamma_b}{2}, \\ \lambda_q(t) &= -i(\Delta_q - \mathcal{B}(t)) + (\gamma_q + \gamma_\phi(t)).\end{aligned} \tag{5.15}$$

Equations (5.12) are the qubit-phonon Maxwell-Bloch equations. We emphasize that such equations include qubit intrinsic dephasing and the readout cavity-induced dephasing. Here

the drive is included in the qubit part, but a displacement transformation $b \longrightarrow b + \varepsilon_d/g_{qb}$ can be made to shift the drive term to the Harmonic oscillator equation.

We can then obtain the steady-state of (5.12) by setting $\partial_t \bar{b} = \partial_t \bar{s}_- = \partial_t \bar{p}_e = 0$ and $\lambda_q(t) \longrightarrow \bar{\lambda}_q$, where $\bar{\lambda}_q$ is obtained by taking $\mathcal{B}(t)$ and $\Gamma(t)$ at $t \longrightarrow \infty$. After some algebra, we get the following expressions for $\bar{s}_-$ and $\bar{s}_z$ in terms of the steady-state value of the phonon amplitude $\bar{b}$:

$$\begin{aligned} \bar{p}_e &= -\frac{2\mathrm{Re}[\bar{\lambda}_q^{-1}]|g_{qb}\bar{b} + \varepsilon_d|^2}{\Gamma_1 + 4\mathrm{Re}[\bar{\lambda}_q^{-1}]|g_{qb}\bar{b} + \varepsilon_d|^2}, \\ \bar{s}_- &= -\frac{i\Gamma_1(g_{qb}\bar{b} + \varepsilon_d)}{\bar{\lambda}_q\left(\Gamma_1 + 4\mathrm{Re}[\bar{\lambda}_q^{-1}]|g_{qb}\bar{b} + \varepsilon_d|^2\right)}. \end{aligned} \tag{5.16}$$

The following non-linear equation gives the phonon steady-state

$$\bar{b} = -\frac{g_{qb}}{\lambda_b \bar{\lambda}_q} \frac{\Gamma_1(g_{qb}\bar{b} + \varepsilon_d)}{\Gamma_1 + 4\mathrm{Re}[\bar{\lambda}_q^{-1}]|g_{qb}\bar{b} + \varepsilon_d|^2}, \tag{5.17}$$

from which we can compute numerically the mean field phonon number $n_b = |\bar{b}|^2$. The above equation can exhibit a bistable behavior depending on the parameter regime, as it is known from theoretical [220–222] and experimental [223] studies of the driven-dissipative Jaynes-Cummings model.

We can solve equation (5.17) numerically and obtain the steady-state phonon number as a function of power. We show the result for the parameters corresponding to the experiment in Fig. 5.8. The mean-field estimation agrees well with the full master equation simulation and can be used as a fast estimator of, e.f., the power required for maximum phonon number, which indicates the upper threshold for the lasing. The discrepancy between mean-field and the full master equation simulations is related to both the mean-field approximation and the procedure that was used to obtain the effective qubit-phonon dynamics.The mean field model also captures the self-quenching of the phonon lasing at higher powers. In fact, as depicted in Fig. 5.8(B), the power for which the phonon population is maximized corresponds to an inflection point in the qubit population (as a function of the drive power). At higher drive powers, the qubit steady-state corresponds to that of a driven two-level system, only slightly perturbed due to the coupling to the phonons. We notice a significant discrepancy between the models for qubit drive powers higher than the upper threshold.

One advantage of the mean field approximation is that it can be used for a quick characterization of the system, which can then be used as a guide for improving the system's design. We can see that by studying the behavior of the maximum achievable steady-state phonon number, and the required qubit drive power as a function of the readout resonator ground state occupancy $\bar{n}_g$, see Section S2.B in [36]. A higher value of $\bar{n}_g$ imply a higher readout-cavity induced dephasing, given Eq. (5.11), thereby reducing the maximum number of steady-state phonons. Such an effect comes on top of the intrinsic qubit dephasing, which defines not only the maximum achievable steady-state phonon number, but also how strong the qubit has to be driven to achieve such maximum. We show the results of such an analysis in Fig. 5.9, which depicts the maximum steady-state phonon number and the corresponding qubit drive power

as a function of $\bar{n}_g$. The results are shown also for several values of the intrinsic qubit dephasing Γ_ϕ. We notice that there is an interplay between achieving a high number of excitations and increasing the qubit drive power. Even if at low values of $\bar{n}_g$ the maximum number of steady-state phonons is higher, the drive powers required to achieve such maximum number also increases. We also notice a non-monotonic behavior of the drive power as a function of $\bar{n}_g$. An increasing in $\bar{n}_g$ also implies a qubit frequency shit. For the parameters used, such a frequency shift can bring the qubit close to resonant with the phonons, consequently lowering the drive power required for maximum phonon number.

We should emphasize that in the experiment $\bar{n}_g$ is itself a function of the qubit drive power , a situation which we did not consider for the results presented in Fig. 5.9, but which is included in the previous mean-field results shown in Fig. 5.8.

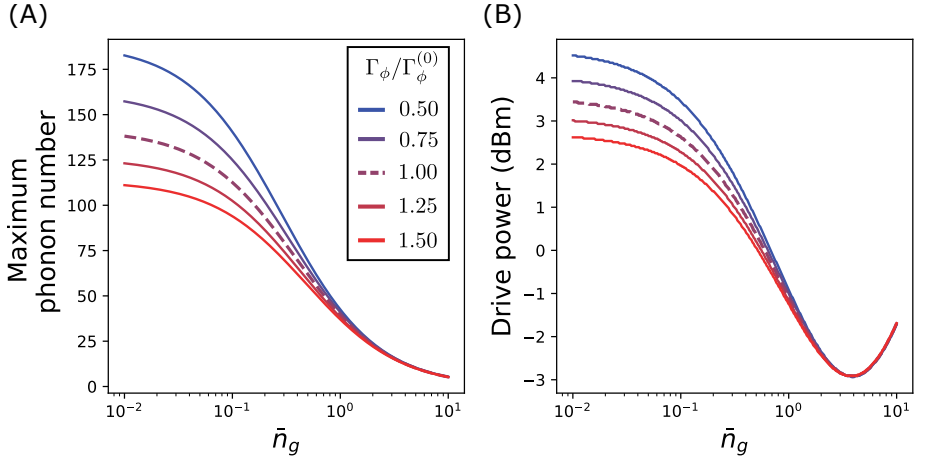

Figure 5.9: Mean Field analysis of the phonon laser (A) Maximum achievable steady state phonon number as a function of the readout resonator ground state occupancy $\bar{n}_g$. (B) Qubit drive power required for achieving maximum phonon occupancy as a function of the readout resonator ground state occupancy $\bar{n}_g$. Both plots show results for different values of the intrinsic qubit dephasing Γ_ϕ, varying from 0.5 $\Gamma_\phi^{(0)}$ to 1.5 $\Gamma_\phi^{(0)}$, where $\Gamma_\phi^{(0)}$ is the value given in Table 5.1. The dashed lines depict the result for the parameters of the experiment. All other parameters used are in Table 5.1.

All research data and code supporting the findings described in this thesis are available in 4TU.Centre for Research Data at **doi: 10.4121**

6

Bogoluibov ghost modes of a strongly-driven superconducting transmon qubit

Science is a way of thinking,
much more than it is a body of knowledge

Carl Sagan

Superconducting qubits are strong nonlinear systems which play a crucial role in research fields like circuit QED and quantum computing. In most applications and experiments qubits are weakly driven to prevent effects like power broadening, which leaves the strongly driven regime rather unexplored. Here, we present a phenomenological study on two-tone spectroscopy measured qubits that are strongly driven with a third (pump) tone. We demonstrate the emergence of subharmonic parametric excitations of the qubit 01 manifold by using two strong drive tones. Increasing the pump power further we observe the appearance of ghost modes that are symmetrically mirrored images of the normal qubit excitations around the pump tone. Using quantum acoustics we probe the nature of the ghost modes and show these do not interact with real systems occupying the same frequency space, suggesting a truth to the statement "you can't touch a ghost".

This chapter is being prepared for publication as *Bogoluibov ghost modes of a strongly-driven superconducting transmon qubit*. **W.J.M. Franse**, & G.A. Steele

6.1. Introduction

The AC-stark effect [219, 226] is a tool used in cQED [24–26] to increasingly shift the resonance frequency of nonlinear superconducting circuits as a function of power (i.e. increasingly large signal amplitudes). The frequency shift of these nonlinear systems is accomplished by introducing an additional separate drive tone, which we here refer to as the Stark tone. The AC Stark shift for the first energy transition $|0\rangle \leftrightarrow |1\rangle$ has been observed and analytically well-defined for multi-level superconducting circuits for both weak [227], and strong [159] anharmonic systems. From literature, we also know that the resonance frequency for nonlinear circuits with strong anharmonicity [159, 160], e.g. qubits, shifts away from the Stark tone, while for weak anharmonic systems [228] (e.g. Kerr nonlinear oscillators, or Duffing oscillators, Duffing (Kerr) oscillator [229]) it always shifts down in frequency independent of the Stark tone frequency. More recently [230–233] a rather peculiar feature of weak anharmonic oscillators has been observed when a fixed (few MHz) detuned pump tone strongly drives the circuit. When strongly driving the system [230, 234, 235], the bare resonance frequency of the cavity (called the signal mode) gets an additional idler mode with net output gain starts to appear. The signal and idler mode are symmetrically spaced around the pump tone, and frequency shift in opposite direction and away from the pump tone for increasing pump power. For strong resonantly driven nanomechanical (Duffing) resonator [236, 237], similar symmetrically located peaks (signal and idler mode) on opposite sides of the driving frequency were observed. The idler mode can also be viewed as an effective negative mass mode [233] having an inversion of dynamical backaction and sideband-cools [96] a coupled low-frequency circuit by a blue-detuned pump field, which can be explained by the inverted energy ladder of a negative mass oscillator.

In the field of cavity polaritons, a similar phenomenon has been observed, which is referred to, in that field, as Bogoliubov "ghost" modes. Observations of ghost modes (or ghost branches) have been reported in a variety of fields such as ultracold atom experiments [238], polariton quantum fluids both resonant [239–242], and nonresonant [243] pump-probe experiments, (non) resonantly excited cavity excitons-polaritons in planar semiconductor microcavities [244–247]. Ghost modes (branches) are described as negative-energy (effective mass [233]) modes that are mirror images of Bogoliubov excitations symmetrical spaced around a pump tone. Due to four-wave mixing (FWM) (i.e. parametric scattering) processes (as described in [239]), the Bogoliubov excitations are directly seeded onto the ghost branch. Here, the ghost mode corresponds to emitted photons associated with real Bogoliubov excitations in polariton systems (related to a photoluminescence process [247]). This then raises the following questions: how much of this physics also exists in qubits, the ultimate limit of a very strong nonlinear oscillator? Are phenomena still present in a system with large anharmonicity (larger than the linewidth $\alpha \gg \kappa$), such as a transmon qubit?

In this work, we explore the phenomena of ghost modes in a transmon qubit [22] with an anharmonicity several times larger than its linewidth [36]. We start by performing two-tone spectroscopy on our transmon qubit, which is dispersively coupled to a readout resonator. By adding a third (Stark) tone several MHz detuned from our transmon's 01-transition frequency, we are able to perform red and blue detuned AC Stark shift. Subsequently, we explore the qubit's response to increasing both the qubit drive and Stark tone power. We show that for sufficiently high qubit drive powers, P_d, and increasing Stark drive power, P_s, not only does the qubit's 01-transition AC Stark shifts but a ghost mode appear symmetrically mirrored around

the Stark drive tone. When increasing either qubit or Stark drive tone even further, we observe multiphoton subharmonic parametric excitation of the qubit 01 manifold and their ghost mode equivalent. Lastly, we probe the nature of a ghost mode by using quantum acoustics, an acoustic equivalent to cQED. With the help of a HBAR we show that the ghost mode has no interaction with expected phononic modes occupying the same frequency space as the ghost mode. Rather, we discovered that the phononic modes found within a ghost mode are a mirage of the normal phononic modes mirrored around the Stark drive tone.

6.2. DEVICE AND DRIVING

We have fabricated a single 10 × 10 mm silicon chip containing a feedline to which we frequency multiplex several devices. The devices consist of a double island pocket transmon capacitively coupled to a coplanar waveguide. The transmon qubits were fabricated from niobium-titanium nitride for the bulk structures with aluminum Josephson junctions. Fig. 6.1(a) shows a zoom-in of our measured device. The Josephson junction induces an anharmonicity $\alpha/2\pi = -260$ MHz, for which we consider the transmon to be in the strong nonlinear limit ($\alpha \gg \kappa$). In the strong anharmonicity limit, the two-level system approximation becomes a good description for our transmon. In the supplementary information 6.7.1, we discuss the differences between weak and strong anharmonic systems and their response to increasingly strong nearby drive tones. For more fabrication details, see supplementary information 6.7.2.

Once the device is mounted on the baseplate of a dilution refrigerator ($T \approx 15$ mK), we weakly probe the system from which we extract the readout resonator frequency $\omega_r/2\pi = 7.4162$ GHz and linewidth of $\gamma/2\pi = 2.074$ MHz. By performing two-tone spectroscopy, see supplementary information 6.7.3, the qubits were read out via the coplanar waveguide resonators using standard cQED techniques [64]. From fits, we extract a resonance frequency for the 01-transition $\omega_{01}/2\pi = 6.09072$ GHz with an intrinsic linewidth of $\kappa/2\pi = 420$ kHz.

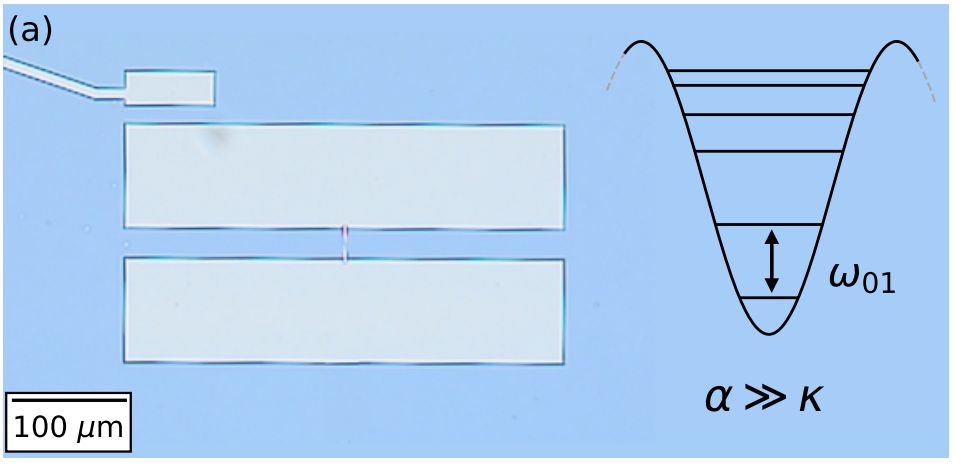

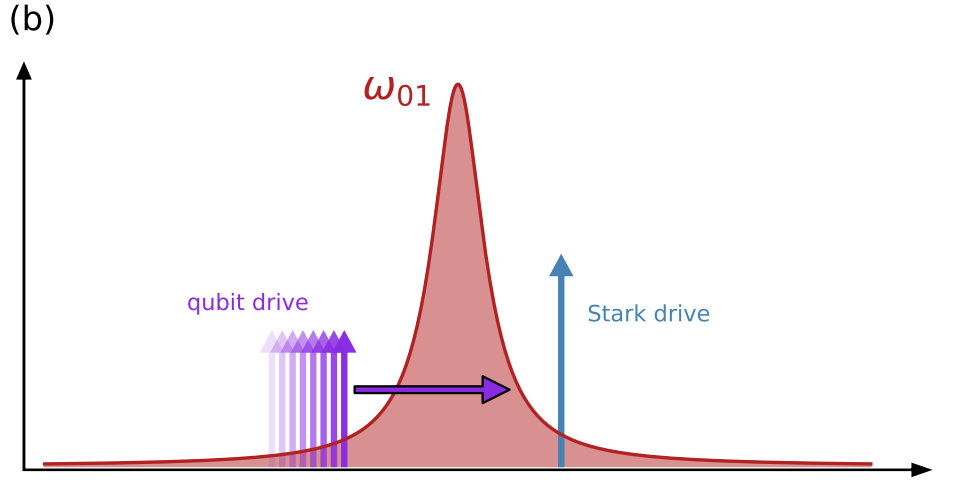

Figure 6.1: Spectroscopy of a Stark-driven transmon qubit. Panel **(a)** shows a micrograph of our device, a superconducting transmon qubit. The device consists of two NbTiN islands which are shorted by an Al/AlO_x/Al Josephson junction. One of the islands is capacitively coupled to a readout resonator (top-left). On the right, we show a schematic of the transmon's energy potential, which due to the Josephson junction and a large anharmonicity ($\alpha \gg \kappa$), has a cosine form. In our work here, we are interested in the ω_{01} energy transition. In panel **(b)**, we show a driving scheme, with which we dispersively readout our transmon in two-tone spectroscopy by sweeping the qubit drive (purple arrow) around the ω_{01} transition frequency. Here we also add a third tone, a near-resonant blue detuned Stark drive (blue arrow).

In Fig. 6.1(b), we present a driving scheme where we blue-detune a Stark drive tone from the qubit's 01-transition frequency. We measure the steady-state qubit population using the dispersive shift of the readout resonator while sweeping a qubit drive frequency for a fixed, sufficiently large drive power, P_d. Following [230], we increase the Stark drive power, P_s, to see to what degree does the same physics occurs within a qubit. In Fig. 6.2, we present data on the qubit's response when strongly driving the system. Fig. 6.2(a) shows a colormap of the

transmission magnitude $|S_{21}|$ versus qubit drive frequency and room temperature Stark drive power set at 6.3240 GHz, as indicated with dotted line.

6.3. STARK SHIFT AND GHOST MODES

We observe a resonance frequency shift of the qubit's "normal" 01-transition (peak on the left of Stark drive tone in Fig. 6.2). For increasing Stark drive power P_s, we see, as expected, a gradual frequency shift to lower frequencies, thus away from the Stark tone, which we assign to the AC Stark shift [248]. In addition to this frequency shift, we also see the emergence of an extra resonance peak. This mode is mirrored around the Stark drive tone and equally distant from it as the 01-transition. This new mode, which we now refer to as ghost mode, shifts towards higher frequencies opposite to the "normal" 01-transition for increasing Stark drive power. In addition, the ghost mode also increases signal response. In contrast to [230, 233], the ghost mode has a positive sign, similar to the "normal" 01-transition; the reason for this is that here we are not measuring the $|S_{21}|$ response of a circuit but rather the dispersive readout of the qubit occupation $\langle\hat{\sigma}_z\rangle$, in contrast to earlier work [230] probing the oscillator susceptibility via coupling directly to an external feedline.

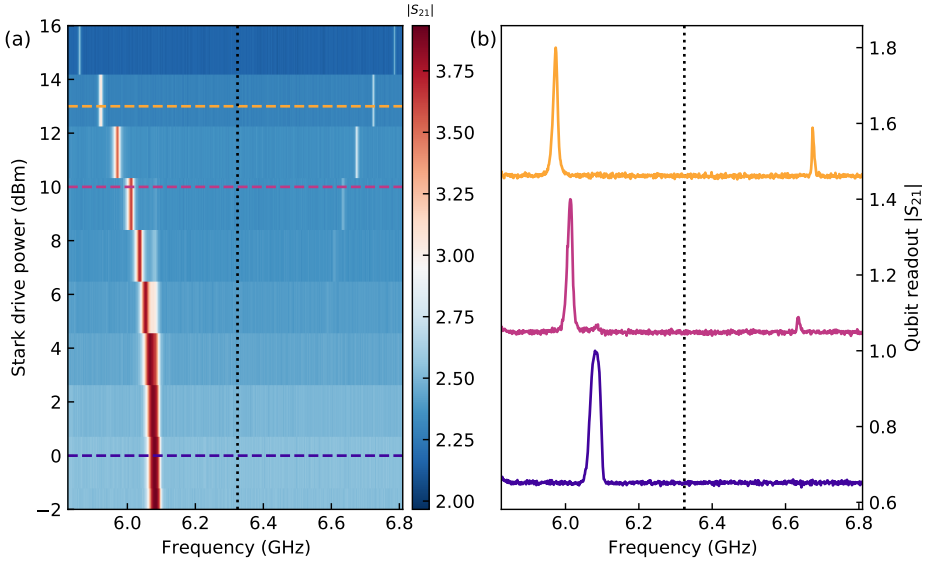

Figure 6.2: AC Stark shift of qubit's 01-transition and its ghost modes. A Stark drive tone is applied near the qubit's 01-transition (ω_{01} = 6.09072 GHz), at 6.32405 GHz and is indicated with a black dotted line in both panels. Panel **(a)** shows the dispersive readout of the qubit via a readout resonator (f_r = 7.4162 GHz, P_r = -10 dBm) for fixed qubit drive power (P_q = +2 dBm). Here, the drive frequency is swept from 5.85 to 6.75 GHz for increasing Stark drive power, P_s, from -2 to +16 dBm. We observe both an AC Stark shifted qubit 01-mode away from the Stark drive tone as well as the appearance of a ghost mode. In panel **(b)**, we show line cuts (from top to bottom) at Stark drive power of 13, 10 and 0 dBm. The line cuts are offset manually by +0.4 each, with the lowest curve being unshifted. For the 10 and 13 dBm line cuts, we see that ghost modes appear equally distanced from the Stark drive tone as the qubit 01-mode is.

Although we only show the +233 MHz blue detuned data in Fig. 6.2 we have seen similar results for both red and blue Stark tones that were ±30 MHz detuned away from the qubit 01-transition. This was done for a range of qubit drive powers, where the "normal" 01-transition always moves away from the Stark tone and an additional ("red" or "blue") ghost modes appear on the opposite side. The keen-eyed observer might have noticed already in Fig. 6.2(a) that from the "normal" 01-transition, an extra line appears (seen as an extra peak for $P_s = 10$ dBm in (b), set power on equipment at room temperature). This extra excitation was not observed before in the Duffing (Kerr) oscillator from [230]. However, since the transmon qubit has a larger nonlinearity than the Duffing oscillator, we expect this to correspond with some strong nonlinear process. See supplementary information 6.7.4 for extra data plots. In Fig. 6.3, we take a closer look where we run the same measurement with a higher resolution in both qubit drive frequency and Stark drive power. For a more clear image, we brought the Stark drive tone closer to the 01-transition frequency (6.3240 ⟶ 6.12072 GHz).

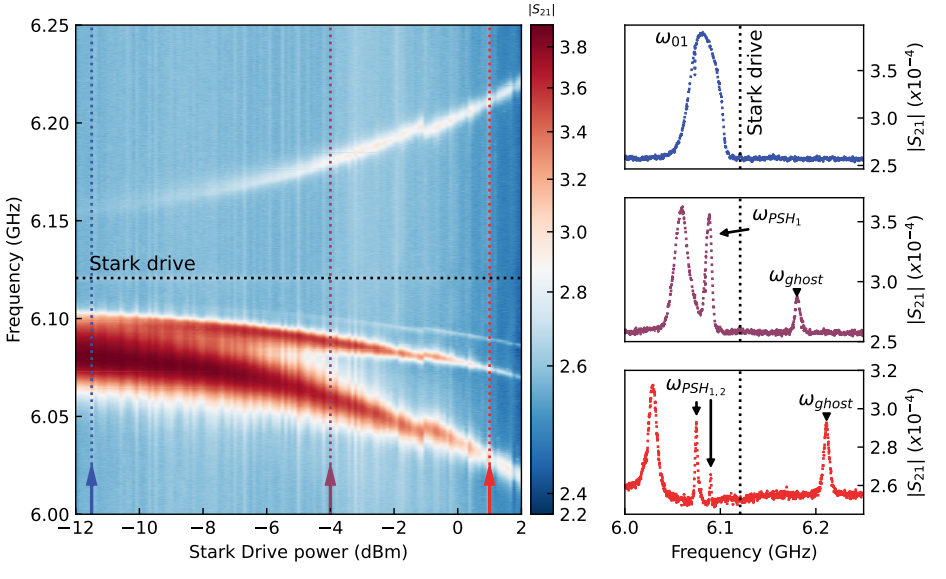

Figure 6.3: Subharmonic parametric excitation of the qubit 01 manifold. Left panel: Zoom in colorplot of qubit's 01-transition, ω_{01}, when applying a fixed frequency Stark tone, which is blue (+30 MHz) detuned from the qubit and increases in power. Here, the qubit drive power is set constant at P_q = +2 dBm while sweeping the qubit drive frequency when dispersively reading out the readout resonator. The same settings as shown in the right panel of Fig. 6.2. Colored line cuts on the right side panels correspond with the colored arrows/dashed lines of the left panel. From top to bottom, the used Stark drive powers are -11.5, -4 and 1 dBm. Line cuts show that when the Stark drive power is increased, not only does the main qubit 01-transition gets shifted and a ghost mode appears (mirrored symmetrically around the Stark drive power), but also multiple parametric subharmonic excitation lines appear as well. Note: we observed similar excitations for a 6.3240 GHz Stark tone.

6.4. FINE STRUCTURE AND ITS GHOST MODE EQUIVALENT

In Fig. 6.3, we observed a fine structure only at the "normal" qubit 01-transition side. For increasing Stark drive power and fixed qubit drive power $P_q = +2$ dBm, we see the appearance of two addition excitations. We refer to these as subharmonic parametric excitation of the qubit 01 manifold in the rotating frame and naively describe this as: $\omega_{PSH,n} = \omega_{01} - \frac{\omega_{01}-\omega_s}{n}$. Here, $\omega_{PSH,n}$ is the n^{th} subharmonic parametric exicitation of the Stark shifted 01-transition ω_{01} compared with the Stark tone, ω_s. Seemingly ω_{01} starts to split off around $P_s = -10$ dBm, an effective two-photon excitation of the qubit in a dressed rotating frame. For further increasing Stark drive power, we see a second thin excitation line appear: three-photon excitation. These are somehow in a rotating frame referenced to a new zero associated with the frequency of the Stark drive. Evidently, this phenomenon is associated with both the strong qubit drive and strong Stark drive power. If this is a nonlinear process in the rotating frame, then this should be a culmination of both the drive power of the qubit and the Stark drive power. To explore this further and see how sensitive this phenomenon is to the qubit drive power, we now set the Stark drive power to a fixed value ($P_s = -10.5$ dBm) and increase the qubit drive power (going from $P_s = -10$ to +12 dBm). Doing that, see Fig. 6.4; more subharmonics start to emerge for increasing qubit drive power.

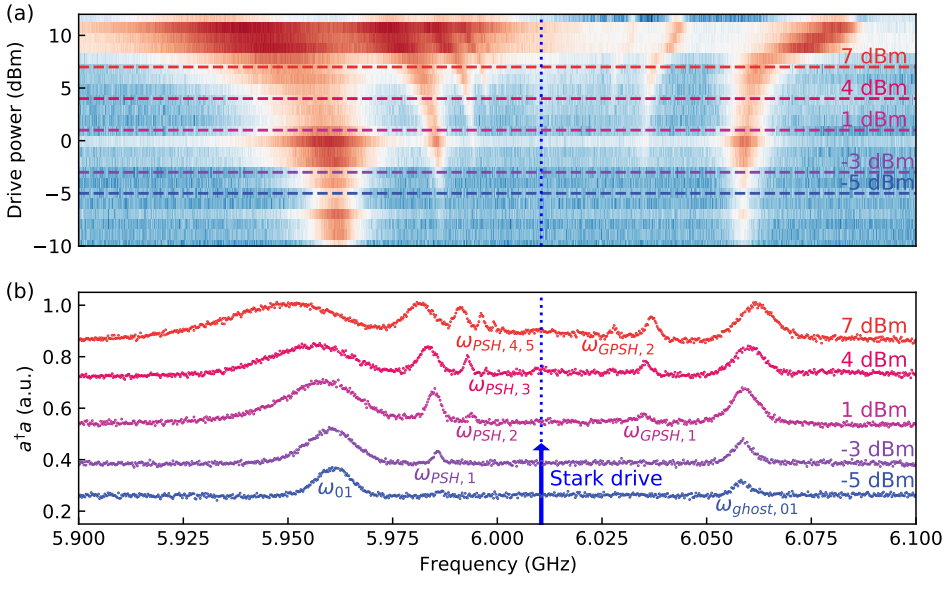

Figure 6.4: Multiphoton subharmonic excitation of the Bogoliubov modes up to fifth order in the rotating frame of the strong drive tone. Top panel: colorplot of qubit's 01-transition, ω_{01}, parametric subharmonics and their ghost mode equivalent. Fixed Stark tone frequency (6.12072 GHz) and power (P_s = -10.5 dBm) is applied while sweeping qubit drive frequency and drive power while dispersively read out the qubit. Colored dashed lines correspond to colored line cuts of the bottom panel. From top to bottom, the qubit drive powers are +7, +4, +1, -3 and -5 dBm. In the bottom panel, each line cut is up-shifted by 0.35 for clarity. Line cuts show that for increasing qubit drive power, the 01-transition, ω_{01}, shifts down in frequency, and power broadens. The first ghost mode, $\omega_{ghost,01}$, also increases in height, power broadens and shifts equally as ω_{01} does. When increasing the qubit drive power further, we see the appearance of multiple parametric subharmonic resonances $\omega_{PSH,1-5}$, and their ghost variants $\omega_{GPSH,1-3}$.

Even more strikingly, not only do these subharmonics emerge on the "normal" qubit 01-transition side, they also start appearing on the ghost mode side and for sufficiently large qubit drive powers, they all start to AC Stark shift. Note that in Fig. 6.4(b) we observe power broadening not only in the "normal" 01-transition but all other subharmonic excitations (both ghost and normal modes). Clearly, the other difference between qubits and Kerr oscillators is now that the stronger nonlinearity allows a culmination of strong Stark and strong qubit driving to generate multiphoton transitions in this rotating frame. This now raises the question: How should we think about these (subharmonic) ghost modes and how "real" are they? The data seems to suggest that, just like [230, 233], the transitions mirrored around the Stark pump are an artifact of FWM. Therefore, we should view the ghost modes, like in the field of polaritons [247], not as "real" excitations of the system.

6.5. Probing the ghost mode using quantum acoustics

So far in this chapter, we have not yet discussed the fact that our transmon qubit is also piezoelectrically coupled to a High-overtone Bulk Acoustic Resonator (HBAR) [1]. The HBAR-transmon device, as previously published in [36], consists of a 650 μm thick sapphire substrate with a $\sim$ 900 nm aluminum nitride piezoelectric layer flipped on top of the transmon qubit, see Fig. 6.5(a). By actuating the piezoelectric, we are able to generate standing acoustic longitudinal waves [2] with a free spectral range (FSR) of 8.538 MHz. This periodic spacing, as shown in Fig. 6.5(b) with the red dotted lines, gives us the opportunity to let the ghost modes interact with "real" acoustic modes occupying the same frequency space. Using the HBAR, we can determine if the ghost modes are something that exists in physical real space or are merely mirages driven by nonlinear physics. Fig. 6.5(c) shows that the ghost mode has an Acoustically Induced Transparency (AIT, see Ch. 5) window, which should represent an interaction with the HBAR. However, with the HBAR spectrum, we predicted that acoustic resonances should occur at 6.055755 and 6.064285 GHz, while Fig. 6.5(c) shows an AIT window (dip) at 6.062215 GHz, which misses both acoustic modes.

[1] The measurements presented so far were performed on HBAR-transmon devices, but were also observed in similar transmon qubits without HBARs.

[2] Longitudinal waves propagate into the bulk of the sapphire substrate and are also called Bulk Acoustic Waves, i.e. BAWs

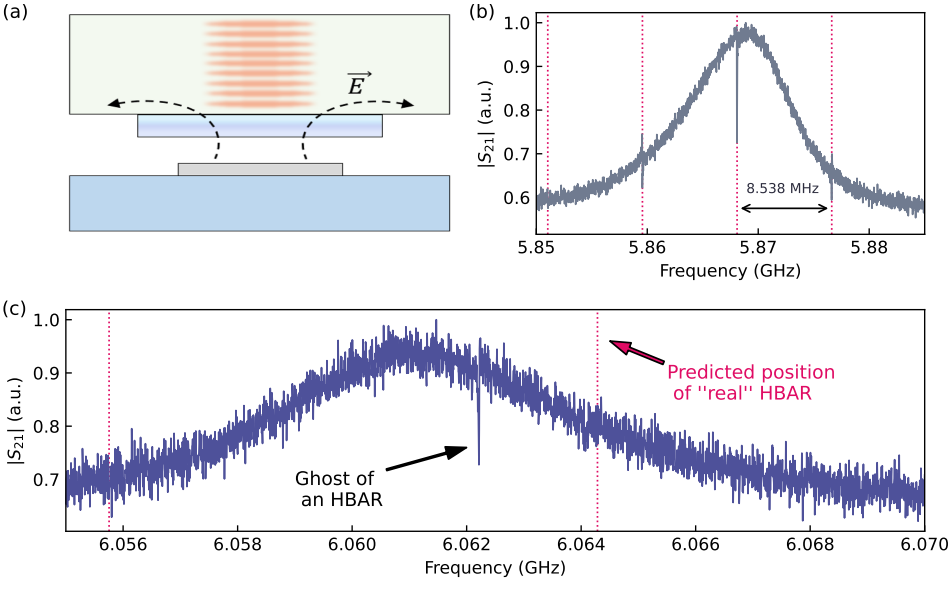

Figure 6.5: Probing the nature of a ghost mode resonance using quantum acoustics. (a) Schematic side view of the device. The transmon qubit (grey) emits an alternating electric field, $\vec{E}$, that actuates the piezoelectric element (AlN, purple/blue gradient), which in turn generates a standing wave (light orange ellipses) in the sapphire substrate (light green). (b) Dispersive readout of our transmon qubit (real ω_{01}) wherein three transparency windows are visible at 5.859565, 5.868095 and 5.876625 GHz where our transmon couples to the HBAR. Here it is also visible that the distance between consecutive HBARs (free spectral range, FSR) is $\sim$ 8.538 MHz. Here the 'real' HBAR frequency places are represented by red dotted lines. (c) Dispersive readout of our transmon qubit at $\omega_{\text{ghost},01}$. The data shows one HBAR within the $\omega_{\text{ghost},01}$ which misses the predicted "real" HBAR at 6.055755 and 6.064285 GHz.

In Fig. 6.5(c) we set the Stark drive tone at 6.01207 GHz with a power of -10.5 dBm, qubit drive power at -2.57 dBm and probed the readout resonator with a -20 dBm continuous wave tone at 7.0654 GHz. The ghost mode of an HBAR at 6.062215 GHz not only misses the "real" acoustic modes but, as it turns out, is a perfect mirror image symmetric around the Stark drive tone from a "real" acoustic mode measured at 5.96193 GHz (not shown in the data above). Moreover, picking out a certain set of Stark drive frequencies and Stark drive power gives us the ability to shift the ghost mode resonance frequency and the acoustic resonance window within for which additional data is presented in the supplementary information 6.7.5. This result suggests that the ghost modes do not interact with "real" acoustic modes occupying the same frequency space but rather show a mirage of an AIT in the "normal" 01-transition. Further research is needed to better understand these experimental results, wherein numerical calculations or theoretical derivations would be helpful in identifying the physics of why the "real" acoustic modes do not interact with our qubit Bogoluibov "ghost" modes.

6.6. Conclusion and outlook

In this work, we have presented a dispersively coupled transmon qubit which we measured using two-tone spectroscopy. By adding a third driving tone (Stark tone) we not only demonstrated that our strong nonlinear system AC Stark shifts, but also revealed the appearance of an additional mode: the ghost mode. Upon further increasing the qubit drive power, along with the increasingly strong Stark drive power, we have shown multiple subharmonic parametric excitations of the qubit 01 manifold in both the "normal" and ghost side symmetrically mirrored around the Stark drive tone. Lastly, we have probed the nature of a ghost mode using quantum acoustics with an HBAR. By selecting a specific combination of Stark drive frequency and power, we have demonstrated that the measured AIT resonance in the ghost mode does not correspond with predicted acoustic modes of the HBAR but that it is rather a mirage of a real acoustic mode in the "normal" 01-transition of the qubit.

Our findings imply that ghost modes, and their subharmonic excitations, are a result of interesting and unexplored nonlinear dynamics in strong anharmonic qubits. The nonlinear quantum physics associated with the strong driving regime of these devices showed that one should be careful with too literal interpretation of ghost modes. We do not yet fully understand why the qubit 01-transition sharpens while the ghost modes emerge for increasing Stark drive tone. For this, further theoretical exploration and numerical calculations would be needed to better understand these experimental results. Treating ghost modes as mirages of "normal" qubit transitions could be an unutilized resource in quantum sensing and quantum applications of qubits. Additional research is needed to explore the application and usage of ghost modes further.

6.7. Supplementary Information

6.7.1. Difference between Kerr-oscillator and qubit

Although both the qubit and the Kerr (Duffing) oscillator are nonlinear systems, they frequency shift differently upon driving the system.

- The strong anharmonic **Qubits**, as depicted in Fig. 6.6.(c,d), always moves away from the applied pump tone for increasing pump strength. As explained in [64, 159], for strong off-resonant driving of a qubit the AC-Stark shift (along with the Lamb shift, or even Bloch-Siegert shift [248]) frequency shifts the bare qubit frequency for increasing number of photons entering the system. For which the number of photons is proportional to the applied power of a continuous wave. The AC-Stark shift term in the Hamiltonina of [64] is described as $\frac{2g^2}{\Delta}\hat{a}^\dagger\hat{a}$, for which g is the coupling rate between readout resonator and qubit, $\hat{a}^{(\dagger)}$ are the annihilation (creation) operators of the qubit, and $\Delta = \omega_q - \omega_s$ is the difference between qubit and, respectively, Stark tone frequency. From this we can already see that for different Stark tones and same bare qubit frequencies the AC-Stark shift term can become negative and shifts to the opposite direction.

- For weak **Kerr/Duffing oscillators**, which is explained in detail in Ch. 2.4 of [249], the frequency shift scales with the negative anharmonicity times the number of photons. As depicted in Fig. 6.6.(a,b) the Duffing oscillator always shifts down in frequency independent of the pump frequency. For weak anharmonic superconducting circuits the

nonlinear element, the Josephson junction, "creates" a negative anharmonicity factor $\beta < 0$, which is responsible for the Kerr shifting of the resonance frequency.

- Even for the **Readout resonator** coupled to the transmon qubit, which becomes weakly anharmonic due to hybridization, we saw that for extremely large driving powers it AC Stark shifts. Like weakly anharmonic Duffing/Kerr oscillators the readout resonator always shifts down in frequency independent of Stark tone placement (even when far detuned). Data not shown in this work.

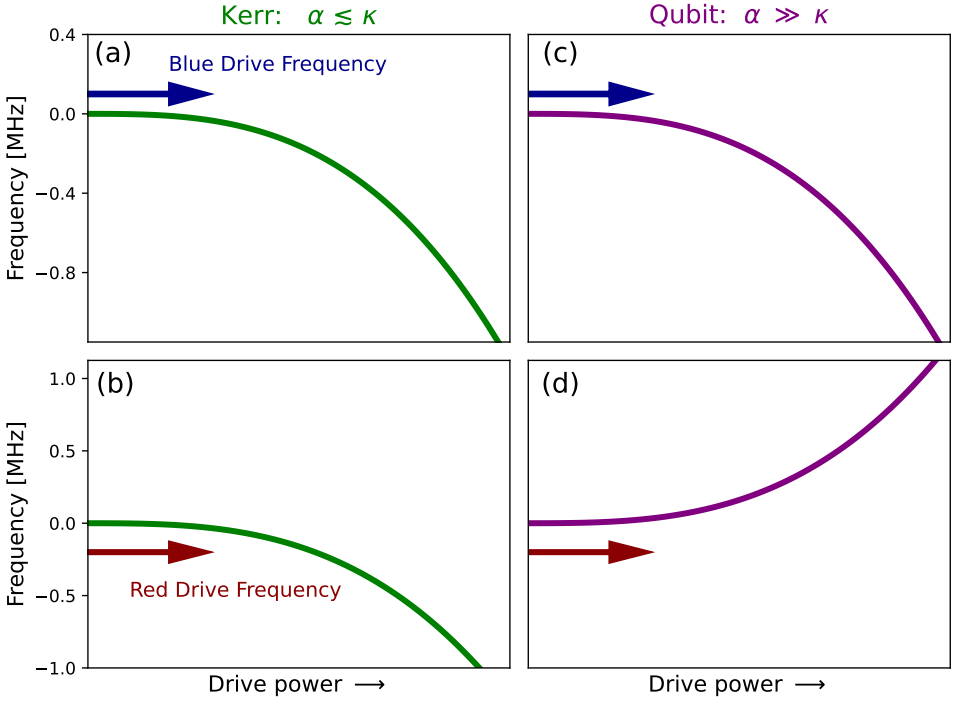

Figure 6.6: Frequency detuning of a Kerr nonlinear oscillator and Qubit using fix frequency pump tone. (a,b) Relatively low drive powers detune a weak anharmonic Kerr nonlinear oscillator with red or, respectively, blue detuned drive tones at fixed frequencies. In both cases, the dressed cavity mode is shifted down in frequency with increasing drive power. (c,d) Driving of large anharmonic system, qubit, with red or, respectively, blue detuned drive tone. Panels (e) and (f) are adapted results from previous work [36].

6.7.2. Device Fabrication

The device fabricated for this work is the same device as presented in [36], but for completeness sake we echo the fabrication process here as well.

Qubit Chip

The device fabrication starts with a 10x10mm chip 525 μm thick high resistivity $\langle 100 \rangle$ silicon deposited with 100 nm of Niobium Titanium Nitride (NbTiN). The NbTiN film was deposited by the Dutch Institute for Space Research (SRON) following the process described in [103]. A layer of photoresist (AR-P 6200.18, 4000 rpm) was patterned, exposed (EBPG 5200, 315 μm/cm^2) and developed (Pentylacetate, O-xylene, IPA) to form the bulk circuitry (transmon islands and coplanar waveguides). The exposed NbTiN was removed using a reactive ion etch (Sentech Etchlab 200, 13.5 sccm SF_6 + 5 sccm O_2, 55 W, 10 μbar) followed by an in-situ oxygen descum (50 sccm O_2,100 W, 10 μbar). After stripping the photoresist, a bilayer resist stack (MAA 8.5% EL6, 2000 rpm and PMMA A6 950k, 1500 rpm; baked for three and five minutes at 180 C°, respectively) was used for patterning the Josephson junctions (190 nm width). The junctions were patterned using e-beam lithography. The bilayer was developed using Cold H_2O: IPA (1:3) and cleaned afterwards with IPA. After cleaning the exposed silicon surface with an oxygen descum (200 sccm, 100 W) and acid clean (BoE(7:1):H_2O, 1:1), the chip was placed in an aluminum evaporator (Plassys MEB550). Double-angle shadow evaporation with intermediate in-situ oxidation was used to create Manhattan-style junctions. The aluminum was evaporated at a 35° angle relative to the substrate at a rotational angle of 0° and 90°. The top and bottom electrodes were 35 and 75 nm thick, respectively. After the first evaporation step, the aluminum was oxidized to create the AlO_x tunnel barriers. Following the second evaporation step, a second oxidation step was performed to cap the junctions with a passivation layer. After performing liftoff in NMP, the qubit chip was finished. Fig. 6.7 below shows a detailed depiction of the process just described.

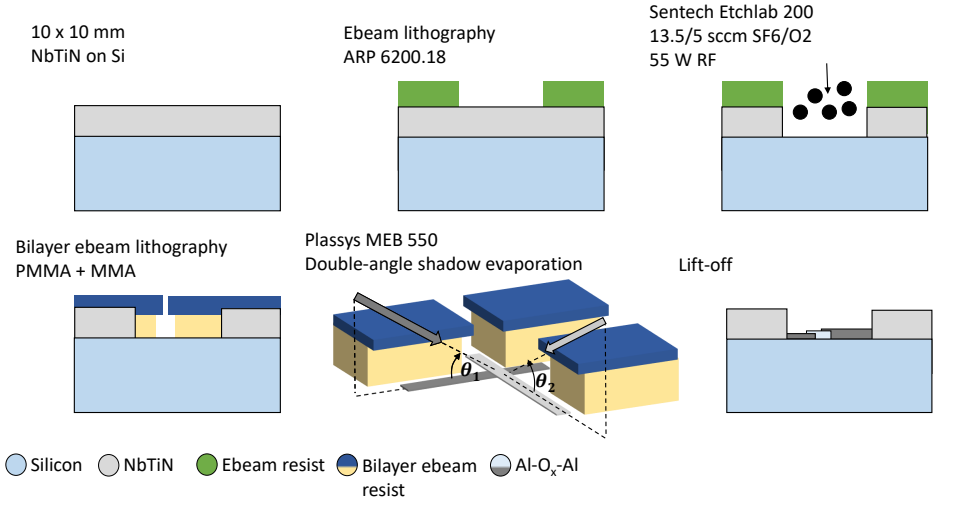

Figure 6.7: Fabrication transmon chip. Drawings show a step-by-step process for fabricating our 2D transmon qubits. Not to scale.

HBAR Chip

The HBAR chip started with double-side polished four-inch sapphire wafers with a 1 μm thick film of c-axis oriented AlN (Kyma technologies, AT.U.100.1000.B). The wafer was diced into 10x10mm chips for easier processing. A photoresist layer (AR-N 4450.10, 6000 rpm) was used to pattern circular regions to mask the AlN. A reactive ion etch in an Oxford 100 was performed to create AlN disks ($Cl_2/BCl_3/Ar$ at 4.0/26.0/10.0 sccm, 350 W ICP power, 70 W RF power). Following the reactive ion etch, the AlN layer has the proper shape but not the correct thickness. After stripping the photoresist, the chip was placed again inside the etcher to etch the AlN to $\sim$ 900 nm thickness. Fig. 6.8 below shows the step-by-step process.

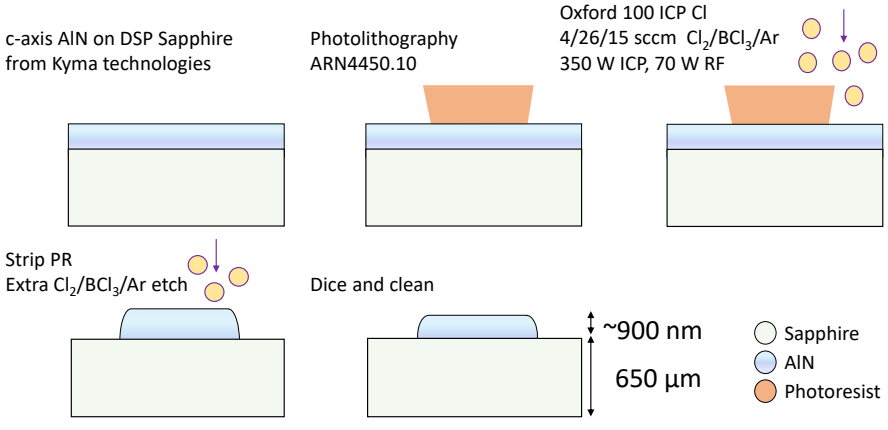

Figure 6.8: Fabrication HBAR. Drawings show step-by-step fabrication for our HBAR chip. Not to scale.

Flip Chip

Once fabrication on both chips was done, we diced the HBAR chip into 8x2 mm chips. The HBAR chip was then flipped on top of the qubit chip with the AlN layer facing down. Using probe needles, the AlN disks were aligned with the transmon antennas. Once aligned, the probe needles held down the chips in position while a tapered fiber was used to apply two-component epoxy (Loctite EA 3430) on the sides of the top chip. After the epoxy was cured, the chip was wire-bonded and installed onto the baseplate of the dilution refrigerator.

6.7.3. Measurement Setup

All measurements were performed within a dilution refrigerator (Triton 200-10 Cryofree dilution refrigerator system) operating at a base temperature $T \sim 20$ mK. A schematic of the dilution refrigerator setup and the room-temperature electronics are shown in Fig. 6.9.(A). The device was mounted on the mixing chamber (MC) plate of the dilution refrigerator and connected to a set of coaxial cables. We measured the device in transmission, with the readout resonators side coupled ('notch'-style) to a feedline. The output signals went into a cryogenic HEMT (High Electron Mobility Transistor) amplifier, followed by additional room-temperature amplification (Miteq AFS3-04000800-07-10P-4). The input line was attenuated at each stage to reduce electron temperature and thermal radiation at the input port of our device, with a total of 48 dB of attenuation.

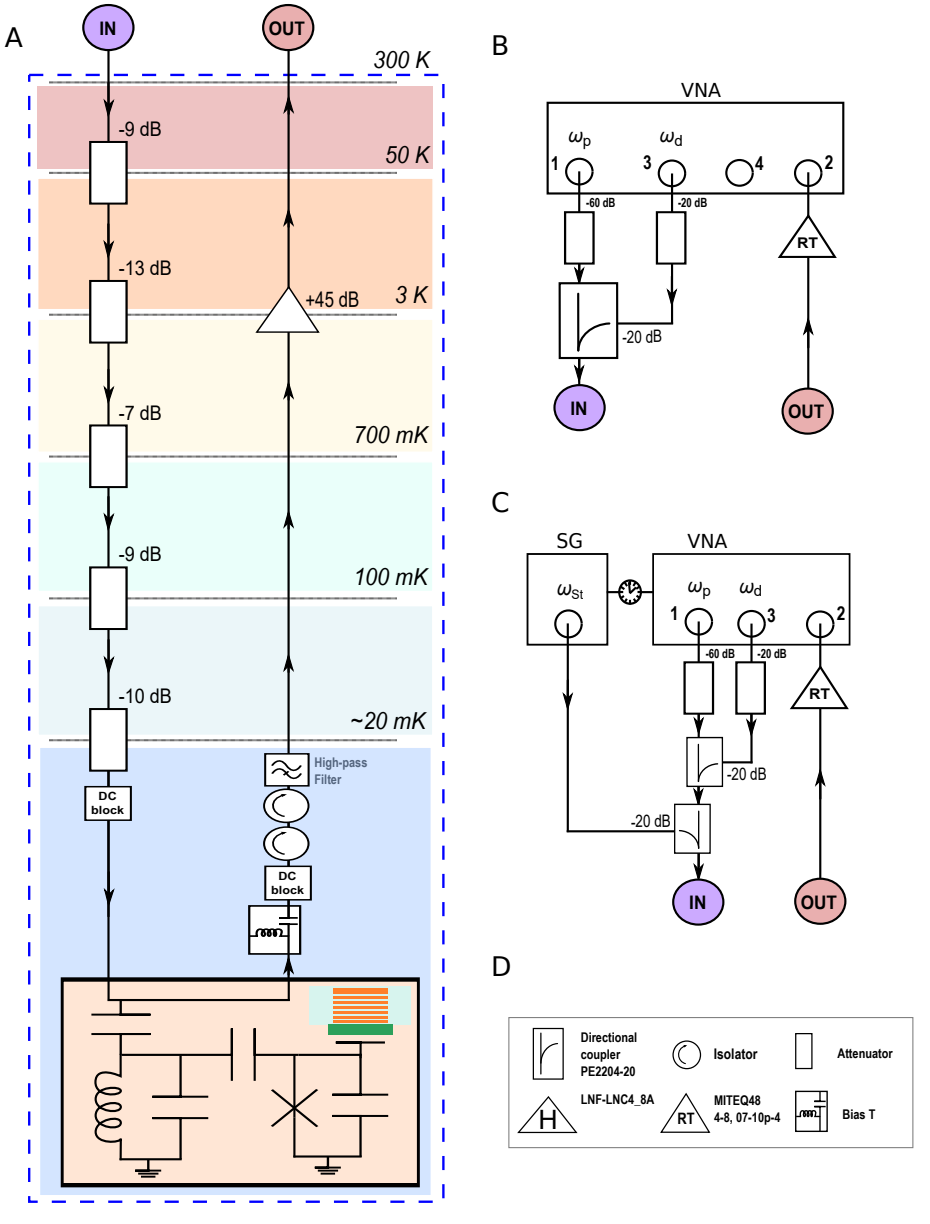

Figure 6.9: Schematic of the measurement setup. To the left **(A)** is the wiring setup inside the Triton 200-10 Cryofree dilution refrigerator system. Outside the Triton, we used two different setups. In **(B)**, we show our Two-tone spectroscopy configuration used for qubit spectroscopy. Here, we sent a weak continuous wave tone (readout resonator probe) from the vector network analyzer (VNA) port 1 and a second continuous wave tone (qubit drive) from the VNA port 3. These two signals are combined by using a directional coupler before entering the dilution refrigerator. The signal from the dilution refrigerator goes through a room-temperature amplifier before it goes to port 2 of the VNA. In **(C)**, we show our Stark drive setup. Here, we perform Two-tone spectroscopy as shown in (B), but added an extra signal generator (SG) to provide the Stark drive tone (ω_{St}). The Stark drive tone is combined with the readout resonator probe and qubit drive using a second directional coupler before entering the dilution refrigerator. **(D)** Shows a legend for all the symbols used in (A),(B), and (C)

The two-tone spectroscopy, see Fig. 6.9.(B), was measured using a vector network analyzer (VNA, Keysight PNA N5222A, 10 MHz-26.5 GHz). Port one and port three were combined using a directional coupler, with port three attached to the -20 dB coupling port. Port one was set into zero span mode and output a constant signal tuned on resonance with the readout resonator, ω_r, with an output power ranging from -30 to -10 dBm at room temperature. An additional 60 dB of attenuation was added to this signal before the directional coupler. Port 3 was used as a qubit drive tone and was swept near the qubit frequency, and its power was varied throughout the experiment. The qubit drive tone had an additional 40 dB of attenuation. The combined signals from port one and there were subsequently connected to the dilution refrigerator's input line. The output from the dilution refrigerator was directly connected to port 2 of the VNA, which was set in zero span mode at the readout resonator frequency ω_r. Two-tone spectroscopy was performed by slowly sweeping the qubit drive tone, ensuring the system has reached its steady state and monitoring the readout resonators transmission spectrum $|S_{21}|$.

In Fig. 6.9.(C) we show the AC Stark shift setup. Here, we added an additional signal generator (SG) to the setup from Fig. 6.9.(B). The Stark drive tone ω_{St} was combined with the signals coming from the VNA ports one and three using a second directional coupler. The Stark drive tone was attached to the -20 dB coupling port giving it a total of 20 dB of attenuation (expluding cables losses) before entering the dilution refrigerator. Two-tone spectroscopy was performed as discussed above with the addition of the Stark drive tone, which was set to a fixed frequency and power while performing the Two-tone measurement. Between Two-tone measurements we sweep either Stark drive power or frequency.

6.7.4. Difference blue vs red Stark shifts

In Fig. 6.10 we show two data sets for a red detuned (left panel) and blue detuned (right panel) Stark tone. In Both data sets we detuned the Stark tone ±30 MHz away from the qubit resonance frequency $\omega_q = 6.09072$ GHz. Both panels show an AC Stark shifted "normal" qubit 01 transition and the appearance of a red or, respectively, blue ghost mode. The ghost modes for both detunings are mirror symmetric around the Stark drive tone (red or blue dashed lines) which we indicate with purple arrows. A less obvious phenomenon can be observed in both detuning as well, which is the changing background. At first glance one might suggest this is amplifier saturation. However, this effect we see for multiple different Stark drive tone power and frequency settings (not shown in this work). The changing background is some readout resonator response which is different for both the blue and the red detuned Stark tone (see Sec. 6.7.6). For the red detuned Stark tone we see mode splitting in the $|S_{21}|$ response of the readout resonator while blue detuned shows squeezing. Likely, as we did not explore this effect further in this work, this effect has to do with a form of four-wave mixing between the Stark shifted ("normal" or ghost) 01-transition and an higher (unshifted) order transition of the qubit.

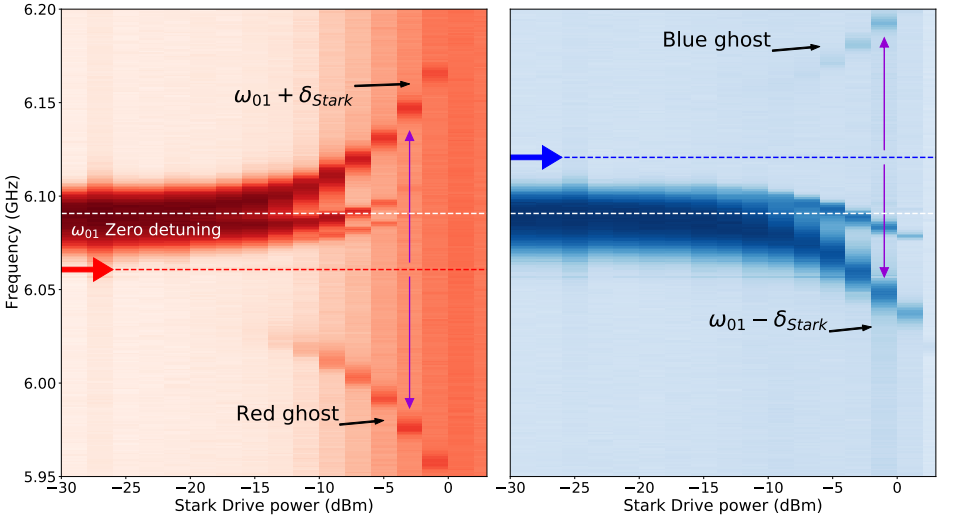

Figure 6.10: Red and blue detuned AC Stark shift of qubit's 01-transition and their ghost modes. A Stark drive tone is applied near the qubit's 01-transition ($\omega_{01} = 6.09072$ GHz), indicated with a white dashed line in both panels. The Stark tones are ±30 MHz either red (red arrow, left panel) or blue (blue arrow, right panel) detuned away from ω_{01}. The data shown here is a dispersive readout of the qubit via a readout resonator (f_r = 7.4162 GHz, P_r = -10 dBm) for fixed qubit drive power (P_q = +2 dBm). Here, the drive frequecy is sweeped from 5.95 to 6.20 GHz for increasing Stark drive power, P_s, from -30 to +3 dBm. For both data sets we see the appearance of a red (left, $P_s \geq -14$ dBm) and blue (right, $P_s \geq -8$ dBm) ghost mode, which are symmetrically mirrored from the shifted ω_{01} around the red/blue Stark drive tones (indicated with purples arrow). Both data sets also show the appearance of parametric subharmonic resonances as modes splitting off of the qubit's 01-transition.

6.7.5. Shifting ghost and HBAR modes

In Fig. 6.11 we show ghost modes of a power broadened 01-transition of the transmon qubit at 5.958 GHz for different Stark tone frequencies. The "real" qubit 01-transition has an AIT window of the acoustic mode at 5.96193 GHz. For all plots shown in the figure we used a readout resonator probe tone with zero span at 7.0654 GHz at -20 dBm while sweeping the qubit frequency from 6.055 to 6.070 GHz with a qubit drive tone at -2.57 dBm. For Stark tone frequencies of 6.0105, 6.01207, and 6.01285 GHz, all set at -10.5 dBm, we see a shift in ghost mode resonance frequency. More importantly the AIT windows inside the ghost mode are found at 6.05907, 6.062215, and, respectively, 6.063775 GHz. The shift between these ghost AIT windows is less than the HBAR's FSR of 8.538 MHz, which shows again that these are not "real" HBAR acoustic modes interacting with the ghost mode. However, the ghost mode AIT shift does correspond with double the frequency difference between consecutive Stark tones. All discussed powers above are the set powers on the equipment at room temperature.

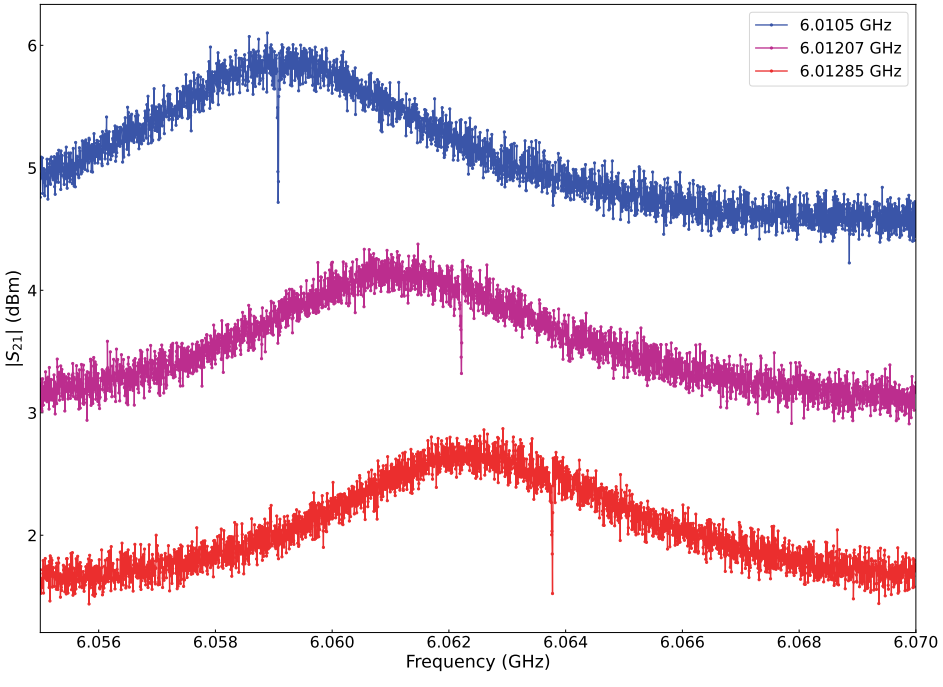

Figure 6.11: Ghost mode of the qubit 01-transition for different Stark tone frequencies. Two-tone spectroscopy data of the readout resonator (7.0654 GHz, -20 dBm) for sweeping a qubit drive tone from 6.055 to 6.070 GHz for a drive power of -2.57 dBm. From top to bottom we show ghost mode when fixing a Stark tone at frequencies 6.0105, 6.01207, and 6.01285 GHz. All measurements had a Stark drive power set at -10.5 dBm. The line cuts are offset manually by +2 each with the lowest curve being unshifted.

6.7.6. Stark shift and ghost modes of the higher excitations

In this section we showcase some of our acquired data traces of our qubit and readout resonator response on strongly driving a fixed frequency Stark tone. In Fig. 6.12 we show detailed data of the higher excitation manifold of the same qubit and setting as shown in Fig. 6.3 (blue inset of Fig. 6.12). Setting of the two-tone spectroscopy data shown below are: +2 dBm qubit drive power, Stark drive power of -20 to + 18 dBm, and Stark frequency of 6.12072 GHz.

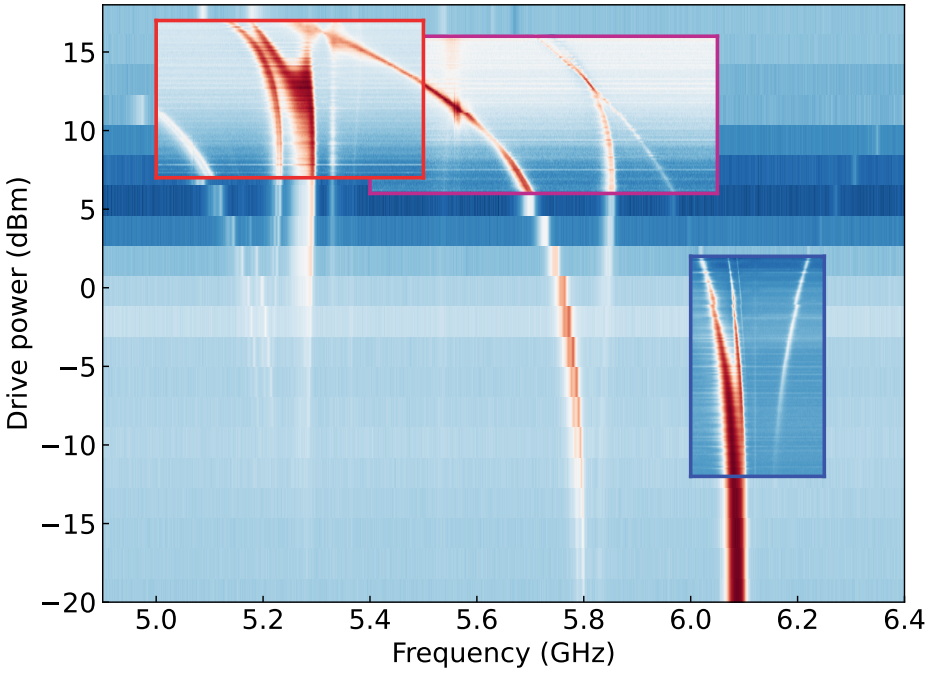

Figure 6.12: Wide detailed two-tone spectroscopy higher qubit excitations. For qubit drive power of +2dBm, sweep from 4.8 to 6.4 GHz, while sweeping a fixed frequency Stark tone (6.12072 GHz) for Stark drive power of -20 to + 18 dBm. Blue inset is same data as shown in Fig. 6.3, which shows 01-transition splitting and ghost mode of 01-transition emerging. Purple inset shows a high resolution measurement where the Stark shifted 01-transition comes into close contact with either multiphoton $\omega_{03}/3$-transition or ω_{12}-transition both starting at 5.836 GHz. Red inset shows high resolution interactions between higher qubit transition modes. More detailed figures can be found in Fig. 6.13 and Fig. 6.14. Colors corresponds to dispersively shifted $|S_{21}|$ response of the readout resonator with blue low and red high.

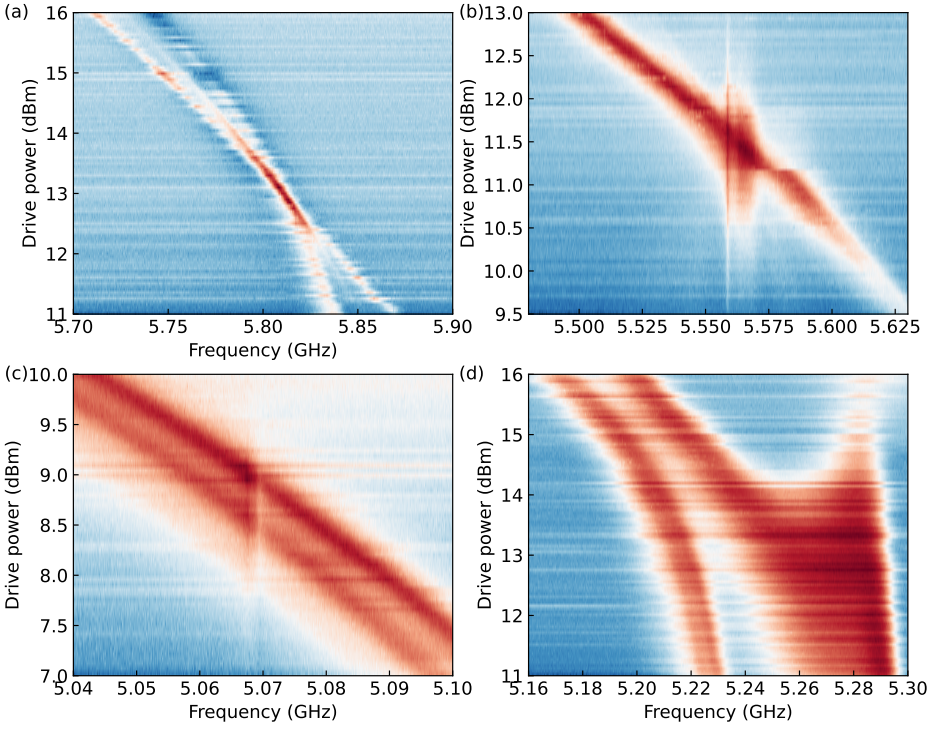

Figure 6.13: High resolution zoom in data of Fig. 6.12, I Showcase of multiple zoom for same qubit drive power (+2dBm) and Stark drive tone (6.12072 GHz sweeped between -20 and + 18 dBm). Colors corresponds to dispersively shifted $|S_{21}|$ response of the readout resonator with blue low and red high.

In Fig. 6.13 and Fig. 6.14 we show high resolution zoom in data for similar settings as shown in Fig. 6.12. As one might notice there seemingly happens a lot due to increasingly strong Stark drive powers for a sufficiently large qubit drive power. We observe, and suspect it to be, combining of qubit transitions (e.g. Fig. 6.13.(a,d) and Fig. 6.14.(a,c)), HBAR modes in the ghost branch (Fig. 6.13.(b)), and splitting/anti-crossings or even dynamical instabilities between qubit modes (e.g. Fig. 6.13.(b,c) and Fig. 6.14.(b,d)). To fully understand the influence of strong drive tones on these interactions, a quantitative follow-up study is needed, which for now is out of the scope of this phenomenological study.

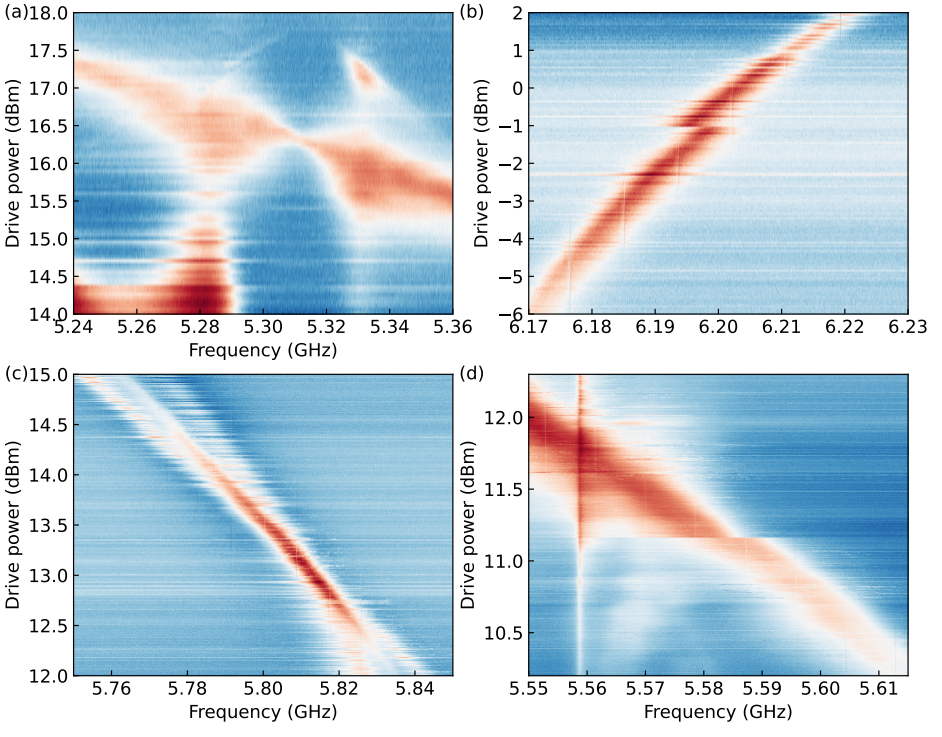

Figure 6.14: High resolution zoom in data of Fig. 6.12, II Showcase of multiple zoom for same qubit drive power (+2dBm) and Stark drive tone (6.12072 GHz sweeped between -20 and + 18 dBm). Colors corresponds to dispersively shifted $|S_{21}|$ response of the readout resonator with blue low and red high.

Next, we show multipanel figures for +30MHz blue detuned Stark tone (Fig. 6.15) and -30MHz red detuned Stark tone (Fig. 6.16). In each panel, for both figures, we performed the same Stark drive power sweep from -30 to +18 dBm for a fixed Stark drive frequency (6.12072 and, respectively, 6.06072 GHz) while sweeping the qubit drive power between panels from -25 to +18 dBm arbitrarily.

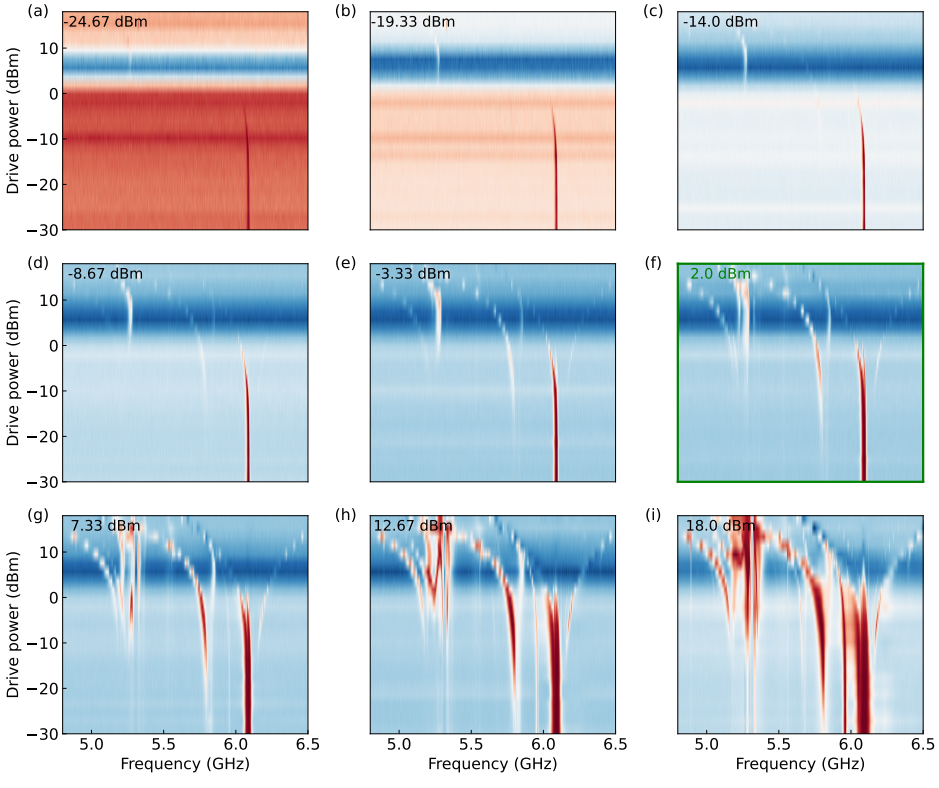

Figure 6.15: Blue detuned Stark and qubit drive power sweep. In each panel the same Stark drive power sweep from -30 to +18 dBm is performed for a fixed Stark drive frequency of 6.12072 GHz. Between panels the qubit drive power is arbitrarily increased from -25 to +18 dBm. Green inset with +2 dBm qubit drive power is the same plot as shown in Fig. 6.12. Colors corresponds to dispersively shifted $|S_{21}|$ response of the readout resonator with blue low and red high.

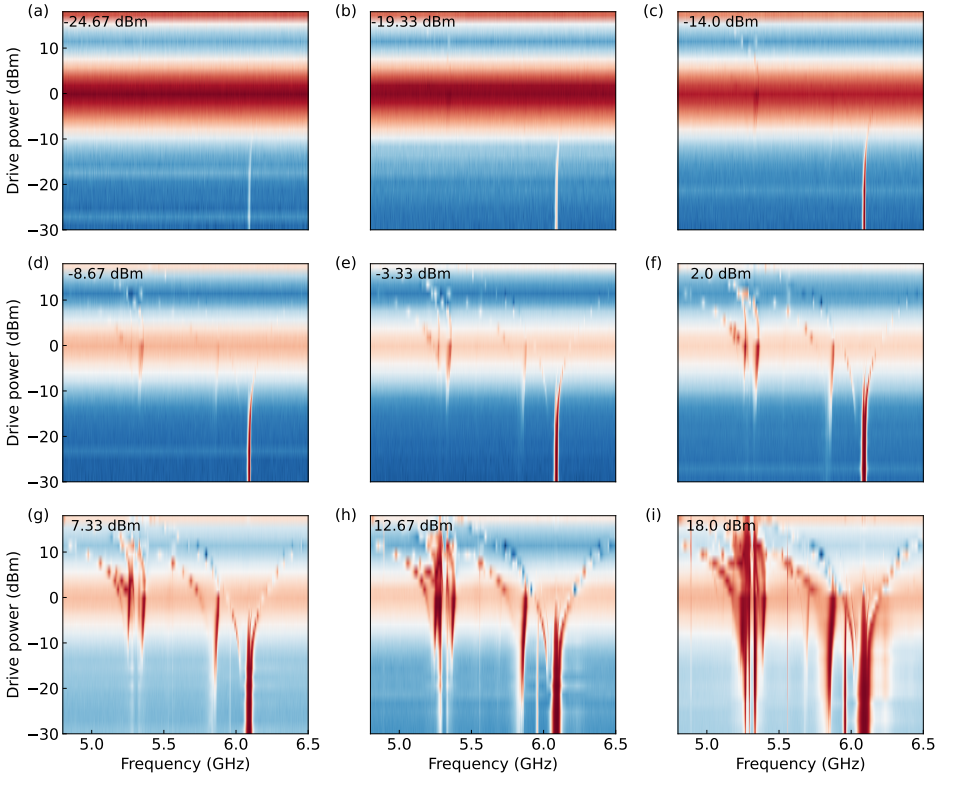

Figure 6.16: Red detuned Stark and qubit drive power sweep. In each panel the same Stark drive power sweep from -30 to +18 dBm is performed for a fixed Stark drive frequency of 6.06072 GHz. Between panels the qubit drive power is arbitrarily increased from -25 to +18 dBm. Colors corresponds to dispersively shifted $|S_{21}|$ response of the readout resonator with blue low and red high.

Both figures show that for increasing qubit drive power more higher order qubit excitations appear which seemingly interact with one another under the influence of the strong Stark drive tone. A quantitative follow-up study is needed to fully understand these interactions.

Lastly, we want to point out that in both Fig. 6.15 and Fig. 6.16 we observed a “band” in the background of the measurements around +6 dBm and, respectively, 0 dBm Stark drive power. This band does not change for increasing qubit drive power and seems to be correlated to the readout resonator and Stark drive tone. In Fig. 6.17 we show the response of the readout resonator for increasing Stark drive power of both red (6.06072 GHz, panel a) and blue (6.12072 GHz, panel b) detuned Stark drive tones. For the red detuned data we observed an anti-crossing happening, which we (for now) suspect that it has to do with the “real“ qubit ω_{12} and the ghost ω_{01} transitions getting closer to one another. This can be observed in Fig. 6.16.(g,h,i) at the 0 dBm Stark power around 5.8 GHz. For the blue detuned data we observe an level attraction which we (for now) suspect that it has to do with the “real“ qubit ω_{01} and ω_{12} transitions getting closer to one another. This can be observed in Fig. 6.15.(g,h,i) at the +6 dBm Stark power around 5.8 GHz. An intuitive explanation for this phenomenon could be

that the qubit ("real" and ghost) mode transitions have different dispersive shifts that the readout resonator experience at the same time. Once more, this is out of the scope of this phenomenological study and a full quantitative follow-up study is needed to research these interactions.

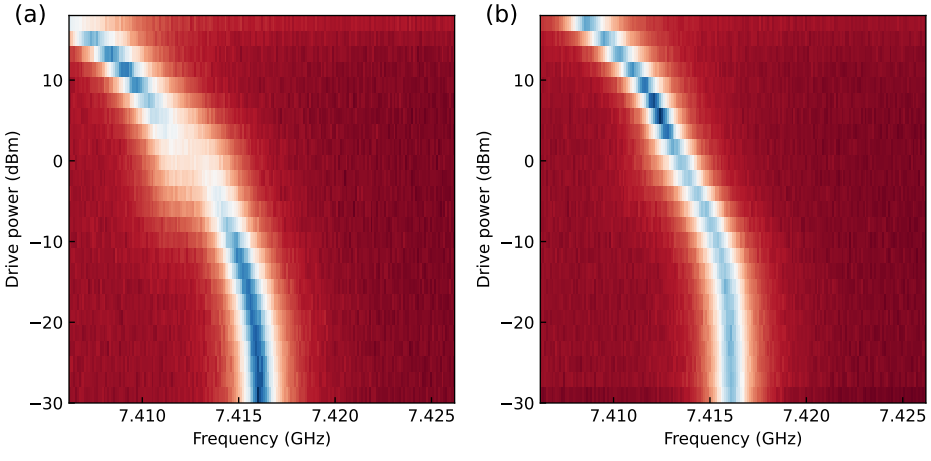

Figure 6.17: Readout resonator response on Stark drive power. Readout resonator (7.4162 GHz) is measured, using a single probe tone (-10 dBm), in transmission while increasing the Stark drive power from -30 to +18 dBm. **(a)** shows anti-crossing within the readout resonator for red detuned Stark drive tone at 6.06072 GHz while **(b)** shows level attraction within the readout resonator for blue detuned Stark tone at 6.12072 GHz. Colors corresponds to $|S_{21}|$ response of the readout resonator with blue low and red high.

All research data and code supporting the findings described in this thesis are available in 4TU.Centre for Research Data at **doi: 10.4121**

7

Conclusion

7.1. The Results of this Thesis

In this thesis, we presented experimental studies on planar superconducting transmon qubits piezoelectrically coupled to HBARs. After thorough explanations on how to design and fabricate such devices, we experimentally studied its use as a superconducting single-atom phonon laser, and used the HBAR to probe the nature of ghost modes in strongly driven qubits.

In **Chapter 4**, we presented experimental results which confirmed the realisation of an quantum-acoustic equivalent of a single-atom laser, the *single-atom phonon laser*. We made use of a single superconducting qubit to drive a coupled HBAR into a phonon lasing state. We observed the absence of a sharp lower lasing threshold and observed the characteristic upper lasing threshold. Here, gated two-tone spectroscopy showed that the qubit's ringdown was extended due to re-excitement of the phonon mode in the lasing state when qubit drive is switched off. We used master equation simulations to fully describe the system and its lasing properties. We used experiments and simulations to demonstrate a maximum phonon number of about 45 phonons in the HBAR using a qubit drive power of -2.0 dBm. This phonon laser contributes an important step in future quantum acoustic applications by providing a highly coherent on-chip phonon source.

In **Chapters 5**, we presented a follow-up study of the phonon laser and used a mean-field solution to explore the parameter space of transmon-HBAR devices in the AIT regime. We showed that the mean-field solution agrees with full master equation simulations and, subsequently, with experimental data. We investigated how the mean-field solutions can be used to reveal phonon laser features such as higher phonon occupancy, lower peak drive power, and upper lasing threshold power. Furthermore, mean-field is used to give means to AIT systems being in the high-cooperativity and weak-coupling regime and their importance for creating a phonon laser. This regime therefore introduces a new region for transmon-HBAR devices to exist and operate within the field of quantum acoustics.

In the final research chapter, **Chapter 6**, we deviated slightly from the acoustic side of our device and focused on the transmon side. We presented a phenomenological study on strongly driven qubits. We measured the qubit's ground-to-excited-state transition in two-tone spectroscopy and applied a strong (third) pump tone, which AC-Stark shifted the qubit. For large enough qubit drive powers we observed the emergence of subharmonic parametric excitations and Bogoliubov "ghost" modes. We showed that ghost modes up to the fifth order in the rotating frame of the strong drive tone, are symmetrically mirrored images of the "normal" qubit excitations around the pump tone. Later in this study, we reverted back to the HBAR and used quantum acoustics to probe the nature of ghost modes. We used the FSR of the acoustic resonator to predict positions of its resonances in frequency space and thereby showed that the ghost modes, for chosen set of pump tone frequencies and powers, do not interact with real systems occupying the same frequency space. Further research is needed to better understand these experimental results, wherein numerical calculations or theoretical derivations would be helpful in identifying the physics of why the "real" acoustic modes do not interact with our qubit Bogoluibov "ghost" modes. So far, these experimental results suggest a truth to the statement "you can't touch a ghost".

7.2. OUTLOOK

In this work, we presented a transmon-HBAR device in flip-chip geometry, which we showed to be in the high-cooperativity and weak-coupling regime. From this point there are different paths we could follow, such as device improvement, single-atom phonon laser applications, and other possible uses of a planar transmon-HBAR device.

CURRENT DEVICE IMPROVEMENTS

Both design method and architecture makes this device easy to fabricate, and scalable for larger complex ensembles of multiple qubits. Although the assembly of the two chips was easy and low effort, the reproducability might be an issue. Even though we did not test this, one can imagine that flipping, pressing down with probe needles, and glueing the chips together by hand is not a guaranteed reproducible process. In particular, glueing by hand makes the flip-chip vulnerable for a slight tilt in the top chip due to unequal amounts of glue sipping between the chips. One suggestion might be to use an automated die bonder, such as in [250]. Do keep in mind that the two chips need to be pressed together in order to reduce the vacuum gap as much as possible for sufficient coupling strength.

As explained in Chapter 4, there is an asymmetry in the qubit spectrum due to a finite number of photon population in the readout resonator. The ground state readout photon population depended on the qubit drive power, which we drove through the readout resonator into the qubit. A possible explanation for this is that the (strong) qubit drive heats the silicon substrate and therefore creating a non-zero photon population in the readout ground state. Adding a dedicated qubit drive line for qubit excitation into our design might reduce, or even circumvent, this problem.

For the phonon laser, and other applications, one might want to tune the qubit in and out of resonance with particular phonon modes. We could use AC-Stark shift, pulsed or continuous wave, to frequency shift the qubit. One down side of this method is that one could naively pump too many photons into the system. By adding dedicated flux lines into the design we can frequency shift our qubit's resonance frequency by flux-tuning using a SQUID instead of a single Josephson junction.

TRANSMON-HBAR AS PHONON LASER

Since the phonon mode is confined in a bulk longitudinal mode within the HBAR's substrate, the phonon laser could be integrated with additional on-chip architectures such as quantum spins. Keep in mind that we are not limited to sapphire substrates, since one could (if calculated and desinged correctly) transition to other substrates. Doing so, we could use the phonons to perform phonon spectroscopy, provided that you have control over your system, on quantum spins or other particles of interest embedded in the substrate of the HBAR.

In our work, we have driven the phonon lasing state with the qubit's $|0\rangle \longrightarrow |1\rangle$ transition which we also used for dispersive readout. A disadvantage of this is that we start to power broaden the qubit linewith and AC-Stark shift our qubit's resonance frequency. Another driving scheme might be more beneficial. For this reason, we want to look into driving the phonon lasing on the $|1\rangle \longrightarrow |2\rangle$ transition and do dispersive readout on the $|0\rangle \longrightarrow |1\rangle$ transition.

What else could we do with HBARs?

In this work we focused on the acoustic side of HBARs and their coupling to superconducting qubits. However, both their use and their applications are versatile. As stated before in the introduction, by using Brillouin scattering and overcoming many different design challenges, the HBAR could become a central node in complex quantum circuits. Here, it can be used to transport quantum information between superconducting circuits, acoustics, and optical fibers for example.

On the other hand, if we stick to our current approaches and ponder on a full chip design, we could realize more complex circuits. For instance, one can already imaging to connect multiple transmons together, each having its own coupled HBAR, via a quantum bus. Fig. 7.1.(a) shows an example quantum circuit consisting of seven transmon qubits (green outline). All qubits are connected to a readout resonator (yellow outline) and can be connected to one-another via quantum busses (red outline). In Fig. 7.1.(b) we show an example zoom in of the chip where the transmons from (a) are replaced by transmons coupled to HBARs (cartoon circle), this can be realized by placing an HBAR chip, with aligned cylindrical piezoelectrics, on top. This gives us the opportunity to utilize HBARs as compact on chip memory storages, or couplers to embedded quantum spins inside the HBAR chip, for more complicated quantum operations.

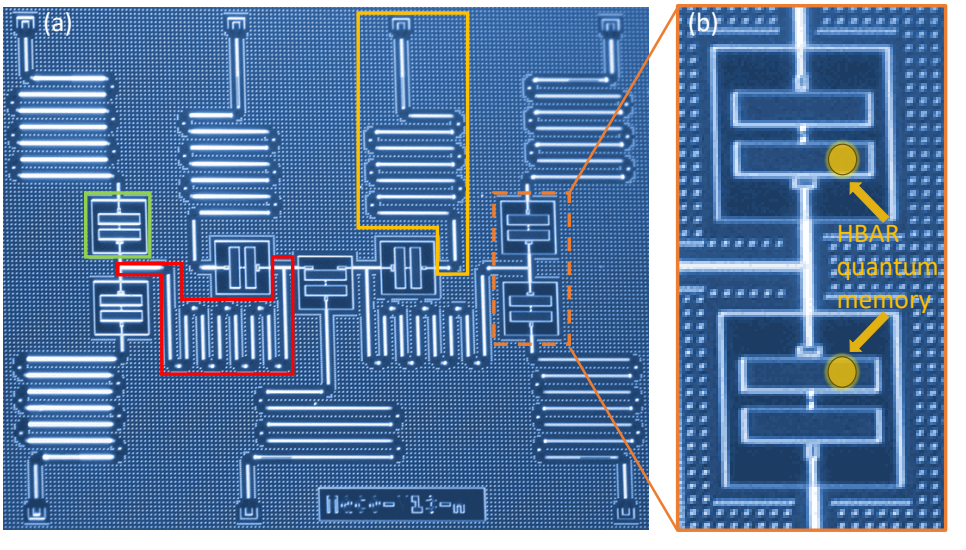

Figure 7.1: Adding quantum memories to a seven qubit chip. (a) Overview of seven transmon qubits are shown with the green outline, readout resonators with the yellow outline, and quantum busses with the red outline. **(b)** Zoom in of transmon qubit, where the transmons are replaced with transmons coupled to HBARs, which would enable a highly coherent quantum memory to each computational node. Figure adapted from adapted from [251].

Another on-chip application might be that of an *acoustic via* where we utilize the direct piezoelectric effect as well. Previously, we only took advantage of the indirect piezoelectric effect and deformed the piezoelectric element with the use of the qubit's alternating electric field.

With an acoustic via, we could place another piezoelectric cylinder on the opposite side of the HBAR chip and transport quantum information from one side to the other. With single chip transmon-HBAR devices [23, 32], we could fabricate circuits on two side of a single chip, as shown in Fig. 7.2.(a) and increase the number of connected qubits. One could do the same in flip-chip geometry, Fig. 7.2.(b), and create a stacked multilayer microwave integrated quantum circuit (MMIQC), see Fig. 7.2.(c).

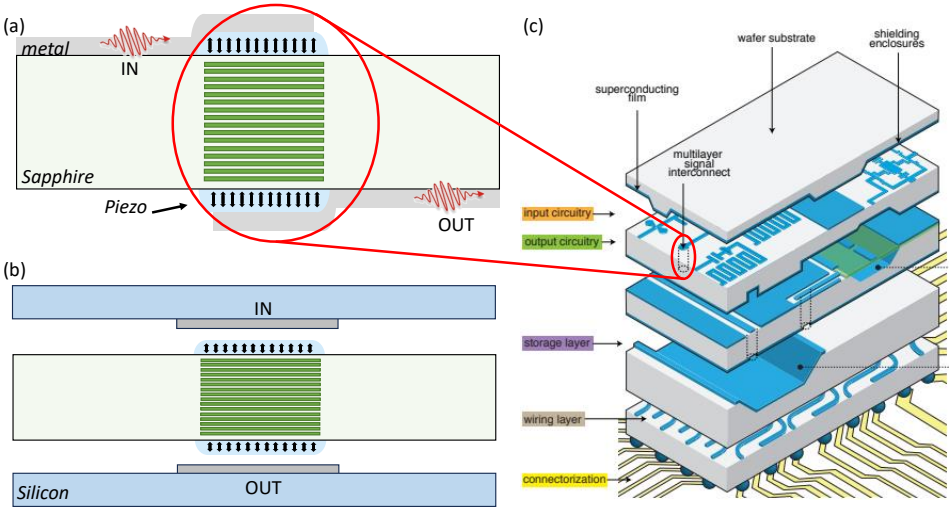

Figure 7.2: HBAR as acoustic vias in multilayer microwave integrated quantum circuit (MMIQC). (a) Single chip acoustic via, where two transmon qubits are placed on top and bottom with a piezoelectric element set between electrode and sapphire substrate. The standing acoustic modes in the HBAR act as a acoustic via and make use of both indirect and direct piezoelectric effect. **(b)** Stacked flip-chip geometry acoustic via, where the HBAR chip presented in this thesis consists now of two piezoelectric elements on top and bottom of chip. Same transmon designs with antenna, from this work, are placed on the bottom and top chip as shown in the panel, where the top chip has the incoming signals and bottom the out going. **(c)** Schematic representation of a MMIQC adapted from [252].

Acknowledgements

Although the PhD journey might feel as a one man's journey, it never truly is. For me, the past few years have been both an emotional roller coaster, and a chaotic juggle in work-lifebalance. Here, I would like to acknowledge a few people that helped me through this journey. Be it help in the lab, me growing as a researcher, giving joy and laughter, or just keeping me sane.

First off, I want to thank **Gary** for giving me this opportunity and helping me along the way. We've met each other several years ago during one of your quantum mechanics courses, when I was a bridging student coming from the Hague university. You might not remember me from back then, but I certainly do. You presented in a way that was not only fun and exciting to listen to, but you were also honest enough to admit that you didn't know something. The enthusiasm you bring into your work, coffee break talks, and our meetings always helped to cheer me up a little. Whenever you helped out or gave advise it always felt to me like I could finally move on a bit. Well... at least till I got stuck on the next problem that is. It always puzzled me how you are able to work on one subject but could totally shift gears and immediately start working on a whole different subject whenever needed. This is a skill I, one day, would like to master. Even though your life as a PI is very busy and lead by your calendar, you always try to make time to help. These past few years have been amazing, despite the rough years of corona which we could both complaint a lot about. I hope that after my defense this will not totally be the end, and that we will run into each other from time to time.

Clinton, you made my final PhD year! You have no idea how much I appreciated your involvement in the HBAR project. I enjoyed our time working together in the lab, behind the computer, and our talks in either the hallway of coffee room. Having you added to the project finally felt like I had a true partner with whom I could have discussions with or come to for advice. Whenever we needed to sit down and you had explained to me project related matter, you always did it was such ease, confidence, and, most importantly, on the level that I needed. These are some of your skills which I not only admire, but am certain of will be your strong points when you start your own research group one day. I've learned a lot from you as a researcher and I hope we have some opportunities to collaborate at some level in the future.

Jacob, we started our PhDs almost a half year apart, but to me it always felt like we started together. It was nice to have a fellow freshman in the group. Thanks to you I've learned a lot about qubit design. You've always been so helpful and ready to answering my crazy questions using your insane amount of cQED knowledge. And, off course, I'll never forget our time at APS Chicago! Crazy green rivers, bellhops, banana sauce, and street rats! Good luck with finishing your thesis, because you're next!

Jean-Paul, on the day of your PhD interview you managed to already show me two sides of your personality: the intellectual and the quirky. Not only did you impress me with how quickly you picked up and participate in discussions, but you also surprised me with asking Gary if he's a "*brony*" during lunch. These two sides I kept enjoying during our time together as PhD-students. Besides our hard work, you always found time in your calendar for a coffee break, brief chat, and fun nights out. I wish you, Ines, and Emily the best!

Robin, although I've known you so for some time in our group, we only started working together in my third year. To me it was a great time wherein we designed and fabricated the qubit reference chip together. Never did we realize back then how often that chip would be used in the group. In between working hours we could always come to each other and either chat about our busy work-lifebalance or just vent about PhD-life. I hope you'll enjoy the rest of your PhD journey working on photon pressure devices. Considering how well all of that is going, I think this shouldn't be a problem.

Sercan, by this point I've already seen you come and go a few times in our lab. First as a BEP, then MEP, and now again as a PhD. You're really becoming a Gary expert at this point. I've been always impressed with how quiet and patient you could listen to discussions, but shoot cleverly sharp questions in between. This kept most people on their feet. Keep up the good work and good luck with the remaining years of your PhD!

Matteo, as my PhD has come to an end, yours is about to start. I first met you as a MEP student in the Steelelab and it was already clear in the first weeks that you are made for research. You're very thorough and get a lot of work done in a short amount of time, which are nice qualities for a PhD-student. Good luck with the next chapter of your life, because you have some great adventures ahead of you.

To all former Steelelab members who I met at the beginning of my PhD and during my MEP. **Adrian, Byoung-Moo, Felix, Hadi, Marios, Sarwan, and Yildiz**, thank you all for helping me out, giving advise, but most of all making me feel welcome in the group. A special thanks goes out to my MEP supervisors **Ines**, **Daniel**, and **Fatemeh**, for teaching me all the ropes of superconducting circuit, design, and performing measurements that I needed to get started with my PhD. Lastly, as of one our Steelelab alumni, I wanted to thank **Mario** who taught me a lot about qubits, measurements, and performing simulations.

To all my Bachelor and Master students, whom I supervised during my PhD, thank you all for showing me what it takes to improve my supervision skills. Our time together, to me, was both exciting and challenging. In chronological order: **Lieuwe**, **Sam**, and **Johanna**.

Sarah, **Erik**, and **Maureen**, unfortunately enough, due to me writing my thesis at home and not being around on campus we haven't seen each other that much. As newest Steelelab members, I hope you'll all enjoy your time in the group as much as I did, but I'm pretty sure that won't be a problem considering your projects.

Simon thank you for being my co-promotor. Most of all I would like to thank you for all your advise you have given me on not only doing research, but also on my well-being during our meetings.

Special thanks to the support team and technicians of *QN*: **Marijke, Heleen, Etty, Maria, Lizzy, Erika, Karin** and **Lidewij** for their efforts regarding the part of the job that most of us have no idea about. I would like to give a very especially thank you to **Tino** for keeping our labs on track.

To my fellow (and former) office mates of D109, **Alex**, **Parsa**, **Liu**, and **Stefanos**, thank you for the fun times in our shared office space. The small talks about either life, or science, put a smile on my face and gave me a pleasant distraction from work.

Thank you to the entire team at DEMO, especially **Erik**, **Jack**, **Kees**, and **Jorn** for support in electrical matters and building PCBs, switch controllers, cables, and most of all: soldering, lots and lots of soldering.

Also a big thanks to the KN staff without whom none of our devices would work! **Anja, Arnold, Charles, Bas, Brian, Eugene, Ewan, Hozanna, Lodi, Marinus, Marc, Marco, Roald, Ron, and Pauline** thank you for your amazing work, keeping the cleanroom running, educating us in using the equipment and help us tackle our fabrication problems.

I would also like to thank my friends and family that weren't in anyway related to my research, but were a huge help and support to me when I was off the clock. A special thanks to my **mom** and **dad**, who've always supported me both financially and emotionally throughout my life, and without whom I probably wouldn't be here. Especially thank you, for teaching me one of the most important lessons, and that is that I should always try to do my best. "*Als je het niet probeert, weet je ook niet of je het wel kan.*"

Since the two of you were my best man at my wedding, I think it's only fair to give you a shout out here as well.

Wessel, thank you for always being interested in my research and sparring with me at JKD to kick the stress (literally) out of my body. I enjoy all our chats, even the ones where you try to help and think about getting my device to work for my research and NO, two piezos is still not going to solve the problem.

Jim, I'm thankful that we could always talk about PhD life and share our experiences in both good and bad times. Even though we weren't even remotely related in scientific field, it felt good to chat about science and discuss our research to one another.

And finally, **Samantha**, my wife, my pal, my love. Thank you for putting up with me during one of the most busiest and most stress full years of my life, and for taking such good care off me. Even though I was such a "stress kip" at home you've always stood by my side and made me feel good about myself in times of doubt.

Delft
11.01.2024

Curriculum Vitæ

Wilfred Jasper Maria Franse

16-08-1993 Born in Haarlem, The Netherlands.

Education

2006–2012 Secondary School
Lyceum Sancta Maria Gymnasium, Haarlem

2012–2016 BSc in Applied Physics
The Hague University, Delft
Internship: Mixing enhancement of Continuous Flow Reactor using Ultrasonic Waves
Company: TNO (Nederlandse organisatie voor toegepast natuurwetenschappelijk onderzoek), Department of Process and Instrument Development

Thesis: Vibrational Studies of Cyanobacteriochromes: Experimental Construction for Cryogenic Measurements
Supervisor: Prof. Dr. D. S. Larsen *(University of California Davis)*

2017–2019 MSc in Applied Physics
Delft University of Technology
Thesis: Design and Fabrication of a Josephson Parametric Amplifier Based on Nanobridge Junctions
Supervisors: Dr. F. Fani Sani, Dr. I. C. Rodrigues, Dr. D. Bothner and Prof. Dr. G. A. Steele

2019-2024 PhD Physics
Technische Universiteit Delft
Thesis: Quantum Acoustics with high-overtone bulk resonators and superconducting qubits
Promotors: Prof. Dr. G. A. Steele and Dr. S. Gröblacher

List of Publications

5. **W.J.M. Franse** and G.A. Steele, *Bogoluibov ghost modes of a strongly drive superconducting transmon qubit*, *In preparation* (2024).

4. **W.J.M. Franse**, V.A.S.V. Bittencourt, C.A. Potts, A. Metelmann and G.A. Steele, *Quantum Acoustics in the High-Cooperativity and Weak-Coupling Regime*, *In preparation* (2024).

3. C.A. Potts, **W.J.M. Franse**, V.A.S.V. Bittencourt, A. Metelmann and G.A. Steele, *A Superconducting Single-Atom Phonon Laser*, *arXiv:**2312.13948*** (2023).

2. Julia S. Kirpich, Che-Wei Chang, **Jasper Franse**, Qinhong Yu, Francisco Velazquez Escobar, Adam J. Jenkins, Shelley S. Martin, Rei Narikawa, James B. Ames, J. Clark Lagarias, and Delmar S. Larsen, *Comparison of the Forward and Reverse Photocycle Dynamics of Two Highly Similar Canonical Red/Green Cyanobacteriochromes Reveals Unexpected Differences*, *Biochemistry* **2021**, 60 (4), 274-288.

1. P.L.M.J. van Neer, L.N.R. Rasmijn, **W.J.M. Franse** L. Geers, A. Rasidovic, and A.W.F. Volker, *Travelling standing waves: a feasibility study*, *2015 IEEE International Ultrasonics Symposium (IUS)* **Pages 1-4** (2015).

Bibliography

[1] Amir Manbachi and Richard S.C. Cobbold. "Development and application of piezoelectric materials for ultrasound generation and detection". English (US). In: *Ultrasound* 19.4 (Nov. 2011), pp. 187–196. ISSN: 1742-271X.

[2] Air Force AFM. U.S. Government Printing Office. *Administrative Practices Glossary of Standardized Terms*. 1961.

[3] www.history-of-american-wars.com. *World War 1 Weapons*. [Online; accessed October 24, 2023]. 2014. Link.

[4] 4Cinvest.lu. *DY-071 PIEZO TC5 NON REFILLABLE*. [Online; accessed October 26, 2023]. 2018. Link.

[5] creativefabrica.com. *Hand Holding a Smart Phone*. [Online; accessed October 24, 2023]. 2018. Link.

[6] Healthkeep. *Body Weight Scale*. [Online; accessed October 24, 2023]. 2022. Link.

[7] Meriglare store. *2 pcs 85mm Audio Speakers Tweeter Piezo Piezoelectric Speaker*. [Online; accessed October 26, 2023]. 2020. Link.

[8] VCS Creative Publishing. *THE HISTORY OF CRYSTAL MICROPHONES AND ARTIFACTS FROM THE SHURE ARCHIVES*. [Online; accessed October 26, 2023]. 2020. Link.

[9] facts.net. *Schematic piezo electric*. [Online; accessed October 24, 2023]. 2023. Link.

[10] wikipedia. *Quantum Acoustics*. [Online; accessed October 24, 2023]. 2022. Link.

[11] Yiwen Chu and Simon Gröblacher. "A perspective on hybrid quantum opto- and electromechanical systems". In: *Applied Physics Letters* 117.15 (Oct. 2020). Link.

[12] Y. Nakamura, Yu. A. Pashkin, and J. S. Tsai. "Coherent control of macroscopic quantum states in a single-Cooper-pair box". In: *Nature* 398.6730 (Apr. 1999), pp. 786–788. Link.

[13] A.D. O'Connell et al. "Quantum ground state and single-phonon control of a mechanical resonator". In: *Nature* 464 (Mar. 2010), pp. 697–703.

[14] Martin V. Gustafsson et al. "Propagating phonons coupled to an artificial atom". In: *Science* 346.6206 (Oct. 2014), pp. 207–211. Link.

[15] R. Manenti et al. "Surface acoustic wave resonators in the quantum regime". In: *Physical Review B* 93.4 (Jan. 2016). Link.

[16] Bradley A. Moores et al. "Cavity Quantum Acoustic Device in the Multimode Strong Coupling Regime". In: *Physical Review Letters* 120.22 (May 2018). Link.

[17] Atsushi Noguchi et al. *Single-photon quantum regime of artificial radiation pressure on a surface acoustic wave resonator*. 2020. arXiv: 1808.03372 [quant-ph].

[18] K. J. Satzinger et al. "Quantum control of surface acoustic-wave phonons". In: *Nature* 563.7733 (Nov. 2018), pp. 661–665. Link.

[19] A. Bienfait et al. “Phonon-mediated quantum state transfer and remote qubit entanglement”. In: *Science* 364.6438 (Apr. 2019), pp. 368–371. Link.

[20] Patricio Arrangoiz-Arriola and Amir H. Safavi-Naeini. “Engineering interactions between superconducting qubits and phononic nanostructures”. In: *Phys. Rev. A* 94 (6 Dec. 2016), p. 063864. Link.

[21] Patricio Arrangoiz-Arriola et al. “Resolving the energy levels of a nanomechanical oscillator”. In: *Nature* 571.7766 (July 2019), pp. 537–540. Link.

[22] Jens Koch et al. “Charge-insensitive qubit design derived from the Cooper pair box”. In: *Phys. Rev. A* 76 (4 Oct. 2007), p. 042319. Link.

[23] Yiwen Chu et al. “Quantum acoustics with superconducting qubits”. In: *Science* 358.6360 (Oct. 2017), pp. 199–202. Link.

[24] Alexandre Blais et al. “Cavity quantum electrodynamics for superconducting electrical circuits: An architecture for quantum computation”. In: *Physical Review A* 69.6 (June 2004). Link.

[25] A. Wallraff et al. “Strong coupling of a single photon to a superconducting qubit using circuit quantum electrodynamics”. In: *Nature* 431.7005 (Sept. 2004), pp. 162–167.

[26] Alexandre Blais et al. “Circuit quantum electrodynamics”. In: *Reviews of Modern Physics* 93.2 (May 2021). Link.

[27] A. Wallraff et al. “Approaching Unit Visibility for Control of a Superconducting Qubit with Dispersive Readout”. In: *Physical Review Letters* 95.6 (Aug. 2005). Link.

[28] D. I. Schuster et al. “Resolving photon number states in a superconducting circuit”. In: *Nature* 445.7127 (Feb. 2007), pp. 515–518. Link.

[29] Yiwen Chu et al. “Creation and control of multi-phonon Fock states in a bulk acoustic-wave resonator”. In: *Nature* 563.7733 (Nov. 2018), pp. 666–670. Link.

[30] Uwe von Lüpke et al. “Parity measurement in the strong dispersive regime of circuit quantum acoustodynamics”. In: *Nature Physics* 18.7 (May 2022), pp. 794–799. Link.

[31] Marius Bild et al. *Schrödinger cat states of a 16-microgram mechanical oscillator*. 2022. arXiv: 2211.00449 [quant-ph].

[32] Mikael Kervinen, Ilkka Rissanen, and Mika Sillanpää. “Interfacing planar superconducting qubits with high overtone bulk acoustic phonons”. In: *Physical Review B* 97.20 (May 2018). Link.

[33] Mikael Kervinen et al. “Landau-Zener-Stückelberg Interference in a Multimode Electromechanical System in the Quantum Regime”. In: *Physical Review Letters* 123.24 (Dec. 2019). Link.

[34] Mikael Kervinen et al. “Sideband Control of a Multimode Quantum Bulk Acoustic System”. In: *Physical Review Applied* 14.5 (Nov. 2020). Link.

[35] Alpo Välimaa et al. *Multiphonon transitions in a quantum electromechanical system*. 2021. arXiv: 2108.06241 [cond-mat.mes-hall].

[36] C. A. Potts et al. “A Superconducting Single-Atom Phonon Laser”. under submission. to appear to appear.

[37] Ze-Liang Xiang et al. “Hybrid quantum circuits: Superconducting circuits interacting with other quantum systems”. In: *Rev. Mod. Phys.* 85 (2 Apr. 2013), pp. 623–653. Link.

[38] M. Veldhorst et al. “An addressable quantum dot qubit with fault-tolerant control-fidelity”. In: *Nature Nanotechnology* 9.12 (Oct. 2014), pp. 981–985. Link.

[39] J. M. Pino et al. “Demonstration of the trapped-ion quantum CCD computer architecture”. In: *Nature* 592.7853 (Apr. 2021), pp. 209–213. Link.

[40] Ofir Milul et al. “Superconducting Cavity Qubit with Tens of Milliseconds Single-Photon Coherence Time”. In: *PRX Quantum* 4 (3 Sept. 2023), p. 030336. Link.

[41] Philipp Gerbert and Frank Ruess. *The Next Decade in Quantum Computing—and How to Play*. [Online; accessed October 25, 2023]. 2018. Link.

[42] M.D. LaHaye et al. “Nanomechanical measurements of a superconducting qubit”. In: *Nature* 459.7249 (June 2009), pp. 960–964. Link.

[43] Y. Kubo et al. “Strong Coupling of a Spin Ensemble to a Superconducting Resonator”. In: *Phys. Rev. Lett.* 105 (14 Sept. 2010), p. 140502. Link.

[44] Deshui Yu et al. “Superconducting qubit-resonator-atom hybrid system”. In: *Quantum Science and Technology* 2.3 (July 2017), p. 035005. Link.

[45] Prashanta Kharel et al. *Ultra-high-Q phononic resonators on-chip at cryogenic temperatures*. 2018. arXiv: 1803.10077 [physics.optics].

[46] Taekwan Yoon et al. *Simultaneous Brillouin and piezoelectric coupling to a high-frequency bulk acoustic resonator*. 2023. arXiv: 2208.06454 [quant-ph].

[47] H. M. Doeleman et al. *Brillouin optomechanics in the quantum ground state*. 2023. arXiv: 2303.04677 [quant-ph].

[48] Amir Ghadimi et al. “Elastic strain engineering for ultralow mechanical dissipation”. In: *Science* 360 (Apr. 2018), eaar6939.

[49] W. H. Renninger et al. “Bulk crystalline optomechanics”. In: *Nature Physics* 14.6 (Apr. 2018), pp. 601–607. Link.

[50] Connor T. Hann et al. “Hardware-Efficient Quantum Random Access Memory with Hybrid Quantum Acoustic Systems”. In: *Phys. Rev. Lett.* 123 (25 Dec. 2019), p. 250501. Link.

[51] Stefanie Miller. “A tunable 20 GHz transmon qubit in a 3D cavity”. en. ETH Zurich.

[52] Sourav Majumder et al. “A Fast Tunable 3D-Transmon Architecture for Superconducting Qubit-Based Hybrid Devices”. In: *Journal of Low Temperature Physics* 207.3-4 (Mar. 2022), pp. 210–219. Link.

[53] Wayne Crump, Alpo Välimaa, and Mika A Sillanpää. “Coupling high-overtone bulk acoustic wave resonators via superconducting qubits”. In: *arXiv preprint arXiv:2307.05544* (2023). Link.

[54] Uri Vool and Michel Devoret. “Introduction to quantum electromagnetic circuits”. In: *International Journal of Circuit Theory and Applications* 45.7 (2017), pp. 897–934.

[55] J. J. Sakurai. *Advanced quantum mechanics*. India: Pearson Education, 1967.

[56] B.D. Josephson. “Possible new effects in superconductive tunnelling”. In: *Physics Letters* 1.7 (1962), pp. 251–253. ISSN: 0031-9163. Link.

[57] Andreas Wallraff et al. “Strong coupling of a single photon to a superconducting qubit using circuit quantum electrodynamics”. In: *Nature* 431.7005 (2004), p. 162.

[58] H Kroger, LN Smith, and DW Jillie. “Selective niobium anodization process for fabricating Josephson tunnel junctions”. In: *Applied Physics Letters* 39.3 (1981), pp. 280–282.

[59] J. Bardeen, L. N. Cooper, and J. R. Schrieffer. “Theory of Superconductivity”. In: *Phys. Rev.* 108 (5 Dec. 1957), pp. 1175–1204. Link.

[60] J. Bardeen. “Tunnelling from a Many-Particle Point of View”. In: *Phys. Rev. Lett.* 6 (2 Jan. 1961), pp. 57–59. Link.

[61] Charles Kittel. *Introduction to Solid State Physics*. 8th ed. Wiley, 2004. ISBN: 9780471415268. Link.

[62] Frank Deppe et al. “Determination of the capacitance of nm scale Josephson junctions”. In: *Journal of Applied Physics* 95 (Mar. 2004), pp. 2607–2613.

[63] M. Kounalakis. “Nonlinear couplings for quantum control of superconducting qubits and electrical/mechanical resonators”. PhD thesis. Delft University of Technology (2019). Link.

[64] Philip Krantz et al. “A quantum engineer’s guide to superconducting qubits”. In: *Applied Physics Reviews* 6 (June 2019), p. 021318.

[65] Michael J. Peterer et al. “Coherence and Decay of Higher Energy Levels of a Superconducting Transmon Qubit”. In: *Phys. Rev. Lett.* 114 (1 Jan. 2015), p. 010501. Link.

[66] L. DiCarlo et al. “Preparation and measurement of three-qubit entanglement in a superconducting circuit”. In: *Nature* 467.7315 (Sept. 2010), pp. 574–578. Link.

[67] C. Bohling and W. Sigmund. “Self-Limitation of Native Oxides Explained”. In: *Silicon* 8.3 (July 2016), pp. 339–343. Link.

[68] S. I. Raider, R. Flitsch, and M. J. Palmer. “Oxide Growth on Etched Silicon in Air at Room Temperature”. In: *Journal of The Electrochemical Society* 122.3 (Mar. 1975), p. 413. Link.

[69] Michael Tinkham. *Introduction to superconductivity*. Courier Corporation, 2004.

[70] A. Bruno et al. “Reducing intrinsic loss in superconducting resonators by surface treatment and deep etching of silicon substrates”. In: *Applied Physics Letters* 106.18 (May 2015). Link.

[71] K. Serniak et al. “Hot Nonequilibrium Quasiparticles in Transmon Qubits”. In: *Phys. Rev. Lett.* 121 (15 Oct. 2018), p. 157701. Link.

[72] Jean-Michel Raimond, M Brune, and Serge Haroche. “Manipulating quantum entanglement with atoms and photons in a cavity”. In: *Reviews of Modern Physics* 73.3 (2001), p. 565.

[73] M. Brune et al. “Manipulation of photons in a cavity by dispersive atom-field coupling: Quantum-nondemolition measurements and generation of “Schrödinger cat” states”. In: *Phys. Rev. A* 45 (7 Apr. 1992), pp. 5193–5214. Link.

[74] Alexander S Gilmour Jr. “Microwave tubes”. In: *Dedham* (1986).

[75] H.W. Ott. *Noise reduction techniques in electronic systems*. 2nd. John Wiley & Sons, 1988. ISBN: 0-471-85068-3.

[76] R.N. Simons. *Coplanar waveguide circuits, components, and systems*. John Wiley & Sons, 2001. ISBN: 0-471-16121-7.

[77] D.M. Pozar. *Microwave engineering*. 4th. John Wiley & Sons, Inc., 2012. ISBN: 978-0-470-63155-3.

[78] M Göppl et al. "Coplanar waveguide resonators for circuit quantum electrodynamics". In: *Journal of Applied Physics* 104.11 (2008), p. 113904.

[79] L. S. Bishop. "Circuit quantum electrodynamics: volume II". PhD thesis. Yale University (2010).

[80] R. Meservey and P. M. Tedrow. "Measurements of the Kinetic Inductance of Superconducting Linear Structures". In: *Journal of Applied Physics* 40 (July 1969), p. 2028.

[81] JJA Baselmans et al. "Development of high-Q superconducting resonators for use as kinetic inductance detectors". In: *Advances in Space Research* 40.5 (2007), pp. 708–713.

[82] Alexandre Blais et al. "Cavity quantum electrodynamics for superconducting electrical circuits: An architecture for quantum computation". In: *Phys. Rev. A* 69 (6 June 2004), p. 062320. Link.

[83] A. Wallraff et al. "Approaching Unit Visibility for Control of a Superconducting Qubit with Dispersive Readout". In: *Phys. Rev. Lett.* 95 (6 Aug. 2005), p. 060501. Link.

[84] Andreas Wallraff et al. "Strong coupling of a single photon to a superconducting qubit using circuit quantum electrodynamics". In: *Nature* 431.7005 (2004), p. 162.

[85] II Rabi. "On the process of space quantization". In: *Phys. Rev.* 49.4 (1936), p. 324.

[86] Edwin T Jaynes and Frederick W Cummings. "Comparison of quantum and semiclassical radiation theories with application to the beam maser". In: *Proceedings of the IEEE* 51.1 (1963), pp. 89–109.

[87] Wei Pang, Hongyu Yu, and Eun Kim. "High-tone bulk acoustic resonators on sapphire, crystal quartz, fused silica, and silicon substrates". In: *Journal of Applied Physics* 99 (June 2006), pp. 124911–124911.

[88] M. Kurosu et al. "Impedance-matched high-overtone bulk acoustic resonator". In: *Applied Physics Letters* 122 (12 Mar. 2023).

[89] Hugo Banderier, Maxwell Drimmer, and Yiwen Chu. "Unified Simulation Methods for Quantum Acoustic Devices". In: *Physical Review Applied* 20.2 (Aug. 2023). Link.

[90] D. Rabus et al. "High-overtone bulk-acoustic resonator gravimetric sensitivity: Towards wideband acoustic spectroscopy". In: *Journal of Applied Physics* 118.11 (Sept. 2015). Link.

[91] Ken-Ya Hashimoto. 2009.

[92] J.F. Li. *Lead-Free Piezoelectric Materials*. Wiley, 2021. ISBN: 9783527345120. Link.

[93] T. Ikeda. *Fundamentals of Piezoelectricity*. Oxford science publications. Oxford University Press, 1990. ISBN: 9780198563396. Link.

[94] A. Arnau. *Piezoelectric Transducers and Applications*. Springer, 2004. ISBN: 9783540209980. Link.

[95] D.A. Steck. *Quantum and Atom Optics*. 2007. Link.

[96] Markus Aspelmeyer, Tobias J. Kippenberg, and Florian Marquardt. "Cavity optomechanics". In: *Reviews of Modern Physics* 86.4 (Dec. 2014), pp. 1391–1452. Link.

[97] W. Rossmann. *Lie Groups: An Introduction Through Linear Groups*. Oxford graduate texts in mathematics. Oxford University Press, 2006. ISBN: 9780199202515. Link.

[98] Zlatko K Minev et al. *Qiskit Metal: An Open-Source Framework for Quantum Device Design & Analysis*. 2021. Link.

[99] Ansys. *Ansys HFSS*. Version 2021R1. Link.

[100] Andrew Addison Houck et al. "Controlling the spontaneous emission of a superconducting transmon qubit". In: *Physical review letters* 101.8 (2008), p. 080502.

[101] Maxime Boissonneault, Jay M Gambetta, and Alexandre Blais. "Dispersive regime of circuit QED: Photon-dependent qubit dephasing and relaxation rates". In: *Physical Review A* 79.1 (2009), p. 013819.

[102] Jay M. Gambetta et al. "Investigating Surface Loss Effects in Superconducting Transmon Qubits". In: *IEEE Transactions on Applied Superconductivity* 27.1 (Jan. 2017), pp. 1–5. Link.

[103] David Johannes Thoen et al. "Superconducting NbTin Thin Films With Highly Uniform Properties Over a 100 mm Wafer". In: *IEEE Transactions on Applied Superconductivity* 27.4 (June 2017), pp. 1–5. Link.

[104] Rami Barends et al. "Noise in NbTiN, Al, and Ta Superconducting Resonators on Silicon and Sapphire Substrates". In: *IEEE Transactions on Applied Superconductivity* 19 (2009), pp. 936–939. Link.

[105] A. P. Reed et al. "Faithful conversion of propagating quantum information to mechanical motion". In: *Nature Physics* 13.12 (Sept. 2017), pp. 1163–1167. Link.

[106] F.E. Schmidt. "Josephson junctions in superconducting coplanar DC bias cavities: Fundamental studies and applications". PhD thesis. Delft University of Technology (2020). Link.

[107] S.R. Peiter. "Cavity electromechanics using flipped silicon nitride membranes". PhD thesis. Delft University of Technology (2022). Link.

[108] B. Ann. "Tunable quantum interfaces between superconducting qubits and microwave photons induced by extreme driving". PhD thesis. Delft University of Technology (2021). Link.

[109] Marius V. Costache et al. "Lateral metallic devices made by a multiangle shadow evaporation technique". In: *Journal of Vacuum Science & Technology. B. Nanotechnology and Microelectronics: Materials, Processing, Measurement, and Phenomena* 30 (2012). Link.

[110] G. J. Dolan and John H. Dunsmuir. "Very small (20 nm) lithographic wires, dots, rings, and tunnel junctions". In: *Physica B-condensed Matter* 152 (1988), pp. 7–13. Link.

[111] G. J. Dolan. "Offset masks for lift-off photoprocessing". In: *Applied Physics Letters* 31 (1977), pp. 337–339. Link.

[112] R Meservey and P M Tedrow. "MEASUREMENTS OF THE KINETIC INDUCTANCE OF SUPERCONDUCTING LINEAR STRUCTURES." In: *J. Appl. Phys., 40: 2028-34(Apr. 1969)*. (Jan. 1969). Link.

[113] S. Hawaldar. *forked from zlatko-minev/pyEPR*. Version 0.8.5.5. June 20, 2022. Link.

[114] S. Hawaldar. *forked from qiskit-community/qiskit-metal*. Version 0.0.4. July 2, 2022. Link.

[115] *R. Schouten engineer junction measurement box*. Accessed: 2023-10-12. Link.

[116] S. Kono. "Quantum Measurement of Itinerant Microwave Photons Using Superconducting Circuits". PhD thesis. The University of Tokyo (2019).

[117] A Tajic et al. "No-drift™ BAW-SMR: Over-moded reflector for temperature compensation". In: *2016 IEEE International Ultrasonics Symposium (IUS)*. IEEE. 2016, pp. 1–4.

[118] *Kavli Nanolab Delft*. Accessed: 2023-09-18. Link.

[119] *S1805 (positive) Datasheet Kavli nanolab*. Accessed: 2023-09-18. Link.

[120] *Full Diced wafer figure*. Accessed: 2023-05-15. Link.

[121] *Disco DAD 3220*. Accessed: 2023-05-15. Link.

[122] *PVA TePla 300 Microwave Plasma System Users Manual*. Accessed: 2023-09-18. Link.

[123] *Productinfo Allresist, Positive E-Beam Resists AR-P 6200 series*. Accessed: 2023-09-18. Link.

[124] *COMPOUND SUMMARY O-Xylene, Pubchem*. Accessed: 2023-09-18. Link.

[125] *Information page of Kavli nanolab's Raith EBPG-5200*. Accessed: 2023-09-18. Link.

[126] *Hardbake of Photoresist Structures, Revised: 2013-11-07 Source*. Accessed: 2023-09-18. Link.

[127] Dmitry Levko, Laurent Garrigues, and Gerjan Hagelaar. "Chemical composition of SF6 low-pressure plasma in magnetic field". In: *Journal of Physics D Applied Physics* 47 (Jan. 2014), p. 045205.

[128] Yoshinori UZAWA et al. "Development of Superconducting Devices Supporting Radio Astronomy". In: *IEICE Transactions on Electronics* E104.C (Mar. 2021).

[129] *Free Radicals and Reactive Oxygen*. Accessed: 2023-09-18. Link.

[130] *Safety Data Sheet, Micro Chem (05/08/2018)*. Accessed: 2023-09-18. Link.

[131] T. Nakanishi et al. "Influence of O2-RIE on silicon substrate -Estimating plasma damage with bipolar transistor characteristics-". In: *Microelectronic Engineering* 41-42 (1998). International Conference on Micro- and Nanofarbication, pp. 399–402. ISSN: 0167-9317. Link.

[132] Nicolae Tomozeiu. "Silicon oxide (SiOx, 0<x<2): A challenging material for optoelectronics". In: Sept. 2011. ISBN: 978-953-307-276-0.

[133] *Photoresist ashing, stripping, and descum. Organic Contamination Removal for Silicon Wafer*. Accessed: 2023-09-18. Link.

[134] Aaron D. O'Connell et al. "Microwave dielectric loss at single photon energies and millikelvin temperatures". In: *Applied Physics Letters* 92.11 (Mar. 2008). Link.

[135] P. Duivestein. "Wafer scale fabrication of Josephson junctions". Delft University of Technology (2021). Link.

[136] *Cleaning Procedures for Silicon Wafers*. Accessed: 2023-09-18. Link.

[137] *Kavli Nanolab procedure for BOE*. Accessed: 2023-09-18. Link.

[138] N. Muthusubramanian et al. *Wafer-scale uniformity of Dolan-bridge and bridgeless Manhattan-style Josephson junctions for superconducting quantum processors*. 2023. arXiv: 2304.09111 [quant-ph].

[139] Andrew Keller et al. "Al transmon qubits on silicon-on-insulator for quantum device integration". In: *Applied Physics Letters* 111 (July 2017), p. 042603.

[140] Nicholas R Johnson et al. "Thermal atomic layer etching of crystalline aluminum nitride using sequential, self-limiting hydrogen fluoride and Sn (acac) 2 reactions and enhancement by H2 and Ar plasmas". In: *Journal of Vacuum Science & Technology A* 34.5 (2016).

[141] Tsung-Ju Lu et al. "Aluminum nitride integrated photonics platform for the ultraviolet to visible spectrum". In: *Opt. Express* 26.9 (Apr. 2018), pp. 11147–11160. Link.

[142] *Kyma produces 300-mm (12-inch) diameter AlN on silicon template*. Accessed: 2023-09-19. Link.

[143] Peter Sigmund. "Sputtering by ion bombardment theoretical concepts". In: *Sputtering by Particle Bombardment I: Physical Sputtering of Single-Element Solids*. Ed. by Rainer Behrisch. Berlin, Heidelberg: Springer Berlin Heidelberg, 1981, pp. 9–71. ISBN: 978-3-540-38514-1. Link.

[144] Yao Yao, Robert F. Davis, and Lisa M. Porter. "Metal Organic Chemical Vapor Deposition 2". In: *Gallium Oxide: Materials Properties, Crystal Growth, and Devices*. Ed. by Masataka Higashiwaki and Shizuo Fujita. Cham: Springer International Publishing, 2020, pp. 171–184. ISBN: 978-3-030-37153-1. Link.

[145] *Photo of 6 Inch Sapphire Based AlN Templates Wafer For 5G BAW Devices Sapphire wafer sapphire window by Zhiming*. Accessed: 2023-09-20. Link.

[146] *VTo7 SERIES Vitrified Bond Blades by Disco*. Accessed: 2023-09-20. Link.

[147] *Productinfo Allresist, Negative Photoresists AR-N 4400 (CAR 44)*. Accessed: 2023-09-20. Link.

[148] *Heidelberg Instruments Laserwriter Kavli nanolab information page*. Accessed: 2023-09-20. Link.

[149] *Heidelberg Instruments Laserwriter information page*. Accessed: 2023-09-20. Link.

[150] E. Douglas et al. "Inductively coupled BCl3/Cl2/Ar plasma etching of Al-rich AlGaN". In: *Journal of Vacuum Science Technology A: Vacuum, Surfaces, and Films* 35 (Mar. 2017), p. 021305.

[151] D. Buttari et al. "Origin of etch delay time in Cl2 dry etching of AlGaN/GaN structures". In: *Applied Physics Letters* 83 (Dec. 2003), pp. 4779–4781.

[152] Anton Kobelev et al. "Boron Trichloride Dry Etching". In: Dec. 2016.

[153] Atsushi Tanide et al. "Effects of BCl 3 addition to Cl 2 gas on etching characteristics of GaN at high temperature". In: *Journal of Vacuum Science Technology B* 37 (Mar. 2019), p. 021209.

[154] *White-Light Michelson Interferometer by LightTrans*. Accessed: 2023-09-22. Link.

[155] A. Välimaa. “Piezoelectric resonators in the quantum regime”. PhD thesis. Aalto University (2022). Link.

[156] *Stock photos from Blue Fors on how the dilution refrigerator works*. Accessed: 2023-09-24. Link.

[157] *Slide show presentation on He3 dilution refrigerator by R. Green*. Accessed: 2023-09-24. Link.

[158] Francesco Giazotto et al. “Opportunities for mesoscopics in thermometry and refrigeration: Physics and applications”. In: *Reviews of Modern Physics* 78.1 (Mar. 2006), pp. 217–274. Link.

[159] D. I. Schuster et al. “ac Stark Shift and Dephasing of a Superconducting Qubit Strongly Coupled to a Cavity Field”. In: *Physical Review Letters* 94.12 (Mar. 2005). Link.

[160] Andre Schneider et al. “Local sensing with the multilevel ac Stark effect”. In: *Physical Review A* 97.6 (June 2018). Link.

[161] Arthur L Schawlow. “Spectroscopy in a new light”. In: *Reviews of Modern Physics* 54.3 (1982), p. 697. Link.

[162] Arthur L Schawlow. “Laser Spectroscopy of Atoms and Molecules: The abundance of new laser techniques is making possible a variety of spectroscopic experiments.” In: *Science* 202.4364 (1978), pp. 141–147. Link.

[163] William D Phillips and Harold Metcalf. “Laser deceleration of an atomic beam”. In: *Physical Review Letters* 48.9 (1982), p. 596. Link.

[164] William D Phillips. “Nobel Lecture: Laser cooling and trapping of neutral atoms”. In: *Reviews of Modern Physics* 70.3 (1998), p. 721. Link.

[165] Mike H Anderson et al. “Observation of Bose-Einstein condensation in a dilute atomic vapor”. In: *science* 269.5221 (1995), pp. 198–201. Link.

[166] Kendall B Davis et al. “Bose-Einstein condensation in a gas of sodium atoms”. In: *Physical review letters* 75.22 (1995), p. 3969. Link.

[167] Benjamin P Abbott et al. “Observation of gravitational waves from a binary black hole merger”. In: *Physical review letters* 116.6 (2016), p. 061102. Link.

[168] S Chaurasiya et al. “Breast cancer gene therapy using an adenovirus encoding human IL-2 under control of mammaglobin promoter/enhancer sequences”. In: *Cancer Gene Therapy* 23.6 (2016), pp. 178–187. Link.

[169] Richard L McCreery. *Raman spectroscopy for chemical analysis*. John Wiley & Sons, 2005.

[170] Ensieh Khalkhal et al. “The evaluation of laser application in surgery: a review article”. In: *Journal of lasers in medical sciences* 10.Suppl 1 (2019), S104. Link.

[171] Prasoon K Shandilya et al. “Optomechanical interface between telecom photons and spin quantum memory”. In: *Nature Physics* 17.12 (2021), pp. 1420–1425. Link.

[172] D Hatanaka et al. “On-chip coherent transduction between magnons and acoustic phonons in cavity magnomechanics”. In: *Physical Review Applied* 17.3 (2022), p. 034024. Link.

[173] Daiki Hatanaka et al. “Phononic Crystal Cavity Magnomechanics”. In: *Physical Review Applied* 19.5 (2023), p. 054071. Link.

[174] Kaiyu Cui et al. “Phonon lasing in a hetero optomechanical crystal cavity”. In: *Photonics Research* 9.6 (2021), pp. 937–943. Link.

[175] T. Behrle et al. “Phonon Laser in the Quantum Regime”. In: *Phys. Rev. Lett.* 131 (4 July 2023), p. 043605. Link.

[176] Tengfang Kuang et al. “Nonlinear multi-frequency phonon lasers with active levitated optomechanics”. In: *Nature Physics* 19.3 (2023), pp. 414–419. Link.

[177] Kerry Vahala et al. “A phonon laser”. In: *Nature Physics* 5.9 (2009), pp. 682–686. Link.

[178] Robert M Pettit et al. “An optical tweezer phonon laser”. In: *Nature Photonics* 13.6 (2019), pp. 402–405. Link.

[179] Jing Zhang et al. “A phonon laser operating at an exceptional point”. In: *Nature Photonics* 12.8 (2018), pp. 479–484. Link.

[180] Ivan S. Grudinin et al. “Phonon Laser Action in a Tunable Two-Level System”. In: *Phys. Rev. Lett.* 104 (8 Feb. 2010), p. 083901. Link.

[181] Clinton A Potts et al. “Dynamical backaction magnomechanics”. In: *Physical Review X* 11.3 (2021), p. 031053. Link.

[182] Peyman Parsa et al. “Feedback Enhanced Phonon Lasing of a Microwave Frequency Resonator”. In: *arXiv preprint arXiv:2308.09130* (2023). Link.

[183] Tobias J Kippenberg and Kerry J Vahala. “Cavity optomechanics: back-action at the mesoscale”. In: *science* 321.5893 (2008), pp. 1172–1176. Link.

[184] WE Bron and W Grill. “Stimulated phonon emission”. In: *Physical Review Letters* 40.22 (1978), p. 1459. Link.

[185] S Wallentowitz et al. “Vibrational amplification by stimulated emission of radiation”. In: *Physical Review A* 54.1 (1996), p. 943. Link.

[186] I Camps et al. “GaAs- Al x Ga 1- x As double-barrier heterostructure phonon laser: A full quantum treatment”. In: *Physical Review B* 64.12 (2001), p. 125311. Link.

[187] Jason McKeever et al. “Experimental realization of a one-atom laser in the regime of strong coupling”. In: *Nature* 425.6955 (2003), pp. 268–271. Link.

[188] François Dubin et al. “Quantum to classical transition in a single-ion laser”. In: *Nature Physics* 6.5 (2010), pp. 350–353. Link.

[189] Kyungwon An et al. “Microlaser: A laser with one atom in an optical resonator”. In: *Physical review letters* 73.25 (1994), p. 3375. Link.

[190] Yi Mu and C.M. Savage. “One-atom lasers”. In: *Physical Review A* 46.9 (1992), p. 5944. Link.

[191] S Ashhab et al. “Single-artificial-atom lasing using a voltage-biased superconducting charge qubit”. In: *New Journal of Physics* 11.2 (2009), p. 023030. Link.

[192] Marius Bild et al. “Schrödinger cat states of a 16-microgram mechanical oscillator”. In: *Science* 380.6642 (2023), pp. 274–278. Link.

[193] M.N. Wybourne and J.K. Wigmore. “Phonon spectroscopy”. In: *Reports on Progress in Physics* 51.7 (1988), p. 923. Link.

[194] O. Romero-Isart et al. “Large Quantum Superpositions and Interference of Massive Nanometer-Sized Objects”. In: *Phys. Rev. Lett.* 107 (2 July 2011), p. 020405. Link.

[195] Uwe von Lüpke et al. “Engineering phonon-phonon interactions in multimode circuit quantum acousto-dynamics”. In: *arXiv preprint arXiv:2303.00730* (2023). Link.

[196] Uwe von Lüpke et al. “Parity measurement in the strong dispersive regime of circuit quantum acoustodynamics”. In: *Nature Physics* 18.7 (2022), pp. 794–799. Link.

[197] Yiwen Chu et al. “Creation and control of multi-phonon Fock states in a bulk acoustic-wave resonator”. In: *Nature* 563.7733 (2018), pp. 666–670. Link.

[198] Yiwen Chu et al. “Quantum acoustics with superconducting qubits”. In: *Science* 358.6360 (2017), pp. 199–202. Link.

[199] Alpo Välimaa et al. “Multiphonon Transitions in a Quantum Electromechanical System”. In: *Phys. Rev. Appl.* 17 (6 June 2022), p. 064003. Link.

[200] Philip Krantz et al. “A quantum engineer’s guide to superconducting qubits”. In: *Applied physics reviews* 6.2 (2019).

[201] MD Reed et al. “High-fidelity readout in circuit quantum electrodynamics using the Jaynes-Cummings nonlinearity”. In: *Physical review letters* 105.17 (2010), p. 173601. Link.

[202] Jay Gambetta et al. “Qubit-photon interactions in a cavity: Measurement-induced dephasing and number splitting”. In: *Physical Review A* 74.4 (2006), p. 042318. Link.

[203] Dany Lachance-Quirion et al. “Resolving quanta of collective spin excitations in a millimeter-sized ferromagnet”. In: *Science Advances* 3.7 (2017), e1603150. Link.

[204] D.I. Schuster et al. “ac Stark shift and dephasing of a superconducting qubit strongly coupled to a cavity field”. In: *Physical Review Letters* 94.12 (2005), p. 123602. Link.

[205] James P Gordon, Herbert J Zeiger, and Charles H Townes. “The maser-new type of microwave amplifier, frequency standard, and spectrometer”. In: *Physical review* 99.4 (1955), p. 1264. Link.

[206] David Johannes Thoen et al. “Superconducting NbTin Thin Films With Highly Uniform Properties Over a 100 mm Wafer”. In: *IEEE Transactions on Applied Superconductivity* 27.4 (2016), pp. 1–5. Link.

[207] J Robert Johansson, Paul D Nation, and Franco Nori. “QuTiP: An open-source Python framework for the dynamics of open quantum systems”. In: *Computer Physics Communications* 183.8 (2012), pp. 1760–1772. Link.

[208] F Rouxinol et al. “Measurements of nanoresonator-qubit interactions in a hybrid quantum electromechanical system”. In: *Nanotechnology* 27.36 (Aug. 2016), p. 364003. Link.

[209] Vijay Jain et al. *Acoustic radiation from a superconducting qubit: From spontaneous emission to Rabi oscillations*. 2022. arXiv: 2211.07475 [quant-ph].

[210] E. Alex Wollack et al. “Quantum state preparation and tomography of entangled mechanical resonators”. In: *Nature* 604.7906 (Apr. 2022), pp. 463–467. Link.

[211] Michael Fleischhauer, Atac Imamoglu, and Jonathan P. Marangos. “Electromagnetically induced transparency: Optics in coherent media”. In: *Rev. Mod. Phys.* 77 (2 July 2005), pp. 633–673. Link.

[212] Stefan Weis et al. “Optomechanically Induced Transparency”. In: *Science* 330.6010 (Dec. 2010), pp. 1520–1523. Link.

[213] A. H. Safavi-Naeini et al. “Electromagnetically induced transparency and slow light with optomechanics”. In: *Nature* 472.7341 (Mar. 2011), pp. 69–73. Link.

[214] Xufeng Zhang et al. “Strongly Coupled Magnons and Cavity Microwave Photons”. In: *Physical Review Letters* 113.15 (Oct. 2014). Link.

[215] C. A. Potts et al. “Dynamical Backaction Magnomechanics”. In: *Physical Review X* 11.3 (Sept. 2021). Link.

[216] C. A. Potts et al. “Dynamical backaction evading magnomechanics”. In: *Physical Review B* 107.14 (Apr. 2023). Link.

[217] J. D. Teufel et al. “Sideband cooling of micromechanical motion to the quantum ground state”. In: *Nature* 475.7356 (July 2011), pp. 359–363. Link.

[218] M. Brune et al. “From Lamb shift to light shifts: Vacuum and subphoton cavity fields measured by atomic phase sensitive detection”. In: *Phys. Rev. Lett.* 72 (21 May 1994), pp. 3339–3342. Link.

[219] Jay Gambetta et al. “Qubit-photon interactions in a cavity: Measurement-induced dephasing and number splitting”. In: *Phys. Rev. A* 74 (4 Oct. 2006), p. 042318. Link.

[220] H. J. Carmichael. “Breakdown of Photon Blockade: A Dissipative Quantum Phase Transition in Zero Dimensions”. In: *Phys. Rev. X* 5 (3 Sept. 2015), p. 031028. Link.

[221] Th. K. Mavrogordatos. “Quantum phase transitions in the driven dissipative Jaynes-Cummings oscillator: From the dispersive regime to resonance”. In: *Europhysics Letters* 116.5 (Jan. 2017), p. 54001. Link.

[222] Leonardo Ermann et al. “Jaynes-Cummings model under monochromatic driving”. In: *Phys. Rev. A* 102 (3 Sept. 2020), p. 033729. Link.

[223] Paul Brookes et al. “Critical slowing down in circuit quantum electrodynamics”. In: *Science Advances* 7.21 (2021), eabe9492. Link.

[224] Jay Gambetta et al. “Quantum trajectory approach to circuit QED: Quantum jumps and the Zeno effect”. In: *Phys. Rev. A* 77 (1 Jan. 2008), p. 012112. Link.

[225] J. R. Schrieffer and P. A. Wolff. “Relation between the Anderson and Kondo Hamiltonians”. In: *Phys. Rev.* 149 (2 Sept. 1966), pp. 491–492. Link.

[226] N B Delone and Vladimir P Krainov. “AC Stark shift of atomic energy levels”. In: *Physics-Uspekhi* 42.7 (July 1999), p. 669. Link.

[227] Frederick W. Strauch et al. “Strong-Field Effects in the Rabi Oscillations of the Superconducting Phase Qubit”. In: *IEEE Transactions on Applied Superconductivity* 17.2 (2007), pp. 105–108.

[228] I. C. Rodrigues, D. Bothner, and G. A. Steele. “Coupling microwave photons to a mechanical resonator using quantum interference”. In: *Nature Communications* 10.1 (Nov. 2019). Link.

[229] Mark Dykman. *Fluctuating Nonlinear Oscillators: From Nanomechanics to Quantum Superconducting Circuits*. Oxford University Press, July 2012. ISBN: 9780199691388. Link.

[230] F. Fani Sani et al. *Level attraction and idler resonance in a strongly driven Josephson cavity*. 2021. arXiv: 2109.01400 [cond-mat.mes-hall].

[231] Daniel Bothner, Ines C. Rodrigues, and Gary A. Steele. "Four-wave-cooling to the single phonon level in Kerr optomechanics". In: *Communications Physics* 5.1 (Feb. 2022). Link.

[232] Ines Corveira Rodrigues, Gary Alexander Steele, and Daniel Bothner. "Parametrically enhanced interactions and nonreciprocal bath dynamics in a photon-pressure Kerr amplifier". In: *Science Advances* 8.34 (Aug. 2022). Link.

[233] Ines C. Rodrigues, Gary A. Steele, and Daniel Bothner. *Photon-Pressure with a Negative Mass Microwave Mode*. 2022. arXiv: 2212.07461 [quant-ph].

[234] M.I. Dykman and M.A. Krivoglaz. "Fluctuations in nonlinear systems near bifurcations corresponding to the appearance of new stable states". In: *Physica A: Statistical Mechanics and its Applications* 104.3 (1980), pp. 480–494. Link.

[235] M. Marthaler and M. I. Dykman. "Switching via quantum activation: A parametrically modulated oscillator". In: *Physical Review A* 73.4 (Apr. 2006). Link.

[236] J. S. Ochs et al. "Amplification and spectral evidence of squeezing in the response of a strongly driven nanoresonator to a probe field". In: *Physical Review A* 103.1 (Jan. 2021). Link.

[237] J. S. Huber et al. "Spectral Evidence of Squeezing of a Weakly Damped Driven Nanomechanical Mode". In: *Physical Review X* 10.2 (June 2020). Link.

[238] J. M. Vogels et al. "Experimental Observation of the Bogoliubov Transformation for a Bose-Einstein Condensed Gas". In: *Physical Review Letters* 88.6 (Jan. 2002). Link.

[239] F. Claude et al. "High-Resolution Coherent Probe Spectroscopy of a Polariton Quantum Fluid". In: *Physical Review Letters* 129.10 (Aug. 2022). Link.

[240] Ferdinand Claude. "High resolution coherent spectroscopy of a polariton fluid : Bogoliubov modes, non equilibrium phase transitions and turbulence". Theses. Sorbonne Université, Nov. 2022. Link.

[241] Irénée Frérot et al. "Bogoliubov excitations driven by thermal lattice phonons in a quantum fluid of light". In: (Apr. 2023).

[242] V. Kohnle et al. "From Single Particle to Superfluid Excitations in a Dissipative Polariton Gas". In: *Physical Review Letters* 106.25 (June 2011). Link.

[243] Maciej Pieczarka et al. "Ghost Branch Photoluminescence From a Polariton Fluid Under Nonresonant Excitation". In: *Physical Review Letters* 115.18 (Oct. 2015). Link.

[244] Maciej Pieczarka et al. "Observation of quantum depletion in a non-equilibrium exciton–polariton condensate". In: *Nature Communications* 11.1 (Jan. 2020). Link.

[245] Joanna M. Zajac and Wolfgang Langbein. "Parametric scattering of microcavity polaritons into ghost branches". In: *Physical Review B* 92.16 (Oct. 2015). Link.

[246] Ryo Hanai, Peter B. Littlewood, and Yoji Ohashi. "Photoluminescence and gain/absorption spectra of a driven-dissipative electron-hole-photon condensate". In: *Physical Review B* 97.24 (June 2018). Link.

[247] M. Pieczarka et al. “Bogoliubov excitations of a polariton condensate in dynamical equilibrium with an incoherent reservoir”. In: *Physical Review B* 105.22 (June 2022). Link.

[248] A. Wallraff et al. “Sideband Transitions and Two-Tone Spectroscopy of a Superconducting Qubit Strongly Coupled to an On-Chip Cavity”. In: *Physical Review Letters* 99.5 (July 2007). Link.

[249] I.C. Corveira Rodrigues. “Coupling Harmonic Oscillators to Superconducting Quantum Interference Cavities”. PhD thesis. Delft University of Technology (2021). Link.

[250] Tresky. *Tresky die bonder T-4909-AE*. 2022.

[251] Abhinav Kandala et al. “Hardware-efficient variational quantum eigensolver for small molecules and quantum magnets”. In: *Nature* 549.7671 (Sept. 2017), pp. 242–246. Link.

[252] T. Brecht et al. *Multilayer microwave integrated quantum circuits for scalable quantum computing*. 2015. arXiv: 1509.01127 [quant-ph].